Creation of Dipolar Quantum Mixtures of Erbium and Dysprosium

– DISSERTATION –

by

Philipp Ilzhöfer, MSc., BSc.

submitted to the Faculty of Mathematics, Computer Science, and Physics of the University of Innsbruck

in partial fulfillment of the requirements for the degree of Doctor of Philosophy (PhD)

advisors:

Univ.-Prof. Dr. Francesca Ferlaino,
Institute for Experimental Physics, University of Innsbruck
Institute for Quantum Optics and Quantum Information of the Austrian Academy of Sciences

Univ.-Prof. Dr. Rudolf Grimm,
Institute for Experimental Physics, University of Innsbruck
Institute for Quantum Optics and Quantum Information of the Austrian Academy of Sciences

Innsbruck, August, 2020

Eidesstattliche Erklärung

Ich erkläre hiermit an Eides statt durch meine eigenhändige Unterschrift, dass ich die vorliegende Arbeit selbständig verfasst und keine anderen als die angegebenen Quellen und Hilfsmittel verwendet habe. Alle Stellen, die wörtlich oder inhaltlich den angegebenen Quellen entnommen wurden, sind als solche kenntlich gemacht.

Die vorliegende Arbeit wurde bisher in gleicher oder ähnlicher Form noch nicht als Magister-/Master-/Diplomarbeit/Dissertation eingereicht.

Statutory declaration

I hereby declare by my personal signature that I have authored this thesis independently and that I have not used other than the declared sources and resources. All material which has been quoted either literally or by content from the used sources has been explicitly marked.

The present thesis has not yet been submitted in the same or a similar form as a Magister/master's/diploma thesis/dissertation.

Philipp Ilzhöfer	Innsbruck, den

Synopsis

Over the past two decades, ultracold atom systems and especially ultracold quantum gas experiments underwent a steep progression curve and emerged as highly versatile experimental platforms. Rapid technological advances opened new paths to a large variety of different experimental techniques allowing nowadays not only for a high degree of control at the quantum level but also for the investigation of the most complex elements within the periodic table of elements. Recently, the highly magnetic lanthanoids erbium and dysprosium, the most magnetic element of all, moved into focus, as both introduce the magnetic dipole-dipole interaction, a long-range anisotropic interaction, to those highly controllable experimental platforms via their intrinsically large magnetic moments.

This PhD thesis presents the first experimental apparatus for heteronuclear quantum-degenerate dipolar mixtures of erbium and dysprosium. Its structure follows the developments over approximately five years from this endeavor's very beginning in early 2015 to the achievement of a state-of-the-art system in the field of dipolar quantum gases today. Following a comparison of both elements' experimentally relevant physical and atomic properties as well as the theoretical description of a (heteronuclear) dipolar Bose-Einstein condensate, it reviews the complete layout of the experimental apparatus and the obtained results in three chapters.

First, it covers a dual-species intercombination-line magneto-optical trap in a novel open-top configuration as starting point for all further experimental steps. This encompasses a detailed description of the ultra-high-vacuum apparatus, the magnetic field systems as well as the laser systems and their integration to the experimental apparatus.

Second, it addresses the production of five different heteronuclear dipolar Bose-Einstein condensates and of one quantum-degenerate Bose-Fermi mixture via evaporative cooling in an optical dipole trap. The experimental results revealed complex evaporation dynamics due to sympathetic cooling as well as first evidence for in-trap interspecies interactions between the Bose-Einstein condensates of erbium and dysprosium.

Third, it presents its contributions to the first experimental realization of supersolid phases in dipolar quantum gases of erbium and dysprosium in early 2019. Among the ground-breaking work in three different research groups, it contributed the achievement of a supersolid phase in a dipolar quantum gas of dysprosium with long lifetimes and the direct evaporative cooling into it, and, in a second study, insights into the phase coherence dynamics of an out-of-equilibrium dysprosium supersolid.

This PhD thesis concludes with a summary of the achieved results and provides an outlook at upgrades to the experimental apparatus, next characterization measurements and first experiments with quantum-degenerate dipolar mixtures of erbium and dysprosium. Further, it discusses prospects for multivalent Rydberg atoms, as the complex valence electron configurations of lanthanoids might facilitate novel Rydberg manipulation methods. For this purpose, this PhD work developed a dedicated science module.

Zusammenfassung

Im Verlauf der letzten zwei Jahrzehnte durchliefen ultrakalte Atomsysteme und insbesondere ultrakalte Quantengas-Experimente eine steile Progressionskurve und gingen hierbei als äußerst vielseitige experimentelle Plattformen hervor. Rapide technologische Fortschritte eröffneten neue Pfade zu einer großen Vielfalt an verschiedenen experimentellen Techniken, die heutzutage nicht nur ein hohes Maß an Kontrolle auf der Quantenebene, sondern auch die Erforschung der komplexesten Elemente im Periodensystem der Elemente ermöglichen. Vor Kurzem rückten die hochmagnetischen Lanthanoide Erbium and Dysprosium, das magnetischste aller Elemente, in den Fokus, da beide durch ihre intrinsisch großen magnetischen Momente die magnetische Dipol-Dipol-Wechselwirkung, eine langreichweitige, anisotrope Wechselwirkung, in diese hochgradig kontrollierbaren experimentellen Plattformen einbringen.

Diese Dissertation präsentiert die erste Versuchsapparatur für heteronukleare, quantenentartete, dipolare Mischungen aus Erbium und Dysprosium. Ihre Struktur folgt hierbei den Entwicklungen über einen Zeitraum von etwa fünf Jahren, von den Anfängen dieses Unterfangens zu Beginn des Jahres 2015, hin zum Erreichen eines hochmodernen Systems auf dem Gebiet der dipolaren Quantengase heute. Anschließend an einen Vergleich der experimentell relevanten physikalischen und atomaren Eigenschaften beider Elemente, sowie der theoretischen Beschreibung eines (heteronuklearen) dipolaren Bose-Einstein-Kondensats, schildert sie in drei Kapiteln das gesamte Layout der Versuchsapparatur sowie die erzielten Forschungsergebnisse.

Zunächst behandelt sie eine magneto-optische Falle für beide Spezien, die auf einer Interkombinationslinie in einer neuartigen *open-top* Konfiguration operiert und als Startpunkt aller weiterer experimenteller Schritte dient. Dies umfasst eine detaillierte Beschreibung der Ultrahochvakuum-Apparatur, der Magnetfeldsysteme, sowie der Lasersysteme und deren Integration in die Versuchsapparatur.

Anschließend befasst sie sich mit der Erzeugung von fünf verschiedenen heteronuklearen, dipolaren Bose-Einstein-Kondensaten und einer quanten-entarteten Bose-Fermi-Mischung durch Verdampfungskühlung in einer optischen Dipolfalle. Die experimentellen Resultate zeigten hierbei eine komplexe Verdampfungsdynamik aufgrund von sympathetischem Kühlens, sowie erste Hinweise auf Interspezies-Wechselwirkungen zwischen den gefangenen Bose-Einstein-Kondensaten von Erbium und Dysprosium.

Drittens stellt sie ihre Beiträge zur ersten experimentellen Realisierung von suprasoliden Phasen in dipolaren Quantengasen aus Erbium und Dysprosium zu Beginn des Jahres 2019 vor. Unter den bahnbrechenden Arbeiten in drei verschiedenen Forschungsgruppen trug sie das Erreichen einer suprasoliden Phase in einem dipolaren Quantengas aus Dysprosium mit langer Lebensdauer und das direkte Verdampfungskühlen in diese, und, in einer zweiten Studie, Einblicke in die Phasenkohärenzdynamik eines Dysprosium-Suprafestkörpers außerhalb seines Gleichgewichts bei.

Diese Dissertation schließt mit einer Zusammenfassung der erreichten Ergebnisse und gibt einen Ausblick auf Erweiterungen der Versuchsapparatur, nächste Charakterisierungsmessungen und erste Experimente mit quanten-entarteten, dipolaren Mischungen aus Erbium und Dysprosium. Außerdem diskutiert sie Perspektiven für multivalente Rydbergatome, da die komplexen Valenzelektronenkonfigurationen der Lanthanoide möglicherweise neue Manipulationsmethoden für Rydbergatome ermöglichen könnten. Für diesen Zweck hat diese Doktorarbeit ein dediziertes Wissenschaftsmodul entwickelt.

Contents

Chapter 1

Introduction

Already in the early days of quantum mechanics, fundamentally important theoretical work devoted to the quantum statistical character of particles. In 1924, Albert Einstein extended Satyendra Nath Bose's approach, to reconcile the photon hypothesis with Planck's law [1], to an ideal gas [2], with a direct proceeding in 1925 [3]. Shortly after, in 1926, Enrico Fermi [4] and Paul Dirac [5] independently described the influence of Pauli's exclusion principle. These initial findings gave rise to the understanding that all integer-spin particles (bosons) follow Bose-Einstein statistics and can undergo a quantum statistical phase transition, the Bose-Einstein condensation, to a macroscopic occupation of a system's lowest energy or ground state [6, 7], whereas half integer-spin particles (fermions) follow the Fermi-Dirac statistics, governing a quantum-degenerate Fermi gas (DFG) [8]. However, for quantum statistics to generally take over, and thus to determine the character of a system, the particles' thermal de Broglie wavelength must be comparable to or larger than the mean interparticle distance [6, 7].

After decades of extensive research, ultracold dilute atomic gases emerged as prime experimental platform to study a regime of dominating quantum statistics in a highly controllable environment. The groundbreaking work on techniques to laser-cool and trap atomic gases, for which Steven Chu, Claude Cohen-Tannoudji and William D. Phillips received the Nobel prize award *for development of methods to cool and trap atoms with laser light* in 1997 [9], eventually led to the first realization of Bose-Einstein condensates (BECs) of rubidium [10] and of sodium [11] in 1995. In the following, a series of experiments confirmed for instance the coherence of a BEC by interfering two BECs in free expansion [12] or the superfluid character of interacting BECs by quantized vortex excitations [13, 14, 15]. The major importance of the first observation of Bose-Einstein condensation led to the prompt Nobel prize award to Eric A. Cornell, Carl E. Wieman and Wolfgang Ketterle *for the achievement of Bose-Einstein condensation in dilute gases of alkali atoms, and for early fundamental studies of the properties of the condensates* soon after in 2001 [16].

Meanwhile, in 1999, Deborah S. Jin's group reported the first realization of a two spin-component DFG of potassium at temperatures as low as half the Fermi temperature [17]. In the following, for instance [18] demonstrated strong interactions in a DFG of lithium or [19] and [20, 21] utilized the BEC-BCS crossover to produce molecular BECs of fermionic potassium and of fermionic lithium, respectively.

Nowadays, there exist BECs of atomic hydrogen [22], all alkali metals except francium [10, 11, 23, 24, 25], the alkaline-earth metals calcium [26] and strontium [27], the

transition metal chromium [28], the lanthanoids dysprosium [29], erbium [30], thulium [31] and ytterbium [32], and the noble gas helium [33], as well as DFGs of potassium [17], lithium [34], strontium [35], chromium [36], dysprosium [37], erbium [38], ytterbium [39] and helium [40]. All these elements differ in their properties starting from their isotopes' quantum statistics ranging over their laser cooling properties to their interactions. The research field of ultracold quantum gases reflects this diversity not only in the vast variety of raised scientific questions to be answered and of pursued research directions, for instance the field of quantum simulation [41] or the field of quantum metrology [42] with exemplarily three-dimensional optical lattice clocks utilizing DFGs [43], but also in the available experimental techniques. A particular strength of ultracold quantum gas experiments lies within the multitude of external control and manipulation parameters.

In general, magnetic traps [7] and single- or crossed-beam optical dipole traps [44] provide ideal conditions for the initial production steps, but their respective working principle can even further extend to tailored trapping potential landscapes specific to an addressed scientific question. Here, optical lattices emerged as a powerful tool to investigate quantum many-body systems and their quantum phase transitions such as the superfluid-Mott insulator transition [45]. In combination with high-resolution imaging, those are even observable at the single-atom level, as for instance [46] and [47] demonstrated with rubidium for the transition to a Mott insulator phase or [48] with fermionic lithium for a transition to an antiferromagnet.

Moreover, ultracold quantum gases offer a precise control over their interparticle interactions. Magnetically tunable Feshbach resonances enable the adjustment of the contact interaction [49], which opens a wide spectrum of research directions already for purely contact-interacting systems. One particular research focus are heteronuclear mixtures of purely contact-interacting elements, as the additional interspecies interactions increase the complexity and open new routes of manipulation. Experiments achieved quantum degeneracy for instance for Bose-Bose mixtures of rubidium and potassium [50], for Bose-Fermi mixtures of sodium and lithium [51] or for Fermi-Fermi mixtures of lithium and potassium [52]. One among many research directions leads along the production of polar ground-state molecules by initially associating weakly-bound heteronuclear Feshbach molecules, such as potassium-rubidium [53], rubidium-cesium [54, 55] or sodium-potassium [56] molecules, and the achievement of quantum degeneracy [57]. As their constituents differ in electronegativity, these molecules have tunable electric dipole moments, and thus give rise to the long-range anisotropic electric dipole-dipole interaction. This aspect is of interest, among others, in the field of ultracold chemistry or for quantum information or quantum simulation applications [58]. Because of the complexity of this approach, however, the direct laser cooling and trapping of polar molecules such as strontium monofluoride [59, 60, 61], yttrium oxide [62], calcium monofluoride [63, 64] or calcium monohydroxide [65] is another viable option.

Alternatively, magnetic elements such as chromium, erbium or dysprosium, the most magnetic one in the periodic table of elements, facilitate direct access to the long-range anisotropic magnetic dipole-dipole interaction via their intrinsically large magnetic moments [66], and thus awakened great interest in the community. The aim of this PhD thesis was the first production of heteronuclear quantum-degenerate dipolar mixtures of erbium and dysprosium. The following Section 1.1 gives a brief overview over the major experimental developments in the field of magnetically dipolar quantum gases up to this PhD work's starting point in early 2015 and Section 1.2 highlights the research topics.

1.1 State of the art

In 2005, [28] reported the first observation of Bose-Einstein condensation of chromium, and thus opened a path to investigate dipolar quantum gases. Consequently, while the influence of the magnetic dipole-dipole interaction already became evident with the demonstration of demagnetization cooling of chromium [67], a series of experiments studied a chromium BEC, for instance its behavior in the strongly dipolar regime [68], its stability diagram depending on the contact interaction strength and the trap geometry [69] or its so-called d-wave collapse [70]. Although these first results represent only a glimpse of the magnetic dipole-dipole interaction's true potential in the context of dipolar quantum gases, they reveal at the same time a major experimental drawback of a chromium BEC, as it generally requires the adjustment of the contact interaction strength to be in the strongly dipolar regime.

Meanwhile, pioneering work on laser cooling and trapping concepts for erbium was underway and, in 2006, led to the first erbium magneto-optical trap (MOT) [71] and soon after, in 2008, to a further extension by a blue-detuned narrow-line MOT [72]. Because of the elements' great similarities, the same techniques are applicable to dysprosium and formed the basis for the first dysprosium MOT in 2010 [73] as well as the first dysprosium BEC, and thus the first intrinsically strongly dipolar Bose-Einstein condensate (dBEC) in 2011 [29]. In the following year 2012, a number of rapid developments occurred: first, [74] presented an intercombination-line MOT for erbium, immediately followed by the first observation of an erbium dBEC [30] and of a dysprosium DFG [37], respectively. For the latter, bosonic dysprosium served as sympathetic coolant but did not reach quantum degeneracy. In 2014, [38] realized the first erbium DFG via pure universal dipolar scattering and [75] adopted the intercombination-line MOT approach to dysprosium.

Subsequent to these fundamental results, which established first production routes for dipolar quantum gases of erbium or dysprosium, first investigations devoted to their respective Feshbach resonance spectra [76, 77]. Here, [77] revealed a chaotic scattering behavior in erbium, which a comparative study confirmed also for dysprosium [78].

1.2 Thesis research topics

This PhD thesis presents the first experimental apparatus for combining erbium and dysprosium in the field of dipolar quantum gases. The endeavor started in early 2015 with an empty lab and the aim to develop and to construct an experimental apparatus for a rapid but highly robust production of heteronuclear quantum-degenerate dipolar mixtures of both elements with a similar or even superior performance in comparison to respective single-species experiments. A second key aspect in the development process was the achievement of a high versatility to allow for more advanced experiments in specialized experimental environments in the future.

The process from initial conceptual ideas to the start of construction took approximately one year. Over the course of the following three years, the experimental apparatus became progressively operational. It first demonstrated a dual-species intercombination-line MOT in a novel open-top configuration and subsequently various heteronuclear dBECs, the binary Bose-Einstein condensation in atomic mixtures of two highly magnetic elements, and a quantum-degenerate Bose-Fermi mixture. In early 2019, it joined in at the forefront of the search for supersolidity in dipolar quantum gases.

This PhD thesis led to four publications in total and highlights the complete PhD work over the next five chapters in the following structure:

Chapter 2 summarizes and compares the most important properties of erbium and dysprosium, encompassing their vapor pressures, electronic ground state structures, magnetic moments as well as laser cooling and trapping properties. Moreover, it examines dBECs and their interactions in the single-species and the heteronuclear case.

Chapter 3 describes the experimental apparatus in the context of this PhD thesis' first publication on a dual-species intercombination-line MOT for erbium and dysprosium in a novel open-top configuration. It details the ultra-high vacuum apparatus, the magnetic field systems, the various laser systems and their integration into the experimental apparatus as well as the imaging and the control system.

Publication I:
Two-species five-beam magneto-optical trap for erbium and dysprosium
Philipp Ilzhöfer, Gianmaria Durastante, Alexander Patscheider, Arno Trautmann, Manfred J. Mark and Francesca Ferlaino
Physical Review A, **97**, 023633, (2018), DOI: 10.1103/PhysRevA.97.023633

Chapter 4 reviews the production of five different heteronuclear dBECs and of a quantum-degenerate Bose-Fermi mixture in the context of this PhD thesis' second publication. It addresses the optical dipole trap, the experimental sequence as well as the evaporation dynamics for all studied isotope mixtures of erbium and dysprosium.

Publication II:
Dipolar Quantum Mixtures of Erbium and Dysprosium Atoms
Arno Trautmann, Philipp Ilzhöfer, Gianmaria Durastante, Claudia Politi, Maximilian Sohmen, Manfred J. Mark and Francesca Ferlaino
Physical Review Letters, **121**, 213601, (2018), DOI: 10.1103/PhysRevLett.121.213601,
Editors' suggestion,
Featured in Physics 11, s135, Synopsis: Making Mixtures of Magnetic Condensates

Chapter 5 highlights supersolidity in dipolar quantum gases in the context of this PhD thesis' third publication, where it contributed the experimental realization of a long-lived dysprosium supersolid, even via direct evaporative cooling, and of its fourth publication on the rigidity of global phase coherence and the rephasing dynamics of an out-of-equilibrium dysprosium supersolid. It briefly reviews past research efforts and discusses the special aspects supporting a supersolid phase in a dipolar quantum gas.

Publication III:
Long-Lived and Transient Supersolid Behaviors in Dipolar Quantum Gases
Lauriane Chomaz, Daniel Petter, Philipp Ilzhöfer, Gabriele Natale, Arno Trautmann, Claudia Politi, Gianmaria Durastante, Rick M. W. van Bijnen, Alexander Patscheider, Maximilian Sohmen, Manfred J. Mark and Francesca Ferlaino
Physical Review X, **9**, 021012 (2019), DOI: 10.1103/PhysRevX.9.021012,
Featured in Physics 12, 38, Viewpoint: Dipolar Quantum Gases go Supersolid

Publication IV:
Phase coherence in out-of-equilibrium supersolid states of ultracold dipolar atoms
Philipp Ilzhöfer, Maximilian Sohmen, Gianmaria Durastante, Claudia Politi, Arno Trautmann, Giacomo Morpurgo, Thierry Giamarchi, Lauriane Chomaz, Manfred J. Mark and Francesca Ferlaino
arXiv-preprint, arXiv:1912.10892

Chapter 6 concludes this PhD thesis and provides an outlook on the next experimental steps employing these first quantum-degenerate dipolar mixtures of erbium and dysprosium. Further, it explores multivalent Rydberg atoms of lanthanoids and describes a dedicated science module, which comprises an in-vacuum three-dimensional electric field control and microchannel plate detectors.

Note that, as this PhD thesis focuses on the two highly magnetic elements erbium and dysprosium, the following discussion and the introduced concepts are exclusively in view of the magnetic dipole-dipole interaction, even if concepts are analogous to an electrically dipolar system.

Chapter 2

Erbium and Dysprosium

Erbium (Er) and dysprosium (Dy) are, as Figure 2.1 shows, both part of the lanthanoid series in the sixth period of the periodic table of elements [79]. As next-nearest neighbors, uniquely characterized by proton numbers $Z_{\mathrm{Er}} = 68$ and $Z_{\mathrm{Dy}} = 66$ and only separated by holmium [79], they manifest qualitatively similar but distinct properties.

This second chapter provides a careful comparison of both elements with a special focus on the experimentally relevant aspects. Section 2.1 starts with their physical properties and isotopes. Then, Section 2.2 studies their atomic properties incorporating energy level diagrams, laser cooling transitions and atomic polarizabilities. Additionally, Section 2.3 explores single-species and heteronuclear dBECs and their interactions.

2.1 Physical properties and isotopes

Assuming room temperature and standard conditions for pressure, erbium and dysprosium exist in solid phases exhibiting a hexagonally close-packed lattice [79] with paramagnetic ordering [81, 82]. Moreover, both have similar densities $\rho_{\mathrm{Er},25\,^\circ\mathrm{C}} = 9.07\,\mathrm{g/cm^3}$ and $\rho_{\mathrm{Dy},25\,^\circ\mathrm{C}} = 8.55\,\mathrm{g/cm^3}$, melting points $T_{\mathrm{m,Er}} = 1529\,^\circ\mathrm{C}$ and $T_{\mathrm{m,Dy}} = 1412\,^\circ\mathrm{C}$ as well as boiling points $T_{\mathrm{b,Er}} = 2868\,^\circ\mathrm{C}$ and $T_{\mathrm{b,Dy}} = 2567\,^\circ\mathrm{C}$ [79].

From an experimental point of view, the great similarity in $T_{\mathrm{m,Er}}$ and $T_{\mathrm{m,Dy}}$ is of particular interest, which, besides the similar laser cooling properties (see Section 2.2.1), facilitates the realization of a dual-species atomic beam source. However, despite these beneficial aspects, the vapor pressures $p_{\mathrm{vap,Er}}$ and $p_{\mathrm{vap,Dy}}$ differ significantly and scale in

57	58	59	60	61	62	63	64	65	66	67	68	69	70	71
La	Ce	Pr	Nd	Pm	Sm	Eu	Gd	Tb	Dy	Ho	Er	Tm	Yb	Lu
138.91	140.12	140.91	144.24	(145)	150.36	151.96	157.25	158.93	162.50	164.93	167.26	168.93	173.05	174.97
$5d6s^2$	$4f5d6s^2$	$4f^36s^2$	$4f^46s^2$	$4f^56s^2$	$4f^66s^2$	$4f^76s^2$	$4f^75d6s^2$	$4f^96s^2$	$4f^{10}6s^2$	$4f^{11}6s^2$	$4f^{12}6s^2$	$4f^{13}6s^2$	$4f^{14}6s^2$	$4f^{14}5d6s^2$
$^2D_{3/2}$	$^1G_4$	$^4I_{9/2}$	$^5I_4$	$^6H_{5/2}$	$^7F_0$	$^8S_{7/2}$	$^9D_2$	$^6H_{15/2}$	$^5I_8$	$^4I_{15/2}$	$^3H_6$	$^2F_{7/2}$	$^1S_0$	$^2D_{3/2}$
$1.2\,\mu_B$	$3.8\,\mu_B$	$3.3\,\mu_B$	$2.4\,\mu_B$	$0.8\,\mu_B$	$0\,\mu_B$	$7.0\,\mu_B$	$5.3\,\mu_B$	$9.9\,\mu_B$	$9.9\,\mu_B$	$9.0\,\mu_B$	$7.0\,\mu_B$	$4.0\,\mu_B$	$0\,\mu_B$	$1.2\,\mu_B$

Figure 2.1: The lanthanoid series in the periodic table of elements. The elements' symbols, proton numbers, standard atomic weights, valence electron configurations and electronic ground states are from [79]. Moreover, equation (2.11) provides with the Landé g-factors g_J in [80] the magnetic moments μ for the stretched states of maximal $|m_J|$ in the ground state manifolds. Erbium and dysprosium are in violet and orange.

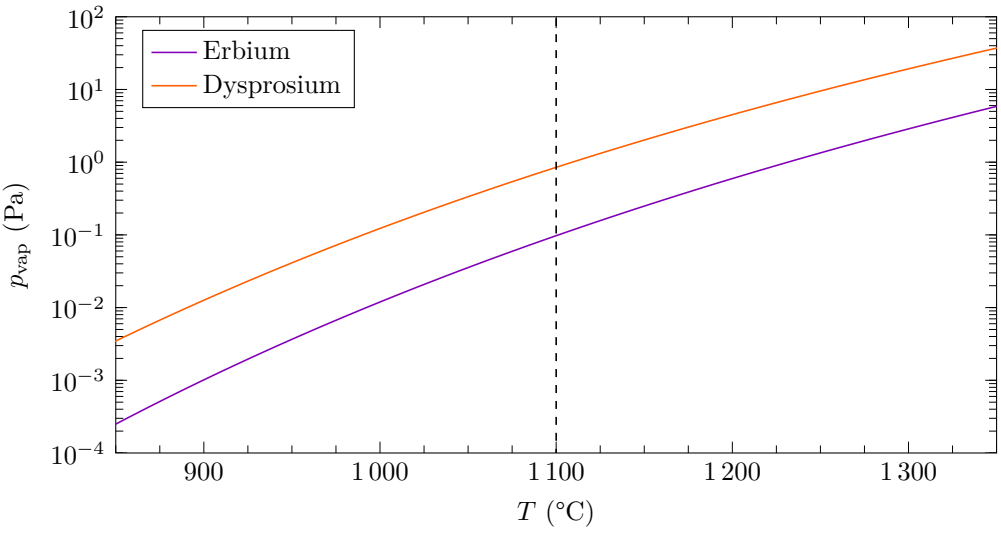

Figure 2.2: Calculated vapor pressures $p_{\mathrm{vap,Er}}$ (violet) and $p_{\mathrm{vap,Dy}}$ (orange) as a function of temperature T in °C by replacing T with $(T + 273.15\,\mathrm{K})$ in equation (2.1). The vertical dashed line indicates $T = 1100\,°\mathrm{C}$ with $p_{\mathrm{vap,Er}} = 0.098\,\mathrm{Pa}$ and $p_{\mathrm{vap,Dy}} = 0.850\,\mathrm{Pa}$.

units of Pa as a function of temperature T in units of K as [79]

$$p_{\mathrm{vap}}\,(T) = 10^{5.006 + A + B/T + C\log_{10} T + D/T^3}. \tag{2.1}$$

The quadruple (A, B, C, D) denotes parameters characteristic to each element with $(9.916, -16642, -1.2154, -)_{\mathrm{Er}}$ or $(9.579, -15336, -1.1114, -)_{\mathrm{Dy}}$ [79]. Figure 2.2 shows $p_{\mathrm{vap,Er}}$ and $p_{\mathrm{vap,Dy}}$ in the temperature range 850 °C to 1350 °C, where $p_{\mathrm{vap,Er}} = 0.098\,\mathrm{Pa}$ and $p_{\mathrm{vap,Dy}} = 0.850\,\mathrm{Pa}$ at a typical atomic beam source temperature of $T = 1100\,°\mathrm{C}$. A possible layout for a dual-species atomic beam source must pay special attention to this factor of close to nine in $p_{\mathrm{vap,Er}}$ and $p_{\mathrm{vap,Dy}}$, and must balance it. Chapter 3 describes a simple modification to a commercial dual-filament effusion cell as one possible solution.

Both elements have multiple naturally occurring stable isotopes varying widely in their abundance [79]. Four isotopes each exhibit an abundance larger than 14 %, large enough for an efficient use in the experiment. Table 2.1 compares their basic characteristics. Considering Table 2.1, it is worth highlighting that for both elements bosonic as well as fermionic isotopes, and thus almost mass-balanced heteronuclear Bose-Bose, Bose-Fermi or Fermi-Fermi mixtures are experimentally accessible.

2.2 Atomic properties

All lanthanoids combine 58 core electrons in a xenon-like configuration ([Xe]) with complicated valence electron configurations [79] (see Figure 2.1). As part of the f-block in the periodic table of elements, their majority exhibits unpaired electrons in the 4f (in specific cases also in the 5d) valence shell, which lies within a surrounding entirely filled 6s valence shell (see Figure 2.3). This submerged structure has far-reaching consequences for the lanthanoids. It is for instance the cause for their anisotropic electronic ground states except europium and ytterbium [79] (see Figure 2.1), or their highly complex

Table 2.1: Characteristics of all erbium and dysprosium isotopes with an abundance larger than 14 % [79]. The atomic masses m, the abundances as well as the nuclear spin quantum numbers I are from [79]. The + and the − sign describe the relative orientation of the nuclear spin **I**. The neutron numbers N result from subtraction of the proton number $Z_{\mathrm{Er}} = 68$ or $Z_{\mathrm{Dy}} = 66$ from the respective isotope's mass number and determine the quantum statistics (B=bosonic or F=fermionic).

		Erbium				Dysprosium			
		^{166}Er	^{167}Er	^{168}Er	^{170}Er	^{161}Dy	^{162}Dy	^{163}Dy	^{164}Dy
Atomic mass (u)	m	165.9	166.9	167.9	169.9	160.9	161.9	162.9	163.9
Abundance (%)		33.50	22.87	26.98	14.91	18.89	25.48	24.90	28.26
Neutron number	N	98	99	100	102	95	96	97	98
Statistics		B	F	B	B	F	B	F	B
Nuclear spin	I	0	$+7/2$	0	0	$+5/2$	0	$-5/2$	0

energy level diagrams featuring valence electron excitations from either the 6s or the 4f valence shell (see Section 2.2.1).

As Figure 2.3 illustrates, erbium and dysprosium in their respective electronic ground state distribute 14 or 12 valence electrons among the partially filled 4f and the full 6s valence shell, leaving two or four electrons unpaired. Hence, their characteristic electron configurations are [79]

$$\text{Er: } [\mathrm{Xe}]\,4\mathrm{f}^{12}6\mathrm{s}^2 \qquad \text{Dy: } [\mathrm{Xe}]\,4\mathrm{f}^{10}6\mathrm{s}^2. \tag{2.2}$$

Commonly, the quantum number triplet (L, S, J) further characterizes their electronic ground states, analogous to all lanthanoids, in accordance with Russel-Saunders coupling. Here, the valence electrons' individual angular momenta **l** and spins **s** couple to the total orbital momentum **L** and the total spin **S**, which combine to the total electronic angular momentum **J** [83]. The resulting fine structure has three states $J_{\mathrm{Er}} \in \{4, 5, 6\}$ or five states $J_{\mathrm{Dy}} \in \{4, 5, \ldots, 8\}$ with the electronic ground states [79]

$$\text{Er: } {}^3\mathrm{H}_6 \qquad \text{Dy: } {}^5\mathrm{I}_8. \tag{2.3}$$

These states characterize all bosons (^{166}Er, ^{168}Er, ^{170}Er, ^{162}Dy and ^{164}Dy), which show no nuclear spin **I** (quantum numbers $I_{\mathrm{Er}} = I_{\mathrm{Dy}} = 0$ [79], see Table 2.1), and have as a direct consequence only a fine structure. The fermions (^{167}Er, ^{161}Dy and ^{163}Dy) are more complex due to the hyperfine coupling of their **I** with **J** to the total atomic angular momentum **F** [83]. Considering $I_{\mathrm{Er}} = 7/2$ and $I_{\mathrm{Dy}} = 5/2$ [79] (see Table 2.1), the emerging hyperfine structure with quantum numbers F has eight states $F_{\mathrm{Er}} \in \{5/2, 7/2, \ldots, 19/2\}$ or six states $F_{\mathrm{Dy}} \in \{11/2, 13/2, \ldots, 21/2\}$ with the electronic ground states

$$^{167}\mathrm{Er}\text{: } {}^3\mathrm{H}_6, F = 19/2 \qquad ^{161}\mathrm{Dy}\text{: } {}^5\mathrm{I}_8, F = 21/2 \qquad ^{163}\mathrm{Dy}\text{: } {}^5\mathrm{I}_8, F = 11/2. \tag{2.4}$$

The inversion in F for ^{163}Dy in comparison to ^{161}Dy is due to the relative orientation of **I** [84] (see Table 2.1). The large **L** introduce an anisotropy in the electronic ground states (2.3) and (2.4). This strongly modifies the atomic polarizabilities as well as the scattering properties, as Sections 2.2.2 and 2.3 discuss in greater detail.

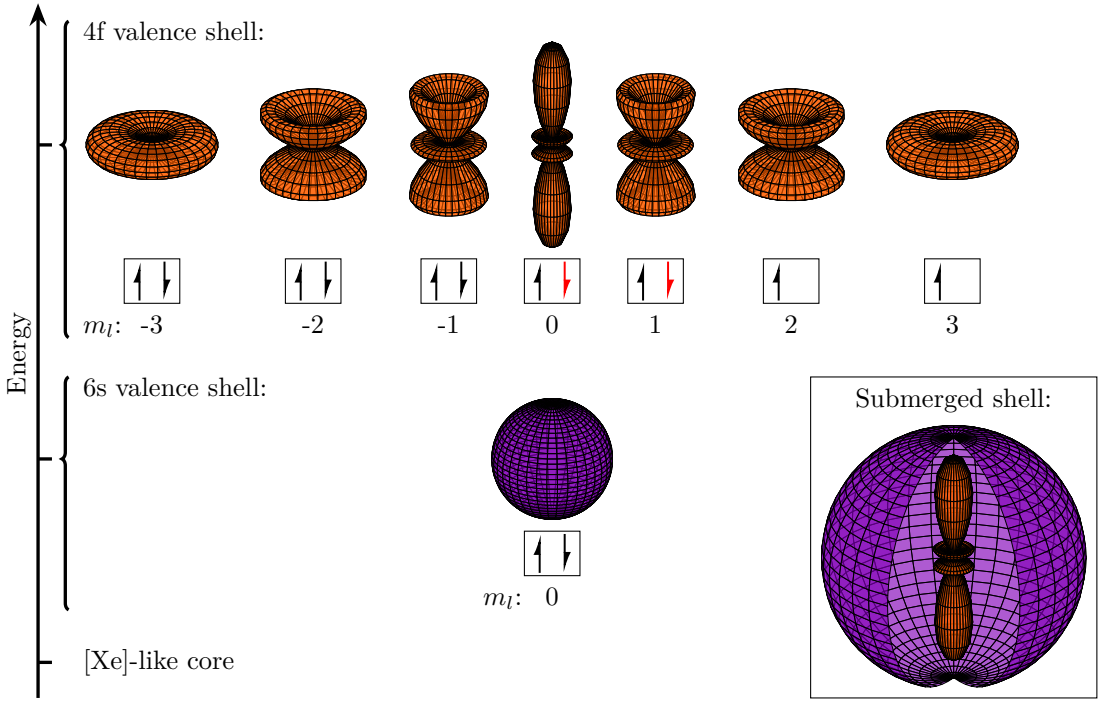

Figure 2.3: Illustration of the electronic ground state structures of erbium and dysprosium. In total 58 electrons form a xenon-like core ([Xe]), while 14 and 12 valence electrons (arrows) distribute over the 4f and the 6s valence shell, respectively. The black arrows indicate the arrangement for dysprosium, whereas the two additional red arrows complete the picture for erbium. Further, the absolute squared of spherical harmonics depict in a l, m_l-basis the anisotropy and the isotropy in the probability densities of the 4f and the 6s valence electrons, respectively. The inset sketches the submerged shell structure for the 4f (orange) and the surrounding 6s (violet) valence shell.

The lanthanoids' unpaired 4f valence electrons can give rise to large magnetic moments $\mu \gtrsim 7\,\mu_\mathrm{B}$ (see Figure 2.1), with the Bohr magneton μ_B. However, it is important to note that an anisotropic electronic ground state not necessarily coincides with a large μ and vice versa. Out of the 15 lanthanoids only europium, terbium, dysprosium, holmium and erbium have $\mu \gtrsim 7\,\mu_\mathrm{B}$. Contrary to the others, europium has the isotropic electronic ground state ${}^8\mathrm{S}_{7/2}$, but its $\mu \approx 7.0\,\mu_\mathrm{B}$ purely arises from $\mathbf{S}$.

This paragraph follows [83] and derives μ as the projection of the atomic magnetic moment $\boldsymbol{\mu}$ onto the system's quantization axis. Depending on the basis, $\boldsymbol{\mu}$ calculates as

$$\boldsymbol{\mu}_J = -g_L \frac{\mu_\mathrm{B}}{\hbar}\mathbf{L} - g_S \frac{\mu_\mathrm{B}}{\hbar}\mathbf{S} \tag{2.5}$$

or

$$\boldsymbol{\mu}_F = -g_J \frac{\mu_\mathrm{B}}{\hbar}\mathbf{J} + g_I \frac{\mu_\mathrm{N}}{\hbar}\mathbf{I} \simeq -g_J \frac{\mu_\mathrm{B}}{\hbar}\mathbf{J}, \tag{2.6}$$

with the Landé g-factors $g_L = 1$, $g_S \approx 2.0023$, g_J and g_I for $\mathbf{L}$, $\mathbf{S}$, $\mathbf{J}$ and $\mathbf{I}$, respectively, the reduced Planck constant $\hbar$ and the nuclear magneton $\mu_\mathrm{N} \ll \mu_\mathrm{B}$. This $\boldsymbol{\mu}$ couples to a weak external magnetic field $\mathbf{B}$ of value B as

$$H = -\boldsymbol{\mu}_{J,F} \cdot \mathbf{B}. \tag{2.7}$$

The projection in equation (2.7) of the single contributions of $\boldsymbol{\mu}_{J,F}$ along the respective basis vector **J** or **F** leads to the Zeeman shift

$$E_{\mathrm{ZS}} = g_{J,F} m_{J,F} \mu_{\mathrm{B}} B. \tag{2.8}$$

The magnetic quantum numbers $m_{J,F}$ describe the projections of **J** and **F** onto the quantization axis with values $\{-J, -(J-1), \ldots, J\}$ or $\{-F, -(F-1), \ldots, F\}$. Furthermore,

$$g_J = \frac{3}{2} + \frac{S(S+1) - L(L+1)}{2J(J+1)} \tag{2.9}$$

and

$$g_F = g_J \frac{F(F+1) + J(J+1) - I(I+1)}{2F(F+1)}. \tag{2.10}$$

From equation (2.8)

$$\mu = -g_{J,F} m_{J,F} \mu_{\mathrm{B}}. \tag{2.11}$$

Equation (2.9) leads with (L, S, J) from (2.3) to $g_{J,\mathrm{Er}} = 1.17$ and $g_{J,\mathrm{Dy}} = 1.25$. However, this simple picture does not fully hold for erbium and dysprosium, and various corrections are necessary to reproduce the experimental g_J [85, 86]. For $g_{J,\mathrm{Er}} = 1.16381$ and $g_{J,\mathrm{Dy}} = 1.24159$ in [80] and the ground state manifolds' stretched states of maximal $|m_{J,\mathrm{Er}}| = 6$ and $|m_{J,\mathrm{Dy}}| = 8$, equation (2.11) results in $|\mu_{\mathrm{Er}}| = 6.982\,86\,\mu_{\mathrm{B}} \approx 7.0\,\mu_{\mathrm{B}}$ and $|\mu_{\mathrm{Dy}}| = 9.932\,72\,\mu_{\mathrm{B}} \approx 9.9\,\mu_{\mathrm{B}}$. This places both among the most magnetic elements in the periodic table of elements. A large μ gives rise to the long-range anisotropic magnetic dipole-dipole interaction, which opens new paths for dipolar quantum gas experiments, as Section 2.3 examines more closely in the context of dBECs.

2.2.1 Energy level diagrams and laser cooling transitions

The first ionization energies for reaching the ionic ground states [Xe] $4f^{12}6s$ and [Xe] $4f^{10}6s$ of erbium and dysprosium, respectively, are $E_{\mathrm{I,Er}} = 6.1077\,\mathrm{eV}$ and $E_{\mathrm{I,Dy}} = 5.9389\,\mathrm{eV}$ [79], which convert to $\lambda_{\mathrm{I,Er}} = 202.997\,\mathrm{nm}$ and $\lambda_{\mathrm{I,Dy}} = 208.766\,\mathrm{nm}$. Figure 2.4 depicts excerpts of the energy level diagrams in the experimentally relevant regime from the electronic ground states up to wavenumbers $\tilde{\nu}$ of $26\,000\,\mathrm{cm}^{-1}$ or wavelengths λ of 384.615 nm [87], which is far below the first ionization thresholds at $E_{\mathrm{I,Er}}$ or $E_{\mathrm{I,Dy}}$. Despite the high complexity due to the submerged shell structure, the level diagrams reveal similar excitation paths. The arrows in Figure 2.4 indicate two transition types, each a transition of a 6s valence electron to the 6p state. Contrary to the electronic ground states, a $J_1 J_2$-coupling scheme characterizes the corresponding excited states via the notation $(J_1, J_2)_J$ [80]. Here, on the one hand the 4f valence electrons, and on the other hand the 6s and the 6p electron, couple **l** and **s** according to the Russell-Saunders scheme to $\mathbf{J}_1$ and $\mathbf{J}_2$ that result in **J** [89]. Following this scheme, both types introduce a $\Delta J = +1$-transition to a singlet $^1\mathrm{P}_1$- or a triplet $^3\mathrm{P}_1$-configuration of the remaining 6s and the excited 6p electron.

The *broad transition* to the singlet $^1\mathrm{P}_1$-configuration addresses the respective excited state [Xe] $4f^{12}\,(^3\mathrm{H}_6)\,6s6p\,(^1\mathrm{P}_1)\,(6,1)_7$ or [Xe] $4f^{10}\,(^5\mathrm{I}_8)\,6s6p\,(^1\mathrm{P}_1)\,(8,1)_9$ (violet and blue arrow in Figure 2.4). It is the strongest transition for both elements at a wavelength $\lambda_{\mathrm{Er}} = 400.910\,\mathrm{nm}$ or $\lambda_{\mathrm{Dy}} = 421.290\,\mathrm{nm}$ with a natural linewidth $\Delta\nu_{\mathrm{Er},401\,\mathrm{nm}} = 29.4\,\mathrm{MHz}$ or $\Delta\nu_{\mathrm{Dy},421\,\mathrm{nm}} = 32.2\,\mathrm{MHz}$ [90] (see Table 2.2).

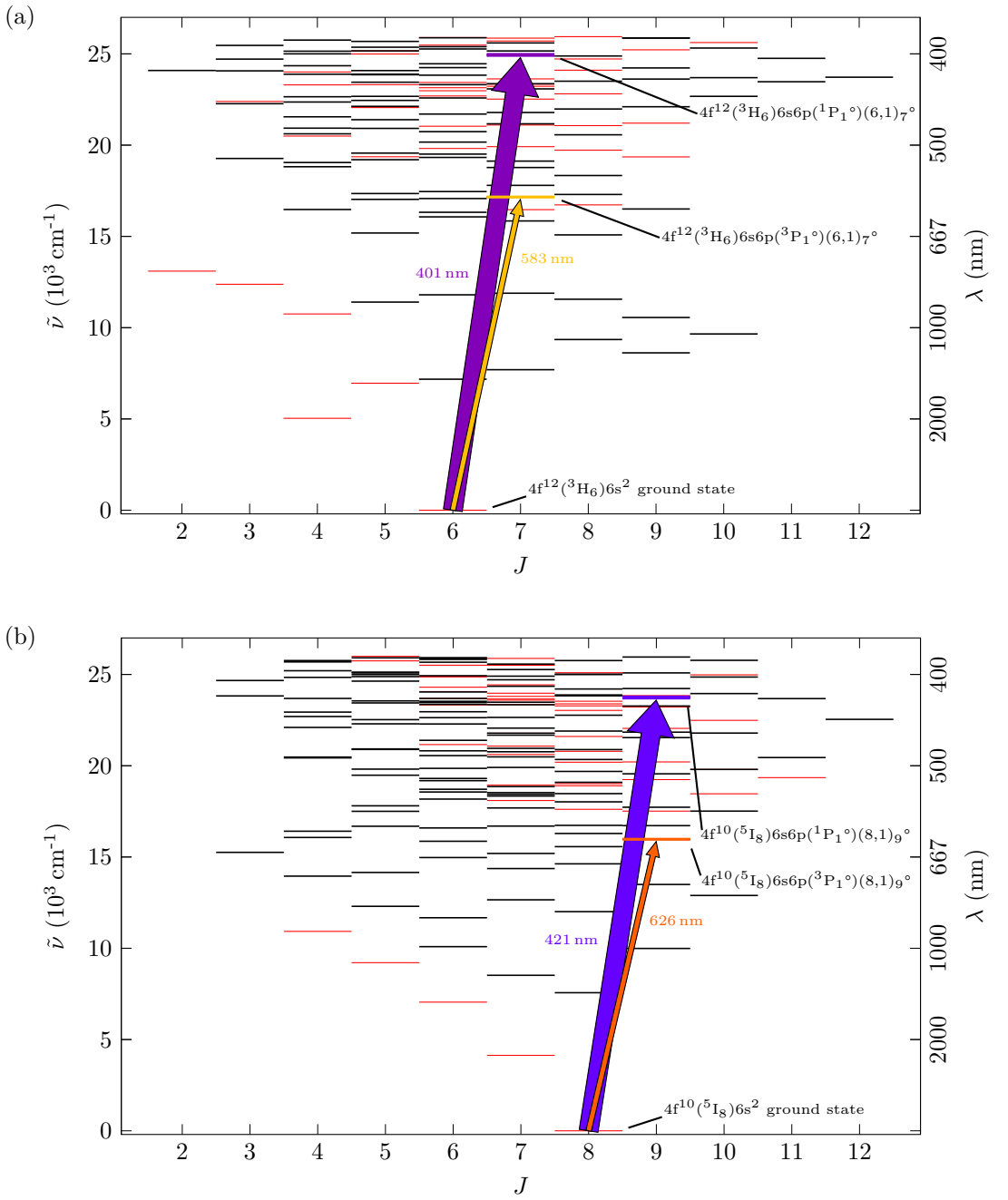

Figure 2.4: Energy level diagrams of (a) erbium and (b) dysprosium up to wavenumbers $\tilde{\nu}$ of 26 000 cm^{-1} or wavelengths λ of 384.615 nm over the total angular momentum quantum number J. The violet and the blue arrow indicate the broad transition to the $\left(^1\mathrm{P}_1\right)(6,1)_7$ and the $\left(^1\mathrm{P}_1\right)(8,1)_9$ state at $\lambda_{\mathrm{Er}} = 400.910\,\mathrm{nm}$ and $\lambda_{\mathrm{Dy}} = 421.290\,\mathrm{nm}$, whereas the yellow and the orange arrow point along the intercombination-line to the $\left(^3\mathrm{P}_1\right)(6,1)_7$ and the $\left(^3\mathrm{P}_1\right)(8,1)_9$ state at $\lambda_{\mathrm{Er}} = 582.842\,\mathrm{nm}$ and $\lambda_{\mathrm{Dy}} = 626.082\,\mathrm{nm}$, respectively. Table 2.2 summarizes and compares the transition properties. The broad transition is ideal for transverse cooling, Zeeman slowing and absorption imaging. The intercombination-line transition serves for a dual-species intercombination-line MOT (see Chapter 3). The figure originates from [88] with data from [87].

Table 2.2: Optical transitions for dual-species laser cooling and trapping of erbium and dysprosium. The wavenumbers $\tilde{\nu}$ from [87] provide the wavelengths $\lambda = 1/\tilde{\nu}$ and frequencies $\nu = c\tilde{\nu}$, with the speed of light c. For erbium, the decay rates Γ in [91] give the lifetimes $\tau = 1/\Gamma$, the natural linewidths $\Delta\nu = \Gamma/2\pi$, the saturation intensities $I_{\mathrm{sat}} = \pi hc\Gamma/3\lambda^3$ and the Doppler temperatures $T_{\mathrm{D}} = h\Gamma/4\pi k_{\mathrm{B}}$. Furthermore, the recoil temperatures $T_{\mathrm{r}} = h^2/m\lambda^2 k_{\mathrm{B}}$. Here, the Planck constant h, the Boltzmann constant k_{B} and the mass m. All formulas are either directly in or straightforwardly extractable from [83]. The dysprosium values are from [90]. The excited state Landé g-factors g'_J in [80] and the electronic ground state Landé g-factors g_J (see Section 2.2) determine the transitions' differential magnetic moments $\Delta\mu = (g'_J m'_J - g_J m_J)\,\mu_{\mathrm{B}}$ [83], with the Bohr magneton μ_{B}, and values exemplarily for the stretched states of maximal $|m'_J|$ and $|m_J|$.

Transition			Erbium		Dysprosium	
			$\left(^1\mathrm{P}_1\right)(6,1)_7$	$\left(^3\mathrm{P}_1\right)(6,1)_7$	$\left(^1\mathrm{P}_1\right)(8,1)_9$	$\left(^3\mathrm{P}_1\right)(8,1)_9$
Wavenumber	(1/cm)	$\tilde{\nu}$	24943.272	17157.307	23736.610	15972.35
Wavelength	(nm)	λ	400.910	582.842	421.290	626.082
Frequency	(THz)	ν	747.781	514.363	711.606	478.839
Decay rate	(1/s)	Γ	1.85×10^8	1.17×10^6	2.02×10^8	8.5×10^5
Lifetime		τ	5.41 ns	0.85 µs	4.94 ns	1.2 µs
Natural linewidth		$\Delta\nu$	29.4 MHz	186 kHz	32.2 MHz	135 kHz
Saturation intensity		I_{sat}	59.7 $\frac{\mathrm{mW}}{\mathrm{cm}^2}$	123 $\frac{\mu\mathrm{W}}{\mathrm{cm}^2}$	56.4 $\frac{\mathrm{mW}}{\mathrm{cm}^2}$	72 $\frac{\mu\mathrm{W}}{\mathrm{cm}^2}$
Doppler temperature		T_{D}	707 µK	4.5 µK	774 µK	3.2 µK
Recoil temperature		T_{r}	712 nK	337 nK	660 nK	298 nK
Landé g-factor		g'_J	1.160	1.195	1.22	1.29
Differential μ	(μ_{B})	$\Delta\mu$	1.137	1.382	1.047	1.677

The *intercombination-line transition* to the triplet $^3\mathrm{P}_1$-configuration couples to the excited state [Xe] $4\mathrm{f}^{12}\left(^3\mathrm{H}_6\right)6\mathrm{s}6\mathrm{p}\left(^3\mathrm{P}_1\right)(6,1)_7$ or [Xe] $4\mathrm{f}^{10}\left(^5\mathrm{I}_8\right)6\mathrm{s}6\mathrm{p}\left(^3\mathrm{P}_1\right)(8,1)_9$ (yellow and orange arrow in Figure 2.4). It has a wavelength of $\lambda_{\mathrm{Er}} = 582.842\,\mathrm{nm}$ or $\lambda_{\mathrm{Dy}} = 626.082\,\mathrm{nm}$ and being dipole-forbidden due to the change of the spin multiplet manifests itself in a natural linewidth $\Delta\nu_{\mathrm{Er},583\,\mathrm{nm}} = 186\,\mathrm{kHz}$ or $\Delta\nu_{\mathrm{Dy},626\,\mathrm{nm}} = 135\,\mathrm{kHz}$ [90] (see Table 2.2).

As first single-species experiments, [74] and [75] employed these two transitions to realize a robust intercombination-line MOT for erbium and dysprosium, respectively, that directly loads from a slowed atomic beam without the need for any optical repumping. The transition comparison in Table 2.2 shows, besides sufficiently large differential magnetic moments $\Delta\mu$, which is generally relevant for laser cooling and trapping techniques, significant differences, which determine the application in the experiment [74, 75, 92]. The broad transition's large decay rate $\Gamma_{\mathrm{Er},401\,\mathrm{nm}}$ or $\Gamma_{\mathrm{Dy},421\,\mathrm{nm}}$ is optimal for transverse cooling or Zeeman slowing of an atomic beam as well as the absorption imaging of cold atomic samples (see Chapter 3). The intercombination-line transition's small $\Gamma_{\mathrm{Er},583\,\mathrm{nm}}$ or $\Gamma_{\mathrm{Dy},626\,\mathrm{nm}}$, on the contrary, results in a more than 100 times smaller Doppler temperature $T_{\mathrm{D,Er},583\,\mathrm{nm}} = 4.5\,\mu\mathrm{K}$ or $T_{\mathrm{D,Dy},626\,\mathrm{nm}} = 3.2\,\mu\mathrm{K}$ [90] (see Table 2.2). This represents an ideal working regime for a MOT on the path to quantum degeneracy. Moreover, because of the great similarities between the two elements, the single-species intercombination-

line MOT approach also extends to their dual-species laser cooling and trapping. The following Chapter 3 focuses on the first experimental realization [88].

For completeness, the first MOTs for erbium [71] and dysprosium [73] operated on the broad transition to the $^1\mathrm{P}_1$ states. Here, the magnetic trapping of metastable states compensates for loss channels due to the broad transition's open character. In the course of creating the first dysprosium dBEC, [29] extended this approach by an additional blue-detuned narrow-line MOT stage at a wavelength of 741 nm, whose concept [72] demonstrated first for erbium at 841 nm. Such multiple MOT stages are not necessary for the intercombination-line MOT approach and a significantly simpler overall layout of the experimental apparatus is possible.

Although the broad and the intercombination-line transition exist in all lanthanoids, the intercombination-line MOT approach is not simply applicable for all series elements. Exemplarily, the laser cooling of europium on its broad transition might require several repumping lasers, and thus an alternative route utilizing a metastable state instead is more favorable [93].

2.2.2 Atomic polarizabilities

In the presence of an external electric field **E**, a neutral atom typically develops an induced electric dipole moment [83, 94]

$$\mathbf{d} = \alpha \cdot \mathbf{E}, \tag{2.12}$$

through which it interacts with the **E**-field. Here, the polarizability α, in a general setting a complex-numbered second-rank tensor and dependent on the **E**-field's angular frequency ω [95, 96], characterizes the initial response of the atom to the **E**-field. Its diagonal and off-diagonal elements determine the response collinear or in the orthogonal plane to the **E**-field. The latter is especially important for elements such as the lanthanoids owing to the **L**-introduced anisotropy in their electronic ground states [97].

As [98] and [99] studied for erbium and dysprosium atoms, respectively, in a laser field, α has a scalar representation with real and imaginary part $\Re\{\alpha\}$ and $\Im\{\alpha\}$. In particular, $\Re\{\alpha\}$ determines the potential of an atom in the laser field [98]

$$\begin{aligned} V(\mathbf{r},\omega) &= -\frac{1}{2\epsilon_0 c} I(\mathbf{r})\, \Re\{\alpha(\omega)\} \\ &= -\frac{1}{2\epsilon_0 c} I(\mathbf{r}) \Big[\Re\{\alpha_{\mathrm{sca}}(\omega)\} + A\cos\theta_{\mathrm{k}} \frac{m_J}{2J} \Re\{\alpha_{\mathrm{vec}}(\omega)\} \\ &\quad + \frac{3m_J^2 - J(J+1)}{J(2J-1)} \frac{3\cos^2\theta_{\mathrm{p}} - 1}{2} \Re\{\alpha_{\mathrm{ten}}(\omega)\} \Big] \end{aligned} \tag{2.13}$$

and $\Im\{\alpha\}$ the photon scattering rate [98]

$$\begin{aligned} R_{\mathrm{scat}}(\mathbf{r},\omega) &= \frac{1}{\hbar\epsilon_0 c} I(\mathbf{r})\, \Im\{\alpha(\omega)\} \\ &= \frac{1}{\hbar\epsilon_0 c} I(\mathbf{r}) \Big[\Im\{\alpha_{\mathrm{sca}}(\omega)\} + A\cos\theta_{\mathrm{k}} \frac{m_J}{2J} \Im\{\alpha_{\mathrm{vec}}(\omega)\} \\ &\quad + \frac{3m_J^2 - J(J+1)}{J(2J-1)} \frac{3\cos^2\theta_{\mathrm{p}} - 1}{2} \Im\{\alpha_{\mathrm{ten}}(\omega)\} \Big], \end{aligned} \tag{2.14}$$

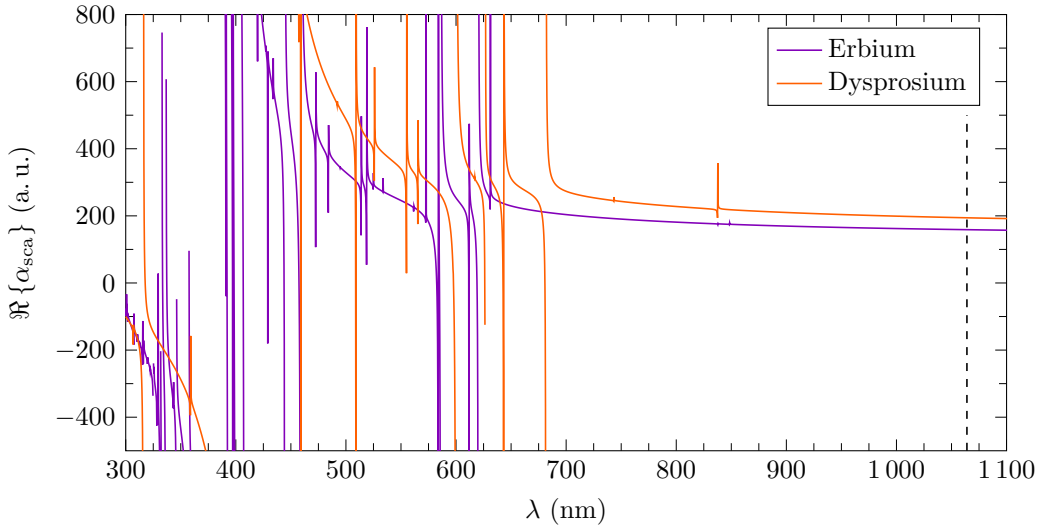

Figure 2.5: Real parts of the theoretical scalar polarizabilities $\Re\{\alpha_{\mathrm{sca}}\}_{\mathrm{Er}}$ (violet) and $\Re\{\alpha_{\mathrm{sca}}\}_{\mathrm{Dy}}$ (orange) as a function of wavelength λ. In the low-wavelength regime, various transitions, in particular the broad transition at $\lambda_{\mathrm{Er}} = 401\,\mathrm{nm}$ or $\lambda_{\mathrm{Dy}} = 421\,\mathrm{nm}$, dominate the individual behavior, whereas above $\lambda = 700\,\mathrm{nm}$ essentially no transitions occur. The vertical dashed line indicates $\lambda = 1064\,\mathrm{nm}$, where $\Re\{\alpha_{\mathrm{sca},1064\,\mathrm{nm}}\}_{\mathrm{Er}} = 161.8\,\mathrm{a.u.}$ and $\Re\{\alpha_{\mathrm{sca},1064\,\mathrm{nm}}\}_{\mathrm{Dy}} = 198.6\,\mathrm{a.u.}$, as a typical ODT regime.

with the vacuum permittivity ϵ_0, the speed of light c and the laser field intensity I at position $\mathbf{r}$. Further, $\Re\{\alpha\}$ and $\Im\{\alpha\}$ each split into three contributions, the real and the imaginary parts of the scalar (α_{sca}), the vector (α_{vec}) and the tensor (α_{ten}) polarizability. Here, θ_{k} and θ_{p} characterize the inclination angles of the light's propagation or polarization axis with respect to the system's quantization axis, and $A \in \{-1, 0, 1\}$ describes the state of polarization. The detailed expressions for the individual contributions are in [98].

Equations (2.13) and (2.14) emphasize the necessity for a deep understanding of α, as it determines the choice of laser wavelength for experimental techniques such as optical dipole traps (ODTs) [44], one- and two-dimensional ODT arrays [100, 101] or optical lattices [102], with the latter for instance at a magic wavelength [103, 104], with underlying double wells [105] or with a species-selective character [106].

In general, however, the precise characterization of α_{Er} and α_{Dy}, the polarizabilities of erbium and dysprosium, is highly demanding. The theoretical model requires detailed knowledge about the energy level diagrams and the transition dipole moments [98, 99], whereas the experimental determination is strongly susceptible to the laser's $1/e^2$-beam waist and power due to the intensity-dependence, as well as to its polarization due to the A- and θ_{p}-dependence in equations (2.13) and (2.14), respectively.

Figure 2.5 shows the real parts of the theoretical scalar polarizabilities $\Re\{\alpha_{\mathrm{sca}}\}_{\mathrm{Er}}$ and $\Re\{\alpha_{\mathrm{sca}}\}_{\mathrm{Dy}}$ as a function of wavelength λ ranging from 300 nm to 1100 nm [107]. Both are entirely independent of either the atom's, or the light's state (see equation (2.13)), and represent the main contribution to $\Re\{\alpha\}_{\mathrm{Er}}$ and $\Re\{\alpha\}_{\mathrm{Dy}}$ for the electronic ground states and linearly polarized laser light (see below). In the shown wavelength regime, a large amount of transitions, especially the broad transition at $\lambda_{\mathrm{Er}} = 401\,\mathrm{nm}$ or $\lambda_{\mathrm{Dy}} = 421\,\mathrm{nm}$, govern the behavior of $\Re\{\alpha_{\mathrm{sca}}\}_{\mathrm{Er}}$ and $\Re\{\alpha_{\mathrm{sca}}\}_{\mathrm{Dy}}$ up to around $\lambda = 700\,\mathrm{nm}$. Above

that point, the individual behavior settles down and $\Re\{\alpha_{\mathrm{sca}}\}_{\mathrm{Er}}$ and $\Re\{\alpha_{\mathrm{sca}}\}_{\mathrm{Dy}}$ approach each other while remaining positive. In the region around $\lambda = 1064\,\mathrm{nm}$ no transitions which could possibly introduce off-resonant scattering exist. This is especially beneficial for the realization of an ODT owing to the availability of commercial high-power laser systems. At $\lambda = 1064\,\mathrm{nm}$ the theoretical values are $\Re\{\alpha_{\mathrm{sca},1064\,\mathrm{nm}}\}_{\mathrm{Er}} = 161.8\,\mathrm{a.u.}$ and $\Re\{\alpha_{\mathrm{sca},1064\,\mathrm{nm}}\}_{\mathrm{Dy}} = 198.6\,\mathrm{a.u.}$, respectively.

Two independent experiments investigated $\Re\{\alpha\}$ at $\lambda = 1064\,\mathrm{nm}$ with linearly polarized laser light ($A = 0$, and thus no vector contribution) and measured in good agreement with theory for erbium $\Re\{\alpha_{1064\,\mathrm{nm}}\}_{\mathrm{Er}} = (166 \pm 3_{\mathrm{stat.}} \pm 61_{\mathrm{syst.}})\,\mathrm{a.u.}$ with the tensorial contribution $\Re\{\alpha_{\mathrm{ten},1064\,\mathrm{nm}}\}_{\mathrm{Er}} = (-1.9 \pm 0.8_{\mathrm{stat.}} \pm 1.2_{\mathrm{syst.}})\,\mathrm{a.u.}$ [97], as well as for dysprosium $\Re\{\alpha_{\mathrm{sca},1064\,\mathrm{nm}}\}_{\mathrm{Dy}} = 184.4(2.4)\,\mathrm{a.u.}$ and $\Re\{\alpha_{\mathrm{ten},1064\,\mathrm{nm}}\}_{\mathrm{Dy}} = 1.7(6)\,\mathrm{a.u.}$ [108].

The great similarity not only in $\Re\{\alpha_{\mathrm{sca}}\}_{\mathrm{Er}}$ and $\Re\{\alpha_{\mathrm{sca}}\}_{\mathrm{Dy}}$ but also in masses m_{Er} and m_{Dy} (see Table 2.1) enables a combined optical trapping approach for both elements. However, as Chapter 4 addresses more thoroughly, the small differences in both properties are already sufficient to play a crucial role for the dynamics during evaporative cooling to quantum degeneracy.

2.3 Dipolar Bose-Einstein condensates

Bose-Einstein statistics predict that an ideal Bose gas in thermodynamic equilibrium at temperature T occupies each state η of an external trap with a mean occupation number [6]

$$N_\eta = \frac{1}{\mathrm{e}^{(E_\eta - \mu_{\mathrm{che}})/k_{\mathrm{B}}T} - 1}, \tag{2.15}$$

with the energy E_η of a considered η, the chemical potential μ_{che} and the Boltzmann constant k_{B}. As T lowers below a critical temperature T_{C}, equation (2.15) reveals quantum degeneracy with a macroscopic occupation of the trap ground state ($\eta = 0$) by a purely quantum statistical phase transition [7], well known as Bose-Einstein condensation. Here, T_{C} depends on the dimensionality of the system as well as on the number density n [6]. Hence, not the Bose gas' T or n alone, but the phase space density (PSD), the product of n and the inverse number of occupied states per unit volume approximately scaling as the thermal de Broglie wavelength λ_{dB} cubed [6]

$$\mathrm{PSD} = n\lambda_{\mathrm{dB}}^3 = n\left(\frac{2\pi\hbar^2}{mk_{\mathrm{B}}T}\right)^{3/2}, \tag{2.16}$$

with the mass m, determines whether a BEC forms. In a three-dimensional box potential the PSD must be equal to or larger than $\zeta(3/2) \approx 2.612$ [6], with the Riemann zeta function ζ. A BEC for an interacting Bose gas within a three-dimensional harmonic trap requires a PSD on the same order of magnitude [109]. This represents together with the evaporation efficiency the figure of merit for evaporative cooling (see Chapter 4).

However, while the quantum statistics of a Bose gas may be at the heart of Bose-Einstein condensation, it is two-body interactions that shape and control a BEC (neglecting three-body processes) [6, 110]. For magnetic elements, and thus for erbium and dysprosium, two interaction types are relevant, the contact interaction as well as the long-range anisotropic magnetic dipole-dipole interaction [66], whose interplay gives rise to a dBEC [29, 30, 66]. The following Section 2.3.1 treats a dBEC in a mean-field description and Section 2.3.2 briefly extends the discussion to the heteronuclear case.

2.3.1 Interactions within the mean-field description

Considering an interacting Bose gas in an external harmonic trap V_{trap}, the time-dependent Gross-Pitaevskii equation (GPE) describes a BEC in a mean-field description as [110]

$$\mathrm{i}\hbar\frac{\partial}{\partial t}\psi_{\mathrm{BEC}}\left(\mathbf{r},t\right)=\left[-\frac{\hbar^2\nabla^2}{2m}+V_{\mathrm{trap}}\left(\mathbf{r},t\right)+\overline{V}_{\mathrm{int}}\left(\mathbf{r},t\right)\right]\psi_{\mathrm{BEC}}\left(\mathbf{r},t\right), \tag{2.17}$$

with the position $\mathbf{r}$, the time t, the kinetic energy term $-\hbar^2\nabla^2/2m$ and the mean-field interactions $\overline{V}_{\mathrm{int}}$. The BEC wave function ψ_{BEC} fulfills the normalization to the BEC atom number [110]

$$N_{\mathrm{BEC}}=\int|\psi_{\mathrm{BEC}}\left(\mathbf{r}\right)|^2\mathrm{d}\mathbf{r} \tag{2.18}$$

and gives the BEC number density [110]

$$n_{\mathrm{BEC}}\left(\mathbf{r}\right)=|\psi_{\mathrm{BEC}}\left(\mathbf{r}\right)|^2. \tag{2.19}$$

For a dBEC, the GPE approach introduces the mean-field contact interaction $\overline{V}_{\mathrm{con}}$ as well as the mean-field magnetic dipole-dipole interaction $\overline{V}_{\mathrm{dd}}$ as [66]

$$\overline{V}_{\mathrm{int}}\left(\mathbf{r},t\right)=\overline{V}_{\mathrm{con}}\left(\mathbf{r},t\right)+\overline{V}_{\mathrm{dd}}\left(\mathbf{r},t\right). \tag{2.20}$$

Contact interaction

At low energies, scattering theory commonly replaces the van der Waals-type interaction between two atoms at positions $\mathbf{r}$ and $\mathbf{r}'$ by the Fermi pseudopotential [6]

$$V_{\mathrm{con}}\left(\mathbf{r},\mathbf{r}'\right)=\frac{2\pi\hbar^2a_{\mathrm{s}}}{m_{\mathrm{r}}}\delta\left(\mathbf{r}-\mathbf{r}'\right), \tag{2.21}$$

with the s-wave scattering length a_{s} and the reduced mass $m_{\mathrm{r}}={}^{(m_1m_2)}/_{(m_1+m_2)}$ of the atoms' individual masses m_1 and m_2, respectively. The Dirac delta function $\delta\left(\mathbf{r}-\mathbf{r}'\right)$ describes a contact-like interaction. The approximation by the isotropic a_{s} holds, as s-wave scattering is the main contribution to low-energy scattering [6]. In the mean-field description, equation (2.21) leads for a single species ($m_1=m_2=m$) to [6, 110]

$$\overline{V}_{\mathrm{con}}\left(\mathbf{r},t\right)=\frac{4\pi\hbar^2a_{\mathrm{s}}}{m}|\psi_{\mathrm{BEC}}\left(\mathbf{r},t\right)|^2. \tag{2.22}$$

Magnetic dipole-dipole interaction

In the experimentally relevant setting of an external $\mathbf{B}$-field, two atoms with atomic magnetic moments $\boldsymbol{\mu}_1$ and $\boldsymbol{\mu}_2$ and at positions $\mathbf{r}$ and $\mathbf{r}'$ interact via the magnetic dipole-dipole interaction as [66]

$$V_{\mathrm{dd}}\left(\mathbf{r},\mathbf{r}'\right)=\frac{\mu_1\mu_2\mu_0}{4\pi}\frac{1-3\cos^2\theta}{|\mathbf{r}-\mathbf{r}'|^3}, \tag{2.23}$$

with the vacuum permeability μ_0 and the magnetic moments μ_1 and μ_2 of the two dipoles, respectively. The scaling by the inverse distance cubed, ${}^1/_{|\mathbf{r}-\mathbf{r}'|^3}$, results in a long-range

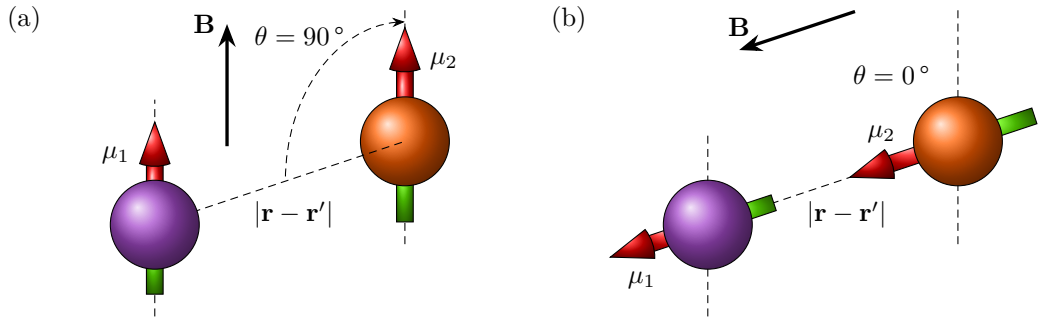

Figure 2.6: Illustration of the magnetic dipole-dipole interaction V_{dd} between two atoms with atomic magnetic moments $\boldsymbol{\mu}_1$ and $\boldsymbol{\mu}_2$ at a distance $|\mathbf{r}-\mathbf{r}'|$ in the presence of an external magnetic field $\mathbf{B}$. The two extremes of V_{dd} are (a) a repulsive side-by-side and (b) an attractive head-to-tail arrangement with $\theta = 90\,^\circ$ or $\theta = 0\,^\circ$ between the two dipoles of magnetic moments μ_1 and μ_2, and the interatomic axis $\mathbf{r}-\mathbf{r}'$.

non-local effect, whereas θ captures the orientation of the two dipoles with respect to the interatomic axis $\mathbf{r}-\mathbf{r}'$, and thus the anisotropic behavior of V_{dd} controllable via the $\mathbf{B}$-field direction. Figure 2.6 depicts the two extremes, a repulsive side-by-side and an attractive head-to-tail arrangement for $\theta = 90\,^\circ$ and $\theta = 0\,^\circ$, respectively. In the mean-field description, equation (2.23) leads for a single species ($\mu_1 = \mu_2 = \mu$) to [6, 66]

$$\overline{V}_{\mathrm{dd}}\left(\mathbf{r},t\right) = \int \frac{\mu^2\mu_0}{4\pi}\frac{1-3\cos^2\theta}{|\mathbf{r}-\mathbf{r}'|^3}|\psi_{\mathrm{BEC}}\left(\mathbf{r}',t\right)|^2\mathrm{d}\mathbf{r}'. \tag{2.24}$$

Equation (2.20) extends with equations (2.22) and (2.24) to

$$\overline{V}_{\mathrm{int}}\left(\mathbf{r},t\right) = \frac{4\pi\hbar^2 a_{\mathrm{s}}}{m}|\psi_{\mathrm{BEC}}\left(\mathbf{r},t\right)|^2 + \int \frac{\mu^2\mu_0}{4\pi}\frac{1-3\cos^2\theta}{|\mathbf{r}-\mathbf{r}'|^3}|\psi_{\mathrm{BEC}}\left(\mathbf{r}',t\right)|^2\mathrm{d}\mathbf{r}'. \tag{2.25}$$

Hence, moving from equation (2.17) to the time-independent GPE [6, 110]

$$\mu_{\mathrm{che}}\psi_{\mathrm{BEC}}\left(\mathbf{r}\right) = \left[-\frac{\hbar^2\nabla^2}{2m} + V_{\mathrm{trap}}\left(\mathbf{r}\right) + \overline{V}_{\mathrm{int}}\left(\mathbf{r}\right)\right]\psi_{\mathrm{BEC}}\left(\mathbf{r}\right) \tag{2.26}$$

and comparing both sides, results under the Thomas-Fermi approximation [6, 110], which neglects the kinetic energy term $-\hbar^2\nabla^2/2m$, and with equations (2.19) and (2.25) in

$$\mu_{\mathrm{che}} = V_{\mathrm{trap}}\left(\mathbf{r}\right) + \frac{4\pi\hbar^2 a_{\mathrm{s}}}{m}n_{\mathrm{BEC}}\left(\mathbf{r}\right) + \int \frac{\mu^2\mu_0}{4\pi}\frac{1-3\cos^2\theta}{|\mathbf{r}-\mathbf{r}'|^3}n_{\mathrm{BEC}}\left(\mathbf{r}'\right)\mathrm{d}\mathbf{r}'. \tag{2.27}$$

In the Thomas-Fermi regime, a dBEC in a V_{trap} of trapping frequencies ω_r and ω_z in the radial $r = (x,y)$- and the axial z-direction, respectively, obtains a quadratic profile [110]

$$n_{\mathrm{BEC}}\left(\mathbf{r}\right) = \hat{n}_{\mathrm{BEC}}\left(1 - \frac{r^2}{R_{\mathrm{TF}}^2} - \frac{z^2}{Z_{\mathrm{TF}}^2}\right) = \frac{15}{8\pi}\frac{N_{\mathrm{BEC}}}{R_{\mathrm{TF}}^2 Z_{\mathrm{TF}}}\left(1 - \frac{r^2}{R_{\mathrm{TF}}^2} - \frac{z^2}{Z_{\mathrm{TF}}^2}\right), \tag{2.28}$$

with the peak number density $\hat{n}_{\mathrm{BEC}}$, the radial and axial Thomas-Fermi radius R_{TF} and Z_{TF} as well as the dipoles along the z-axis. Contrary to a purely contact-interacting BEC,

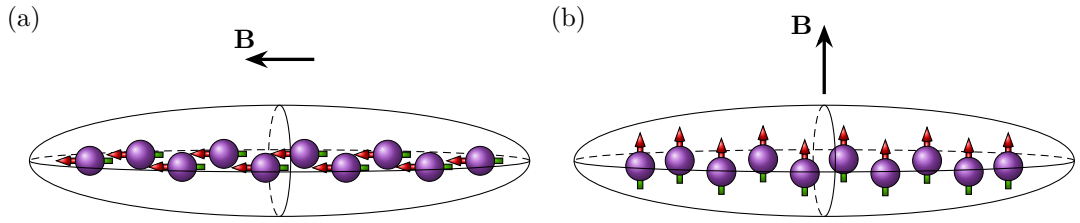

Figure 2.7: Illustration of the mean-field magnetic dipole-dipole interaction $\overline{V}_{\mathrm{dd}}$ in a dBEC within a cigar-shaped harmonic trap V_{trap}. An external magnetic field $\mathbf{B}$ aligns the dipoles, where the two extremes of (a) a parallel and (b) an orthogonal orientation with respect to the symmetry axis of V_{trap} result in an attractive or a repulsive $\overline{V}_{\mathrm{dd}}$.

however, a dBEC deforms under the influence of V_{dd} and its aspect ratio $\kappa = {}^{R_{\mathrm{TF}}}/_{Z_{\mathrm{TF}}}$ differs from the trap aspect ratio $\chi = {}^{\omega_z}/_{\omega_r}$ with [110]

$$R_{\mathrm{TF}} = \left(\frac{15\hbar^2}{m^2} \frac{\kappa a_{\mathrm{s}} N_{\mathrm{BEC}}}{\omega_r^2} \left[1 + \epsilon_{\mathrm{dd}} \left(\frac{3}{2} \frac{\kappa^2 f(\kappa)}{1-\kappa^2} - 1 \right) \right] \right)^{1/5} \tag{2.29}$$

$$Z_{\mathrm{TF}} = \frac{1}{\kappa} \left(\frac{15\hbar^2}{m^2} \frac{\kappa a_{\mathrm{s}} N_{\mathrm{BEC}}}{\omega_r^2} \left[1 + \epsilon_{\mathrm{dd}} \left(\frac{3}{2} \frac{\kappa^2 f(\kappa)}{1-\kappa^2} - 1 \right) \right] \right)^{1/5}. \tag{2.30}$$

At this [110]

$$f(\kappa) = \frac{1+2\kappa^2}{1-\kappa^2} - \frac{3\kappa^2}{(1-\kappa^2)^{3/2}} \tanh^{-1} \sqrt{1-\kappa^2} \tag{2.31}$$

and κ and χ follow the condition [110]

$$3\kappa^2 \epsilon_{\mathrm{dd}} \left[\left(\frac{\chi^2}{2} + 1 \right) \frac{f(\kappa)}{1-\kappa^2} - 1 \right] + (\epsilon_{\mathrm{dd}} - 1)\left(\kappa^2 - \chi^2\right) = 0. \tag{2.32}$$

Equations (2.29) and (2.30) capture the interplay between $\overline{V}_{\mathrm{dd}}$ and $\overline{V}_{\mathrm{con}}$ via the ratio of the dipolar length a_{dd} and a_{s} [66]

$$\epsilon_{\mathrm{dd}} = \frac{a_{\mathrm{dd}}}{a_{\mathrm{s}}} = \frac{m\mu_0}{12\pi\hbar^2} \frac{\mu^2}{a_{\mathrm{s}}}, \tag{2.33}$$

with $\epsilon_{\mathrm{dd}} > 1$ in the dipolar regime. It reveals two possibilities to adjust the impact of $\overline{V}_{\mathrm{dd}}$, either by μ via $m_{J,F}$ (see equation (2.11)) or by a_{s} via Feshbach resonances [49]. While the first method is limited by dipolar relaxation processes [111], the second one is of particular experimental interest, but has its own complexity. For lanthanoids, even the van der Waals interaction is anisotropic due to the anisotropic electronic ground states (for instance $J_{\mathrm{Er}} = 6$ or $J_{\mathrm{Dy}} = 8$, see Section 2.2), and thus facilitates couplings to rotating bound states [112, 113]. This results for erbium and dysprosium in particularly complex Feshbach spectra [76, 77, 78]. For completeness, [114] investigated recently the Feshbach spectrum in thulium and observed a temperature-dependent transition from random to chaotic statistics. Alternatively, as a second method, a rotating $\mathbf{B}$-field allows for the control over V_{dd} [66], as [115] demonstrated in a dysprosium dBEC.

For a dBEC to be stable, the Thomas-Fermi energy [110]

$$\frac{E}{N_{\mathrm{BEC}}} = \frac{1}{14} m\omega_r^2 R_{\mathrm{TF}}^2 \left(2 + \frac{\chi^2}{\kappa^2} \right) + \frac{15\hbar^2}{7m} \frac{a_{\mathrm{s}} N_{\mathrm{BEC}}}{R_{\mathrm{TF}}^2 Z_{\mathrm{TF}}} \left(1 - \epsilon_{\mathrm{dd}} f(\kappa) \right), \tag{2.34}$$

the sum of trap and interaction energy, must remain positive. As a repulsive $\overline{V}_{\mathrm{dd}}$ can equate an attractive $\overline{V}_{\mathrm{con}}$ and vice versa, and due to the anisotropy of V_{dd}, the geometry of V_{trap} influences the stability of a dBEC, where the critical scattering length [69, 110]

$$a_{\mathrm{s,crit}} = a_{\mathrm{dd}} f\left(\kappa\left(\chi\right)\right). \tag{2.35}$$

The unstable regime for $a_{\mathrm{s}} < a_{\mathrm{s,crit}}$ gives rise to a mean-field instability, the so-called d-wave collapse [70]. In view of Chapter 5 on supersolidity in dipolar quantum gases, it should not be confused with the roton-instability [66, 116].

Considering the asymptotic behavior of equation (2.35), $a_{\mathrm{s,crit}} = a_{\mathrm{dd}}$ for $\chi \to 0$ and $a_{\mathrm{s,crit}} = -2a_{\mathrm{dd}}$ for $\chi \to \infty$ [66, 69], respectively, for the initially defined alignment of the dipoles along the z-axis and $\chi = \omega_z/\omega_r$. The difference in $a_{\mathrm{s,crit}}$ arises from the change in $\overline{V}_{\mathrm{dd}}$ for the different geometries of V_{trap}, since a cigar-shaped V_{trap} ($\chi \to 0$) leads to a predominant head-to-tail arrangement of the dipoles, and thus to an attractive $\overline{V}_{\mathrm{dd}}$, and a pancake-shaped V_{trap} ($\chi \to \infty$) to a predominant side-by-side arrangement of the dipoles, and thus to a repulsive $\overline{V}_{\mathrm{dd}}$.

In general, this stability consideration depends on the orientation of the dipoles with respect to the symmetry axis of V_{trap}. Figure 2.7 exemplarily illustrates the two extremes for a dBEC in a cigar-shaped V_{trap}. If a **B**-field aligns the dipoles parallel to the trap symmetry axis, $\overline{V}_{\mathrm{dd}}$ turns attractive and acts destabilizing (see Figure 2.7 (a)). On the contrary, if a **B**-field, and thus the dipoles point orthogonal to the trap symmetry axis, $\overline{V}_{\mathrm{dd}}$ is repulsive and stabilizes the dBEC (see Figure 2.7 (b)). In an analog discussion, a dBEC in a pancake-shaped V_{trap} shows an inverted behavior.

2.3.2 Heteronuclear dipolar Bose-Einstein condensates

The previous Section 2.3.1 laid the foundation to describe a heteronuclear dBEC, the binary Bose-Einstein condensation in an atomic mixture of two highly magnetic elements. A coupled GPE approach extends equation (2.27) for two highly magnetic elements 1 and 2, respectively, with the interspecies mean-field contact interaction $\overline{V}_{\text{inter-con}}$ and the interspecies mean-field magnetic dipole-dipole interaction $\overline{V}_{\text{inter-dd}}$ to

$$\begin{aligned}
\mu'_{\mathrm{che},1} &= \mu_{\mathrm{che},1} + \overline{V}_{\text{inter-con},12}\left(\mathbf{r}\right) + \overline{V}_{\text{inter-dd},12}\left(\mathbf{r}\right) \\
&= \mu_{\mathrm{che},1} + \frac{2\pi\hbar^2 a_{\mathrm{s},12}}{m_{\mathrm{r}}} n_2\left(\mathbf{r}\right) + \int \frac{\mu_1\mu_2\mu_0}{4\pi} \frac{1-3\cos^2\theta}{\left|\mathbf{r}-\mathbf{r}'\right|^3} n_2\left(\mathbf{r}'\right) \mathrm{d}\mathbf{r}' \qquad (2.36) \\
\mu'_{\mathrm{che},2} &= \mu_{\mathrm{che},2} + \overline{V}_{\text{inter-con},21}\left(\mathbf{r}\right) + \overline{V}_{\text{inter-dd},21}\left(\mathbf{r}\right) \\
&= \mu_{\mathrm{che},2} + \frac{2\pi\hbar^2 a_{\mathrm{s},12}}{m_{\mathrm{r}}} n_1\left(\mathbf{r}\right) + \int \frac{\mu_1\mu_2\mu_0}{4\pi} \frac{1-3\cos^2\theta}{\left|\mathbf{r}-\mathbf{r}'\right|^3} n_1\left(\mathbf{r}'\right) \mathrm{d}\mathbf{r}', \qquad (2.37)
\end{aligned}$$

with the interspecies scattering length $a_{\mathrm{s},12}$. Here, $\overline{V}_{\text{inter-con}}$ and $\overline{V}_{\text{inter-dd}}$ deduce from the general settings (different masses, $m_1 \neq m_2$, and magnetic moments, $\mu_1 \neq \mu_2$) in equations (2.22) and (2.24) as well as by extending the basic theoretical concepts for a purely contact-interacting mixture in [6].

This PhD thesis' second publication [117] reported on the first production of such heteronuclear dBECs by combining erbium and dysprosium (see Chapter 4). However, their experimental investigation and understanding are still at the beginning, where for instance even the interspecies scattering length of erbium and dysprosium $a_{\mathrm{s,Er\text{-}Dy}}$ is still unknown. Accordingly, Chapter 6 briefly presents the next steps for a first thorough characterization of these heteronuclear quantum-degenerate dipolar mixtures.

Chapter 3

Dual-species intercombination-line magneto-optical trap

The first milestone of this PhD work was the development and the construction of the first experimental apparatus for heteronuclear quantum-degenerate dipolar mixtures of erbium and dysprosium. This milestone proved successful with the realization of a dual-species MOT operating in an open-top configuration on the intercombination-line transition to the $^3P_1$ state at $\lambda_{Er} = 583\,\text{nm}$ and $\lambda_{Dy} = 626\,\text{nm}$ [88], respectively.

The experimental apparatus' core element is an ultra-high vacuum (UHV) apparatus, as Figure 3.1 illustrates, very much reminiscent of a single-species experiment. Its layout combines three experiment stages for the loading of the dual-species MOT. First, as part of a dual-species atomic beam source, a dual-filament effusion cell evaporates both elements and a transverse cooling (TC) unit collimates the emitted atomic beam. Next, a 350 mm long spin-flip Zeeman slower (ZS) decelerates the atomic beam starting from initial velocity classes of up to $370\,\text{m/s}$, and finally, the dual-species MOT itself traps and cools slowed atoms arriving with around $5\,\text{m/s}$ at the center of the main chamber.

Typically, a MOT loading time $t_{MOT} = 3\,\text{s} - 5\,\text{s}$ provides sufficiently high atom numbers to apply a compression phase to a compressed MOT (cMOT) (see Section 3.3.3) and to transfer both elements into the same ODT for evaporative cooling to quantum degeneracy. Chapter 4 discusses this step in the experimental sequence more thoroughly.

This third chapter describes the complete experimental apparatus. The initial Section 3.1 covers the UHV apparatus, followed by Section 3.2 about the magnetic field systems featuring the spin-flip ZS. Section 3.3 reviews the laser systems operating on the broad and the intercombination-line transition, respectively, as well as their implementation into the UHV apparatus. The next two Sections 3.4 and 3.5 give more information on the imaging and the control system. Section 3.6 concludes with presenting the first publication *Two-species five-beam magneto-optical trap for erbium and dysprosium* [88]. Some information provided throughout this chapter might coincide with [88] and is not explicitly referenced. Further, experimental parameters might differ from the published ones [88], as the production of quantum-degenerate dipolar mixtures requires a slightly different parameter regime than the sole MOT operation.

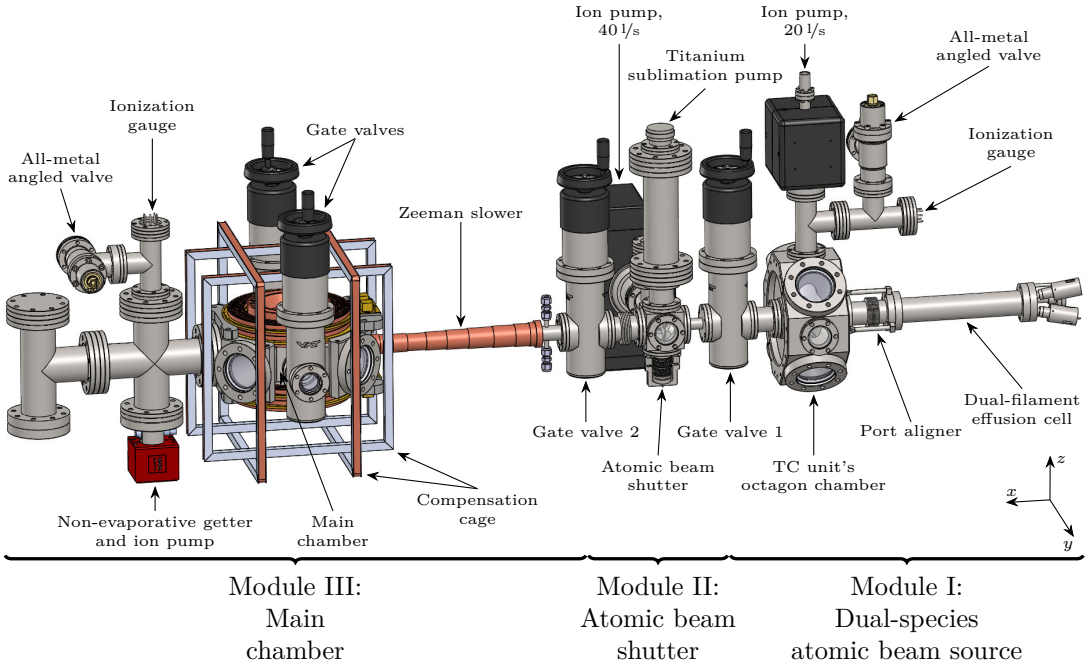

Figure 3.1: Ultra-high vacuum apparatus for heteronuclear quantum-degenerate dipolar mixtures of erbium and dysprosium. It consists of three individual modules, the dual-species atomic beam source (I), the atomic beam shutter (II) and the main chamber (III). Module I emits a collimated atomic beam of both elements, which propagates along the system's x-axis through Module II into Module III. Here, a spin-flip ZS slows the atomic beam (see Section 3.2.1) and a dual-species MOT traps and cools slow atoms at the center of the main chamber (see Section 3.3.3). Additionally, the main chamber provides various **B**-field coil systems for homogeneous or quadrupole **B**-fields (see Section 3.2.2).

3.1 Ultra-high vacuum apparatus

From the project's very beginning, the development process focused on the UHV apparatus (see Figure 3.1) and especially on the main chamber. The primary objective was the realization of a highly specialized but at the same time highly versatile platform for state-of-the-art experiments with heteronuclear quantum-degenerate dipolar mixtures. This process strongly benefited from the first-generation erbium experiment in Innsbruck [89].

The UHV apparatus comprises three individual modules separable via gate valves[1] (Gate valve 1 and Gate valve 2 in Figure 3.1), namely the dual-species atomic beam source, the atomic beam shutter and the main chamber. Each of these three sub-assemblies has an ionization gauge[2] and an all-metal angled valve[3] for an independent pressure measurement and the use of an external pumping station, respectively. Additionally, two all-metal gate valves[4] at the main chamber provide the possibility to attach two science modules for more advanced experiments.

[1] VAT Vakuumventile AG, 48132-CE01-0002
[2] Agilent Technologies, Bayard-Alpert gauge tube with tungsten filaments, UHV-24P
[3] VAT Vakuumventile AG, 54132-GE02-0001
[4] VAT Vakuumventile AG, 48132-CE01-AHL1 and 48132-CE01-X

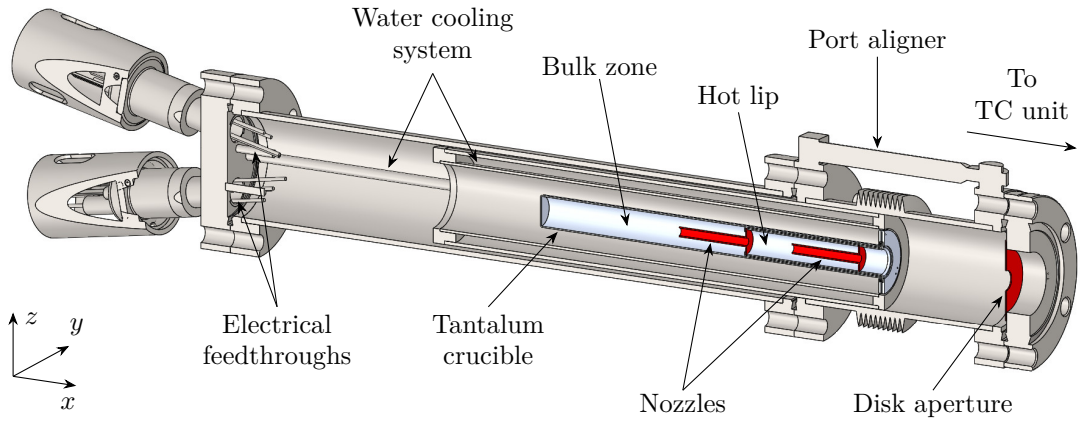

Figure 3.2: Vertical sectional view of the dual-filament effusion cell along the atomic beam propagation axis (x-axis). Two heating circuits (not shown) operate the crucible's bulk zone at a temperature $T_{\mathrm{BZ}} = 1100\,^{\circ}\mathrm{C}$ and its hot-lip at $T_{\mathrm{HL}} = 1200\,^{\circ}\mathrm{C}$. The internal water cooling system is necessary due to these high operating temperatures. The nozzles within the crucible have a length of 30 mm and a 3 mm aperture, whereas the disk aperture close to the transverse cooling (TC) unit is 0.5 mm thick and provides an 8 mm aperture. The crucible and all apertures are from tantalum.

Throughout the entire UHV apparatus, all stainless steel components are from 1.4404 and/or 1.4429 stainless steel. Both types inherently do not develop a large magnetic permeability during machining. In this regard, 1.4429 stainless steel is slightly superior. This material property is particularly important since magnetized steel parts would compromise the ability to achieve the highly precise **B**-field control needed. The TC unit's octagon chamber as well as the main chamber are from 1.4429 stainless steel and have a surface finish via electrolytic polishing [118], a common technique to improve the vacuum quality by reducing the surface roughness of UHV components.

Module I: Dual-species atomic beam source

The first module is an atomic beam source for both elements, whose construction benefited from the great similarities in melting points $T_{\mathrm{m,Er}}$ and $T_{\mathrm{m,Dy}}$ as well as in laser cooling properties (see Chapter 2). Its two central components are a dual-filament effusion cell[5] and a TC unit, which together produce a collimated atomic beam. The atomic beam propagation axis, starting from the atomic beam source, points along the system's x-axis through the atomic beam shutter as well as the spin-flip ZS into the main chamber, and is fine-adjustable via a port aligner (see Figure 3.1).

Because of $T_{\mathrm{m,Er}} = 1529\,^{\circ}\mathrm{C}$ and $T_{\mathrm{m,Dy}} = 1412\,^{\circ}\mathrm{C}$ [79], the decision was to implement a commercial dual-filament effusion cell. Its working principle relies on heating the material of interest in a crucible to a given target temperature. As the vapor pressure increases, material evaporates and passes as vapor through one or more apertures geometrically shaping the atomic beam. The chosen type of evaporator is commonly in use in epitaxy applications but also operates successful in the first-generation erbium experiment [89].

[5] Createc Fischer & Co. GmbH, DFC-40-10-WK-2B

Figure 3.2 shows a vertical sectional view of the installed dual-filament effusion cell. It has two heating circuits that establish two temperature regions in a tantalum crucible. In standard operation, the bulk zone, which serves as reservoir for a granulated alloy of erbium and dysprosium in a ratio of 33 % to 67 %, is at a temperature $T_{\mathrm{BZ}} = 1100\,^{\circ}\mathrm{C}$ and the hot-lip at a temperature $T_{\mathrm{HL}} = 1200\,^{\circ}\mathrm{C}$. The temperature gradient prevents condensation of evaporated material on the crucible's internal apertures, as they are at the same temperature as the hot-lip. However, as Chapter 2 discussed, the vapor pressures $p_{\mathrm{vap,Er}}$ and $p_{\mathrm{vap,Dy}}$ differ by a factor of close to nine in the given temperature region. By exploiting this temperature gradient, enriching the hot-lip with additional pure granulated erbium helps to compensate the difference in $p_{\mathrm{vap,Er}}$ and $p_{\mathrm{vap,Dy}}$, as it individually increases the atomic flux, and thus the MOT loading rate of erbium.

In total three tantalum apertures provide an initial geometric collimation of the emitted atomic beam, namely two 30 mm long nozzles with an aperture of 3 mm diameter at the bulk zone and the hot-lip, respectively, as well as an external 0.5 mm thick disk aperture with an aperture of 8 mm diameter right in front of the TC unit's octagon chamber. The implementation of the latter results in a more favorable overall performance [119]. In comparison to the aperture setup in the first-generation erbium experiment [89, 119], a nozzle at the hot-lip, instead of another disk aperture, achieves a stronger geometric collimation of the here additionally evaporated pure erbium.

The TC unit includes an octagon chamber featuring two pairs of anti-reflection coated CF63 viewports[6] under 45 ° to the horizontal x-y plane and two uncoated CF40 viewports for additional optical access within the plane (see Figure 3.12). A single 20 l/s ion pump[7] at the top connection port of the octagon chamber maintains the pressure of the entire module at a low 10^{-10} mbar level.

Module II: Atomic beam shutter

The next module is the atomic beam shutter (ABS). After the MOT loading, an external servo drives a simple in-vacuum stainless steel plate, which intrudes into the atomic beam path, from its open to closed position. This prevents the atomic beam from entering the main chamber, and thus any possible influence on the experiments.

Furthermore, this sub-assembly is at the center of the UHV apparatus' differential pumping system. Here, a 50 mm long connector tube with an inner diameter of 8 mm acts as an aperture to the atomic beam source, whereas the spin-flip ZS accomplishes this for the opposite side with respect to the main chamber. A 40 l/s ion pump[8] completes the differential pumping scheme and establishes a vacuum pressure of a few 10^{-11} mbar in the entire module. The additional titanium sublimation pump[9] refreshes only after an exchange of the dual-filament effusion cell.

Module III: Main chamber

The final module is the main chamber, the core element for all experiments during this PhD work. Its adjunct pumping assembly includes an additional viewport and an

[6] Anti-reflection coating for 401 nm, 421 nm, 532 nm, 583 nm, 626 nm and 1550 nm
[7] Agilent Technologies, VacIon Plus 20 StarCell
[8] Agilent Technologies, VacIon Plus 40 StarCell
[9] Agilent Technologies, titanium sublimation pump

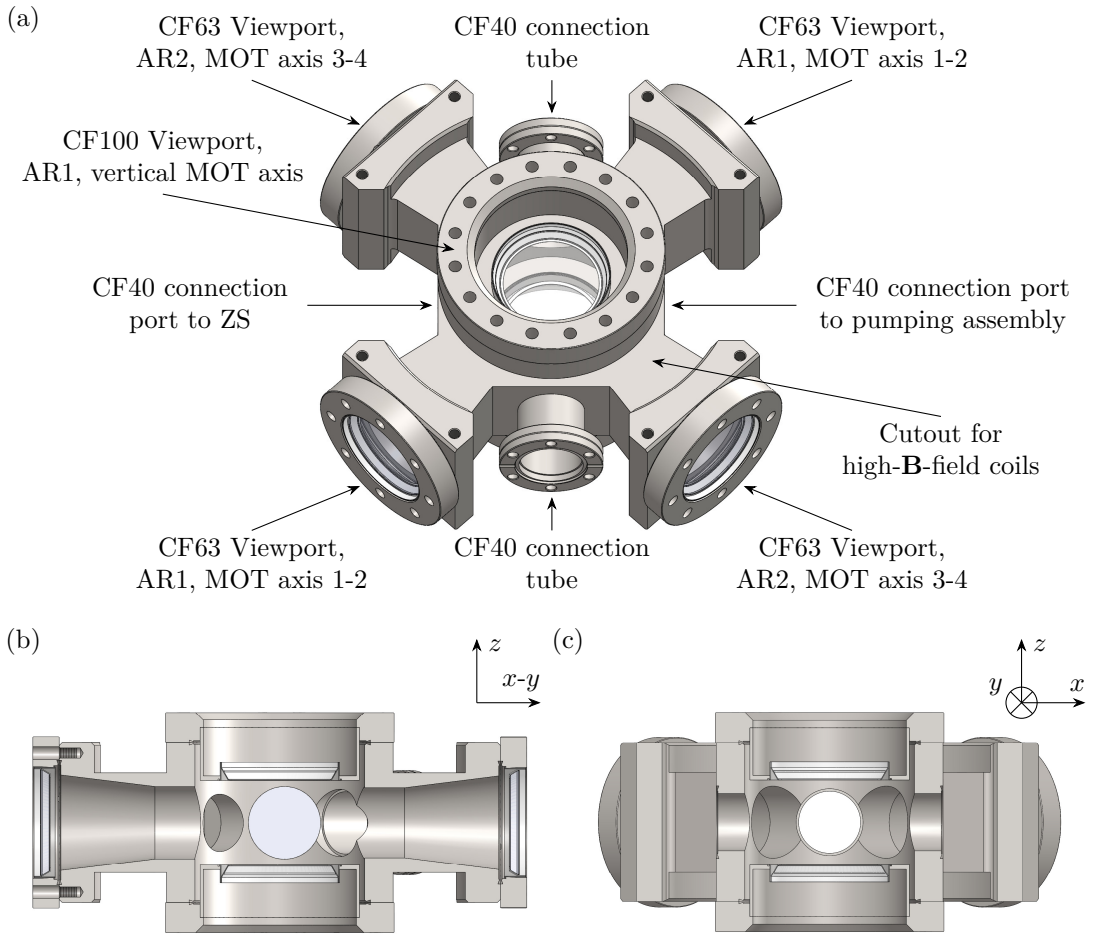

Figure 3.3: Custom-made main chamber from 1.4429 stainless steel in (a) a top view and vertical sectional views along (b) the MOT axis 1-2 and (c) the atomic beam propagation axis (x-axis). Along the three orthogonal MOT axes, the main chamber features four CF63 viewports (x-y plane) as well as two CF100 inverted viewports (z-axis) with anti-reflection coatings AR1 or AR2 (see text). The inverted viewports minimize the working distance along the vertical z-axis to 35 mm. The CF40 connection ports for the ZS and the pumping assembly as well as the CF40 connection tubes for the gate valves reduce the distance to the chamber center to 75 mm and 124 mm, respectively. The cutouts at the top and the bottom allow for high-**B**-field coils (see Section 3.2.2 and Figure 3.5).

in-vacuum aluminum mirror[10] for incoupling of the ZS light (see Section 3.3.3) as well as a single pump[11] that combines a non-evaporative getter material with an ion pump and keeps the vacuum pressure of the entire sub-assembly on a low 10^{-11} mbar level. The spin-flip ZS (see Section 3.2.1) interfaces the main chamber with the previous Module II.

The main chamber itself is entirely custom-made. Its layout adapts to the stringent experimental requirements (see below), whereas providing a high versatility at the same time. Figure 3.3 depicts the main chamber in various views.

[10]Kugler GmbH, optical-grade aluminum mirror (AlSi1MgMn)
[11]SAES Getters S.p.A., NEXTorr D500-5 with mu-metal shielding

Along the vertical z-axis, two CF100 inverted viewports offer a clear aperture of 64 mm and reduce the distance from chamber center to the viewports' outside to 35 mm. The inverting serves two purposes. First, the reduced working distance allows in combination with the large field of view for the implementation of a vertical high-resolution imaging system (see Chapter 6). Second, it facilitates the integration of various low-**B**-field coils close to the atoms (see Section 3.2.2).

In the horizontal x-y plane, two orthogonal pairs of CF63 viewports provide sufficient optical access for MOT beams with $1/e^2$-waists $w_{\mathrm{MOT}} = 19\,\mathrm{mm}$ (see Section 3.3.3). These enable a large MOT capture volume, which is necessary for the direct loading of a dual-species intercombination-line MOT for erbium and dysprosium due to not only the small MOT capture velocities (see Section 3.2.1) but also the substantial spatial downshift of the MOT position (see Section 3.3.3) [74, 75, 88, 92].

The majority of viewports has an anti-reflection coating[12] (AR1) for the most important laser cooling and trapping wavelengths, while two CF63 viewports along one of the horizontal MOT axes have a broad anti-reflection coating (AR2) for the wavelength regime ranging from 400 nm to 800 nm. This combination ensures a high flexibility of usable laser wavelengths. Figure 3.3, 3.13, and 3.14 illustrate the coating arrangements.

Besides optimized optical access, the main chamber also features a special shape. The recessed CF40 connection ports for the spin-flip ZS and the pumping assembly leave a distance of 75 mm to the chamber center. This increases the amount of slow atoms entering the MOT capture volume and improves the pump performance within the chamber. Further, the welded CF40 connection tubes permit a close installation of the two gate valves at a distance of 124 mm to the chamber center. This minimizes the transport distance to either of the two (possible) future science modules. Finally, cutouts around the CF100 inverted viewports create space for two additional high-**B**-field coils in a Helmholtz (HH) and an anti-Helmholtz (AHH)-like configuration (see Section 3.2.2).

3.2 Magnetic field systems

Many experimental techniques in ultracold atom experiments, such as Zeeman slowing or magneto-optical trapping, rely on atom-light interactions under the influence of an external magnetic field **B** [83, 120]. Equally important, as Chapter 2 briefly addressed, the contact and the magnetic dipole-dipole intra- and interspecies interactions are tunable by varying the strength or the orientation of a **B**-field. This is a crucial aspect not only for evaporative cooling but also for more advanced experiments. The different experimental techniques and application areas require specific **B**-field systems. Section 3.2.1 covers the spin-flip ZS, including a short review of its basic working principle, and Section 3.2.2 describes the layout of the various **B**-field coils at the main chamber.

3.2.1 Spin-flip Zeeman slower

The dual-filament effusion cell operates at $T_{\mathrm{BZ}} = 1100\,^{\circ}\mathrm{C}$ and $T_{\mathrm{HL}} = 1200\,^{\circ}\mathrm{C}$ in order to achieve sufficiently high $p_{\mathrm{vap,Er}}$ and $p_{\mathrm{vap,Dy}}$ for a high atomic flux towards the main chamber. Thus, the emitted atomic beam has longitudinal velocity distributions peaking at calculated values of $\hat{v}_{\mathrm{Er}} = 451\,\mathrm{m/s}$ and $\hat{v}_{\mathrm{Dy}} = 457\,\mathrm{m/s}$. This makes it necessary to

[12] Anti-reflection coating for 401 nm, 421 nm, 532 nm, 583 nm, 626 nm, 1064 nm and 1550 nm

decelerate the atomic beam down to the MOT capture velocities $v_{\mathrm{cap,Er}}$ and $v_{\mathrm{cap,Dy}}$, the maximum velocities at which the dual-species MOT can still capture erbium or dysprosium atoms. An efficient technique is Zeeman slowing, as [121] first reported in 1982 for sodium. Its working principle relies on slowing atoms with velocity v via the scattering force F_{scat} of a counterpropagating red-detuned laser beam with wavenumber k, while simultaneously compensating the change in the Doppler shift kv via a Zeeman shift E_{ZS} of the atoms' energy levels (see equation (2.8)). Many textbooks, for instance [83] or [120], offer a detailed description.

The following discussion considers the steps in [83] and derives the optimal **B**-field profile B_{opt} for Zeeman slowing. In a ZS along the x-axis, an atom is subject to the scattering force of a counterpropagating red-detuned laser beam as

$$F_{\mathrm{scat}}\left(2\pi\delta + kv\right) = \frac{1}{2}\hbar k\Gamma \frac{{}^{I}/_{I_{\mathrm{sat}}}}{1 + {}^{I}/_{I_{\mathrm{sat}}} + {}^{4(2\pi\delta+kv)^2}/_{\Gamma^2}}, \tag{3.1}$$

with the photon momentum $\hbar k$ and $k = {}^{2\pi}/_{\lambda} = {}^{2\pi\nu}/_{c}$, the decay rate Γ, the laser beam intensity I, and the light detuning $\delta = \nu - \nu_0$ from resonance to an atomic transition at frequency ν_0 and with saturation intensity I_{sat}. If F_{scat} saturates at ${}^{\hbar k\Gamma}/_{2}$ in the high-intensity limit, integrating for the resulting acceleration of the atom with mass m

$$\frac{\mathrm{d}v}{\mathrm{d}t} = \frac{\mathrm{d}x}{\mathrm{d}t}\frac{\mathrm{d}v}{\mathrm{d}x} = v\frac{\mathrm{d}v}{\mathrm{d}x} = -\frac{F_{\mathrm{scat}}}{m} = -\frac{\hbar k\Gamma}{2m} \tag{3.2}$$

from the initial velocity v_{ini} to the final velocity v_{fin} and from $x' = 0$ to $x' = x$, with the deceleration length x, leads to

$$v_{\mathrm{ini}}^2 - v_{\mathrm{fin}}^2 = s\frac{\hbar k\Gamma}{m}x. \tag{3.3}$$

The safety factor $s \in (0, 1)$ controls the actual acceleration below the maximal value in equation (3.2). Equation (3.3) yields the position-dependent final velocity

$$v_{\mathrm{fin}}\left(x\right) = v_{\mathrm{ini}}\sqrt{1 - s\frac{\hbar k\Gamma}{m v_{\mathrm{ini}}^2}x}. \tag{3.4}$$

This illustrates the superiority of the broad transition to the ${}^1\mathrm{P}_1$ state for Zeeman slowing, as the large $\Gamma_{\mathrm{Er,401\,nm}}$ or $\Gamma_{\mathrm{Dy,421\,nm}}$ (see Table 2.2) and the large $\hbar k_{\mathrm{Er,401\,nm}}$ or $\hbar k_{\mathrm{Dy,421\,nm}}$ reduce x for slowing to a target v_{fin}. Further, equation (3.4) gives an estimate for $v_{\mathrm{cap,Er}}$ and $v_{\mathrm{cap,Dy}}$. The MOT beams with ${}^1/e^2$-waists $w_{\mathrm{MOT}} = 19\,\mathrm{mm}$ under $45\,^\circ$ to the atomic beam propagation axis set $x = \sqrt{2} \times 38\,\mathrm{mm}$. For $v_{\mathrm{fin}} = 0$ and $s = 1$, $v_{\mathrm{cap,Er}} = 16.0\,\mathrm{m/s}$ and $v_{\mathrm{cap,Dy}} = 13.4\,\mathrm{m/s}$. Tables 2.1 and 2.2 provide the necessary values for m, λ and Γ.

By comparing kv_{fin} to $2\pi\delta$ and the differential E_{ZS} of the transition, the resonance condition is

$$kv_{\mathrm{ini}}\sqrt{1 - s\frac{\hbar k\Gamma}{m v_{\mathrm{ini}}^2}x} = -2\pi\delta + \frac{\Delta\mu}{\hbar}B_{\mathrm{opt}}\left(x\right), \tag{3.5}$$

with the transition's differential magnetic moment $\Delta\mu$ (see Chapter 2), and as a result

$$B_{\mathrm{opt}}\left(x\right) = \frac{\hbar k v_{\mathrm{ini}}}{\Delta\mu}\sqrt{1 - s\frac{\hbar k\Gamma}{m v_{\mathrm{ini}}^2}x} + \frac{\hbar 2\pi\delta}{\Delta\mu}. \tag{3.6}$$

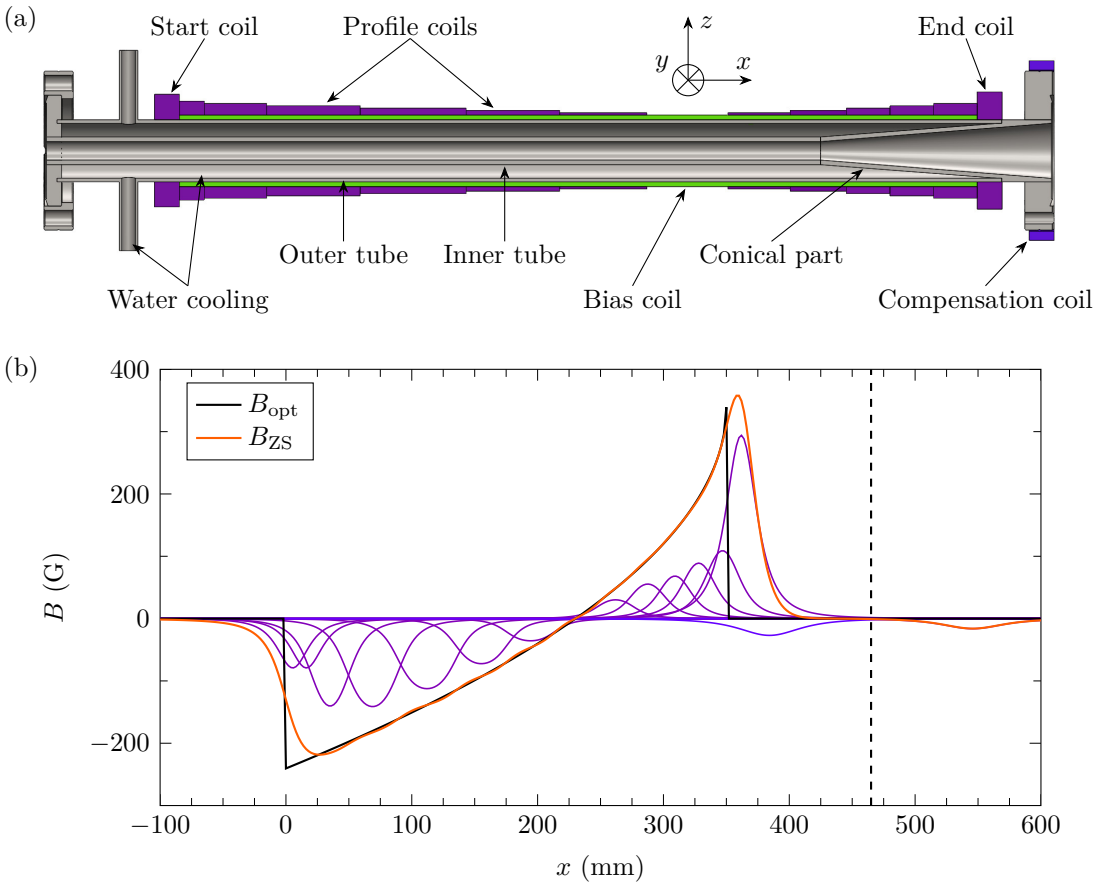

Figure 3.4: Spin-flip ZS for erbium and dysprosium. (a) Vertical sectional view along the atomic beam propagation axis (x-axis). The ZS tube consists of two 435 mm long stainless steel tubes with 2 mm wall thickness and outer diameters of 26 mm and 10 mm, respectively. The inner tube conically expands over the last 100 mm. The ZS's start, end and profile coils are in violet, whereas its bias coil and its first compensation coil are in green and blue. (b) Calculated spin-flip ZS **B**-field profile B_{ZS} as a function of position x. In total 13 individual coils, the start, the end and the profile coils (violet), model B_{ZS} (orange) to reproduce the optimal **B**-field profile B_{opt} (black) for a slowing distance of 350 mm. The ZS's compensation coils (blue) compensate the leakage field at the center of the main chamber (vertical dashed line). The start of B_{opt} defines the zero position.

For the present endeavor, the realization of a dual-species atomic beam source and the similar laser cooling properties (see Table 2.2), again becoming evident in the similar $v_{\mathrm{cap,Er}}$ and $v_{\mathrm{cap,Dy}}$, allow for a single ZS for both elements. Conveniently, such an approach requires only fine adjustments due to the elements' differences in order to obtain an optimal ZS performance.

Figure 3.4 (a) displays a vertical sectional view through the ZS. A 435 mm long stainless steel tube with an outer diameter of 26 mm and 2 mm wall thickness holds a 370 mm long stack of 14 **B**-field coils[13]. The atomic beam travels through a second 435 mm long inner stainless steel tube with an outer diameter of 10 mm and 2 mm wall thickness, which

[13]Wire material: copper, geometry: 2.7 mm × 1.0 mm

conically increases its diameter over the last 100 mm where it connects to the outer tube. This reduces the probability of slow atoms colliding with the tube wall, and thus increases the fraction of atoms arriving within the MOT capture volume. Moreover, the inner tube completes the differential pumping scheme between Modules II and III of the UHV apparatus (see Section 3.1), whereas the hollow volume in between both tubes serves as water circulation path as part of the water cooling system for the coil stack.

The ZS operates on the broad transition at $\lambda_{\mathrm{Er}} = 401\,\mathrm{nm}$ or $\lambda_{\mathrm{Dy}} = 421\,\mathrm{nm}$ with an increasing **B**-field in spin-flip configuration. It decelerates initial velocity classes of up to $v_{\mathrm{ini,Er}} = 370\,\mathrm{m/s}$ and $v_{\mathrm{ini,Dy}} = 358\,\mathrm{m/s}$ over a total distance of 350 mm down to $v_{\mathrm{fin,Er}} = v_{\mathrm{fin,Dy}} = 5\,\mathrm{m/s}$, which corresponds to $s_{\mathrm{Er}} = 0.35$ and $s_{\mathrm{Dy}} = 0.31$. Here, as a precaution, $v_{\mathrm{fin,Er}} < v_{\mathrm{cap,Er}}$ and $v_{\mathrm{fin,Dy}} < v_{\mathrm{cap,Dy}}$. Figure 3.4 (b) compares the calculated spin-flip ZS **B**-field profile B_{ZS} to the optimal **B**-field profile B_{opt} (see equation (3.6)). In total 13 out of the 14 coils, the start, the end and 11 profile coils, differing in layers and windings (values range between 1-11 and 4-17), shape B_{ZS} such that it deviates from B_{opt} by only 1.5 % from $x = 25\,\mathrm{mm}$ to $x = 345\,\mathrm{mm}$, and thus almost over the entire slowing distance. Further, a bias coil, with two layers of 128 windings, can tune the zero-crossing of B_{ZS}, and thus v_{ini}. Two coils, each with four layers of four windings, at a distance of 75 mm around the center of the main chamber compensate the leakage **B**-field.

3.2.2 Layout of the main chamber coils

The main chamber holds eight sets of coil pairs symmetrically around its center for homogeneous and/or quadrupole **B**-fields. Every coil pair serves a specific purpose and is individually controllable. Figure 3.1 illustrates the complete coil assembly at the UHV apparatus, whereas Figure 3.5 shows the coil pairs along the main chamber's vertical z-axis in sectional views. The following description[14] characterizes the generated **B**-fields around the center of the main chamber by the calculated total **B**-field value $(B_{\mathrm{tot}})_{x,y,z} = \sqrt{B_x^2 + B_y^2 + B_z^2}$ along the x-, y- and z-axis, respectively, as well as by the respective gradient $(\nabla B_{\mathrm{tot}})_{x,y,z} = \partial_{x,y,z}\,(B_{\mathrm{tot}})_{x,y,z}$.

Low-magnetic-field coils

The inverted viewports along the vertical z-axis of the main chamber support each a copper mounting cylinder with an inner diameter of 81 mm (see Figure 3.5 (a)). It has a cutout preventing eddy currents and a conical cut to fit the future high-resolution imaging system along this axis (see Figure 3.5 (b)). Each cylinder stacks the individual coils for in total four different coil pairs at an inner diameter of 85 mm as close as possible to the center of the main chamber. The internal water cooling system maintains the coils at a steady-state temperature of 28 °C at a maximum coil current of 10 A.

The first coil pair combines two 100 mm distant coils[15], each with six layers of ten windings, in an AHH-like connection scheme. Around the center, it produces a quadrupole **B**-field $\mathbf{B}_{\mathrm{AH}}$ with $|\,(\nabla B_{\mathrm{tot}})_{x,y}\,| = 0.775\,^{(\mathrm{G/cm})}/_{\mathrm{A}}$ and $|\,(\nabla B_{\mathrm{tot}})_{z}\,| = 1.550\,^{(\mathrm{G/cm})}/_{\mathrm{A}}$ (see Figure 3.6 (a)). For the MOT, this AHH-like coil provides the quadrupole **B**-field $\mathbf{B}_{\mathrm{AH,MOT}}$ with typical gradient values $\left(\nabla B_{\mathrm{AH,MOT}}\right)_{x,y} = 2.25\,^{\mathrm{G}}/_{\mathrm{cm}}$ and $\left(\nabla B_{\mathrm{AH,MOT}}\right)_{z} = 4.50\,^{\mathrm{G}}/_{\mathrm{cm}}$.

[14] The upcoming PhD thesis of Gianmaria Durastante will provide a more detailed discussion of the entire coil system including characterization measurements.

[15] Wire material: copper, geometry: 2.7 mm × 1.0 mm, same for the HH-like coil

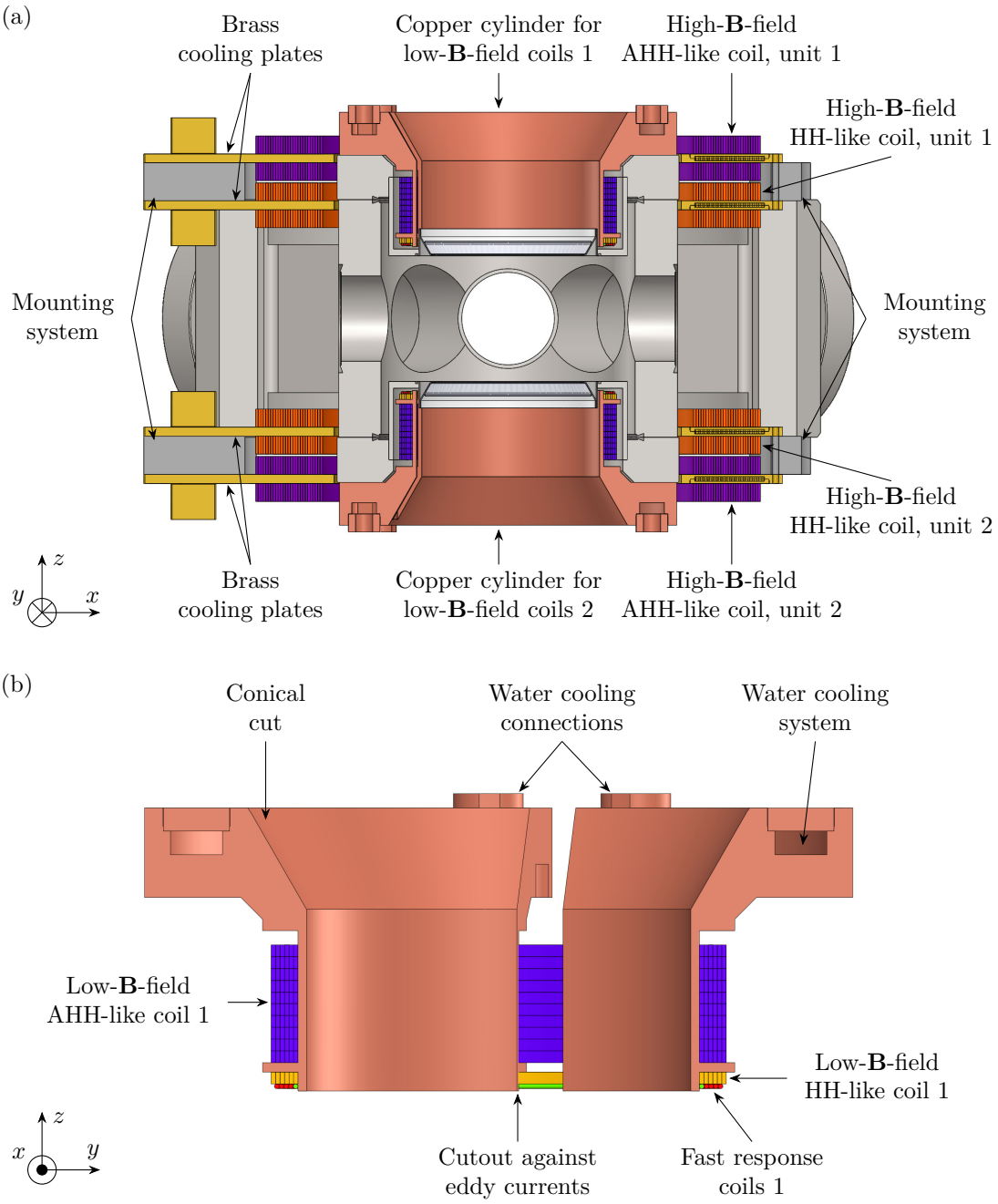

Figure 3.5: Coil systems at the main chamber. (a) Vertical sectional view of the main chamber along the atomic beam propagation axis (x-axis). The main chamber holds six **B**-field coil pairs in close proximity symmetrically around its center. The high-**B**-field anti-Helmholtz (AHH)-like (violet) and Helmholtz (HH)-like (orange) coil pair operate in the designated cutouts. The respective coil units include a brass water cooling plate with a slit against eddy currents (out of sectional plane). The remaining four coil pairs are for low **B**-fields and within copper cylinders in the CF100 inverted viewports. (b) Vertical sectional view of a single copper cylinder in the y-z plane. The four coils are part of an AHH-like (blue) and a HH-like (yellow) coil pair as well as fast response coil pairs (green and red). The cylinder has a water cooling system and a cutout against eddy currents.

The second one pairs two coils, each with six layers of a single winding, at a distance of 70 mm in a HH-like connection scheme. It produces a homogeneous **B**-field $\mathbf{B}_{\mathrm{HH}}$ of $(B_{\mathrm{tot}})_{x,y,z} = 0.779\,\mathrm{G/A}$ with a (relative) flatness of 10^{-4} within ± 0.5 mm of the center pointing along the z-axis (see Figure 3.6 (b)). For the MOT loading, this HH-like coil shifts the origin of the quadrupole **B**-field $\mathbf{B}_{\mathrm{AH,MOT}}$ via a bias **B**-field $\mathbf{B}_{\mathrm{HH,MOT}}$ of typically $B_{\mathrm{HH,MOT}} = -3.245\,\mathrm{G}$ below the center of the main chamber. Moreover, it maintains a homogeneous **B**-field $\mathbf{B}_{\mathrm{HH,evap}}$ of constant value during evaporative cooling and can provide precise **B**-fields for low-field Feshbach spectroscopy.

The two remaining coil pairs have one and four layers of a single winding per coil[16], respectively. This makes both ideal for homogeneous and time-varying **B**-fields with a short time response.

High-magnetic-field coils

The designated cutouts in the main chamber allow for two additional coil pairs along the z-axis, one in an AHH- and the other one in a HH-like connection scheme (see Figure 3.5 (a)). The individual coil units are 145 mm and 105 mm apart, respectively. Each of the four coil units consists of two coils[17], each with an inner diameter of 165 mm and 27 layers of a single winding, and a 4 mm thick brass water cooling plate inbetween. The cooling plate has a slit to prevent eddy currents and its internal water cooling system allows for coil currents of up to 100 A at a steady-state temperature of 40 °C.

Figure 3.7 summarizes the performance of both coil pairs. The AHH-like coil generates a quadrupole **B**-field with $|\,(\nabla B_{\mathrm{tot}})_{x,y}\,| = 0.240\,(\mathrm{G/cm})/\mathrm{A}$ and $|\,(\nabla B_{\mathrm{tot}})_{z}\,| = 0.480\,(\mathrm{G/cm})/\mathrm{A}$ around the center (see Figure 3.7 (a)), whereas the HH-like coil provides a homogeneous **B**-field of $(B_{\mathrm{tot}})_{x,y,z} = 4.372\,\mathrm{G/A}$ with a flatness of 10^{-4} within ± 1.5 mm of the center pointing along the z-axis (see Figure 3.7 (b)). Furthermore, the AHH-like coil can switch to a HH-like operation, where it creates a homogeneous **B**-field of $(B_{\mathrm{tot}})_{x,y,z} = 3.244\,\mathrm{G/A}$ with a flatness of 10^{-4} within ± 1 mm of the center. This is particularly interesting for Feshbach spectroscopy in order to extend the **B**-field range up to 800 G in steady state.

Compensation cage

The experimental apparatus also controls the **B**-field in the horizontal x-y plane. For that purpose, two square coil pairs of 380 mm × 380 mm and 350 mm × 350 mm, respectively, surround the main chamber along the system's x- and y-axis and form a cage (see Figure 3.1). Each coil[18] has eleven layers of two windings within an aluminum U-channel. The larger coil pair produces a homogeneous **B**-field of $(B_{\mathrm{tot}})_{x,y,z} = 1.04\,\mathrm{G/A}$ pointing along the x-axis, whereas the smaller one achieves $(B_{\mathrm{tot}})_{x,y,z} = 1.12\,\mathrm{G/A}$ pointing along the y-axis, both with a flatness of 2×10^{-6} within ± 0.5 mm of the center. The maximum current rating for both is 10 A.

During the experimental sequence, this cage compensates external **B**-fields, for instance the earth's **B**-field in the horizontal x-y plane, and rotates the **B**-field for absorption imaging (see Section 3.4). Moreover, its combined operation with the HH-like coil within the inverted viewports generates **B**-fields of up to 5 G in any direction on a sphere.

[16] Wire material: copper, geometry: 1.0 mm diameter
[17] Wire material: copper, geometry: 8.0 mm × 1.0 mm
[18] Wire material: copper, geometry: 4.0 mm × 1.0 mm

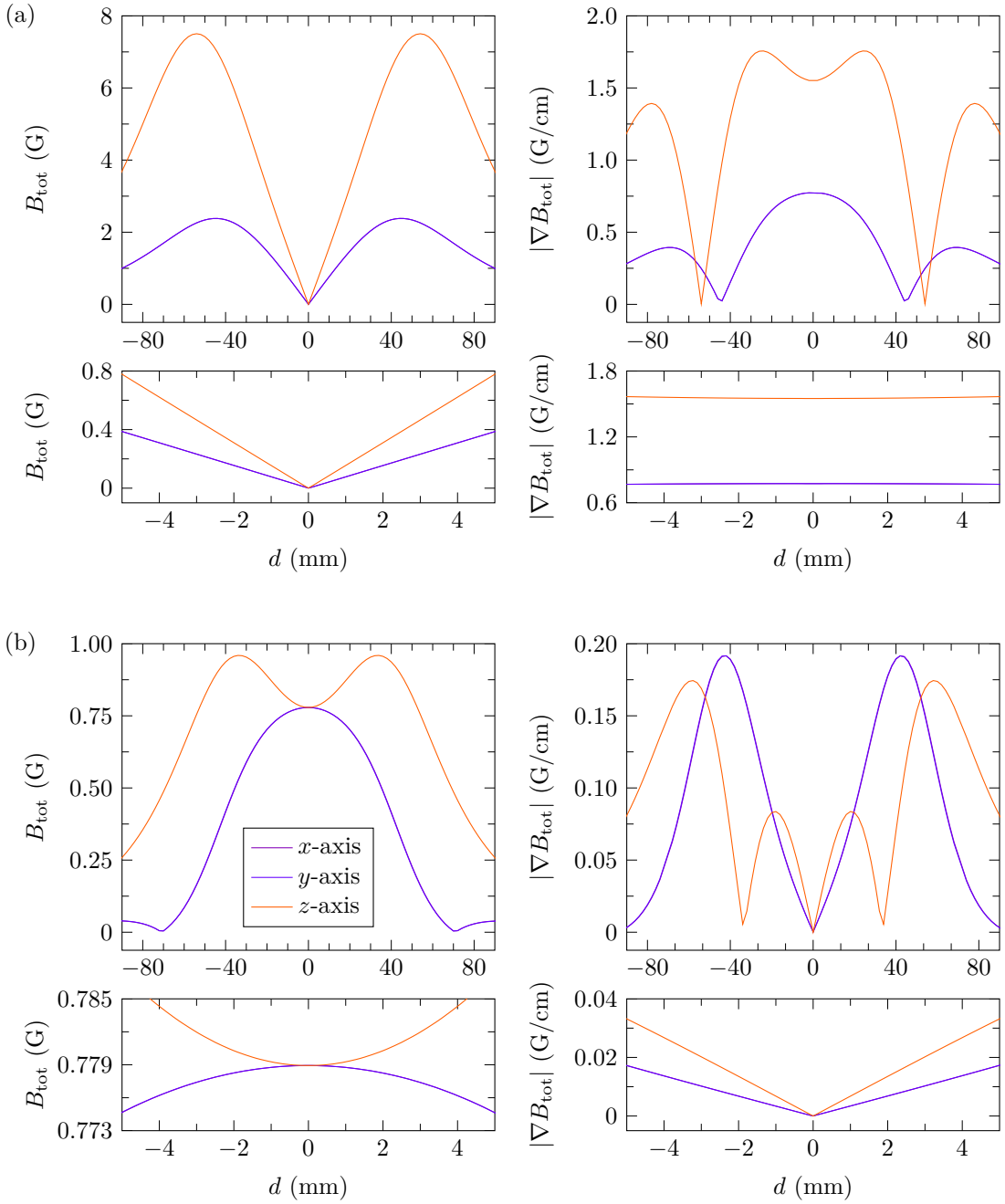

Figure 3.6: Calculated total **B**-field value $(B_{\mathrm{tot}})_{x,y,z}$ (left column) and the corresponding gradient $(\nabla B_{\mathrm{tot}})_{x,y,z}$ (right column) as a function of distance d from the center of the main chamber for the low-**B**-field (a) anti-Helmholtz (AHH)-like and (b) Helmholtz (HH)-like coil within the inverted viewports (see Figure 3.5). The orange data shows the behavior along the z-axis, whereas the violet and blue data corresponds to the orthogonal plane along the x- and y-axis, respectively. The current for the calculation is 1 A. The AHH-like coil produces a quadrupole **B**-field $\mathbf{B}_{\mathrm{AH}}$ with $|\,(\nabla B_{\mathrm{tot}})_{x,y}\,| = 0.775\,^{(\mathrm{G/cm})}/_{\mathrm{A}}$ and $|\,(\nabla B_{\mathrm{tot}})_{z}\,| = 1.550\,^{(\mathrm{G/cm})}/_{\mathrm{A}}$ around the center, whereas the HH-like coil generates a homogeneous **B**-field $\mathbf{B}_{\mathrm{HH}}$ of $(B_{\mathrm{tot}})_{x,y,z} = 0.779\,^{\mathrm{G}}/_{\mathrm{A}}$ with a flatness of 10^{-4} within ± 0.5 mm of the center pointing along the z-axis.

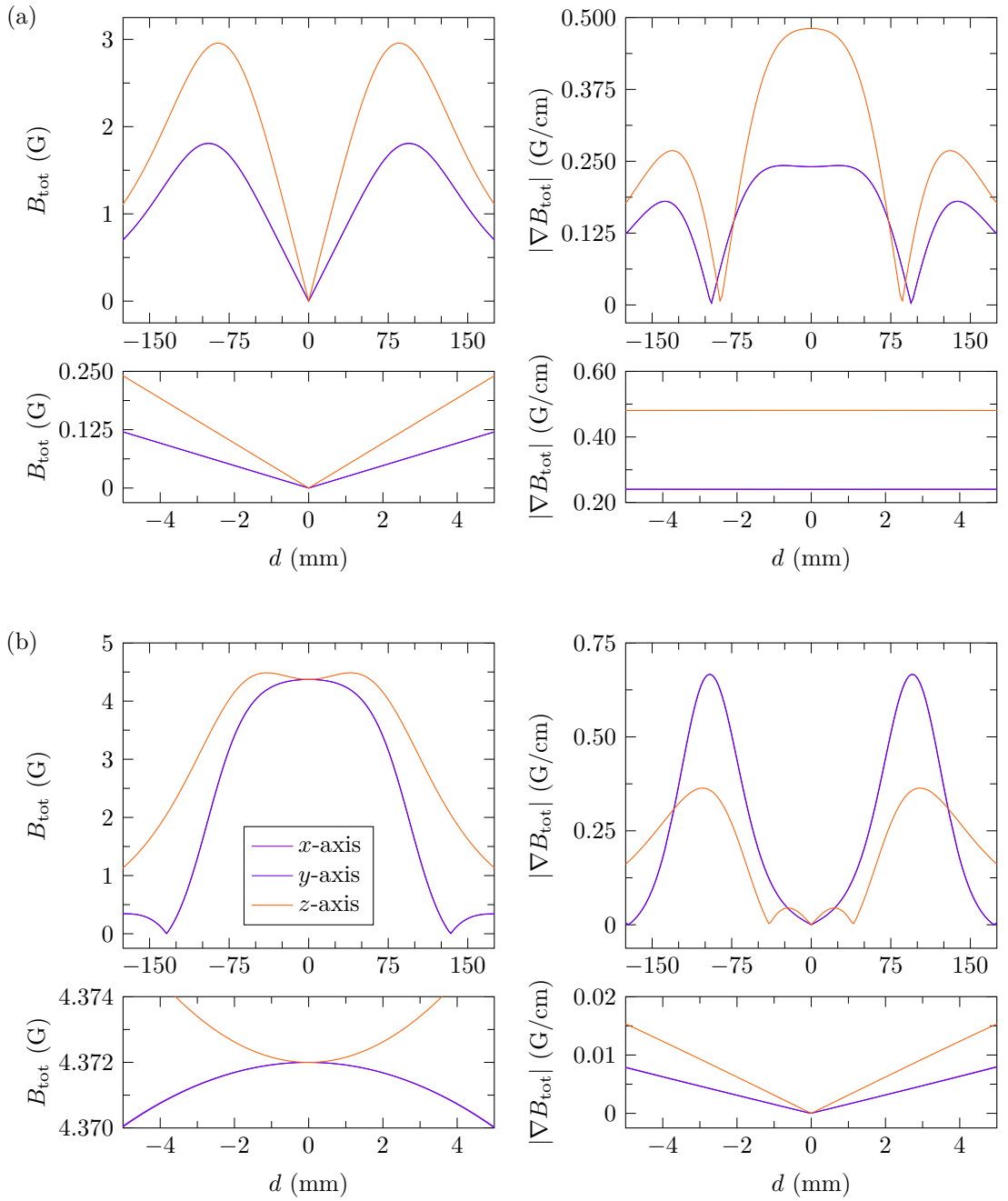

Figure 3.7: Calculated total **B**-field value $(B_{\mathrm{tot}})_{x,y,z}$ (left column) and the corresponding gradient $(\nabla B_{\mathrm{tot}})_{x,y,z}$ (right column) as a function of distance d from the center of the main chamber for the high-**B**-field (a) anti-Helmholtz (AHH)-like and (b) Helmholtz (HH)-like coil within the main chamber's cutouts (see Figure 3.5). The orange data shows the behavior along the z-axis, whereas the violet and blue data corresponds to the orthogonal plane along the x- and y-axis, respectively. The current for the calculation is 1 A. The AHH-like coil produces a quadrupole **B**-field $\mathbf{B}_{\mathrm{AH}}$ with $|\,(\nabla B_{\mathrm{tot}})_{x,y}\,| = 0.240\,(\mathrm{G/cm})/\mathrm{A}$ and $|\,(\nabla B_{\mathrm{tot}})_{z}\,| = 0.480\,(\mathrm{G/cm})/\mathrm{A}$ around the center, whereas the HH-like coil generates a homogeneous **B**-field of $(B_{\mathrm{tot}})_{x,y,z} = 4.372\,\mathrm{G/A}$ with a flatness of 10^{-4} within ± 1.5 mm of the center pointing along the z-axis.

3.3 Laser systems and optical setups

The efficient and robust operation of the dual-species MOT relies on the broad and the intercombination-line transition to the $^1\mathrm{P}_1$ and the $^3\mathrm{P}_1$ states, respectively, as Chapter 2 discussed. This section reviews the laser systems, their individual optical setups as well as their combined implementation and operation at the UHV apparatus. Section 3.3.1 starts with the laser systems for $\lambda_{\mathrm{Er}} = 401\,\mathrm{nm}$ and $\lambda_{\mathrm{Dy}} = 421\,\mathrm{nm}$, driving the broad transition for the TC, the spin-flip ZS, an absorption imaging as well as a blow beam. Next, Section 3.3.2 introduces the $\lambda_{\mathrm{Er}} = 583\,\mathrm{nm}$ and the $\lambda_{\mathrm{Dy}} = 626\,\mathrm{nm}$ laser system for the dual-species MOT itself. Finally, Section 3.3.3 addresses the various optical setups at the UHV apparatus for the TC unit, the spin-flip ZS as well as the dual-species MOT.

3.3.1 Broad transition: 401 nm and 421 nm

The laser setups at $\lambda_{\mathrm{Er}} = 401\,\mathrm{nm}$ (see Figure 3.8) and at $\lambda_{\mathrm{Dy}} = 421\,\mathrm{nm}$ (see Figure 3.9) are essentially identical. Hence, the following discussion considers the basic structure of a single laser setup only for simplicity, but emphasizes their differences.

The optical setup arranges around a commercial multi-staged laser system[19] employing second harmonic generation (SHG). A grating-stabilized diode (master) laser, which emits at $\lambda_{\mathrm{Er}} = 802\,\mathrm{nm}$ or $\lambda_{\mathrm{Dy}} = 842\,\mathrm{nm}$, seeds a tapered amplifier (TA), while some of the master laser's light is available for monitoring on a fiber-coupled wavemeter[20]. The high output power from the TA optically pumps a resonant SHG unit combining a nonlinear crystal with a ring resonator in bow-tie configuration. This concept delivers a maximum second-harmonic power $P_{401\,\mathrm{nm,SHG}} = 2\,\mathrm{W}$ or $P_{421\,\mathrm{nm,SHG}} = 1.3\,\mathrm{W}$. After an initial beam shaping, the frequency-doubled laser light splits among five beam paths.

The spectroscopy path provides the possibility to frequency stabilize the laser system to an atomic reference. A first single-pass acusto-optic modulator[21] (AOM) frequency-shifts the laser light by $\nu_{401\,\mathrm{nm,spec}} = \nu_{421\,\mathrm{nm,spec}} = 110\,\mathrm{MHz}$, which then arrives polarization-maintaining (PM) fiber-coupled at the spectroscopy setup. Here, a modulation transfer spectroscopy generates a dispersive signal for frequency stabilization utilizing a hollow-cathode lamp[22] (HCL) and a home-built electro-optic modulator (EOM) [122, 123]. Thus, considering the initial $\nu_{401\,\mathrm{nm,spec}}$ or $\nu_{421\,\mathrm{nm,spec}}$, the stabilized laser system has an effective detuning $\delta_{401\,\mathrm{nm}} = \delta_{421\,\mathrm{nm}} = -110\,\mathrm{MHz}$ to the $\left(^1\mathrm{P}_1\right)(6,1)_7$ and the $\left(^1\mathrm{P}_1\right)(8,1)_9$ state, respectively. This approach reduces the total amount of required AOMs in the other beam paths and makes a single-pass operation for their majority possible. The experiences from [89] suggested that the modulation transfer signals of the fermionic isotopes are too small to be suited for frequency stabilization. Hence, this beam path contains one additional double-pass AOM[23] for the $\lambda_{\mathrm{Er}} = 401\,\mathrm{nm}$ and two additional double-pass AOMs[24] for the $\lambda_{\mathrm{Dy}} = 421\,\mathrm{nm}$ laser setup. This allows for adjusting the laser system's overall $\delta_{401\,\mathrm{nm}}$ or $\delta_{421\,\mathrm{nm}}$ such that the experiment addresses a fermionic isotope, while the master laser remains stabilized to a bosonic isotope. Contrary to [89], however,

[19] TOPTICA Photonics AG, DLC TA-SHG PRO
[20] HighFinesse GmbH/Ångstrom, WS/6-200
[21] Gooch & Housego PLC, 3100-125, center frequency 100 MHz, bandwidth 25 MHz
[22] Heraeus Holding GmbH, 3QQAY/Er for erbium and 3QQAY/Dy for dysprosium, each with 4 mbar of argon, high-voltage power supply FuG Elektronik GmbH, MCP 350-650
[23] Gooch & Housego PLC, 3080-125 center, frequency 80 MHz, bandwidth 25 MHz
[24] Brimrose Corporation, TEF-270-100-401, center frequency 270 MHz, bandwidth 100 MHz

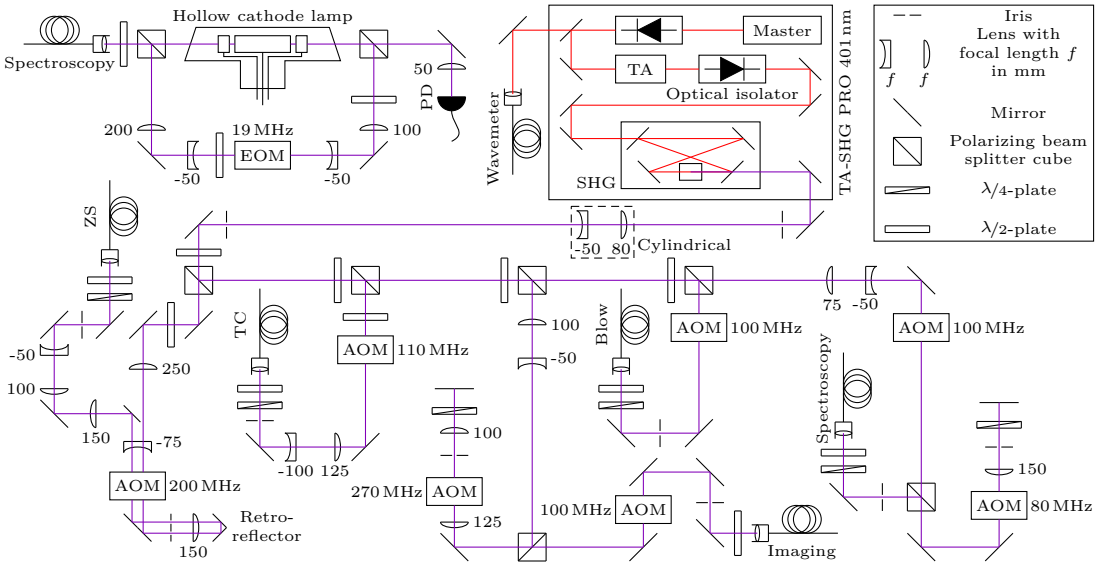

Figure 3.8: Optical setup for the $\lambda_{\mathrm{Er}} = 401\,\mathrm{nm}$ laser system driving the transition to the $\left({}^1\mathrm{P}_1\right)(6,1)_7$ state in erbium. The laser light that a SHG unit generates from an amplified 802 nm master laser distributes between five different beam paths. Each individually frequency-shifts and subsequently PM fiber-couples the light to its designated location at the UHV apparatus (see Section 3.3.3). The modulation transfer spectroscopy setup in the top left serves for the frequency stabilization of the master laser. The various frequency values specify the AOM center frequencies, whereas the actual frequencies are in the main text.

a direct frequency stabilization to the fermionic isotopes is possible for the present laser systems without any notable influence for instance on the long-term stability during the production of quantum-degenerate Bose-Fermi mixtures (see Chapter 4).

The beam paths for the TC unit and the spin-flip ZS are the two high-power paths of the laser system. Each utilizes a quartz AOM to reduce thermal lensing in the AOM crystal owing to the wavelength regime. A single double-pass AOM[25] in the ZS path detunes the laser light by additional $\nu_{401\,\mathrm{nm,ZS}} = -410\,\mathrm{MHz}$ or $\nu_{421\,\mathrm{nm,ZS}} = -420\,\mathrm{MHz}$ further to the red. Here, a retroreflector from two square mirrors under 90 ° helps overcome the strong polarization dependence of the diffraction efficiency, typical for a quartz AOM, and thus ensures a high double-pass efficiency. In the TC path, a single-pass AOM[26] frequency-shifts the laser light back towards resonance by an experimentally optimized value $\nu_{401\,\mathrm{nm,TC}} = 106\,\mathrm{MHz}$ and $\nu_{421\,\mathrm{nm,TC}} = 108\,\mathrm{MHz}$, respectively.

The remaining two beam paths are for an imaging and a blow beam, respectively. In each beam path, a single-pass AOM[27] compensates the initial $\nu_{401\,\mathrm{nm,spec}}$ or $\nu_{421\,\mathrm{nm,spec}}$. Moreover, the imaging light is further detunable via a double-pass AOM[28]. This will be necessary when switching the future vertical high-resolution imaging from absorption imaging to an insitu technique such as phase-contrast imaging [7] (see Chapter 6).

[25] Gooch & Housego PLC, 3200-1210, center frequency 200 MHz, bandwidth 100 MHz
[26] Gooch & Housego PLC, I-M110-2C10B6-3-GH26, center frequency 110 MHz
[27] Gooch & Housego PLC, 3100-125, center frequency 100 MHz, bandwidth 25 MHz
[28] Brimrose Corporation, TEF-270-100-401, center frequency 270 MHz, bandwidth 100 MHz

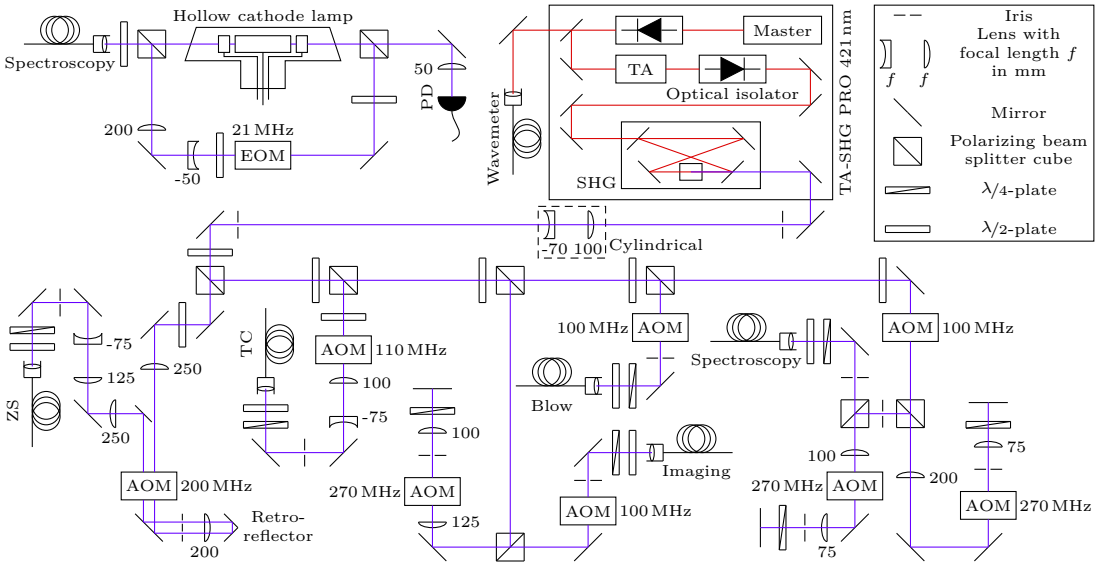

Figure 3.9: Optical setup for the $\lambda_{\mathrm{Dy}} = 421\,\mathrm{nm}$ laser system driving the transition to the $\left({}^1\mathrm{P}_1\right)(8,1)_9$ state in dysprosium. The laser light that a SHG unit generates from an amplified 842 nm master laser distributes between five different beam paths. Each individually frequency-shifts and subsequently PM fiber-couples the light to its designated location at the UHV apparatus (see Section 3.3.3). The modulation transfer spectroscopy setup in the top left serves for the frequency stabilization of the master laser. The various frequency values specify the AOM center frequencies, whereas the actual frequencies are in the main text.

Finally, PM single mode fibers connect the different beam paths to their designated optical setups at the UHV apparatus (see Section 3.3.3). While for the low-power paths standard PM single mode fibers are sufficient, for the ZS as well as the TC path high-power PM single mode fibers[29] with end caps and a pure silica core are in operation without any obvious signs of degradation since their implementation at the very beginning of construction.

3.3.2 Intercombination-line transition: 583 nm and 626 nm

The $\lambda_{\mathrm{Er}} = 583\,\mathrm{nm}$ laser system relies on the combination of a grating-stabilized diode laser[30] at $\lambda_{\mathrm{Er}} = 1166\,\mathrm{nm}$ and a Raman-fiber amplifier[31] (see Figure 3.10). An integrated fiber-coupled SHG unit in single-pass configuration operates at 65.0 °C to achieve phase matching [96], and produces a maximum second-harmonic power $P_{583\,\mathrm{nm,SHG}} = 1.7\,\mathrm{W}$.

Similar to single-species experiments with dysprosium [124], the $\lambda_{\mathrm{Dy}} = 626\,\mathrm{nm}$ laser system is a sum-frequency generation (SFG) setup in single-pass configuration (see Figure 3.10). The optical pumping stage utilizes a 40 mm long magnesium oxide doped periodically poled lithium niobate (MgO:PPLN) crystal[32] and its entire layout is in

[29] Schäfter + Kirchhoff GmbH, PMC-E-400Si-2.8-NA011-3-APC.EC-750-P
[30] TOPTICA Photonics AG, DLC DL PRO
[31] MPB Communications Inc., VRFA-P-1800-583-SF
[32] Covesion Ltd, MSFG626-0.5-40

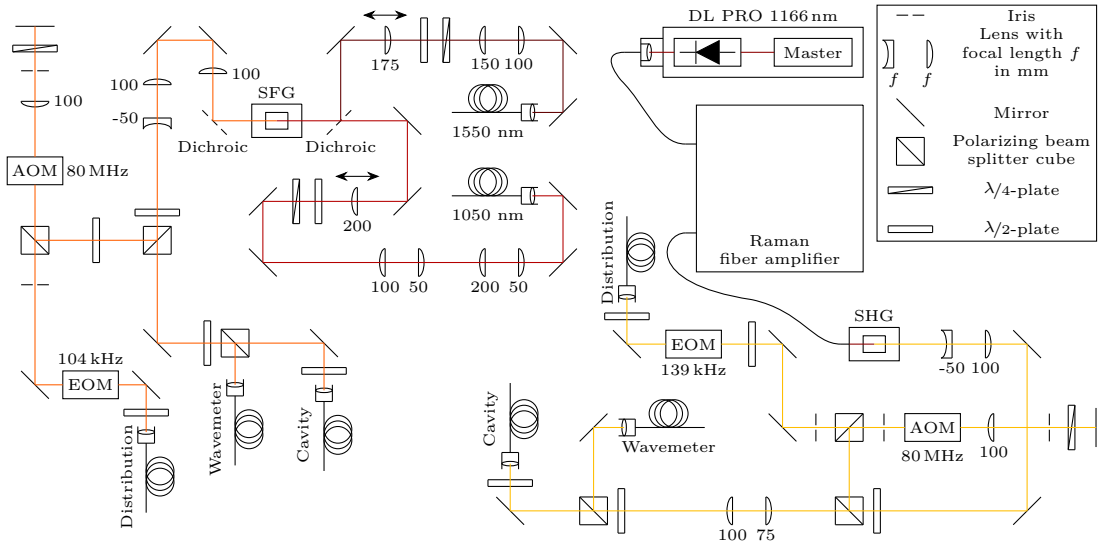

Figure 3.10: Optical setups for the $\lambda_{\mathrm{Er}} = 583\,\mathrm{nm}$ (right) and the $\lambda_{\mathrm{Dy}} = 626\,\mathrm{nm}$ (left) laser system driving the intercombination-line transition to the $\left({}^3\mathrm{P}_1\right)(6,1)_7$ and the $\left({}^3\mathrm{P}_1\right)(8,1)_9$ state in erbium and dysprosium, respectively. The $\lambda_{\mathrm{Er}} = 583\,\mathrm{nm}$ laser system comprises a grating-stabilized diode laser at $\lambda_{\mathrm{Er}} = 1166\,\mathrm{nm}$ and a Raman fiber amplifier with a fiber-coupled single-pass SHG unit, whereas for the $\lambda_{\mathrm{Dy}} = 626\,\mathrm{nm}$ laser system two amplified DFB fiber lasers at $\lambda_{\mathrm{Dy}} = 1050\,\mathrm{nm}$ and $\lambda_{\mathrm{Dy}} = 1550\,\mathrm{nm}$ pump a SFG process in a MgO:PPLN crystal. In both setups, a fiber-coupled EOM guides laser light to a reference cavity setup for a PDH frequency stabilization (see Figure 3.11 (a)), while a spectral-broadening EOM enhances the MOT light's spectral width right in front of the PM fiber coupling to the MOT distribution (see Figure 3.11 (b)).

accordance to the Boyd-Kleinmann model [96, 125], which generally predicts a pump beam's ideal $1/e^2$-waist at the center of a non-linear crystal as [96]

$$w_{\mathrm{SFG},\lambda} = \sqrt{\frac{l\lambda}{2.84 \times 2\pi n_\lambda}}, \tag{3.7}$$

with the crystal length l, the pump light wavelength λ and the corresponding refractive index n_λ[33]. Two distributed feedback (DFB) fiber lasers[34] at $\lambda_{\mathrm{Dy}} = 1050\,\mathrm{nm}$ and $\lambda_{\mathrm{Dy}} = 1550\,\mathrm{nm}$, respectively, seed amplifier units with 5 W output power each. The emitted pump beams pass through initial beam shaping optics to achieve the required $1/e^2$-waists $w_{\mathrm{SFG},1050\,\mathrm{nm}} = 33\,\mu\mathrm{m}$ and $w_{\mathrm{SFG},1550\,\mathrm{nm}} = 40\,\mu\mathrm{m}$. Translation stages for the last focusing lenses and the crystal facilitate a precise centering of both foci in the center of the crystal. A dichroic mirror[35] overlaps both pump beams right in front of the crystal. Further, a commercial oven[36] stabilizes the crystal at 168.70 °C in order to maintain the phase matching condition of the SFG process. At peak performance, a second dichroic mirror[37] separates a sum-frequency power $P_{626\,\mathrm{nm,SFG}} = 1.6\,\mathrm{W}$ from the pump light.

[33] MgO:PPLN: $n_{1050\,\mathrm{nm}} = 2.203$ and $n_{1550\,\mathrm{nm}} = 2.222$
[34] NKT Photonics A/S, Koheras Boostik Y10 at 1050 nm and Koheras Boostik E15 at 1550 nm
[35] Thorlabs Inc., DMSP1180
[36] Covesion Ltd, PV40 in combination with the temperature controller OC1
[37] Thorlabs Inc., DMLP650R

In a first step, lenses reshape the visible laser light, which then distributes among three beam paths leading to a reference cavity for frequency stabilization (see Figure 3.11 (a)), a MOT distribution setup (see Figure 3.11 (b)), as well as the wavemeter for monitoring.

The beam path leading via a PM fiber coupling to the MOT distribution guides most of the power $P_{583\,\mathrm{nm}}$ or $P_{626\,\mathrm{nm}}$. An initial double-pass AOM[38] switches the laser light on and off during the experimental sequence, and stabilizes $P_{583\,\mathrm{nm}}$ or $P_{626\,\mathrm{nm}}$ in the MOT distribution. Additionally, a spectral-broadening EOM[39] in front of the PM fiber coupling enhances the spectral width of the MOT light. This technique enables a five- and twofold MOT loading improvement for erbium and dysprosium [88], respectively. Originally, the AOM operated in a single-pass configuration. However, thermal drifts in the AOM crystal led to fluctuations in the fiber-coupling efficiency, and thus in $P_{583\,\mathrm{nm}}$ or $P_{626\,\mathrm{nm}}$ within the MOT distribution, which resulted in an unstable MOT operation.

Reference cavity

Because of the intercombination-line transition's small natural linewidth $\Delta\nu_{\mathrm{Er},583\,\mathrm{nm}}$ or $\Delta\nu_{\mathrm{Dy},626\,\mathrm{nm}}$ (see Table 2.2), a home-built plano-concave cavity under vacuum serves as frequency reference via the Pound-Drever-Hall (PDH) technique [126, 127]. For both laser systems, a fiber-coupled EOM[40] delivers low-power laser light to the cavity setup, as Figure 3.11 (a) sketches. Here, a dichroic mirror[41] combines the $\lambda_{\mathrm{Er}} = 583\,\mathrm{nm}$ and the $\lambda_{\mathrm{Dy}} = 626\,\mathrm{nm}$ laser beam, and a single lens focuses the bichromatic beam through the cavity's concave mirror onto its plane mirror. In each beam path, a fine-adjustable collimation lens in the fiber coupler and two mirrors facilitate an individual mode-matching to the TEM_{00}-mode of the resonator. A $^{50}/_{50}$-beam splitter cube separates the respective back-reflected light, which a photodiode detects for the derivation of the PDH signal. The cavity transmission signal is for coupling and monitoring purposes.

For the cavity and its vacuum setup, [128] provides a detailed description and various characterization measurements. The entire cavity is from ultra-low expansion (ULE) glass and has an experimentally determined zero-crossing temperature of the coefficient of thermal expansion $T_0 = 21.78\,^{\circ}\mathrm{C}$ [128]. Further measured characteristics are a free spectral range $\mathrm{FSR} = 989(8)\,\mathrm{MHz}$ and a finesse $\mathcal{F} = 1636(4)$ at $\lambda_{\mathrm{Dy}} = 626\,\mathrm{nm}$ [128].

All three master lasers exhibit an excellent short-term stability[42]. Thus, the PDH frequency stabilization mainly acts against long-term frequency drifts by feeding back to the $\lambda_{\mathrm{Er}} = 1166\,\mathrm{nm}$ diode laser and to the $\lambda_{\mathrm{Dy}} = 1050\,\mathrm{nm}$ DFB fiber laser. The $\lambda_{\mathrm{Dy}} = 1550\,\mathrm{nm}$ DFB fiber laser remains free-running, as it is intrinsically stable enough.

The fiber-coupled EOM has a large bandwidth, and thus serves two purposes, modulating sidebands for the PDH signal as well as tunable sidebands for a variable stabilization point. Hence, the laser frequency is dynamically modifiable during the experimental sequence without the need for a complex frequency shifting setup involving multiple double-pass AOMs. This flexibility is advantageous for both, adjusting the detuning $\delta_{583\,\mathrm{nm}}$ or $\delta_{626\,\mathrm{nm}}$ for an efficient MOT loading to a value $\delta_{583\,\mathrm{nm,MOT}}$ or $\delta_{626\,\mathrm{nm,MOT}}$ and reducing it to $\delta_{583\,\mathrm{nm,cMOT}}$ or $\delta_{626\,\mathrm{nm,cMOT}}$ during the compression phase (see Section 3.3.3).

[38] Gooch & Housego PLC, 3080-125, center frequency 80 MHz, bandwidth 25 MHz
[39] QUBIG GmbH, EO-0.1M3-VIS, resonance frequency 139 kHz for erbium and 104 kHz for dysprosium
[40] JENOPTIK Optical Systems GmbH, PM594 for erbium and PM635 for dysprosium
[41] Thorlabs Inc., DMLP605
[42] Manufacturer information: 1166 nm diode laser $< 20\,\mathrm{kHz}$ (over 5 µs), 1050 nm and 1550 nm DFB fiber laser $< 20\,\mathrm{kHz}$ and $< 1\,\mathrm{kHz}$ (timescales not specified)

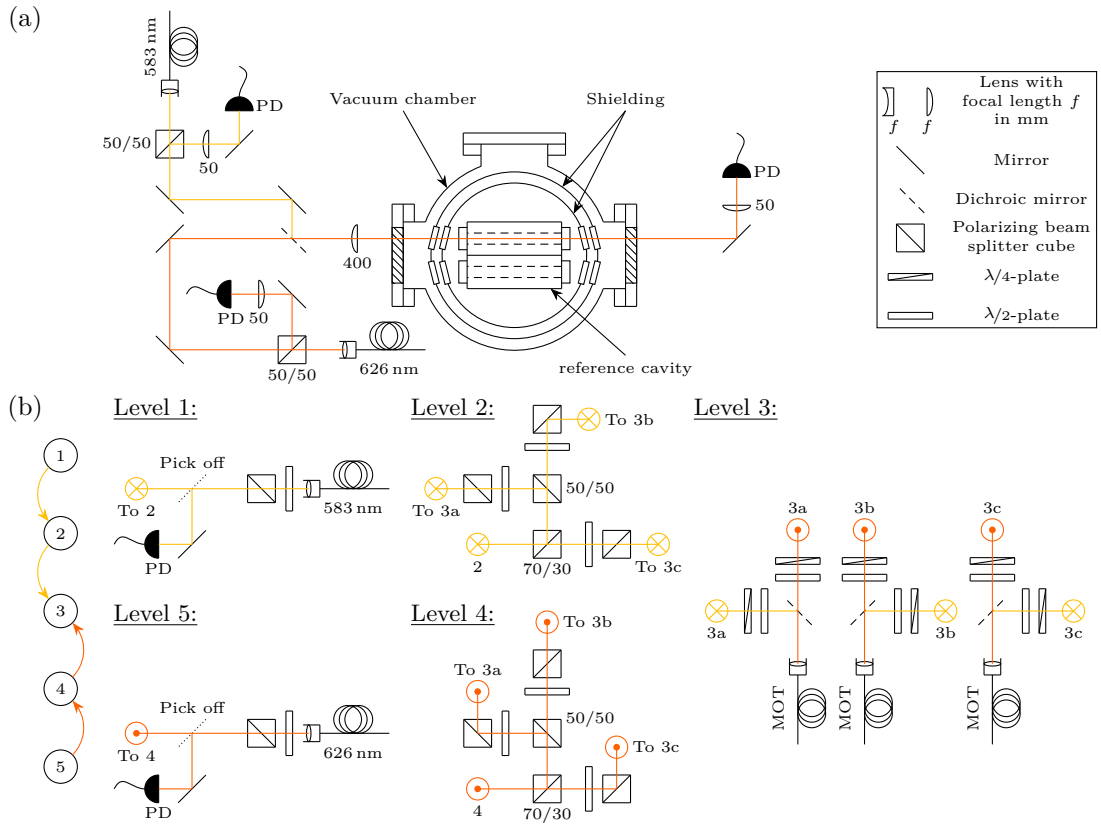

Figure 3.11: Reference cavity and MOT distribution. (a) Optical setup for the PDH frequency stabilization to the home-built reference cavity. A vacuum chamber and two surrounding shieldings against thermal radiation isolate the reference cavity from the environment. Photodiodes detect the back-reflected light for the PDH signals as well as the transmission for coupling and monitoring, respectively. Additionally, the ULE spacer hosts a second reference cavity ranging from 380 nm to 450 nm [128]. (b) MOT distribution and the arrangement of its five individual levels according to the scheme on the left. The arrival levels 1 and 5 transfer the $\lambda_{\mathrm{Er}} = 583\,\mathrm{nm}$ and the $\lambda_{\mathrm{Dy}} = 626\,\mathrm{nm}$ laser light to the subsequent levels 2 and 4, which divide the respective laser light with a fixed power ratio among three beam paths. The center level 3 combines the laser light in three PM single mode fibers guiding it to the MOT setup (see Section 3.3.3).

Magneto-optical trap distribution

The dual-species MOT employs retroreflected bichromatic MOT beams for a robust and low-maintenance operation (see Section 3.3.3). For this purpose, a home-built MOT distribution overlaps the $\lambda_{\mathrm{Er}} = 583\,\mathrm{nm}$ and the $\lambda_{\mathrm{Dy}} = 626\,\mathrm{nm}$ laser light in three standard PM single mode fibers, one for each MOT axis, as Figure 3.11 (b) depicts. It consists of five levels on top of each other for a compact overall layout. Two mirrors in each beam path interconnect the different levels, and thus ensure complete alignment autonomy.

First, at the incoming level 1 and level 5, respectively, some part of the polarization-cleaned $\lambda_{\mathrm{Er}} = 583\,\mathrm{nm}$ and $\lambda_{\mathrm{Dy}} = 626\,\mathrm{nm}$ laser light splits off for a power stabilization

feedback loop via the AOM in the respective laser setup. This allows for an exponential reduction of $P_{583\,\mathrm{nm}}$ or $P_{626\,\mathrm{nm}}$ in the MOT distribution during the compression phase, and thus of all MOT beams powers simultaneously (see Section 3.3.3).

In the following level, 2 for the $\lambda_{\mathrm{Er}} = 583\,\mathrm{nm}$ and 4 for the $\lambda_{\mathrm{Dy}} = 626\,\mathrm{nm}$ laser light, a $70/30$- and a $50/50$-beam splitter cube divide the laser beam with a fixed power ratio in three. Each is individually adjustable via a motorized $\lambda/2$-plate and a polarizing beam splitter cube to control the power ratio of the individual MOT beams (see Table 3.1).

Finally in level 3, a dichroic mirror[43] in front of each of the three outgoing PM single mode fibers overlaps both wavelengths. Two mirrors, one $\lambda/4$-plate as well as one $\lambda/2$-plate allow for an individual PM fiber coupling of each laser beam.

3.3.3 Integration into the experimental apparatus

For a rapid and robust MOT loading, the three experiment stages, the TC unit, the spin-flip ZS and the dual-species MOT, must seamlessly integrate and adjust to each other. The following paragraphs describe their optical setups at the UHV apparatus.

Transverse cooling unit

The TC unit, as part of the dual-species atomic beam source, is a crucial aspect for the MOT loading. Its collimation effect on the emitted atomic beam along two orthogonal axes in transverse direction strongly improves the MOT loading rates (see below). The collimation along each of the two axes relies on an optical molasses technique [120], where an atom with velocity v along a molasses axis experiences the scattering forces F_{scat} (see equation (3.1)) from two counterpropagating red-detuned laser beams as [83]

$$F_{\mathrm{mol}} = F_{\mathrm{scat}}\left(2\pi\delta - kv\right) - F_{\mathrm{scat}}\left(2\pi\delta + kv\right), \tag{3.8}$$

with the linearization [83]

$$F_{\mathrm{mol}} = -\alpha v = -4\hbar k^2 \frac{I}{I_{\mathrm{sat}}} \frac{-2(2\pi\delta + kv)/\Gamma}{\left[1 + 4(2\pi\delta + kv)^2/\Gamma^2\right]^2} v \tag{3.9}$$

for small v along the molasses axis. As F_{mol} points opposite to v, it damps the transversal atomic motion, and thus leads to an effective collimation of the atomic beam [120].

Figure 3.12 sketches the layout of the TC unit. First, PM single mode fibers guide the $\lambda_{\mathrm{Er}} = 401\,\mathrm{nm}$ and the $\lambda_{\mathrm{Dy}} = 421\,\mathrm{nm}$ laser light from their respective laser setup (see Figures 3.8 and 3.9) to the TC unit's octagon chamber (see Figure 3.12 (a)). In each beam path, a telescope expands the polarization-cleaned laser light to an $1/e^2$-waist $w_{\mathrm{TC}} = 3\,\mathrm{mm}$. Subsequently, a dichroic mirror[44] overlaps both laser beams. The emerging bichromatic beam splits into two beams, which then travel up into the TC axes (see Figure 3.12 (b)). A $50/50$-beam splitter cube ensures an equal power ratio between the two TC axes, and thus a balanced transverse cooling of the atomic beam. Figure 3.12 (c) depicts the optical setup along each of the two orthogonal TC axes. Initially, a custom-made dichroic $\lambda/4$-plate[45] changes the light's polarization to circular. A cylindrical telescope reshapes

[43] Thorlabs Inc., DMLP605R
[44] Chroma Technology Corp., T412lpxt-UF3
[45] LENS-Optics GmbH, multi order $\lambda/4$-plate for 401 nm and 421 nm

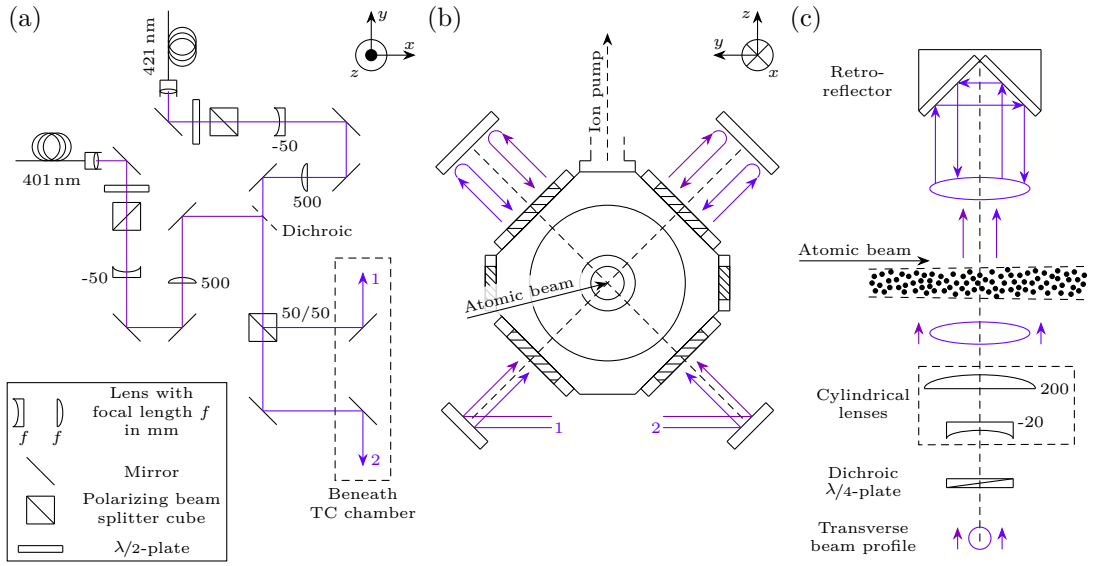

Figure 3.12: Overview over the TC unit. (a) Optical setup for a bichromatic beam of $\lambda_{\mathrm{Er}} = 401\,\mathrm{nm}$ and $\lambda_{\mathrm{Dy}} = 421\,\mathrm{nm}$ laser light. Telescopes collimate the two laser beams individually to $1/e^2$-waists $w_{\mathrm{TC}} = 3\,\mathrm{mm}$. A dichroic mirror overlaps both wavelengths and the emerging bichromatic beam splits subsequently with an equal power ratio into two. (b) Front view of the TC unit's octagon chamber in the y-z plane. The two incoming bichromatic TC beams travel diagonally upwards along the TC axes. After the octagon chamber, retroreflectors send both TC beams back, balancing the TC for the atomic beam, which propagates into the plane. (c) Optical setup along each of the TC axes. The setup includes a dichroic $\lambda/4$-plate, a cylindrical telescope and a retroreflector.

the TC beam and increases its major axis parallel to the atomic beam propagation axis (x-axis) from $w_{x,\mathrm{TC}} = 3\,\mathrm{mm}$ to $w'_{x,\mathrm{TC}} = 30\,\mathrm{mm}$. A retroreflector[46] completes the TC concept, while maintaining the circular polarization of the laser light.

For dysprosium, the TC saturates at $P_{421\,\mathrm{nm,TC}} = 60\,\mathrm{mW}$ along each TC axis, corresponding to a peak intensity $\hat{I}_{421\,\mathrm{nm,TC}} = 0.8 I_{\mathrm{sat},421\,\mathrm{nm}}$, with a sixfold improvement of the MOT loading rate [88]. For erbium, on the contrary, despite $P_{401\,\mathrm{nm,TC}} = 150\,\mathrm{mW}$ in each TC beam ($\hat{I}_{401\,\mathrm{nm,TC}} = 1.8 I_{\mathrm{sat},401\,\mathrm{nm}}$) and a tenfold increase of the MOT loading rate [88], the TC effect does not show any saturation. A possible explanation might be that the dual-filament effusion cell additionally evaporates pure erbium from its hot-lip to compensate the difference in $p_{\mathrm{vap,Er}}$ and $p_{\mathrm{vap,Dy}}$ (see Section 3.1). As this contribution to the atomic beam only passes through two of the in total three apertures (see Figure 3.2), this might result in a broader transverse velocity distribution requiring higher $P_{401\,\mathrm{nm,TC}}$.

Spin-flip Zeeman slower

Figure 3.13 includes the optical setup for the spin-flip ZS. Identical to the TC unit, the overlapping of polarization-cleaned $\lambda_{\mathrm{Er}} = 401\,\mathrm{nm}$ and $\lambda_{\mathrm{Dy}} = 421\,\mathrm{nm}$ laser light via a dichroic mirror leads to a bichromatic ZS beam. A telescope collimates the ZS beam

[46] Two 2" × 2" UV-enhanced aluminum mirrors (Thorlabs, PFSQ20-03-F01) under 90°

to an $1/e^2$-waist $w_{\mathrm{ZS}} = 4\,\mathrm{mm}$ and a vertical periscope guides it onto a dichroic $\lambda/4$-plate, identical to the TC unit, which rotates the light's polarization to circular. A dichroic mirror[47] (Img-DM) reflects the ZS beam upwards through a CF63 viewport into the UHV apparatus, where an in-vacuum aluminum mirror subsequently deflects the ZS beam into the spin-flip ZS (see sectional view in the inset of Figure 3.13).

An efficient ZS operation requires $P_{401\,\mathrm{nm,ZS}} = 57\,\mathrm{mW}$ ($\hat{I}_{401\,\mathrm{nm,ZS}} = 3.8 I_{\mathrm{sat},401\,\mathrm{nm}}$) and $P_{421\,\mathrm{nm,ZS}} = 120\,\mathrm{mW}$ ($\hat{I}_{421\,\mathrm{nm,ZS}} = 8.5 I_{\mathrm{sat},421\,\mathrm{nm}}$).

Dual-species intercombination-line magneto-optical trap

A textbook-like MOT traps atoms in all three dimensions by combining three orthogonal pairs of counterpropagating red-detuned circularly-polarized laser beams with a quadrupole **B**-field [83], as [129] first realized in 1987 with sodium. Neglecting gravity, it exerts a force along each of the three orthogonal MOT beam axes l as [83]

$$\begin{aligned} F_{\mathrm{MOT},l} &= F_{\mathrm{scat}}^{\sigma^-}(2\pi\delta - kv - \beta l) - F_{\mathrm{scat}}^{\sigma^+}(2\pi\delta + kv + \beta l) \\ &\simeq -\alpha v - \frac{\alpha}{k}\beta l \\ &= -\alpha v - \frac{\alpha}{k}\frac{\Delta\mu}{\hbar}(\nabla B)_l l, \end{aligned} \tag{3.10}$$

with α in equation (3.9), the wavenumber k and the circular polarization's handedness $\sigma^{\pm}$ with respect to a fixed quantization axis. The position-dependent term βl describes the Zeeman shift E_{ZS} due to the quadrupole **B**-field, and depends on the MOT transition's differential magnetic moment $\Delta\mu$, the gradient $(\nabla B)_l$ and the position l along the MOT beam axis. It gives rise to the restoring force character of F_{MOT} that allows a MOT to act not only in momentum space, such as an optical molasses, but also as a trap [83].

The dual-species intercombination-line MOT at $\lambda_{\mathrm{Er}} = 583\,\mathrm{nm}$ and $\lambda_{\mathrm{Dy}} = 626\,\mathrm{nm}$ operates with orthogonal bichromatic MOT beams in the horizontal x-y plane and along the vertical z-axis. Its narrow-line laser cooling character results in very low final MOT temperatures close to the Doppler temperatures $T_{\mathrm{D,Er},583\,\mathrm{nm}} = 4.5\,\mu\mathrm{K}$ and $T_{\mathrm{D,Dy},626\,\mathrm{nm}} = 3.2\,\mu\mathrm{K}$ [88] (see Table 2.2), however, in comparison to a textbook-like MOT, its working regime is entirely different. For an efficient MOT loading, the dual-species MOT requires MOT light detunings $\delta_{583\,\mathrm{nm}}$ and $\delta_{626\,\mathrm{nm}}$ of typically several tens of $\Delta\nu_{\mathrm{Er},583\,\mathrm{nm}}$ and $\Delta\nu_{\mathrm{Dy},626\,\mathrm{nm}}$ (see Table 2.2). As [130] investigated for strontium, such a trapping regime provides hard walls rather than a linear restoring force over the entire MOT (see equation (3.10)). In particular, the interplay between gravity, the scattering forces F_{scat} and the MOT temperature T_{MOT} determines the MOT trapping behavior along the vertical z-axis and results in atoms accumulating at the MOT bottom [130]. For the dual-species MOT, this not only leads to an intrinsic spin-polarization in the lowest Zeeman sublevel [74, 92] but also makes the top-down MOT beam redundant, allowing for a novel open-top MOT configuration along the vertical z-axis with [130]

$$F_{\mathrm{MOT},z} = F_{\mathrm{scat}}^{\sigma^-}(2\pi\delta - kv - \beta z) - mg, \tag{3.11}$$

with the gravitational acceleration g. This PhD thesis' first publication [88] provided corresponding characterization measurements (see Section 3.6).

[47] LENS-Optics GmbH, highly reflective for 401 nm and 421 nm and highly transmittive for 532 nm, 583 nm, 626 nm, 1064 nm and 1550 nm

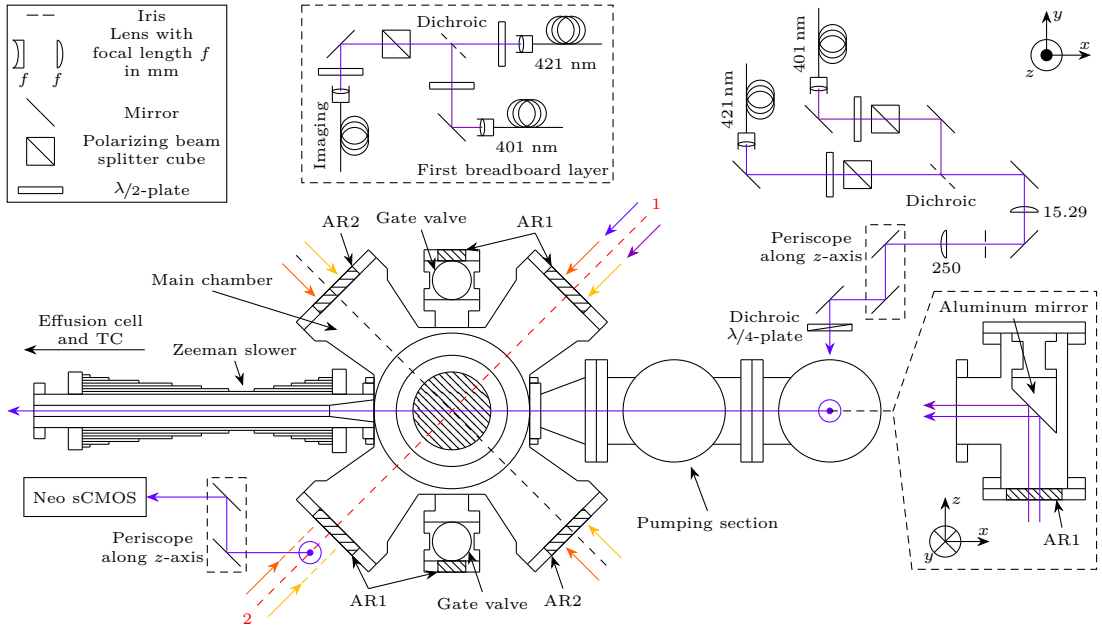

Figure 3.13: Top view on the UHV apparatus around the main chamber with nearby optical setups. At the main chamber, arrows indicate the arrangement for the horizontal MOT beams (yellow and red arrows) and for the horizontal imaging beam (violet and blue arrows, see Section 3.4). Figure 3.14 illustrates the optical setup along the horizontal MOT axis 1-2 in greater detail. A preparation setup next to the main chamber overlaps the imaging light at $\lambda_{\mathrm{Er}} = 401\,\mathrm{nm}$ and $\lambda_{\mathrm{Dy}} = 421\,\mathrm{nm}$, and PM fiber-couples it into the imaging path. A periscope after the main chamber guides the imaging light onto a sCMOS camera. The ZS setup in the top right prepares a bichromatic ZS beam of $\lambda_{\mathrm{Er}} = 401\,\mathrm{nm}$ and $\lambda_{\mathrm{Dy}} = 421\,\mathrm{nm}$ laser light. A telescope expands the ZS beam to a $1/e^2$-waist $w_{\mathrm{ZS}} = 4\,\mathrm{mm}$ and an in-vacuum aluminum mirror reflects it into the spin-flip ZS, as the inset depicts in a vertical sectional view along the atomic beam propagation axis (x-axis). The corresponding dichroic mirror is out of the sectional plane. AR1 and AR2 label the viewports' antireflection coatings (see Section 3.1).

Figure 3.13 illustrates the arrangement of the two retroreflected horizontal MOT beams in a top view and Figure 3.14 shows a vertical sectional view along one of the horizontal MOT axis. The inset of Figure 4.1 includes the optical setup for the vertical MOT beam. For each of the three orthogonal MOT axes, the MOT distribution provides an individual PM single mode fiber guiding the $\lambda_{\mathrm{Er}} = 583\,\mathrm{nm}$ and the $\lambda_{\mathrm{Dy}} = 626\,\mathrm{nm}$ laser light to the main chamber (see Section 3.3.2). A fiber-coupled achromatic beam expander[48] extends the bichromatic MOT beam to a $1/e^2$-waist $w_{\mathrm{MOT}} = 19\,\mathrm{mm}$, then a dichroic mirror[49] (MOT-DM) reflects the MOT beam into the main chamber (see Figures 3.14 and 4.1). The achromatic beam expander includes a dichroic $\lambda/4$-plate, and thus fixes the light's polarization to the required circular polarization. The MOT-DMs' dielectric coating has an optimized PM performance especially preserving the polarization's ellipticity.

[48] Schäfter + Kirchhoff GmbH, 60FC-Q-4-M200-04-amag

[49] LENS-Optics GmbH, highly reflective for 583 nm and 626 nm and highly transmittive for 401 nm, 421 nm, 1064 nm and 1550 nm

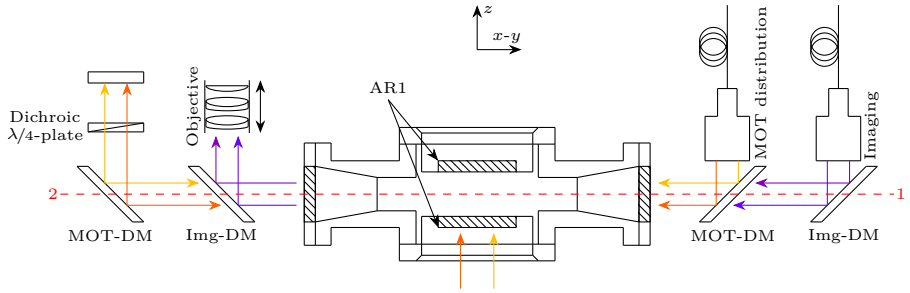

Figure 3.14: Vertical sectional view along the horizontal MOT axis 1-2 (see Figure 3.13). Starting from the achromatic beam expander, a MOT-DM deflects the incoming bichromatic MOT beam of $\lambda_{\mathrm{Er}} = 583\,\mathrm{nm}$ and $\lambda_{\mathrm{Dy}} = 626\,\mathrm{nm}$ laser light into the main chamber. On the opposite side, a retroreflection setup, which consists of a second MOT-DM, a dichroic $\lambda/4$-plate and a broadband dielectric mirror under 0 °, reflects the MOT beam back. Additionally, this particular MOT axis includes the horizontal imaging setup. It comprises an achromatic beam expander for the imaging light at $\lambda_{\mathrm{Er}} = 401\,\mathrm{nm}$ and $\lambda_{\mathrm{Dy}} = 421\,\mathrm{nm}$, two Img-DMs as well as a home-built objective (see Section 3.4). The influence of the Img-DM on the retroreflected MOT beam, and thus on the dual-species MOT is negligible. AR1 refers to the viewports' antireflection coating (see Section 3.1).

For each horizontal MOT axis, a second MOT-DM after the main chamber reflects the horizontal MOT beam out of the horizontal optical axis through a dichroic $\lambda/4$-plate[50] on a broadband dielectric mirror under 0 ° serving as retroreflector (see Figure 3.14). This arrangement moves the required $\lambda/4$-plate out of the horizontal optical axis, but still ensures the correct polarization for the retroreflected MOT beam. The two incoming horizontal MOT beams arrive opposite to the spin-flip ZS port to support the initial MOT trapping by providing their higher powers counter-propagating to the arriving atoms (in comparison to the retroreflected MOT beams).

Despite the large MOT beams on each axis, the combination of achromatic beam expander, dichroic mirrors and retroreflection setup is extremely compact and provides sufficient optical access for laser beams of different wavelengths for future experiments.

For an efficient MOT loading, a bias **B**-field $\mathbf{B}_{\mathrm{HH,MOT}}$ additionally shifts the origin of the quadrupole **B**-field $\mathbf{B}_{\mathrm{AH,MOT}}$ below the center of the main chamber (see Section 3.2.2). Hence, considering the initial working regime of the dual-species MOT at large MOT light detunings $\delta_{583\,\mathrm{nm}}$ and $\delta_{626\,\mathrm{nm}}$, the atoms accumulate at the MOT bottom well below the center of the main chamber. Thus, subsequent to the MOT loading, a compression phase of $t_{\mathrm{comp}} = 400\,\mathrm{ms}$ moves the MOT up towards the center of the main chamber, while reducing its size as well as its temperatures from $T_{\mathrm{MOT,Er}}$ and $T_{\mathrm{MOT,Dy}}$ to $T_{\mathrm{cMOT,Er}}$ and $T_{\mathrm{cMOT,Dy}}$ in the cMOT, respectively. Table 3.1 summarizes typical operating parameters for the MOT loading and the cMOT, while Figure 4.2 shows their time traces in the complete experimental sequence. During the compression phase, $\delta_{583\,\mathrm{nm}}$ and $\delta_{626\,\mathrm{nm}}$ change by $\Delta\delta_{583\,\mathrm{nm}} = \delta_{583\,\mathrm{nm,MOT}} - \delta_{583\,\mathrm{nm,cMOT}}$ and $\Delta\delta_{626\,\mathrm{nm}} = \delta_{626\,\mathrm{nm,MOT}} - \delta_{626\,\mathrm{nm,cMOT}}$ of tens of $\Delta\nu_{\mathrm{Er},583\,\mathrm{nm}}$ and $\Delta\nu_{\mathrm{Dy},626\,\mathrm{nm}}$ (see Table 2.2), respectively. Their precise values depend on the chosen isotopes as well as the operating state of the system correlating with all other parameters, and thus Table 3.1 does not provide reference values.

[50] LENS-Optics GmbH, multi-order $\lambda/4$-plate for 583 nm and 626 nm

Table 3.1: Typical operating parameters for the dual-species intercombination-line MOT at $\lambda_{\mathrm{Er}} = 583\,\mathrm{nm}$ and $\lambda_{\mathrm{Dy}} = 626\,\mathrm{nm}$ in an open-top configuration. The compression phase to the cMOT, changes the **B**-field bias value B_{HH} and the gradient value ∇B_{AH} linearly, and reduces the horizontal and vertical MOT beam powers P_{hor} and P_{ver} exponentially.

Parameters			MOT loading	cMOT
Bias	B_{HH} (G)	x,y,z	−3.245	1.020
Gradient	∇B_{AH} ($^{\mathrm{G}}/_{\mathrm{cm}}$)	x,y	2.25	1.94
		z	4.50	3.88
Horizontal beams (values per beam)	P_{hor} (mW)	583 nm	36	0.12
		626 nm	69	0.25
	$\hat{I}_{\mathrm{hor}}$ (I_{sat})	583 nm	52	0.17
		626 nm	168	0.61
Vertical beam	P_{ver} (mW)	583 nm	32	0.10
		626 nm	64	0.24
	$\hat{I}_{\mathrm{ver}}$ (I_{sat})	583 nm	46	0.15
		626 nm	157	0.59

3.4 Imaging system

An absorption imaging on the broad transition at $\lambda_{\mathrm{Er}} = 401\,\mathrm{nm}$ and $\lambda_{\mathrm{Dy}} = 421\,\mathrm{nm}$ images the cMOT or the ODT (see Chapter 4). The laser light first arrives PM fiber-coupled from the laser setups (see Figures 3.8 and 3.9) at a preparation setup next to the UHV apparatus (see Figure 3.13). A dichroic mirror[51] overlaps both polarization-cleaned beams to a bichromatic beam and a PM single mode fiber leads to the imaging setup.

Figure 3.14 sketches the imaging path at the main chamber. Initially, a fiber-coupled achromatic beam expander[52] with an integrated dichroic $\lambda/4$-plate provides a circularly polarized bichromatic imaging beam with a $1/e^2$-waist $w_{\mathrm{img}} = 5\,\mathrm{mm}$. An Img-DM deflects the imaging beam through the MOT-DM into the main chamber. On the outgoing side, in order to avoid aberrations, a second Img-DM reflects the imaging beam directly in front of the MOT beam's retroreflection setup out of the horizontal optical axis upwards to the objective. Subsequently, a periscope guides the imaging beam onto a scientific-CMOS-based camera[53] (see Figure 3.13).

The objective is home-built and consists of a 2 "-lens triplet[54]. The imaging system operates at a working distance of 257 mm, a magnification of 3.2 and provides a diffraction limited resolution of 3.5 µm at $\lambda_{\mathrm{Er}} = 401\,\mathrm{nm}$ and $\lambda_{\mathrm{Dy}} = 421\,\mathrm{nm}$, respectively.

At the beginning of the absorption imaging sequence, the camera takes a cleaning image, the trap as well as the inverted-viewport HH-like coil switch off and the compensation cage rotates the **B**-field within 9 ms into the imaging axis. The camera's field of view

[51] Chroma Technology Corp., T412lpxt-UF3

[52] Schäfter + Kirchhoff GmbH, 60FC-Q-4-M50L-01-AM

[53] Andor Neo 5.5 sCMOS, 16.6 mm × 14.0 mm chip size, 2560 × 2160 pixel, 6.5 µm × 6.5 µm pixel size, AR-coated window for 401 nm,421 nm,583 nm and 626 nm

[54] Thorlabs, two achromatic doublets, AR coating 400 nm-700 nm, focal length $f = 500\,\mathrm{mm}$, one plano-convex lens, AR coating 350 nm-700 nm, $f = 1000\,\mathrm{mm}$

allows for a variable time-of-flight (TOF) expansion of up to 27 ms, after which the camera records the required pictures in the following order. First, it captures the erbium and dysprosium samples on two individual pictures 10 µs apart. Following a processing time of 40 ms, it then takes the reference pictures for the imaging light with the same time delay of 10 µs, and finally, with another wait time of 40 ms, it records a dark picture.

A compact CMOS camera[55] images the cMOT along the second horizontal MOT axis by collecting its fluorescence for 70 ms directly at the beginning of either a cMOT holding time or a ODT loading time (see Chapter 4). A reference picture at the very end of the experimental sequence completes the fluorescence imaging. This imaging is non-destructive and especially beneficial for experiments in the ODT, where otherwise no information about the MOT or the cMOT performance is available.

3.5 Control system

A network of four computers controls and monitors the entire experimental apparatus. A control computer provides the possibility to define the consecutive sequence commands in script format and to set the individual sequence parameters in a graphical user interface. For every experimental repetition, this unit compiles the experimental sequence and programs a digital I/O PCI card[56]. It transfers its output via a BUS system to racks holding individually programmable direct digital synthesizers and analog or digital output channels, which for instance generate the AOMs' or fiber-coupled EOMs' RF signals, set RF power levels or provide the camera triggers. The time resolution between single sequence commands is 5 µs. The second computer interfaces the cameras for absorption and fluorescence imaging (see Section 3.4) and stores the obtained images. At the end of every experimental repetition, a third computer accesses, analyzes and stores these images fully automatically. This provides essentially a real-time analysis of the obtained data. The last computer monitors all laser systems and the controller of the dual-filament effusion cell as well as records data from a temperature and a cooling water monitoring.

[55] Allied Vision, Guppy PRO F503B mono, 2588x1940 pixel, 2.2 µm × 2.2 µm pixel size
[56] National Instruments PCI-6534

3.6 Publication I:

Two-species five-beam magneto-optical trap for erbium and dysprosium

P. Ilzhöfer[1,2,†], G. Durastante[1,2], A. Patscheider[1,2], A. Trautmann[1], M. J. Mark[1,2] and F. Ferlaino[1,2]

[1] *Institut für Experimentalphysik und Zentrum für Quantenoptik, Universität Innsbruck, Technikerstrasse 25, 6020 Innsbruck, Austria*

[2] *Institut für Quantenoptik und Quanteninformation, Österreichische Akademie der Wissenschaften, 6020 Innsbruck, Austria*

Physical Review A, **97**, 023633, (2018), DOI: 10.1103/PhysRevA.97.023633,
received 20 November 2017, published 26 February 2018

Note: All atom numbers within this publication are a factor of 1.4 too large due to a miscalibration of the imaging system.

[†] The author of this PhD thesis participated in the development and the construction of the experimental apparatus, the data recording and analysis as well as in the writing process of this publication.

Two-species five-beam magneto-optical trap for erbium and dysprosium

P. Ilzhöfer,[1,2] G. Durastante,[1,2] A. Patscheider,[1,2] A. Trautmann,[2,*] M. J. Mark,[1,2] and F. Ferlaino[1,2,†]
[1]*Institut für Experimentalphysik und Zentrum für Quantenoptik, Universität Innsbruck, Technikerstrasse 25, 6020 Innsbruck, Austria*
[2]*Institut für Quantenoptik und Quanteninformation, Österreichische Akademie der Wissenschaften, 6020 Innsbruck, Austria*

(Received 20 November 2017; published 26 February 2018)

We report on the first realization of a two-species magneto-optical trap (MOT) for the highly magnetic erbium and dysprosium atoms. The MOT operates on an intercombination line for the respective species. Owing to the narrow-line character of such a cooling transition and the action of gravity, we demonstrate a trap geometry employing only five beams in the orthogonal configuration. We observe that the mixture is cooled and trapped very efficiently, with up to 5×10^8 Er atoms and 10^9 Dy atoms at temperatures of about 10 μK. Our results offer an ideal starting condition for the creation of a dipolar quantum mixture of highly magnetic atoms.

DOI: 10.1103/PhysRevA.97.023633

Within the very active research field of ultracold quantum gases, heteronuclear mixtures of different atomic species offer unique possibilities to study a broad range of quantum phenomena. In the past 15 years, various atomic species have been combined to produce quantum degenerate mixtures. Each such quantum mixture has its own characteristic traits. Among the widely used alkali mixtures (e.g., [1,2]), the mass imbalance and the selective tuning of the intra- and interspecies interaction have allowed to investigate fascinating phenomena, such as heteronuclear Efimov states [3–6], polaron and impurity physics in both bosonic and fermionic backgrounds [7–11], and heteronuclear molecules with large electric dipole moments [12–14].

The latter development is mainly driven by the interest in studying phenomena arising from long-range and anisotropic dipole-dipole interactions among the molecules [15]. As an alternative approach, magnetic atoms have proven to be a robust system for study of few- and many-body dipolar physics. The strength of magnetic atoms for the study of dipolar physics was first shown using Bose-Einstein condensates of chromium atoms [16,17]. More recently, both erbium (Er) and dysprosium (Dy), among the most magnetic and isotope-rich atomic species, have been individually brought to quantum degeneracy [18–21]. Using these species, remarkable many-body dipolar phenomena have been observed, including the observation of deformed Fermi surfaces [22], quantum droplets [23–25], and roton excitations [26] and the recent study of thermalization in many-body dipolar gases [27].

Adding the flexibility of mixtures to the richness of magnetic atoms, we here report on the first combination of the two highly magnetic atomic species Er and Dy in a single experimental apparatus. The Er-Dy system extends the collection of available quantum mixtures by an unexplored case, as the interplay between the interspecies contact and dipolar interactions and the dipolar imbalance among the two species provides a new dimension in the parameter space of accessible quantum phenomena. This impacts, e.g., the miscibility properties of the mixture [28]. Although imbalanced dipolar mixture systems have not yet been considered in theory, they are good candidates for observation of, e.g., long-range dominated polarons, dipolar pairing, and the anisotropic BEC-BCS crossover with deformed Fermi surfaces.

While single-species magneto-optical traps (MOTs) of Er [29–31] and Dy [32–34] as well as other lanthanoid atoms [35–37] have already been attained, we simultaneously cool and trap Er and Dy in a two-species MOT operating on intercombination lines. We observe a remarkably robust operation of the dual MOT, with atom numbers similar or even surpassing the typical ones recorded in the single-species Er or Dy experiments. Moreover, we demonstrate magneto-optical trapping using a unique beam configuration, allowing us to efficiently operate the MOT using only five beams (5B) in an orthogonal *open-top* configuration; see Fig. 1(b). The working principle of our orthogonal 5B MOT relies on the combined effect of the narrow-line cooling and gravity [30,31,33–35,38] and contrasts with the classical six-beam (6B) approach.

A beneficial factor for combining the multivalence-electron atoms Er and Dy is their similarity in atomic properties [see table in Fig. 1(e)]. They both have several stable isotopes with a high natural abundance, >14%; in total, five bosonic (^{166}Er, ^{168}Er, ^{170}Er, ^{162}Dy, ^{164}Dy) and three fermionic (^{167}Er, ^{161}Dy, ^{163}Dy) isotopes. This isotope variety will allow us to prepare ultracold Bose-Bose, Bose-Fermi, and Fermi-Fermi quantum mixtures of Er and Dy. Whereas all bosonic isotopes have zero nuclear spin, the fermionic isotopes possess nuclear spins of $I_{\mathrm{Er}} = 7/2$ and $I_{\mathrm{Dy}} = 5/2$, leading to eight and six hyperfine states in the electronic ground state, respectively. Both elements exhibit a rich atomic energy spectrum, arising from their submerged-shell electronic configuration, featuring a [Xe] core, a partially filled inner $4f$ shell, and a closed outer $6s$ shell. The electron vacancy in the $4f$ shell is responsible for the large orbital quantum numbers and the respective high magnetic moments, i.e., $7\mu_B$ and $10\mu_B$ for Er and Dy, with μ_B being the Bohr magneton.

Figures 1(c) and 1(d) show the electronic levels of Er and Dy for wave numbers up to 26 000 cm^{-1} [39]. While most of

*arno.trautmann@uibk.ac.at
†Corresponding author: Francesca.Ferlaino@uibk.ac.at

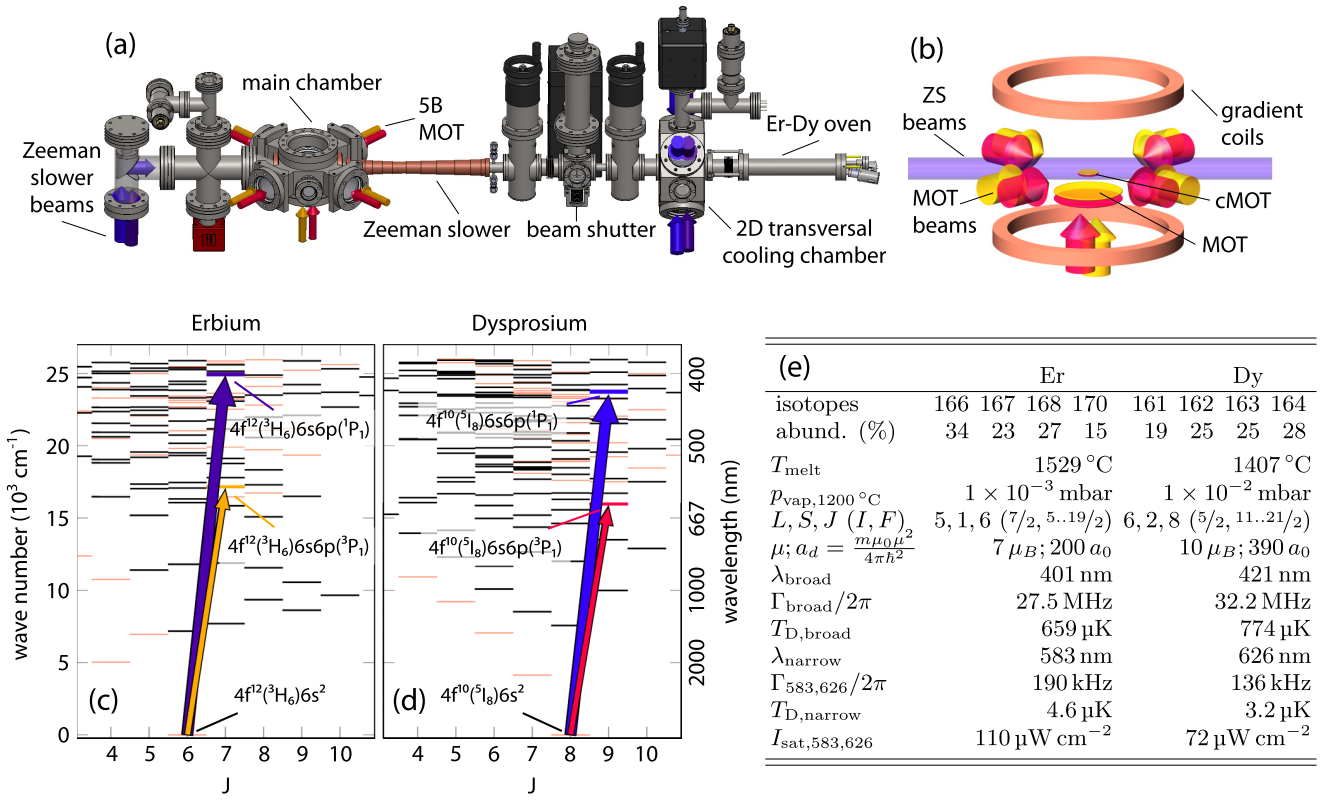

(e)	Er				Dy			
isotopes	166	167	168	170	161	162	163	164
abund. (%)	34	23	27	15	19	25	25	28
T_{melt}	1529 °C				1407 °C			
$p_{\mathrm{vap,1200\,°C}}$	1×10^{-3} mbar				1×10^{-2} mbar			
$L,S,J\ (I,F)$	$5,1,6\ (^7/_2,{}^{5..19}/_2)$				$6,2,8\ (^5/_2,{}^{11..21}/_2)$			
$\mu;a_d=\frac{m\mu_0\mu^2}{4\pi\hbar^2}$	$7\,\mu_B;200\,a_0$				$10\,\mu_B;390\,a_0$			
λ_{broad}	401 nm				421 nm			
$\Gamma_{\mathrm{broad}}/2\pi$	27.5 MHz				32.2 MHz			
$T_{\mathrm{D,broad}}$	659 µK				774 µK			
$\lambda_{\mathrm{narrow}}$	583 nm				626 nm			
$\Gamma_{583,626}/2\pi$	190 kHz				136 kHz			
$T_{\mathrm{D,narrow}}$	4.6 µK				3.2 µK			
$I_{\mathrm{sat},583,626}$	110 µW cm^{-2}				72 µW cm^{-2}			

FIG. 1. Illustration of the vacuum apparatus, including the optical setup for the 5B MOT, and atomic properties of Er and Dy. (a) Er-Dy vacuum apparatus, including the high-temperature oven, transversal cooling chamber, Zeeman slower (ZS), and main chamber. The atomic beam propagates from right to left. The ZS beam is reflected by a metallic mirror in vacuum. (b) Sketch of the working principle of the open-top MOT. Arrows depict MOT beams, and the blue region indicates the ZS beam. For clarity, we depict the atomic clouds displaced from each other. (c, d) Energy level diagrams for Er and Dy up to 26 000 cm^{-1} at different total electronic angular momentum quantum numbers J. States with odd (even) parity are indicated by black (orange) horizontal lines. Arrows show the broad and narrow laser-cooling transitions. (e) Table listing the atomic properties of Er and Dy.

the possible transitions are dipole forbidden, both species offer one particularly broad transition, suitable for laser cooling, to the respective singlet $6s6p$ state [blue arrows in Figs. 1(c) and 1(d)], which we label *broad* in the following. The blue transition light has a wavelength of 401 nm(421 nm), and the transition line width is $\Gamma_{\mathrm{broad}}/2\pi = 27.5$ MHz (32.2 MHz) for Er (Dy) [30,33]. We use this transition for transversal cooling, Zeeman slowing, and absorption imaging. The laser light, driving the broad transition, is derived from grating-stabilized laser diodes, followed by tapered amplifiers and frequency-doubling cavities. The laser systems emit more than 1W of power each. Both systems are frequency-stabilized using signals from modulation-transfer spectroscopy in hollow-cathode lamps [30].

Following previous single-species experiments with Yb [35], Er [30], and Dy [33,34], we produce the MOT using an intercombination line driving the transition from the ground state to the triplet $6s6p$ state [yellow (red) arrow in Figs. 1(c) and 1(d)] at a wavelength of 583 nm(626 nm) in Er (Dy) and a line width of $\Gamma_{583}/2\pi = 190$ kHz($\Gamma_{626}/2\pi = 136$ kHz). The narrow-width character of these transitions leads to the conveniently low Doppler temperatures of $T_{\mathrm{D,Er}} = 4.6\ \mu$K and $T_{\mathrm{D,Dy}} = 3.2\ \mu$K. The laser system for the Er MOT is based on a Raman fiber-amplified diode laser at 1166 nm and a single-pass frequency-doubling stage, with an output power above 1.7 W. The laser system for the Dy MOT is based on two fiber lasers operating at 1050 and 1550 nm, which are amplified and frequency-converted in a single-pass sum-generation stage, resulting in more than 1.6 W of output power. Both MOT laser systems are frequency-stabilized against long-term drifts on a home-built ultralow expansion cavity via a Pound-Drever-Hall lock [40] and have line widths below 100 kHz.

The experimental procedure generalizes our previously demonstrated single-species MOT approach [30] to two-species operation. The very similar strengths and wavelengths of the laser-cooling transitions of Er and Dy and their similar masses and melting points greatly simplify the design of the vacuum apparatus and the experimental procedure for the mixture. Figure 1(a) shows the experimental apparatus. Er and Dy atoms are emitted from a single high-temperature oven, consisting of two sections: The first section (effusion cell) operates at a temperature of 1100 °C, and the second one (hot lip) operates at 1200 °C, unless otherwise stated. Three apertures of different diameters, placed inside the oven, geometrically collimate the Er-Dy atomic beam before it enters the transversal-cooling chamber. We operate the transversal cooling resonantly on the broad transitions with total powers of 300 mW(120 mW) for Er (Dy) and elliptic waists of

approximately $w_{\text{horiz}} = 30$ mm and $w_{\text{vert}} = 6$ mm. We observe that the transversal cooling increases the MOT loading rate by a factor of 10 (6) for Er (Dy). The two-species atomic beam is slowed down to about 5 m/s using a two-species Zeeman slower (ZS) about 35 cm long in the spin-flip configuration. The magnetic-field values along the ZS are experimentally optimized for Dy and work equally well for Er. The two light beams for the ZS of Er and Dy are overlapped using dichroic optics and guided through the ZS via a metallic in-vacuum mirror [41]; see Fig. 1(a). The optimal performance of the ZS has been found for laser powers of 57 mW(121 mW) with beam waists of 4 mm at a detuning of −520 MHz(−530 MHz) for Er (Dy).

The slow atoms are then captured into a two-species MOT, operating on the respective intercombination line. Taking advantage of the similar wavelengths, we combine the MOT beams for both species into the same fibers. The MOT light is spectrally broadened utilizing electro-optic modulators with resonance frequencies of 139 kHz(102 kHz) for Er (Dy), which increases the capture range and thus the number of atoms in the MOT by a factor of 5 (2). The recapture volume is further enhanced by using large MOT beams, with diameters of about 36 mm. We observe an optimal loading for peak intensities of each laser beam of $I_{583} = 50 I_{\text{sat},583}$ and $I_{626} = 160 I_{\text{sat},626}$. Additionally, we endow our main chamber with inverted top and bottom view ports with large clear apertures of 64 mm. As discussed later, our special 5B MOT geometry allows us to completely free the top view, where we will implement a high-resolution *in situ* imaging with a numerical aperture of 0.45, which can resolve structures down to 600 nm. A pair of vertical coils creates a magnetic quadrupole field for the MOT of $\nabla B = 4.6$ G/cm. A vertical bias field of $B_0 = 2.9$ G shifts the zero point of the quadrupole field downwards. Additional coil pairs in the horizontal plane compensate for external magnetic fields.

We produce and study the Er-Dy MOT using two beam configurations. In the first one, we use a standard 6B geometry with three pairs of orthogonal retroreflected beams. For the second configuration, we remove the top → bottom MOT beam, demonstrating for the first time a 5B geometry with an open top; see Fig. 1(b). Although this 5B MOT would not work for alkali MOTs [42], we here demonstrate a very robust operation for our lanthanoid mixture. In the first set of experiments, we study the loading performance of our two-species MOT in both the 6B and the 5B configurations for ^{168}Er and ^{164}Dy. For all atom numbers we report in this paper, we load the MOTs at the optimized detuning for each setting as discussed later (see Fig. 3), apply a compression phase after MOT loading, and detect the atomic clouds using absorption imaging, as described later. Figure 2 shows the Er and Dy atom numbers as a function of the MOT loading time. From a fit to the data using a standard loading function, $N(t) = N_{\text{ss}}(1 - e^{-\gamma t})$, we extract the loading rate R and decay rate γ with the steady-state atom number $N_{\text{ss}} = R/\gamma$ (see Table I). In both the 6B and the 5B configurations, we observe a very efficient loading of the two-species MOT. After about 10 s of loading, the atom numbers approach their steady-state value of some 10^8 atoms (see Table I). We do not observe any mutual influence of one species on the other, as reported for some alkaline mixtures, as, e.g., shown in Refs. [43] and [44].

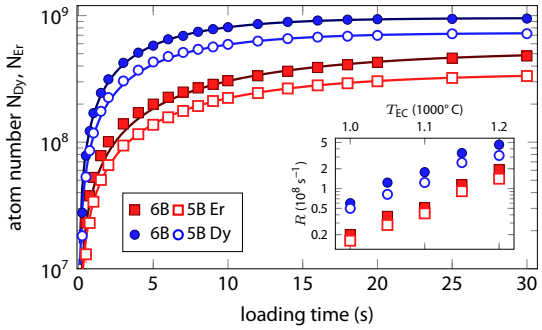

FIG. 2. Loading curve of the two-species MOT for the 6B and 5B configurations. Filled and open squares (circles) show data for the 6B and 5B Er (Dy) MOTs, respectively. The corresponding lines are fits to the data, as detailed in the text. Fit parameters are listed in Table I. Inset: Loading rate of the two species dependent on the effusion cell temperature T_{EC}. Note that the hot lip is always kept at $T_{\text{HL}} = T_{\text{EC}} + 100\,^{\circ}$C.

Given the complex scattering properties and optical spectra of multielectron lanthanoids, this surprising result enables the simultaneous MOT operation and greatly simplifies the experimental sequence.

The difference in the loading curves between Er and Dy is due to their different vapor pressures. The ratio of vapor pressures of Er and Dy is typically higher than 10 at the same temperature [45] and strongly temperature dependent, which would prevent an efficient simultaneous MOT loading. To mitigate this, we selectively heat up the atoms exploiting the two-section design of the oven. We fill the effusion cell with a 33%/67% alloy of Er/Dy and the hot-lip section with pure Er. We operate the oven with a differential temperature of 100 °C between the two sections. In the temperature range from 1000 °C to 1200 °C for the first section, we expect to reduce the vapor-pressure ratio among the two species to about 2.3. We investigate this effect by repeating the loading experiments for different temperatures of the effusion cell, while keeping the hot lip always 100 °C hotter; see Fig. 2 (inset). We observe a roughly constant loading ratio of between 2.5 and 3.5, which confirms the above expectations and shows that our concept of differential heating works very efficiently.

We remarkably find that the performance of the 5B MOT is only slightly below that of the 6B MOT. Moreover, even our 5B double-species MOT shows atom numbers similar to or larger than those previously reported for single-species Er or Dy MOT experiments [29,30,32–34]. Judging from our experience with

TABLE I. Loading rates R, decay rates γ, and steady-state atom numbers N_{ss} obtained from fits to the data shown in Fig. 2. Values for both species in the 5B and 6B configurations are listed. Also listed are the lifetimes obtained from the data in Fig. 4.

	Er		Dy	
	5B	6B	5B	6B
R (10^8 s^{-1})	0.35(1)	0.45(2)	1.21(4)	1.79(3)
γ (s^{-1})	0.100(2)	0.086(6)	0.166(7)	0.187(5)
N_{ss} (10^8)	3.5(1)	4.5(3)	7.3(4)	9.6(3)
Lifetime cMOT (ms)	515(65)	475(50)	374(44)	345(23)

Er [30], we are thus confident that these numbers are sufficient for reaching quantum degeneracy. The 5B MOT configuration has the advantage of automatically spin-polarizing the atoms and providing full optical access through the vertical top view port, allowing implementation of optical setups which require large numerical apertures, e.g., high-resolution imaging or angle-resolved Bragg spectroscopy.

The simultaneous cooling and polarization of the intercombination MOT in lanthanoids has been studied for single-species Er [30] and Dy [34] 6B MOTs. In brief, the combined effects of a narrow-line MOT and gravity yield a peculiar semi-shell-shaped MOT with its center lying below the zero of the magnetic quadrupole field; see Fig. 1(b). The center position of the MOT can be adjusted by changing the MOT detuning. For large enough vertical displacement of the MOT, i. e., detuning, the atoms predominantly absorb σ^--polarized photons, which are coming from the bottom-top beam. As a consequence, the atoms are spin-polarized into the lowest Zeeman sublevel. For lower detuning, the atoms can absorb both σ^+ and σ^- light and the sample is unpolarized [34]. With our 5B MOT, we bring this concept to the extreme: We completely remove the (σ^+) top-bottom beam and force the atoms to sit only below the zero of the magnetic field. We verified the spin polarization by performing spin-resolved absorption imaging using the Stern-Gerlach technique. Within our experimental resolution, we do not detect atoms in higher Zeeman sublevels [46]. Thanks to this spontaneous spin polarization, optical-pumping schemes are not necessary. The spin purity is very beneficial for future loading of the mixture into an optical dipole trap, where the presence of additional spin states can lead to atomic losses via inelastic dipolar relaxation processes.

In the second set of experiments, we systematically study the effect of MOT-light detuning from the respective resonant atomic frequency on the atom number and compare the results for the 6B and 5B configurations after 5s of loading; see Fig. 3. For both species, we see a clear rise of atom numbers with increasing detuning. After reaching a maximum value the numbers undergo a sharp decrease at large detunings. This decrease can be simply explained by the spatial downshift of the MOT position with increasing detuning, eventually causing the atoms to leave the recapture volume. Here, the equal behavior of the 6B and 5B MOTs indicates that the top-bottom beam does not play a significant role. At intermediate detunings, however, the two configurations clearly show different behaviors. In particular, the 6B MOT has a much broader range of operation than the 5B configuration. We believe that this difference is due to the fact that the central cloud position approaches the magnetic-field zero point with decreasing detuning. In the absence of the top-bottom beam, atoms above the magnetic-field zero do not experience a restoring light force towards the trap center and may escape from the MOT. Contrariwise, in the 6B approach, these atoms are retrapped, resulting in the broader operation range in terms of detuning.

As observed in previous experiments [33], the Dy atom number shows a small dip at detunings around $-70\Gamma_{626\,\mathrm{nm}}$. We attribute this feature to a partial overlap of the cloud with the ZS light beam, which drives off-resonant pumping processes resulting in atom losses [30]. For Er, the influence of the ZS light is weaker due to its lower light intensity and larger relative detuning, and this effect is not observed.

Finally, we study the lifetime of the mixture in the compressed MOT (cMOT). The compression phase is essential to efficiently load an optical dipole trap in future experiments, as the compression reduces the temperature and increases the density of the mixture. After loading the MOT, we switch off the spectral broadening electro-optic modulators, the ZS beams, and block the atomic beam with a mechanical shutter. The compression has a duration of 200 ms, during which we (i) reduce the detuning of the MOT light to $10\,\Gamma_{583}$ ($18\,\Gamma_{626}$), (ii) decrease the MOT-beam power to $I_{583} = 0.17 I_{\mathrm{sat},583}$ and $I_{626} = 0.6 I_{\mathrm{sat},626}$, (iii) ramp down the magnetic-field gradient to $\nabla B = 4.3$ G cm^{-1}, and (iv) switch off the vertical bias magnetic field. As shown in Fig. 4, we observe that the double-species cMOT has a lifetime that is fully sufficient for loading of atoms into an optical dipole trap, which typically requires a holding time of about 100 ms. The data are taken in dual operation, with both species present in all settings. Again,

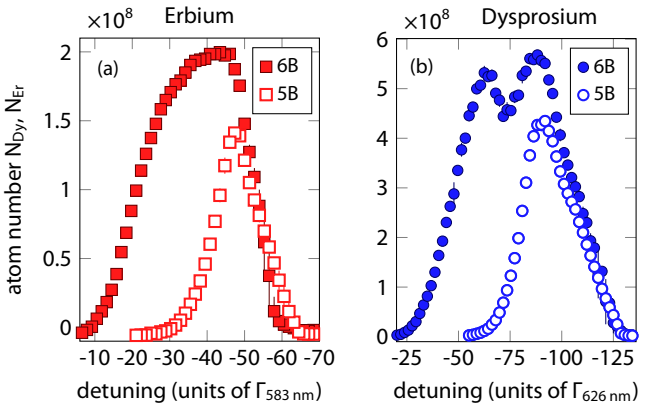

FIG. 3. Dependence of atom numbers in the cMOT on the initial MOT detuning, in units of the respective linewidth of the narrow transition of $\Gamma_{583}/2\pi = 190$ kHz($\Gamma_{626}/2\pi = 136$ kHz) for Er (Dy). Both species show broad ranges of detuning for efficient MOT loading in the 6B configuration, while 5B shows a narrower range. The optimal detunings are nearly equal for the 5B and 6B configurations. Data were taken for 5 s of MOT loading.

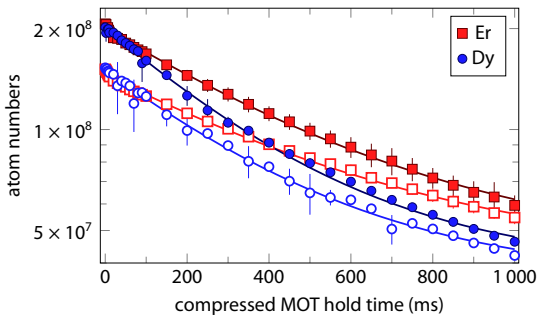

FIG. 4. Lifetime of the cMOT for both Er (red) and Dy (blue) in the 5B (open symbols) and 6B (filled symbols) configurations. We adjust the MOT loading time to compare samples with equal atom numbers. Solid lines show exponential fits to the respective data. From the fits we extract lifetimes of 515(65) and 475(5) ms [374(44) and 345(23) ms] for Er [Dy] in the 5B and 6B cMOTs, respectively.

we do not see any interplay between the species. The results of fits to the lifetime data are listed in Table I. Additionally, we extract temperatures of 11(1) μK [10(1) μK] for Er [Dy] in both the 5B and the 6B configurations from time-of-flight measurements. We observe that lower temperatures close to the Doppler temperatures can be achieved with different sets of parameters, at the expense of lower atom numbers. From our experience, we are certain that the observed lifetimes and temperatures are fully sufficient for efficient loading into an optical dipole trap as the next step towards quantum degeneracy.

The data we present here refer to the mixture of ^{168}Er and ^{164}Dy. Moreover, we are also able to trap and cool all other abundant bosonic isotopes with equally good performance, except for the ^{170}Er MOT, which has smaller numbers, as expected from its low natural abundance. For future studies of the fermionic isotopes, no changes in the experimental apparatus are necessary.

In conclusion, we have demonstrated efficient cooling and trapping of an Er-Dy mixture in a two-species MOT operating on narrow-line transitions. In addition, we demonstrate a beam geometry for our two-species MOT which consists of only five laser beams in an open-top orthogonal setting. This geometry has the big advantage of providing free optical access from the top with a large numerical aperture, greatly simplifying the implementation, e.g., of high-resolution imaging, as well as optical lattices. Our recorded temperatures and atom numbers provide ideal conditions for subsequent evaporative cooling, towards the first production of a quantum-degenerate dipolar mixture. Optimization of the optical-trap loading and evaporative cooling is under way in our laboratory.

We acknowledge A. Frisch, T. Pyragius, and C. Zhang for support in the initial phase of the experiment. We thank the ERBIUM and the Dy-K teams in Innsbruck, the Er team at Harvard, and M. Sohmen and C. Politi for fruitful discussions. This work was supported by an ERC Consolidator Grant (RARE; No. 681432) and a FET Proactive Project (RySQ; No. 640378) of EU H2020. G.D. acknowledges support from the Austrian Science Fund FWF within DK-ALM: W1259-N27.

[1] Z. Hadzibabic, C. A. Stan, K. Dieckmann, S. Gupta, M. W. Zwierlein, A. Görlitz, and W. Ketterle, Phys. Rev. Lett. **88**, 160401 (2002).
[2] G. Roati, F. Riboli, G. Modugno, and M. Inguscio, Phys. Rev. Lett. **89**, 150403 (2002).
[3] G. Barontini, C. Weber, F. Rabatti, J. Catani, G. Thalhammer, M. Inguscio, and F. Minardi, Phys. Rev. Lett. **103**, 043201 (2009).
[4] R. Pires, J. Ulmanis, S. Häfner, M. Repp, A. Arias, E. D. Kuhnle, and M. Weidemüller, Phys. Rev. Lett. **112**, 250404 (2014).
[5] S.-K. Tung, K. Jiménez-García, J. Johansen, C. V. Parker, and C. Chin, Phys. Rev. Lett. **113**, 240402 (2014).
[6] L. J. Wacker, N. B. Jørgensen, D. Birkmose, N. Winter, M. Mikkelsen, J. Sherson, N. Zinner, and J. J. Arlt, Phys. Rev. Lett. **117**, 163201 (2016).
[7] A. Schirotzek, C.-H. Wu, A. Sommer, and M. W. Zwierlein, Phys. Rev. Lett. **102**, 230402 (2009).
[8] M. Koschorreck, D. Pertot, E. Vogt, B. Fröhlich, M. Feld, and M. Köhl, Nature **485**, 619 (2012).
[9] C. Kohstall, M. Zaccanti, M. Jag, A. Trenkwalder, P. Massignan, G. M. Bruun, F. Schreck, and R. Grimm, Nature **485**, 615 (2012).
[10] T. Rentrop, A. Trautmann, F. A. Olivares, F. Jendrzejewski, A. Komnik, and M. K. Oberthaler, Phys. Rev. X **6**, 041041 (2016).
[11] N. B. Jørgensen, L. Wacker, K. T. Skalmstang, M. M. Parish, J. Levinsen, R. S. Christensen, G. M. Bruun, and J. J. Arlt, Phys. Rev. Lett. **117**, 055302 (2016).
[12] K.-K. Ni, S. Ospelkaus, M. H. G. de Miranda, A. Pe'er, B. Neyenhuis, J. J. Zirbel, S. Kotochigova, P. S. Julienne, D. S. Jin, and J. Ye, Science **322**, 231 (2008).
[13] T. Takekoshi, L. Reichsöllner, A. Schindewolf, J. M. Hutson, C. R. Le Sueur, O. Dulieu, F. Ferlaino, R. Grimm, and H.-C. Nägerl, Phys. Rev. Lett. **113**, 205301 (2014).
[14] P. K. Molony, P. D. Gregory, Z. Ji, B. Lu, M. P. Köppinger, C. R. Le Sueur, C. L. Blackley, J. M. Hutson, and S. L. Cornish, Phys. Rev. Lett. **113**, 255301 (2014).
[15] G. Pupillo, A. Micheli, H. P. Büchler, and P. Zoller, in *Cold Molecules: Creation and Applications*, edited by R. V. Krems, B. Friedrich, and W. C. Stwalley (Taylor & Francis, London, 2004), pp. 266–290.
[16] A. Griesmaier, J. Werner, S. Hensler, J. Stuhler, and T. Pfau, Phys. Rev. Lett. **94**, 160401 (2005).
[17] Q. Beaufils, R. Chicireanu, T. Zanon, B. Laburthe-Tolra, E. Maréchal, L. Vernac, J.-C. Keller, and O. Gorceix, Phys. Rev. A **77**, 061601 (2008).
[18] M. Lu, N. Q. Burdick, S. H. Youn, and B. L. Lev, Phys. Rev. Lett. **107**, 190401 (2011).
[19] M. Lu, N. Q. Burdick, and B. L. Lev, Phys. Rev. Lett. **108**, 215301 (2012).
[20] K. Aikawa, A. Frisch, M. Mark, S. Baier, A. Rietzler, R. Grimm, and F. Ferlaino, Phys. Rev. Lett. **108**, 210401 (2012).
[21] K. Aikawa, A. Frisch, M. Mark, S. Baier, R. Grimm, and F. Ferlaino, Phys. Rev. Lett. **112**, 010404 (2014).
[22] K. Aikawa, S. Baier, A. Frisch, M. Mark, C. Ravensbergen, and F. Ferlaino, Science **345**, 1484 (2014).
[23] H. Kadau, M. Schmitt, M. Wenzel, C. Wink, T. Maier, I. Ferrier-Barbut, and T. Pfau, Nature **530**, 194 (2016).
[24] M. Schmitt, M. Wenzel, F. Böttcher, I. Ferrier-Barbut, and T. Pfau, Nature **539**, 259 (2016).
[25] L. Chomaz, S. Baier, D. Petter, M. J. Mark, F. Wächtler, L. Santos, and F. Ferlaino, Phys. Rev. X **6**, 041039 (2016).
[26] L. Chomaz, R. M. W. van Bijnen, D. Petter, G. Faraoni, S. Baier, J. H. Becher, M. J. Mark, F. Waechtler, L. Santos, and F. Ferlaino, arXiv:1705.06914.
[27] Y. Tang, W. Kao, K.-Y. Li, S. Seo, K. Mallayya, M. Rigol, S. Gopalakrishnan, and B. L. Lev, arXiv:1707.07031.
[28] R. K. Kumar, P. Muruganandam, L. Tomio, and A. Gammal, J. Phys. Commun. **1**, 035012 (2017).
[29] A. J. Berglund, S. A. Lee, and J. J. McClelland, Phys. Rev. A **76**, 053418 (2007).
[30] A. Frisch, K. Aikawa, M. Mark, A. Rietzler, J. Schindler, E. Zupanič, R. Grimm, and F. Ferlaino, Phys. Rev. A **85**, 051401 (2012).

[31] J. Ulitzsch, D. Babik, R. Roell, and M. Weitz, Phys. Rev. A **95**, 043614 (2017).
[32] M. Lu, S. H. Youn, and B. L. Lev, Phys. Rev. Lett. **104**, 063001 (2010).
[33] T. Maier, H. Kadau, M. Schmitt, A. Griesmaier, and T. Pfau, Opt. Lett. **39**, 3138 (2014).
[34] D. Dreon, L. A. Sidorenkov, C. Bouazza, W. Maineult, J. Dalibard, and S. Nascimbene, J. Phys. B **50**, 065005 (2017).
[35] T. Kuwamoto, K. Honda, Y. Takahashi, and T. Yabuzaki, Phys. Rev. A **60**, R745(R) (1999).
[36] D. Sukachev, A. Sokolov, K. Chebakov, A. Akimov, S. Kanorsky, N. Kolachevsky, and V. Sorokin, Phys. Rev. A **82**, 011405 (2010).
[37] J. Miao, J. Hostetter, G. Stratis, and M. Saffman, Phys. Rev. A **89**, 041401 (2014).
[38] H. Katori, T. Ido, Y. Isoya, and M. Kuwata-Gonokami, Phys. Rev. Lett. **82**, 1116 (1999).
[39] A. Kramida, Yu. Ralchenko, J. Reader, and NIST ASD Team, *NIST Atomic Spectra Database (version 5)* [online]. Available at: http://physics.nist.gov/asd. Accessed: 13 February 2018.
[40] R. W. P. Drever, J. L. Hall, F. V. Kowalski, J. Hough, G. M. Ford, A. J. Munley, and H. Ward, Appl. Phys. B **31**, 97 (1983).
[41] The atomic beam of Er and Dy might deposit an additional metallic layer on the mirror. However, we have tested this effect in our running Er machine and did not observe any sizable reduction in the reflectivity of the mirror.
[42] For the sake of completeness, we note that early MOT experiments on alkali atoms have explored MOT geometries with five non–orthogonally intersecting beams (e.g., at an angle of 120°) [47,48], which constitutes a very different scenario compared to our open-top approach.
[43] U. Schlöder, H. Engler, U. Schünemann, R. Grimm, and M. Weidemüller, Eur. Phys. J. D **7**, 331 (1999).
[44] M. Taglieber, A.-C. Voigt, F. Henkel, S. Fray, T. W. Hänsch, and K. Dieckmann, Phys. Rev. A **73**, 011402 (2006).
[45] C. E. Habermann and A. H. Daane, J. Chem. Phys. **41**, 2818 (1964).
[46] Since the large spatial extension of the MOT might mask residual atoms in higher spin states, we performed preliminary Stern-Gerlach mapping after loading the atoms into an optical dipole trap. Again, we did not detect atoms in higher Zeeman sublevels.
[47] J. Arlt, P. Bance, S. Hopkins, J. Martin, S. Webster, A. Wilson, K. Zetie, and C. J. Foot, J. Phys. B **31**, L321 (1998).
[48] A. di Stefano, D. Wilkowski, J. Müller, and E. Arimondo, Appl. Phys. B **69**, 263 (1999).

Chapter 4

Heteronuclear dipolar quantum mixtures

Upon accomplishing the first milestone, the dual-species intercombination-line MOT [88], the experimental efforts aimed for the second milestone, the first production of heteronuclear dBECs for various bosonic isotope mixtures of erbium and dysprosium [117].

The figure of merit for Bose-Einstein condensation to occur is the phase space density [6]

$$\mathrm{PSD} = n \left(\frac{2\pi\hbar^2}{m k_\mathrm{B} T} \right)^{3/2}, \tag{4.1}$$

as Chapter 2 described in equation (2.16). The PSD scaling with n and $T^{-3/2}$ implies a large number density n at a low temperature T in order to achieve the critical point of the phase transition. Hence, ultracold quantum gas experiments typically switch from the initially applied laser cooling to evaporative cooling [6, 131] either in an ODT [44, 132] or in a magnetic trap [7, 133]. Only recently experiments achieved Bose-Einstein condensation in strontium [134] and rubidium [135, 136] via laser cooling.

The dual-species MOT, after a loading time of $t_\mathrm{MOT} = 3\,\mathrm{s}$ and after the compression phase, provides atom numbers of up to $N_\mathrm{Er} = 6.7(1) \times 10^7$ and $N_\mathrm{Dy} = 2.1(1) \times 10^8$ at temperatures $T_\mathrm{cMOT,Er}$ and $T_\mathrm{cMOT,Dy}$ close to the Doppler temperatures $T_\mathrm{D,Er,583\,nm} = 4.5\,\mu\mathrm{K}$ and $T_\mathrm{D,Dy,626\,nm} = 3.2\,\mu\mathrm{K}$ [88] (see Table 2.2). These are ideal conditions for a direct transfer from the cMOT into an ODT to increase the PSD via evaporative cooling. This is necessary, since the intercombination-line MOT approach results in PSDs several orders of magnitudes below the phase transition's critical point for erbium [74] and dysprosium [75]. Following single-species experiments [29, 30], the experimental apparatus operates with an ODT at $\lambda = 1064\,\mathrm{nm}$. As it is red-detuned from the broad transition at $\lambda_\mathrm{Er} = 401\,\mathrm{nm}$ or $\lambda_\mathrm{Dy} = 421\,\mathrm{nm}$ and far off-resonant from any other optical transitions (see Chapter 2), the ODT provides for both elements a conservative trap with low off-resonant scattering.

This fourth chapter highlights the production of heteronuclear quantum-degenerate dipolar mixtures of erbium and dysprosium. First, Section 4.1 covers the ODT setup at 1064 nm, then, Section 4.2 moves to the evaporative cooling to quantum degeneracy, providing details on the experimental sequence and on the evaporation dynamics. Finally, Section 4.3 presents the second publication *Dipolar Quantum Mixtures of Erbium and Dysprosium Atoms* [117]. Some information provided throughout this chapter might coincide with [117] and is not explicitly referenced.

4.1 Optical dipole trap: 1064 nm

A high evaporative cooling efficiency requires a high elastic collision rate, which scales linearly with the number density n. [7, 131]. This imposes two rather contrary requirements on the ODT setup in order to achieve high n throughout evaporative cooling. First, a maximal mode matching between cMOT and ODT with a sufficiently deep ODT potential V_{ODT} for a high transfer efficiency during the initial ODT loading, and second, a tightly confining ODT for a small trapping volume during the later stages of evaporative cooling. A combined approach of a large reservoir ODT and of a tightly focused ODT can fulfill both requirements. However, the present ODT setup utilizes a time-averaged potential technique for a geometrically tunable ODT, as [137] successfully demonstrated for erbium. This approach additionally provides control over the final trapping geometry, which is advantageous due to the geometrical stability requirements of a dBEC (see Chapter 2).

In general, the V_{ODT} an atom experiences in a laser field is

$$V_{\mathrm{ODT}} = V(\mathbf{r}, \omega) = -\frac{1}{2\epsilon_0 c} I(\mathbf{r}) \, \Re\{\alpha(\omega)\}, \tag{4.2}$$

as Chapter 2 covered in equation (2.13). Because of the linear dependence on the intensity I, V_{ODT} benefits from a high power at the cMOT position. Even more, since the applied time-averaged potential technique increases the mode matching to the cMOT during the ODT loading at the expense of the V_{ODT} depth.

The entire ODT setup operates directly next to the UHV apparatus, as Figure 4.1 depicts. Avoiding any fiber couplings prevents loss in power, and thus increases the power reserves during the experimental sequence. However, the resulting long beam paths make the ODT more susceptible to mechanical instabilities within the experimental apparatus.

A commercial master oscillator power amplifier (MOPA) system[57] at $\lambda = 1064\,\mathrm{nm}$ produces a total output power $P_{1064\,\mathrm{nm}} = 55\,\mathrm{W}$ with a specified linewidth as low as 1 kHz over a timescale of 100 ms. It combines a master laser, which employs a non-planar ring resonator in a neodymium-doped yttrium aluminum garnet (Nd:YAG) crystal, with multiple amplifier modules. Directly behind the laser output, an optical isolator[58] protects the laser system from back reflections and a set of lenses optimizes the beam shape.

The laser light splits among two beam paths, one for a horizontal and another one for a vertical ODT (h/vODT) forming together a crossed ODT (xODT) at the cMOT position. A motorized rotation mount controls a $\lambda/2$-plate and allows for a dynamic distribution of $P_{1064\,\mathrm{nm}}$ between hODT (P_{hODT}) and vODT (P_{vODT}) during the evaporative cooling. This is necessary, since the initial ODT loading requires for the hODT the maximally available $P_{\mathrm{hODT}} = 32\,\mathrm{W}$ at the cMOT position (see Section 4.2.1).

Each beam path has an AOM[59] for switching as well as for power stabilization. Accordingly, photodiodes monitor P_{hODT} in the periscope setup and P_{vODT} above the main chamber for a power stabilization feedback loop, respectively. The AOM in the hODT path enables the geometrically tunable ODT [137], where the modulation of the AOM's carrier frequency leads effectively to an increase of the horizontal beam waist, and thus to a time-averaged potential. A gain voltage G_{hODT} dynamically adjusts the modulation amplitude, and thus the hODT aspect ratio (AR), the ratio of horizontal to vertical beam waist, during the experimental sequence.

[57] Coherent Inc., Mephisto MOPA 55 W
[58] Electro-Optics Technology, Inc., 110-23052-0002-ISO, 5 mm, 1045 nm – 1080 nm, WPO, ULTRA
[59] Gooch & Housego PLC, 3110-197, center frequency 110 MHz, bandwidth 15 MHz

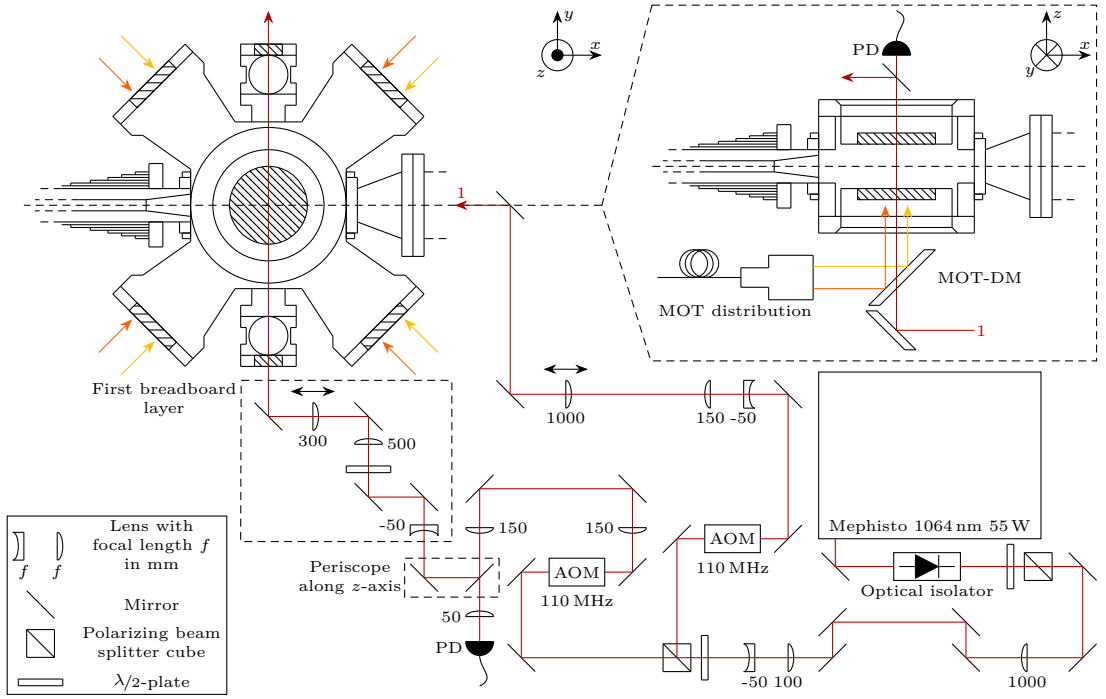

Figure 4.1: Optical setup for the ODT at $\lambda = 1064\,\text{nm}$ directly next to the main chamber. The MOPA laser light distributes between the horizontal and the vertical ODT (h/vODT) with a dynamically adjustable power ratio by a motorized $\lambda/2$-plate. Both AOMs are for switching and for power stabilization, while the one in the hODT additionally produces a time-averaged potential [137]. In the main chamber, the ODT beams have foci with $1/e^2$-waists $w_{\text{hODT}} = 22\,\mu\text{m}$ and $w_{\text{vODT}} = 130\,\mu\text{m}$ for the hODT and the vODT, respectively. In the inset, a vertical sectional view along the atomic beam propagation axis (x-axis) illustrates the optical setup for the vertical MOT beam and for the vODT.

The remaining optical setup subsequently guides the laser beams to the main chamber and focuses the hODT and the vODT to $1/e^2$-waists $w_{\text{hODT}} = 22\,\mu\text{m}$ and $w_{\text{vODT}} = 130\,\mu\text{m}$. As an additional degree of freedom, translation stages enable the position adjustment of the last focusing lenses, and thus of the focus positions for a precisely overlapping xODT at the cMOT position. Furthermore a $\lambda/2$-plate rotates the polarization of the hODT to minimize off-resonant scattering (R_{scat}, see equation (2.14)).

4.2 Evaporative cooling to quantum degeneracy

This PhD thesis' second publication [117] reported on the production of five different heteronuclear dBECs as well as of one quantum-degenerate Bose-Fermi mixture (^{168}Er-^{161}Dy) at $T/T_{\text{F}} \approx 0.5$, with the Fermi temperature T_{F}. Since the production steps are very similar for the different isotope mixtures, [117] almost exclusively focused on experimental data for ^{166}Er-^{164}Dy. This section reviews the remaining isotope mixtures in greater detail highlighting the experimental sequence in Section 4.2.1 and their PSD evolution during evaporative cooling in Section 4.2.2. The discussion also includes the isotope mixture ^{166}Er-^{162}Dy, which so far has not reached a heteronuclear dBEC.

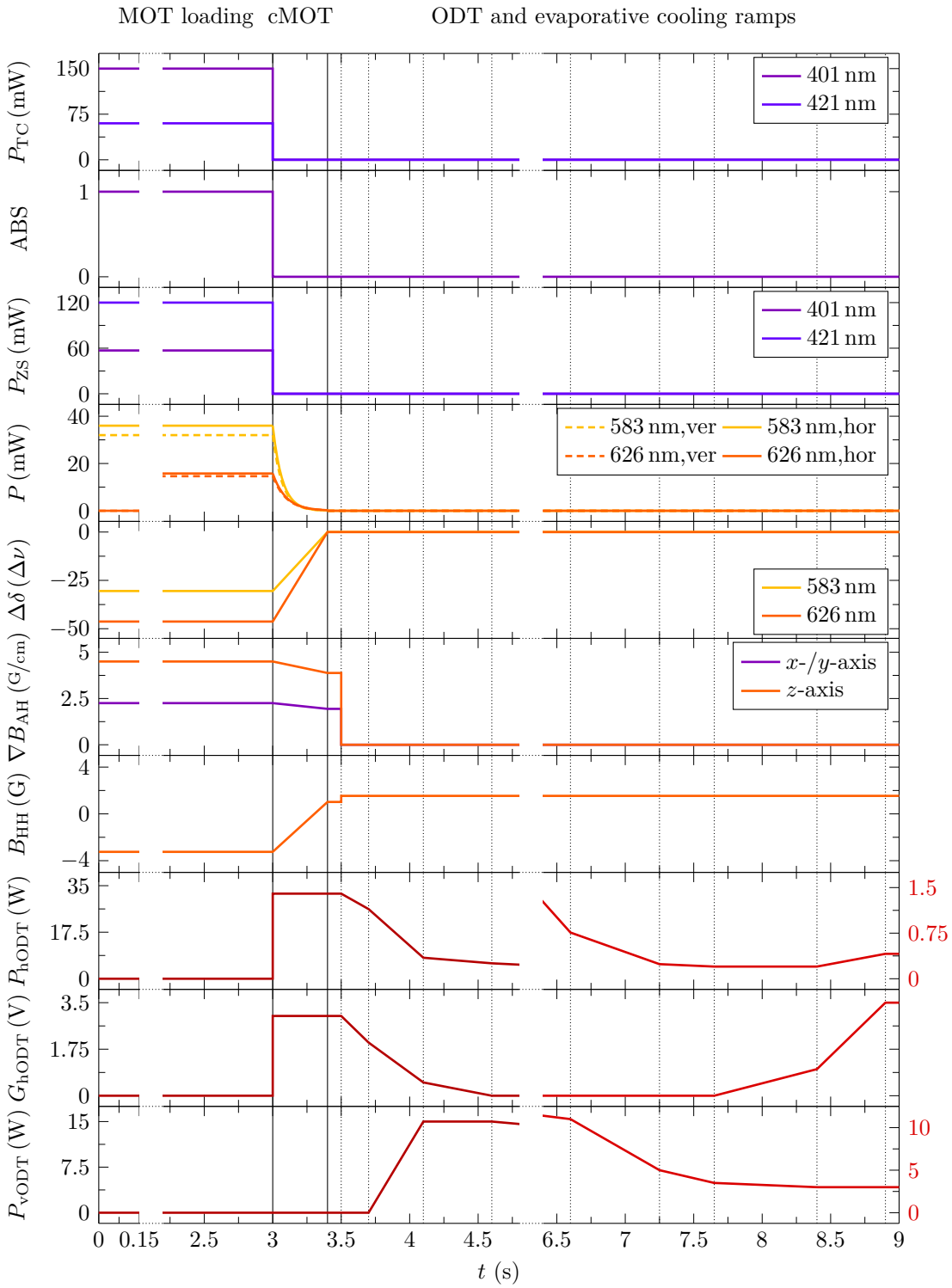

Figure 4.2: Experimental sequence with time t exemplarily for ^{170}Er-^{162}Dy. The time traces detail the temporal development of all relevant experimental parameters during the MOT loading, the compression phase, and the ODT and the evaporative cooling ramps. Note that, the time axis interrupts at ramp four to provide a higher resolution and $P_{626\,,\mathrm{MOT}}$ deviates from its typical values in Table 3.1 (see text).

4.2.1 Experimental Sequence

The following paragraphs discuss the generic steps for the production of quantum-degenerate dipolar mixtures. The experimental sequence consists of three steps, the MOT loading, the compression phase as well as the ODT and the evaporative cooling ramps. Figure 4.2 depicts the individual time traces of the various experimental parameters with values exemplarily for the production of a heteronuclear dBEC of ^{170}Er-^{162}Dy.

Initially, the TC and the ZS are active, the ABS is in open position and the dual-species MOT loads at its typical operating parameters, in particular at MOT beam powers $P_{583\,\mathrm{nm,MOT}}$ and $P_{626\,\mathrm{nm,MOT}}$, MOT light detunings $\delta_{583\,\mathrm{nm,MOT}}$ and $\delta_{626\,\mathrm{nm,MOT}}$, a quadrupole **B**-field $\mathbf{B}_{\mathrm{AH}}$ with $\nabla B_{\mathrm{AH,MOT}}$ and a bias **B**-field $\mathbf{B}_{\mathrm{HH}}$ with $B_{\mathrm{HH,MOT}}$ (see Table 3.1). All investigated isotope mixtures, however, require dysprosium as minority since erbium acts as sympathetic coolant [117] (see Section 4.2.2). For all achieved heteronuclear dBECs, this imbalance is achievable by adjusting the individual MOT loading times to $t_{\mathrm{MOT,Dy}} < t_{\mathrm{MOT,Er}}$ (see Table 4.1), and by reducing $P_{626\,\mathrm{nm,MOT}}$, depending on the system's operating state, below the values in Table 3.1, but keeping the ratio. On the contrary, the Bose-Fermi mixture ^{168}Er-^{161}Dy requires $t_{\mathrm{MOT,Dy}} > t_{\mathrm{MOT,Er}}$ at the typical MOT loading parameters due to the weaker MOT loading performance of ^{161}Dy arising from the hyperfine structure of the fermionic isotopes (see Chapter 2).

In the next step, the TC and the ZS deactivate and the ABS blocks the atomic beam. Simultaneously, the hODT switches on at its maximal $P_{\mathrm{hODT}} = 32\,\mathrm{W}$ with AR = 4 ($G_{\mathrm{hODT}} = 3\,\mathrm{V}$) to prevent thermal drifts during the actual ODT loading. Within the next $t_{\mathrm{comp}} = 400\,\mathrm{ms}$, the MOT compresses and moves upwards as the compression phase reduces the operating parameters to their final values $P_{583\,\mathrm{nm,cMOT}}$, $P_{626\,\mathrm{nm,cMOT}}$, $\delta_{583\,\mathrm{nm,cMOT}}$, $\delta_{626\,\mathrm{nm,cMOT}}$ and $\nabla B_{\mathrm{AH,cMOT}}$, respectively, while $\mathbf{B}_{\mathrm{HH}}$ inverts its direction to $B_{\mathrm{HH,cMOT}}$ (see Table 3.1). The cMOT's small size and low temperatures $T_{\mathrm{cMOT,Er}}$ and $T_{\mathrm{cMOT,Dy}}$ together with the increased AR of the hODT optimize the ODT transfer efficiency, facilitating an ODT loading time of $t_{\mathrm{load}} = 100\,\mathrm{ms}$. Then, the MOT systems turn off and the homogeneous $\mathbf{B}_{\mathrm{HH}}$ jumps to a constant evaporation field value $B_{\mathrm{HH,evap}}$.

At this stage, the first evaporative cooling ramp starts by lowering P_{hODT} and G_{hODT} in linear ramps. During the second ramp, the motorized $\lambda/2$-plate redistributes P_{hODT} and the vODT increases to $P_{\mathrm{vODT}} = 15\,\mathrm{W}$ to form a xODT. At the end of the third ramp, the aspect ratio of the hODT reaches AR = 1 ($G_{\mathrm{hODT}} = 0\,\mathrm{V}$). The evaporative cooling continues as P_{hODT} and P_{vODT} decrease further. In ramp seven and eight, the last two evaporation steps, the hODT reshapes to AR = 5 ($G_{\mathrm{hODT}} = 3.5\,\mathrm{V}$) and, in order to compensate for the accompanying reduction in V_{ODT}, increases to $P_{\mathrm{hODT}} = 0.41\,\mathrm{W}$. The vODT remains constant at $P_{\mathrm{vODT}} = 3\,\mathrm{W}$. After a hold time in the xODT of up to $t_{\mathrm{hold}} = 100\,\mathrm{ms}$, the imaging system records absorption images with a variable TOF expansion of up to 27 ms (see Chapter 3).

The switching between different isotope mixtures requires the adjustment, besides of $t_{\mathrm{MOT,Dy}}$, $t_{\mathrm{MOT,Er}}$ and $P_{626\,\mathrm{nm,MOT}}$, additionally of the MOT light detuning, $\delta_{583\,\mathrm{nm}}$ or $\delta_{626\,\mathrm{nm}}$, and of the evaporation field value $B_{\mathrm{HH,evap}}$. The precise detuning values for the MOT loading and the cMOT depend on the isotopes, whereas the change in $B_{\mathrm{HH,evap}}$ adjusts the intra- and interspecies contact interactions that drive the thermalization during evaporative cooling. All other experimental parameters stay unchanged (except the final ODT parameters for ^{168}Er-^{161}Dy [117]). Table 4.1 summarizes t_{MOT} and $B_{\mathrm{HH,evap}}$ for the various isotope mixtures as well as all for single-species dBECs. This includes values for a dBEC of ^{170}Er, which this PhD work achieved for the first time.

Table 4.1: MOT loading times t_{MOT} and evaporation field values $B_{\mathrm{HH,evap}}$ for all achieved (heteronuclear) dBECs and for the quantum-degenerate Bose-Fermi mixture (^{168}Er-^{161}Dy) in the investigated **B**-field range $B_{\mathrm{HH,evap}} = 0.1\,\mathrm{G} - 5\,\mathrm{G}$. Additionally, γ_{ini} and γ_{sym} characterize the efficiency of the evaporative cooling at the underlined values of $B_{\mathrm{HH,evap}}$ (see Section 4.2.2). Here, [117] published all values with (*). The values for γ_{ini} do not provide an error (see text). Note that, ^{166}Er-^{162}Dy did not reach a heteronuclear dBEC within the investigated **B**-field range (see text).

Isotopes		t_{MOT} (s)	$B_{\mathrm{HH,evap}}$ (G)	γ_{ini}	γ_{sym}
^{166}Er		3–5	2.075	-	-
^{168}Er		3–5	4.795	-	-
^{170}Er		3–5	1.500	-	-
^{162}Dy		3–5	4.795	-	-
^{164}Dy		3–5	2.500	-	-
^{168}Er-^{162}Dy	Er	3	<u>3.300</u>*, 3.700, 4.400, 4.795	1.1	2.6 (0.3)
	Dy	2		1.6	6.0 (2.0)*
^{170}Er-^{162}Dy	Er	3	<u>1.540</u>*, 4.060	0.9	2.2 (0.6)
	Dy	2		1.0	11.0 (7.7)*
^{166}Er-^{164}Dy	Er	3	<u>2.075</u>*, 5.900-6.100	1.2	2.2 (0.4)
	Dy	1		1.1	7.2 (1.8)*
^{168}Er-^{164}Dy	Er	3	<u>3.300</u>*	0.8	2.1 (1.0)
	Dy	1		1.0	5.9 (1.6)*
^{170}Er-^{164}Dy	Er	3	<u>3.210</u>*	0.6	1.3 (0.7)
	Dy	1		1.5	3.3 (0.6)*
^{168}Er-^{161}Dy	Er	3.5	<u>3.455</u>*	1.6	1.8 (1.4)
	Dy	5		0.7	4.1 (1.1)*
^{166}Er-^{162}Dy	Er	3	<u>1.600</u>	1.0	1.4 (0.5)
	Dy	1		1.3	2.3 (0.5)

4.2.2 Evaporation dynamics

The difference in the real part of the scalar polarizabilities, $\Re\{\alpha_{\mathrm{sca,1064\,nm}}\}_{\mathrm{Er}}$ and $\Re\{\alpha_{\mathrm{sca,1064\,nm}}\}_{\mathrm{Dy}}$, at $\lambda = 1064\,\mathrm{nm}$ (see Chapter 2) manifests itself in differing trapping potentials $V_{\mathrm{ODT,Er}}$ and $V_{\mathrm{ODT,Dy}}$, and thus plays a crucial role in the evaporation dynamics. Figure 4.3 compares $V_{\mathrm{ODT,Er}}$ and $V_{\mathrm{ODT,Dy}}$ for ^{170}Er-^{162}Dy along the system's vertical z-axis including gravity for three settings, namely (a) the ODT loading, (b) the xODT at the beginning of ramp four and (c) the final ODT during t_{hold}. While gravity only weakly influences the settings (a) and (b), it becomes noticeable as $V_{\mathrm{ODT,Er}}$ and $V_{\mathrm{ODT,Dy}}$ get shallower, until it has a major influence in (c). As $\Re\{\alpha_{\mathrm{sca,1064\,nm}}\}_{\mathrm{Er}} < \Re\{\alpha_{\mathrm{sca,1064\,nm}}\}_{\mathrm{Dy}}$, $V_{\mathrm{ODT,Er}}$ is shallower than $V_{\mathrm{ODT,Dy}}$, and thus, as for the masses $m_{\mathrm{Er}} > m_{\mathrm{Dy}}$, the relative influence of gravity is larger for $V_{\mathrm{ODT,Er}}$ than for $V_{\mathrm{ODT,Dy}}$. These differences lead in a shallow trapping regime to sympathetic cooling of dysprosium by erbium [117].

This behavior occurs for all investigated isotope mixtures in their PSD evolution during the evaporative cooling. Because of the non-uniform density distribution in a harmonic

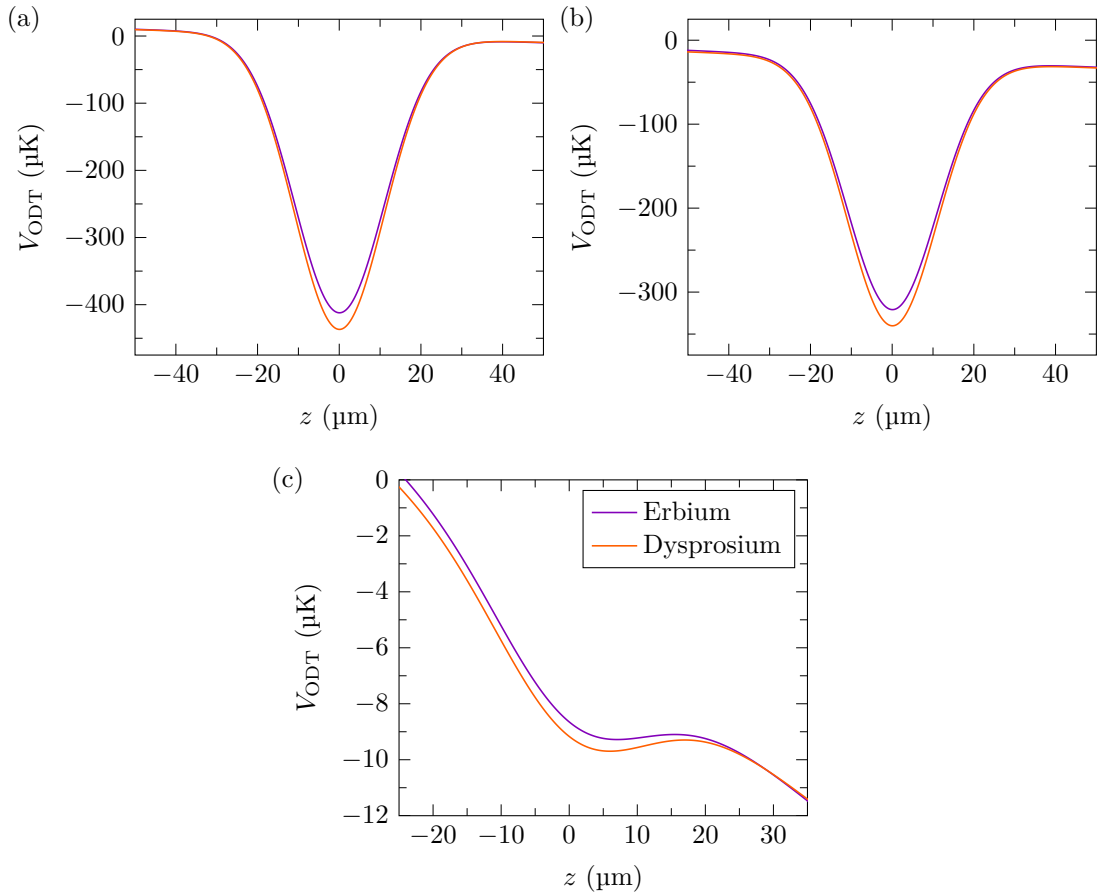

Figure 4.3: Calculated ODT potentials $V_{\mathrm{ODT,Er}}$ (violet) and $V_{\mathrm{ODT,Dy}}$ (orange) for ^{170}Er-^{162}Dy along the system's vertical z-axis under the influence of gravity. The calculation parameters are (a) ODT loading, $P_{\mathrm{hODT}} = 32\,\mathrm{W}$, $P_{\mathrm{vODT}} = 0\,\mathrm{W}$ and hODT AR = 4 ($G_{\mathrm{hODT}} = 3\,\mathrm{V}$), (b) xODT at the beginning of ramp four, $P_{\mathrm{hODT}} = 5.8\,\mathrm{W}$, $P_{\mathrm{vODT}} = 15\,\mathrm{W}$ and hODT AR = 1 ($G_{\mathrm{hODT}} = 0\,\mathrm{V}$), (c) final xODT, $P_{\mathrm{hODT}} = 0.41\,\mathrm{W}$, $P_{\mathrm{vODT}} = 3\,\mathrm{W}$ and hODT AR = 5 ($G_{\mathrm{hODT}} = 3.5\,\mathrm{V}$). The calculation employs the ODT beam parameters in Section 4.1, for dysprosium the real part of the scalar polarizability $\Re\{\alpha_{\mathrm{sca},1064\,\mathrm{nm}}\}_{\mathrm{Dy}} = 184.4\,\mathrm{a.u.}$ from [108] and for simplicity the ratio $\Re\{\alpha_{\mathrm{sca},1064\,\mathrm{nm}}\}_{\mathrm{Er}} = \Re\{\alpha_{\mathrm{sca},1064\,\mathrm{nm}}\}_{\mathrm{Dy}}/1.06$ [117].

trap, equation (4.1) replaces the number density n by the peak number density $\hat{n}$. The harmonic oscillator density distribution [6]

$$n(\mathbf{r}) = \frac{N}{\pi^{3/2} R_x R_y R_z} \mathrm{e}^{-x^2/R_x^2} \mathrm{e}^{-y^2/R_y^2} \mathrm{e}^{-z^2/R_z^2}, \tag{4.3}$$

with the position $\mathbf{r}$, the atom number N, $R_{x,y,z} = \sqrt{2k_{\mathrm{B}}T/m\omega_{x,y,z}^2}$ and the trapping frequency $\omega_{x,y,z}$ along the corresponding x-, y- or z-axis, gives

$$\hat{n} = \left(\frac{m}{2\pi k_{\mathrm{B}} T}\right)^{3/2} N(\omega_x \omega_y \omega_z). \tag{4.4}$$

Hence, absorption images after each ramp provide via N and T together with calculated $\omega_{x,y,z}$ sufficient information to extract the PSDs via equation (4.1). Starting from the second ramp, Figure 4.4 shows for each ramp $\ln\left({}^{\mathrm{PSD}}/_{\mathrm{PSD}_0}\right)$ over $\ln\left({}^{\mathrm{N}}/_{\mathrm{N}_0}\right)$ at the underlined values of $B_{\mathrm{HH,evap}}$ in Table 4.1. The second ramp's PSD_0 and N_0 serve as normalization to the individual PSD and N. Identical to ^{166}Er-^{164}Dy [117] (see Section 4.3), all other isotope mixtures display a change in the evaporation efficiency [131]

$$\gamma = -\frac{\mathrm{d}\ln\left({}^{\mathrm{PSD}}/_{\mathrm{PSD}_0}\right)}{\mathrm{d}\ln\left({}^{\mathrm{N}}/_{\mathrm{N}_0}\right)} \tag{4.5}$$

upon evaporative cooling from the xODT at ramp four. Linear fits (dashed and solid lines) access γ up to and starting from ramp four, γ_{ini} and γ_{sym}, respectively, to characterize the change in the evaporation behavior. The gain in γ is significantly larger for $\gamma_{\mathrm{sym,Dy}}$ than for $\gamma_{\mathrm{sym,Er}}$ indicating sympathetic cooling of dysprosium by erbium [117]. Table 4.1 summarizes the results, which [117] already partially published. The limited amount of data points prevents a thoroughly fitting of γ_{ini}. Hence, Table 4.1 does not provide the corresponding errors and the dashed lines in Figure 4.4 are a guide to the eye.

For the investigated **B**-field range $B_{\mathrm{HH,evap}} = 0.1\,\mathrm{G} - 5\,\mathrm{G}$, ^{166}Er-^{162}Dy did not reach a heteronuclear dBEC. A possible explanation might involve the low gain in $\gamma_{\mathrm{sym,Dy}}$ in comparison to the other isotope mixtures, even for the best evaporation performance at $B_{\mathrm{HH,evap}} = 1.600\,\mathrm{G}$ (see Table 4.1). However, to conclude for instance on either increased losses from the isotope mixture or an unfavorable thermalization behavior in the investigated **B**-field range, further experimental studies are necessary.

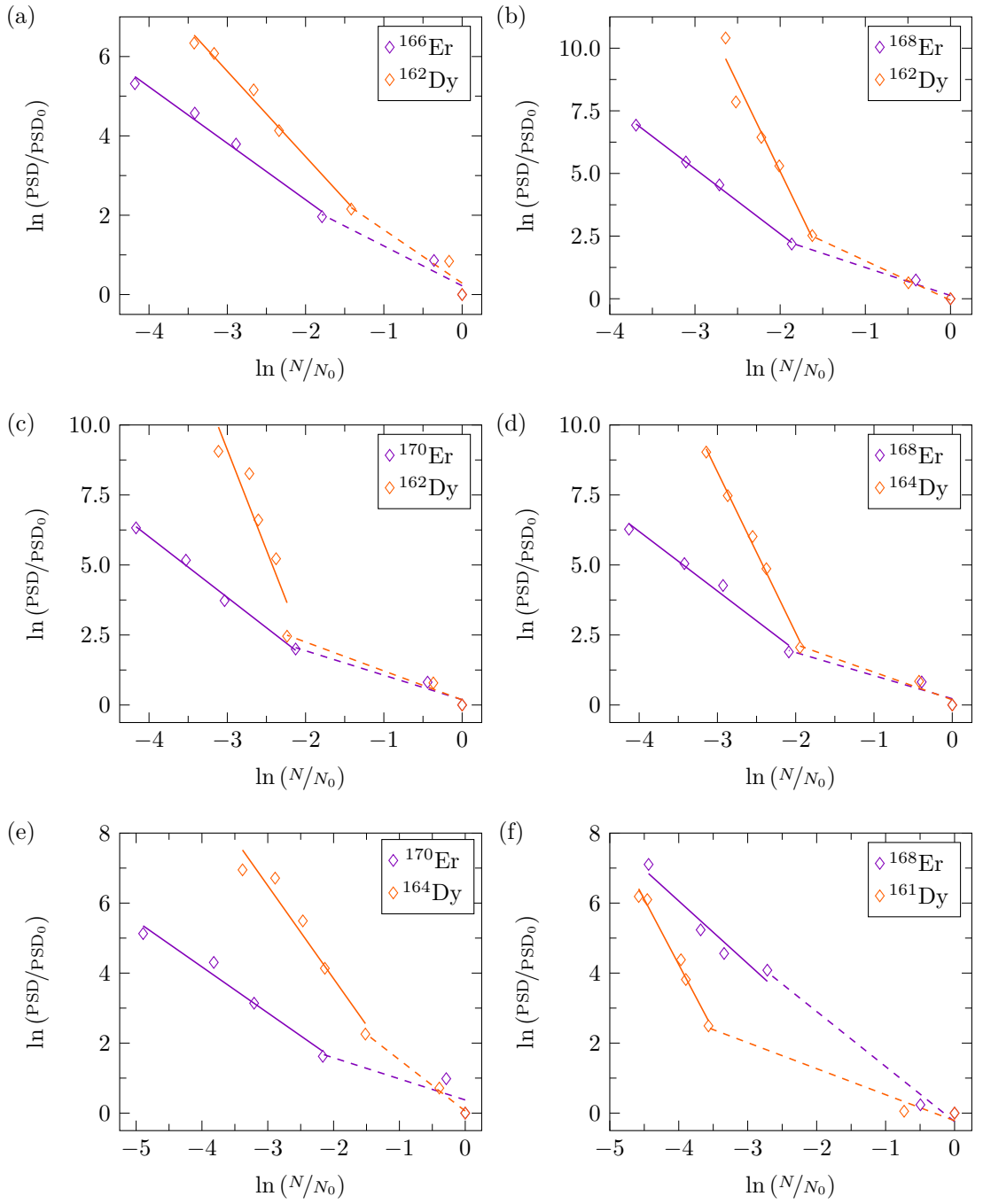

Figure 4.4: Evolution of the phase space density PSD over the atom number N from the second ramp onwards for (a) ^{166}Er-^{162}Dy, (b) ^{168}Er-^{162}Dy, (c) ^{170}Er-^{162}Dy, (d) ^{168}Er-^{164}Dy, (e) ^{170}Er-^{164}Dy and (f) ^{168}Er-^{161}Dy. Each plot shows $\ln(\mathrm{PSD}/\mathrm{PSD}_0)$ over $\ln(\mathrm{N}/\mathrm{N}_0)$ with the second ramp's PSD_0 and N_0 serving as normalization. The violet and orange lines are linear fits to the experimental data (violet and orange diamonds) to extract the evaporation efficiencies γ_{ini} up to (dashed lines) and γ_{sym} starting from (solid lines) ramp four for erbium and dysprosium, respectively. Table 4.1 provides the MOT loading times t_{MOT} and the evaporation field values $B_{\mathrm{HH,evap}}$ for the individual data sets and lists the fit results. Note, ^{166}Er-^{162}Dy did not reach a heteronuclear dBEC.

4.3 Publication II:

Dipolar Quantum Mixtures of Erbium and Dysprosium Atoms

A. Trautmann[1], P. Ilzhöfer[1,2,†], G. Durastante[1,2], C. Politi[1], M. Sohmen[1,2], M. J. Mark[1,2], F. Ferlaino[1,2]

[1] *Institut für Quantenoptik und Quanteninformation, Österreichische Akademie der Wissenschaften, 6020 Innsbruck, Austria*

[2] *Institut für Experimentalphysik und Zentrum für Quantenoptik, Universität Innsbruck, Technikerstrasse 25, 6020 Innsbruck, Austria*

Physical Review Letters, **121**, 213601, (2018), DOI: 10.1103/PhysRevLett.121.213601, received 20 July 2018, revised 8 October 2018, published 21 November 2018, Editors' suggestion

Featured in Physics 11, s135, Synopsis: Making Mixtures of Magnetic Condensates

[†] The author of this PhD thesis participated in the data recording and analysis as well as in the writing process of this publication.

Editors' Suggestion | Featured in Physics

Dipolar Quantum Mixtures of Erbium and Dysprosium Atoms

A. Trautmann,[1,*] P. Ilzhöfer,[1,2,*] G. Durastante,[1,2] C. Politi,[1] M. Sohmen,[1,2] M. J. Mark,[1,2] and F. Ferlaino[1,2]
[1]*Institut für Quantenoptik und Quanteninformation, Österreichische Akademie der Wissenschaften, 6020 Innsbruck, Austria*
[2]*Institut für Experimentalphysik und Zentrum für Quantenoptik, Universität Innsbruck, Technikerstraße 25, 6020 Innsbruck, Austria*

(Received 20 July 2018; revised manuscript received 8 October 2018; published 21 November 2018)

We report on the first realization of heteronuclear dipolar quantum mixtures of highly magnetic erbium and dysprosium atoms. With a versatile experimental setup, we demonstrate binary Bose-Einstein condensation in five different Er-Dy isotope combinations, as well as one Er-Dy Bose-Fermi mixture. Finally, we present first studies of the interspecies interaction between the two species for one mixture.

DOI: 10.1103/PhysRevLett.121.213601

In recent years, the field of atomic dipolar quantum gases has witnessed an impressive expansion as researchers have made substantial headway in using and controlling a novel class of atoms, the highly magnetic rare-earth species. Since the first experimental successes in creating Bose and Fermi quantum gases of Dy [1,2] or Er [3,4], fascinating many-body phenomena based on the dipole-dipole interaction (DDI) have been observed, including Fermi surface deformation [5], quantum-stabilized droplet states [6–8], and roton quasiparticles [9]. Remarkably, for Dy and Er, the intriguing physics within reach comes with comparatively simple experimental approaches to achieve quantum degeneracy. Several research groups have either recently reported on new experimental realizations of quantum gases with Dy [10,11] or Er [12] or are actively pursuing it [13,14].

An alternative route to access dipolar quantum physics is provided by polar molecules, possessing an electric dipole moment. Up to now, ultracold gases of polar molecules have been created from nondipolar binary quantum mixtures of alkali atoms [15–18] and dipolar spin-exchange interactions have been recently observed with lattice-confined molecules [19]. Besides molecule creation, heteronuclear quantum mixtures have been used as powerful resources to realize a broad class of many-body quantum states (e.g., [20–27]), in which intra- and interspecies short-range contact interactions are at play.

In the experiment described in this Letter, we merge for the first time the physics of heteronuclear mixtures with the one of magnetic dipolar quantum gases. Our motivations to create quantum mixtures by combining two different dipolar species, Er and Dy, are numerous. First, the coupling between the two components acquires an anisotropic and long-range character due to the strong interspecies DDI, in contrast to purely contact-interacting mixtures. The emergent physical richness of the system has only begun to be uncovered by theory. Recent studies include the prediction of anisotropic boundaries in the dipolar immiscibility-miscibility phase diagram [28,29], roton immiscibility [30], vortex lattice formation [31], and impurity physics both in dipolar quantum droplets [32] and dipolar Binary Bose-Einstein condensates (BECs) [33,34]. Moreover, the magnetic moments are large, yet different (7 bohr magneton for Er and 10 for Dy), leading to a DDI twice as strong in Dy as in Er. Such a difference is on one hand advantageous to deeper elucidate the complex scattering and many-body physics by performing comparative single-species studies with Er and Dy in the same experimental environment. On the other hand, we also anticipate

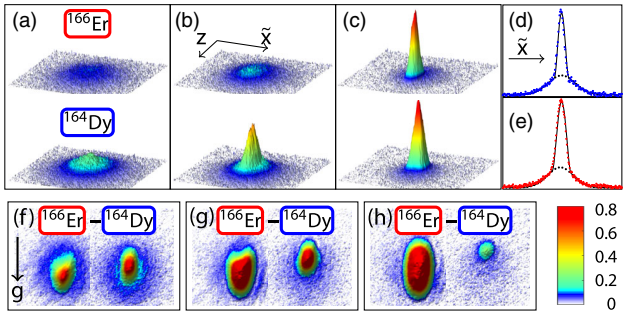

FIG. 1. Binary Bose-Einstein condensation in a ^{166}Er-^{164}Dy mixture. (a)–(c) Pairs of TOF absorption images at different evaporation stages, showing (a) a thermal mixture at about 180 nK, (b) an Er cloud at the onset of condensation coexisting with a thermal Dy gas at about 80 nK, and (c) the binary dipolar BEC with total atom numbers $N = 3.4 \times 10^4 (2.6 \times 10^4)$ for Er(Dy) with condensate fractions of about 45%. $\tilde{x}$ denotes the horizontal axis perpendicular to the imaging axis. (d),(e) Density profiles integrated along z, extracted from (c). Solid lines depict the 1D bimodal fit, the dotted lines show Gaussian fits to the thermal components. (f)–(h) BECs with a controlled number imbalance giving about $N^{\mathrm{Er}} = (3.2, 6.4, 9.2) \times 10^4$ with (35, 70, 85)% condensate fraction and $N^{\mathrm{Dy}} = (3.1, 2.9, 0.9) \times 10^4$ with (30, 55, 30)% condensate fraction for (f)–(h), respectively. The deformations and the relative displacement of the clouds are caused by interspecies interaction (see main text). The color bar indicates the optical density.

that, in mixture experiments, the imbalance in dipolar strength, combined with the interspecies interactions, promises fascinating prospects for creating long-lived quantum-droplet states and for accessing exotic fermionic superfluidity, for which the degree of deformation of the Fermi surface is species-dependent [5].

Second, the rich, but different atomic spectra of Er and Dy open promising prospects for implementing species-dependent optical manipulations schemes, including species-selective optical potentials at magic wavelengths and checkerboard-pattern-like lattice structures. Third, Er and Dy feature many stable bosonic and fermionic isotopes (both elements have four isotopes with natural abundances above 15%). Such an isotope variety allows us to create dipolar Bose-Bose, Bose-Fermi, and Fermi-Fermi heteronuclear mixtures. Last, mixtures composed of two different magnetic species serve as an ideal platform to produce ground-state polar molecules with both an electric and magnetic dipole moment, offering novel degrees of control and competing long-range interactions [35–37].

We here report on the first experimental realization of quantum-degenerate dipolar mixtures of Er and Dy atoms, using an all-optical approach for trapping and cooling. Taking advantage of the isotope richness in Er and Dy, we produce dipolar Bose-Bose mixtures with five different isotope combinations, as well as one Bose-Fermi mixture. We note that, prior to this work, the production of a Dy isotope mixture of a degenerate Fermi gas and a Bose gas near condensation has been reported [2] and, more recently, a doubly degenerate Fermi-Fermi mixture has been created from two Er spin states [39]. Experimental efforts are also devoted to creating Dy-K mixtures [40].

In the following, we detail the production of a double dipolar Bose-Einstein condensate (ddBEC) of ^{166}Er and ^{164}Dy. The same procedure is used for the other isotope mixtures. Our experiment starts with a double magneto-optical trap (MOT) of Er and Dy, as reported in our recent work [41]. For both species, the MOT operates on narrow intercombination lines and yields cold and spin-polarized samples in the absolute lowest Zeeman sublevels [10,13,41,42]. After loading the double MOT, we optically compress the mixture in 400 ms (cMOT phase) by reducing the detuning and power of the MOT beams as well as the magnetic-field gradient.

We then transfer the mixture into an optical dipole trap (ODT) by superposing it with the cMOT for 100 ms. Initially, the ODT consists of a single laser beam at 1064 nm, propagating along the horizontal (y) axis. The beam has a fixed vertical (z) focus of about 22 μm, whereas the horizontal waist can be controlled via a time-averaging-potential technique (see, e.g., [43]). This leads to an elliptic beam with variable aspect ratio (AR). Best transfer efficiency is observed for a beam power of 32 W and an AR of 4, which provides good spatial overlap between the cMOT and the ODT. We then switch off the MOT beams and magnetic-field gradient, and start a 5-sec evaporation sequence, during which we apply a bias magnetic field B_{evap} along the gravity (z) axis to preserve spin polarization.

Our strategy for evaporative cooling can be divided into three main stages. (i) During the initial 600 ms, we reduce the AR to unity while lowering the power of the single-beam ODT. This increases the density of the mixture at a roughly constant trap depth. (ii) We start forced evaporation in the horizontal ODT and add a vertically propagating dipole trap beam. The vertical beam is derived from the same laser source as the horizontal one and has a power of 15 W and a waist of 130 μm. (iii) We proceed with forced evaporation in the crossed ODT by reducing the powers of both beams nearly exponentially until the mixture is close to quantum degeneracy. In the final stage of the evaporation, we increase the AR to 5 to create a pancakelike trapping geometry and further decrease the trap depth until we reach double quantum degeneracy. To probe the atomic mixture, we switch off the ODT and, after a time-of-flight (TOF) expansion of 25 ms, we perform sequential absorption imaging with a resonant light pulse at 401 nm for Er and 500 μs later at 421 nm for Dy [3,44]; both pulses have a duration of 50 μs. The imaging light propagates horizontally with an angle of 45° with respect to the y axis.

Unlike many alkali mixtures [45–48], Er and Dy exhibit very comparable atomic polarizabilities α because of their similar atomic spectra. From single-species experiments [14,49], a ratio $\alpha_{\mathrm{Dy}}/\alpha_{\mathrm{Er}} = 1.06$ at 1064 nm is expected. For our initial ODT parameters, we calculate trap frequencies of about $\nu^{\mathrm{Er}} = (490, 5, 1980)$ Hz and $\nu^{\mathrm{Dy}} = (505, 5, 2050)$ Hz [50], corresponding to trap depths of 380 and 410 μK for Er and Dy, respectively. Although small, the difference in trap depths has an important effect on the evaporation trajectory of the mixture. We observe that the more weakly trapped Er atoms act as a coolant for Dy and are preferentially evaporated from the trap ("sympathetic losses" [47,51]). To sustain Er atom numbers high enough to achieve double quantum degeneracy, we imbalance the initial atom number in the MOT with Er as the majority component. The atom number imbalance can be easily controlled by individually changing the MOT loading time and beam power. This strategy is often employed in multispecies experiments, e.g., [52,53].

Figures 1(a)–1(c) show the phase transition from a thermal Er-Dy mixture (a) to a ddBEC (c). The TOF absorption images reveal the textbooklike fingerprint of condensation, the emergence of a bimodal density distribution, as plotted in Fig. 1(d). The condensation series [Figs. 1(a)–1(c)] is taken for an Er(Dy) MOT loading time of 3 s (1 s), for which we transfer 8×10^6 (7×10^5) Er(Dy) atoms into our ODT and measure a temperature of about 35 μK; this parameter set allows us to create number-balanced ddBECs. In agreement with the expected polarizabilities, we measure ODT trap frequencies of $\nu^{\mathrm{Er}} = (48.6(3), 29.7(9), 144(1))$ Hz and $\nu^{\mathrm{Dy}} = (50.6(3), 30.2(9),$

160(1)) Hz [54]. The resultant gravitational sag between the two species is 2.1(2) μm. By varying the imbalance of the MOT loading, we can produce degenerate mixtures with different atom number ratios and condensate fractions, which is exemplified in Figs. 1(f)–1(h). For large condensates, one directly observes a deformation of the density profiles due to interspecies interaction, as we discuss later in more detail.

To quantify the cooling efficiency, we plot the normalized phase-space density ($\mathrm{PSD}/\mathrm{PSD}_0$) as a function of normalized atom numbers (N/N_0) during the evaporation stages ii and iii [see Fig. 2(a)]. PSD_0 and N_0 are the respective initial values at stage ii. From this plot, we extract $\gamma = -d\ln(\mathrm{PSD}/\mathrm{PSD}_0)/d\ln(N/N_0)$ [55], which captures the evaporation efficiency, via a linear fit to the data. In the single-beam ODT (stage ii), we see similar efficiencies both in mixture and single-species operations, with $\gamma \approx 1.2$. In the crossed ODT (stage iii), we find $\gamma^{\mathrm{Er}} = 2.4(9)$ for Er in the mixture operation. This value is comparable to state-of-the-art single-species Er experiments [56] and, as expected, little affected by a small admixture of Dy atoms. Contrarily, the cooling efficiency of Dy in stage (iii) strongly benefits from the sympathetic cooling by Er: We observe a steep increase of the Dy PSD in the mixture and extract $\gamma^{\mathrm{Dy}}_{\mathrm{sym}} = 7(2)$, whereas for the same N_0^{Dy} but in single-species operation, the evaporation efficiency is considerably lower and would not suffice for condensation. However, with higher N_0^{Dy} we can still produce large Dy BECs in single-species operation.

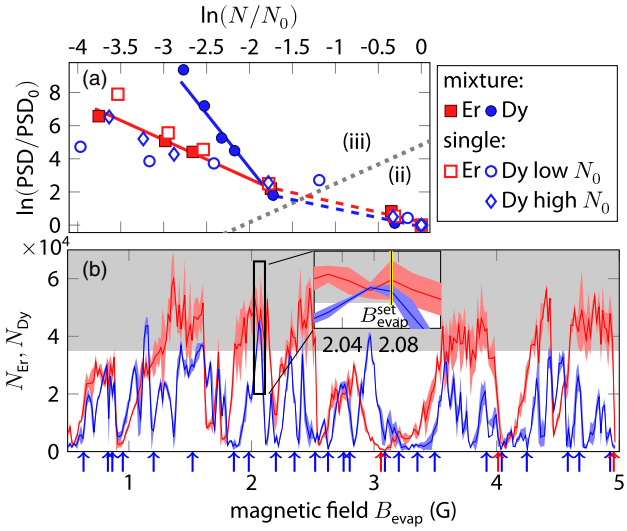

FIG. 2. (a) Evaporation trajectories: $\mathrm{PSD}/\mathrm{PSD}_0$ as a function of N/N_0. Filled squares (circles) indicate the Er(Dy) trajectory in mixture operation. The lines are linear fits to the data for evaporation in the single-beam (ii) and crossed-beam (iii) ODT (see main text). Open symbols show the single-species operation for Er (squares) and for Dy with small (circles) and large (diamonds) initial atom numbers. In the latter case, Dy condenses alone. (b) Atom numbers in the mixture of Er (red) and Dy (blue) at the onset of condensation as a function of the magnetic-field value during evaporation. Condensation is reached for atom numbers above about 3.5×10^4 (gray region). We record the best performance for a ddBEC around 2.075 G. Arrows indicate the position of known single-species Feshbach resonances [57–59].

The proper choice of B_{evap} plays an important role for cooling magnetic rare-earth atoms and becomes even more critical in mixture operation. It has indeed been observed in single-species experiments [57–59] that both Er and Dy exhibit extremely dense and temperature-dependent spectra of homonuclear Feshbach resonances. Figure 2(b) shows the atom numbers of the ^{166}Er-^{164}Dy mixture at the onset of condensation as a function of B_{evap} in a small magnetic-field range from 0.5 to 5 G. As expected, we find a number of broad and narrow loss features. Some of them are connected to known homonuclear Feshbach resonances [57–59], others we attribute to unknown high-temperature resonances or detrimental interspecies scattering conditions. In a few narrow magnetic-field windows, we observe atom numbers large enough for both components to condense. Our magnetic-field stability of about 2 mG is sufficient to reliably operate in most of these small windows. The optimal value of B_{evap}, listed in Table I, depends on the isotope combination.

Combining Er and Dy offers an unprecedented variety of heteronuclear mixtures with 16 possible isotope configurations, including Bose-Bose, Bose-Fermi, and Fermi-Fermi quantum gases (see Table I). Using the cooling and trapping procedure optimized for ^{166}Er-^{164}Dy, we are able to produce five ddBECs and one Bose-Fermi mixture. Concerning the remaining combinations, we know from previous experiments that both ^{167}Er and ^{163}Dy need a different experimental approach since ^{167}Er undergoes light-induced losses in a 1064-nm ODT [4], whereas ^{163}Dy, never brought to quantum degeneracy so far, has an inverted hyperfine structure, requiring most probably additional optical pumping stages. Both isotopes will be investigated for future studies of Fermi-Fermi mixtures.

Figures 3(a)–3(d) show absorption pictures of our doubly degenerate isotope mixtures. We are able to

TABLE I. (Left) List of optimal B_{evap} and $\gamma^{\mathrm{Dy}}_{\mathrm{sym}}$ for the quantum-degenerate Er-Dy mixtures. (Right) Chart of the available isotope mixtures: (✓) realized double-degenerate mixtures, (×) thermal mixtures, where degeneracy is not yet reached. (⋯) Mixtures with ^{167}Er and ^{163}Dy are not investigated here.

mixture	B_{evap}(G)	$\gamma^{\mathrm{Dy}}_{\mathrm{sym}}$
^{166}Er-^{164}Dy	2.075	7(2)
^{168}Er-^{162}Dy	3.300	6(2)
^{168}Er-^{164}Dy	3.300	6(2)
^{170}Er-^{162}Dy	1.540	11(7)
^{170}Er-^{164}Dy	3.210	3(1)
^{168}Er-^{161}Dy	3.455	4(1)

Dy \ Er	166	167	168	170
161	×	⋯	✓	×
162	×	⋯	✓	✓
163	⋯	⋯	⋯	⋯
164	✓	⋯	✓	✓

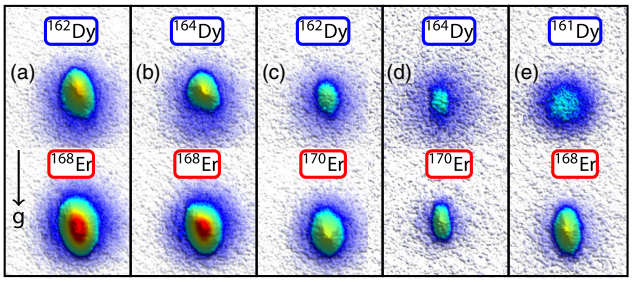

FIG. 3. Absorption pictures of the double-degenerate Bose-Bose mixtures (a)–(d) and the Bose-Fermi mixture (e). The pictures are averaged over 5–10 single shots. For all combinations, degeneracy is reached with the evaporation ramp optimized for the ^{166}Er-^{164}Dy mixture (cf. Fig. 1). B_{evap} is listed in Table I. Typical condensate fractions are around 30%, total atom numbers range between 1×10^4 and 3.5×10^4 atoms. For the imbalanced case, higher condensate fractions can be achieved (see Fig. 1). For the ^{161}Dy Fermi gas, $N = 8 \times 10^3$, $T/T_F \approx 0.5$, and TOF $= 15$ ms.

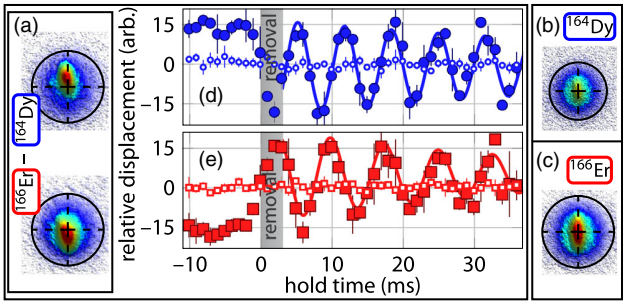

FIG. 4. Evidence of interspecies interactions in the ^{166}Er-^{164}Dy mixture: absorption pictures of Er and Dy in mixture (a) and single-species (b),(c) operation. (d),(e) Filled symbols show the c.m. position along z of the Dy BEC (d) and the Er BEC (e) after removal of the other species with resonant light. The gray region indicates the transient time until full removal. The solid lines are damped sine fits to the oscillations. For comparison, open symbols show the c.m. position in a thermal mixture.

condense all Bose-Bose isotope mixtures with the exception of ^{166}Er-^{162}Dy, for which we record severe losses during the evaporation, potentially due to a very large interspecies scattering length. For all degenerate mixtures, we observe sympathetic cooling of Dy by Er. The atom numbers in the ddBECs differ significantly for the different mixtures, while the initial atom numbers in the MOT are very similar. This points to different intra- and interspecies scattering properties during evaporation. The optimal B_{evap} and the extracted $\gamma_{\mathrm{sym}}^{\mathrm{Dy}}$ are listed in Table I.

We also prepare one Bose-Fermi mixture [see Fig. 3(e)], in which a ^{168}Er BEC coexists with a degenerate Fermi gas of ^{161}Dy. Although the cooling process of spin-polarized fermions can differ substantially from bosons, we are able to reach Bose-Fermi degeneracy with a similar evaporation scheme [60]. We measure a temperature of the Fermi gas of $T/T_F \approx 0.5$, with the Fermi temperature $T_F = 140$ nK. We expect that deeper degeneracy might be reached by using smaller ODT beam waists [4].

Remarkably, in the TOF images in Figs. 1 and 3 hints of interspecies interactions can be spotted: in mixture operation, the center-of-mass (c.m.) position of each BEC is vertically displaced with respect to its thermal-cloud center [see also Fig. 4(a)]. The two BECs are displaced in opposite directions, with the heavier (lighter) Er(Dy) always shifted down (up). Contrarily, in single-species operation the condensates and their thermal clouds are centered [see Figs. 4(b) and 4(c)].

To confirm that the displacement after TOF originates from in-trap interspecies interaction, we prepare a ddBEC, let it equilibrate for 50 ms, and then selectively remove either of the two species from the ODT using a resonant light pulse [61]. After a variable hold time in the ODT, we release the remaining cloud and record its c.m. position after TOF. As shown in Figs. 4(d) and 4(e), we observe a very pronounced c.m. oscillation of the remaining BEC component with a frequency close to its bare trap frequency. The oscillations of Er [removing Dy, Fig. 4(d)] and of Dy [removing Er, Fig. 4(e)] proceed in counterphase, as expected from their initial separation in trap. Repeating the same measurement with a thermal-thermal mixture, or a mixture with just one condensed component (not shown), yields negligible or significantly weaker oscillations, respectively.

The spatial separation between the two condensed components and their oscillating behavior after removal indicate that, for our trap geometry, the overall interspecies interaction—contact plus dipolar—has a repulsive character. We note that the interspecies scattering length, governing the contact interaction, and its Feshbach tuning are presently unknown and beyond reach of state-of-the-art scattering models [57,62]. To isolate the different sources of interaction and determine their signs, future dedicated experiments studying the interplay between trap geometry, dipole orientation, and interspecies scattering length, combined with simulations based on generalized coupled Gross-Pitaeskvii equations are necessary. Indeed, the DDI breaks the angular symmetry of the mean-field interspecies potentials and is expected to render the strength and the sign of the overall interspecies interaction anisotropic and trap dependent.

In conclusion, we have produced heteronuclear dipolar quantum mixtures by combining two strongly magnetic atomic species, Er and Dy. Their isotope variety, the richness of their interactions, the imbalance in the dipolar strength, and simple laser-cooling schemes make Er-Dy mixtures a powerful experimental platform to access many-body quantum phenomena, in which contact and dipolar intra- and interspecies interactions are at play.

This work is supported by the ERC Consolidator Grant (RARE, No. 681432) and a NFRI Grant (MIRARE,

No. ÖAW0600) from the Austrian Academy of Science. G. D. and M. S. acknowledge support by the Austrian Science Fund FWF within the DK-ALM: W1259-N27. We thank the ERBIUM team and the Dy-K team in Innsbruck and the ERBIUM team of Markus Greiner for fruitful discussions.

*These authors contributed equally to this work.

[1] M. Lu, N. Q. Burdick, S. H. Youn, and B. L. Lev, Strongly Dipolar Bose-Einstein Condensate of Dysprosium, Phys. Rev. Lett. **107**, 190401 (2011).
[2] M. Lu, N. Q. Burdick, and B. L. Lev, Quantum Degenerate Dipolar Fermi Gas, Phys. Rev. Lett. **108**, 215301 (2012).
[3] K. Aikawa, A. Frisch, M. Mark, S. Baier, A. Rietzler, R. Grimm, and F. Ferlaino, Bose-Einstein Condensation of Erbium, Phys. Rev. Lett. **108**, 210401 (2012).
[4] K. Aikawa, A. Frisch, M. Mark, S. Baier, R. Grimm, and F. Ferlaino, Reaching Fermi Degeneracy via Universal Dipolar Scattering, Phys. Rev. Lett. **112**, 010404 (2014).
[5] K. Aikawa, S. Baier, A. Frisch, M. Mark, C. Ravensbergen, and F. Ferlaino, Observation of Fermi surface deformation in a dipolar quantum gas, Science **345**, 1484 (2014).
[6] H. Kadau, M. Schmitt, M. Wenzel, C. Wink, T. Maier, I. Ferrier-Barbut, and T. Pfau, Observing the Rosensweig instability of a quantum ferrofluid, Nature (London) **530**, 194 (2016).
[7] L. Chomaz, S. Baier, D. Petter, M. J. Mark, F. Wächtler, L. Santos, and F. Ferlaino, Quantum-Fluctuation-Driven Crossover from a Dilute Bose-Einstein Condensate to a Macrodroplet in a Dipolar Quantum Fluid, Phys. Rev. X **6**, 041039 (2016).
[8] M. Schmitt, M. Wenzel, F. Böttcher, I. Ferrier-Barbut, and T. Pfau, Self-bound droplets of a dilute magnetic quantum liquid, Nature (London) **539**, 259 (2016).
[9] L. Chomaz, R. M. W. van Bijnen, D. Petter, G. Faraoni, S. Baier, J. H. Becher, M. J. Mark, F. Wächtler, L. Santos, and F. Ferlaino, Observation of roton mode population in a dipolar quantum gas, Nat. Phys. **14**, 442 (2018).
[10] T. Maier, H. Kadau, M. Schmitt, A. Griesmaier, and T. Pfau, Narrow-line magneto-optical trap for dysprosium atoms, Opt. Lett. **39**, 3138 (2014).
[11] E. Lucioni, L. Tanzi, A. Fregosi, J. Catani, S. Gozzini, M. Inguscio, A. Fioretti, C. Gabbanini, and G. Modugno, Dysprosium dipolar Bose-Einstein condensate with broad feshbach resonances, Phys. Rev. A **97**, 060701 (2018).
[12] J. Ulitzsch, D. Babik, R. Roell, and M. Weitz, Bose-Einstein condensation of erbium atoms in a quasielectrostatic optical dipole trap, Phys. Rev. A **95**, 043614 (2017).
[13] D. Dreon, L. A. Sidorenkov, C. Bouazza, W. Maineult, J. Dalibard, and S. Nascimbene, Optical cooling and trapping of highly magnetic atoms: The benefits of a spontaneous spin polarization, J. Phys. B **50**, 065005 (2017).
[14] C. Ravensbergen, V. Corre, E. Soave, M. Kreyer, S. Tzanova, E. Kirilov, and R. Grimm, Accurate Determination of the Dynamical Polarizability of Dysprosium, Phys. Rev. Lett. **120**, 223001 (2018).
[15] K.-K. Ni, S. Ospelkaus, M. H. G. de Miranda, A. Pe'er, B. Neyenhuis, J. J. Zirbel, S. Kotochigova, P. S. Julienne, D. S. Jin, and J. Ye, A high phase-space-density gas of polar molecules, Science **322**, 231 (2008).
[16] T. Takekoshi, L. Reichsöllner, A. Schindewolf, J. M. Hutson, C. R. Le Sueur, O. Dulieu, F. Ferlaino, R. Grimm, and H.-C. Nägerl, Ultracold Dense Samples of Dipolar RBCS Molecules in the Rovibrational and Hyperfine Ground State, Phys. Rev. Lett. **113**, 205301 (2014).
[17] P. K. Molony, P. D. Gregory, Z. Ji, B. Lu, M. P. Köppinger, C. R. Le Sueur, C. L. Blackley, J. M. Hutson, and S. L. Cornish, Creation of Ultracold $^{87}Rb^{133}Cs$ Molecules in the Rovibrational Ground State, Phys. Rev. Lett. **113**, 255301 (2014).
[18] S. Moses, J. Covey, M. Miecnikowski, D. Jin, and J. Ye, New frontiers for quantum gases of polar molecules, Nat. Phys. **13**, 13 (2016).
[19] B. Yan, S. A. Moses, B. Gadway, J. P. Covey, K. R. A. Hazzard, A. M. Rey, D. S. Jin, and J. Ye, Observation of dipolar spin-exchange interactions with lattice-confined polar molecules, Nature (London) **501**, 521 (2013).
[20] T.-L. Ho and V. B. Shenoy, Binary Mixtures of Bose Condensates of Alkali Atoms, Phys. Rev. Lett. **77**, 3276 (1996).
[21] S. Ospelkaus, C. Ospelkaus, O. Wille, M. Succo, P. Ernst, K. Sengstock, and K. Bongs, Localization of Bosonic Atoms by Fermionic Impurities in a Three-Dimensional Optical Lattice, Phys. Rev. Lett. **96**, 180403 (2006).
[22] S. Will, T. Best, S. Braun, U. Schneider, and I. Bloch, Coherent Interaction of a Single Fermion with a Small Bosonic Field, Phys. Rev. Lett. **106**, 115305 (2011).
[23] J. Heinze, S. Götze, J. S. Krauser, B. Hundt, N. Fläschner, D.-S. Lühmann, C. Becker, and K. Sengstock, Multiband Spectroscopy of Ultracold Fermions: Observation of Reduced Tunneling in Attractive Bose-Fermi Mixtures, Phys. Rev. Lett. **107**, 135303 (2011).
[24] N. Spethmann, F. Kindermann, S. John, C. Weber, D. Meschede, and A. Widera, Dynamics of Single Neutral Impurity Atoms Immersed in an Ultracold Gas, Phys. Rev. Lett. **109**, 235301 (2012).
[25] N. B. Jørgensen, L. Wacker, K. T. Skalmstang, M. M. Parish, J. Levinsen, R. S. Christensen, G. M. Bruun, and J. J. Arlt, Observation of Attractive and Repulsive Polarons in a Bose-Einstein Condensate, Phys. Rev. Lett. **117**, 055302 (2016).
[26] M.-G. Hu, M. J. Van de Graaff, D. Kedar, J. P. Corson, E. A. Cornell, and D. S. Jin, Bose Polarons in the Strongly Interacting Regime, Phys. Rev. Lett. **117**, 055301 (2016).
[27] T. Rentrop, A. Trautmann, F. A. Olivares, F. Jendrzejewski, A. Komnik, and M. K. Oberthaler, Observation of the Phononic Lamb Shift with a Synthetic Vacuum, Phys. Rev. X **6**, 041041 (2016).
[28] G. Gligorić, A. Maluckov, M. Stepić, L. Hadžievski, and B. A. Malomed, Transition to miscibility in linearly coupled binary dipolar Bose-Einstein condensates, Phys. Rev. A **82**, 033624 (2010).
[29] R. K. Kumar, P. Muruganandam, L. Tomio, and A. Gammal, Miscibility in coupled dipolar and non-dipolar Boseeinstein condensates, J. Phys. Commun. **1**, 035012 (2017).
[30] R. M. Wilson, C. Ticknor, J. L. Bohn, and E. Timmermans, Roton immiscibility in a two-component dipolar Bose gas, Phys. Rev. A **86**, 033606 (2012).

[31] R. K. Kumar, L. Tomio, B. A. Malomed, and A. Gammal, Vortex lattices in binary Bose-Einstein condensates with dipole-dipole interactions, Phys. Rev. A **96**, 063624 (2017).
[32] M. Wenzel, T. Pfau, and I. Ferrier-Barbut, A fermionic impurity in a dipolar quantum droplet, Phys. Scr. **93**, 104004 (2018).
[33] B. Kain and H. Y. Ling, Polarons in a dipolar condensate, Phys. Rev. A **89**, 023612 (2014).
[34] L. A. P. Ardila and T. Pohl, Ground-state properties of dipolar bose polarons, arXiv:1804.06390.
[35] E. Abrahamsson, T. V. Tscherbul, and R. V. Krems, Quantum chaos in ultracold collisions of gas-phase erbium atoms, J. Chem. Phys. **127**, 044302 (2007).
[36] T. M. Rvachov, H. Son, A. T. Sommer, S. Ebadi, J. J. Park, M. W. Zwierlein, W. Ketterle, and A. O. Jamison, Observation of Low-Field Fano-Feshbach Resonances in Ultracold Gases of Dysprosium, Phys. Rev. Lett. **119**, 143001 (2017).
[37] The electric dipole moment of ErDy is currently unknown; Ref. [38] reports the calculation for another rare-earth combination, EuYb, with −0.13 D. Based on electronegativity arguments, a similar value can be expected in ErDy.
[38] M. Tomza, Ab initio properties of the ground-state polar and paramagnetic europium–alkali-metal-atom and 5 europium–alkaline-earth-metal-atom molecules, Phys. Rev. A **90**, 022514 (2014).
[39] S. Baier, D. Petter, J. H. Becher, A. Patscheider, G. Natale, L. Chomaz, M. J. Mark, and F. Ferlaino, Realization of a Strongly Interacting Fermi Gas of Dipolar Atoms, Phys. Rev. Lett. **121**, 093602 (2018).
[40] R. Grimm (private communication).
[41] P. Ilzhöfer, G. Durastante, A. Patscheider, A. Trautmann, M. J. Mark, and F. Ferlaino, Phys. Rev. A **97**, 023633 (2018).
[42] A. Frisch, K. Aikawa, M. Mark, A. Rietzler, J. Schindler, E. Zupanič, R. Grimm, and F. Ferlaino, Narrow-line magneto-optical trap for erbium, Phys. Rev. A **85**, 051401 (2012).
[43] S. Baier, An optical dipole trap for Erbium with tunable geometry, Master's thesis, University of Innsbruck, 2012.
[44] M. Lu, S. H. Youn, and B. L. Lev, Trapping Ultracold Dysprosium: A Highly Magnetic Gas for Dipolar Physics, Phys. Rev. Lett. **104**, 063001 (2010).
[45] G. Modugno, M. Modugno, F. Riboli, G. Roati, and M. Inguscio, Two Atomic Species Superfluid, Phys. Rev. Lett. **89**, 190404 (2002).
[46] Z. Hadzibabic, C. A. Stan, K. Dieckmann, S. Gupta, M. W. Zwierlein, A. Görlitz, and W. Ketterle, Two-Species Mixture of Quantum Degenerate Bose and Fermi Gases, Phys. Rev. Lett. **88**, 160401 (2002).
[47] M. Mudrich, S. Kraft, K. Singer, R. Grimm, A. Mosk, and M. Weidemüller, Sympathetic Cooling with Two Atomic Species in an Optical Trap, Phys. Rev. Lett. **88**, 253001 (2002).
[48] M. Gröbner, P. Weinmann, F. Meinert, K. Lauber, E. Kirilov, and H.-C. Nägerl, A new quantum gas apparatus for ultracold mixtures of K and Cs and KCs ground-state molecules, J. Mod. Opt. **63**, 1829 (2016).
[49] J. H. Becher, S. Baier, K. Aikawa, M. Lepers, J.-F. Wyart, O. Dulieu, and F. Ferlaino, Anisotropic polarizability of erbium atoms, Phys. Rev. A **97**, 012509 (2018).
[50] We use the notation $\nu^{\mathrm{Er,Dy}} = (\nu_x, \nu_y, \nu_z)$.
[51] A. Mosk, S. Kraft, M. Mudrich, K. Singer, W. Wohlleben, R. Grimm, and M. Weidemüller, Mixture of ultracold lithium and cesium atoms in an optical dipole trap, Appl. Phys. B **73**, 791 (2001).
[52] Y. Tang, A. Sykes, N. Q. Burdick, J. L. Bohn, and B. L. Lev, s-wave scattering lengths of the strongly dipolar bosons ^{162}Dy and ^{164}Dy, Phys. Rev. A **92**, 022703 (2015).
[53] C.-H. Wu, I. Santiago, J. W. Park, P. Ahmadi, and M. W. Zwierlein, Strongly interacting isotopic bose-fermi mixture immersed in a fermi sea, Phys. Rev. A **84**, 011601 (2011).
[54] The trap frequencies along the y and z axes are extracted from center-of-mass-oscillation measurement; the frequency along x is calculated based on the beam waist, calibrated via the z frequency, and our knowledge of the polarizability [14,49].
[55] W. Ketterle and N. V. Druten, in *Evaporative Cooling of Trapped Atoms*, edited by B. Bederson and H. Walther, Advances in Atomic, Molecular, and Optical Physics Vol. 37 (Academic Press, New York, 1996), pp. 181–236.
[56] A. Frisch, Dipolar quantum gases of erbium, Ph.D. thesis, University of Innsbruck, 2014.
[57] A. Frisch, M. Mark, K. Aikawa, F. Ferlaino, J. L. Bohn, C. Makrides, A. Petrov, and S. Kotochigova, Nature (London) **507**, 475 (2014).
[58] K. Baumann, N. Q. Burdick, M. Lu, and B. L. Lev, Observation of low-field fano-feshbach resonances in ultracold gases of dysprosium, Phys. Rev. A **89**, 020701 (2014).
[59] T. Maier, H. Kadau, M. Schmitt, M. Wenzel, I. Ferrier-Barbut, T. Pfau, A. Frisch, S. Baier, K. Aikawa, L. Chomaz, M. J. Mark, F. Ferlaino, C. Makrides, E. Tiesinga, A. Petrov, and S. Kotochigova, Emergence of Chaotic Scattering in Ultracold Er and Dy, Phys. Rev. X **5**, 041029 (2015).
[60] For the Bose-Fermi mixture, slightly different final trap parameters are required, with typically $\nu^{\mathrm{Er}} = (95(5), 33(1), 120(1))$, $\nu^{\mathrm{Dy}} = (106(5), 34(1), 142(1))$.
[61] The light pulse at the respective imaging transition has a duration of 1 ms. We have checked that the resonant light of one species does not affect the other.
[62] S. Kotochigova, Controlling interactions between highly magnetic atoms with feshbach resonances, Rep. Prog. Phys. **77**, 093901 (2014).

Chapter 5

Supersolidity in dipolar quantum gases of dysprosium

In 1969, A. F. Andreev and I. M. Lifshitz [138] and, in 1970, G. V. Chester [139] and A. J. Leggett [140] suggested a new state of matter, the so-called supersolid, which at the same time exhibits the crystalline order of a crystal and the flow of a superfluid. A more rigorous description connects to the spontaneous formation of a density long-range order as well as of an off-diagonal long-range order in a homogeneous system [141]. The first implies a broken translational symmetry intrinsic to crystalline solidity, whereas the latter attributes for delocalization characteristic to superfluidity [141]. Because of these contradicting properties, supersolidity attracted a wide interest across different research fields in physics.

In a first proposal, [140] considered the possibility to observe in solid helium a supersolid state of matter via its non-classical rotational inertia, also present in the superfluid phase of helium. Eventually, torsional oscillator experiments with solid ^{4}He, first within a porous Vycor glass disk [142] and then in bulk form [143], observed a non-classical rotational inertia and interpreted their results as signature of supersolidity. A refined apparatus, however, disproved the initial claims, putting also the results in the bulk case in question [144]. Although over the years various alternative techniques arose [145], for instance the search for mass flow [141, 145] or fourth sound propagation [146] through a supersolid, none achieved a positive outcome. Hence, all efforts to confirm supersolidity in solid ^{4}He, even with more recent studies [147], miss definite evidence so far [141, 145].

Ultracold quantum gas systems joined the endeavor as an alternative platform due to their high degree of control. Experiments with purely contact-interacting quantum gases reported for instance the softening of a roton-type mode at the phase transition to a supersolid utilizing an optical cavity [148], a supersolid in vicinity of two optical cavities [149] and the characterization of its Higgs and Goldstone mode [150], or a spin-orbit-coupled BEC with supersolid properties [151]. Despite the indisputable significance of these results, all these system impose a stiff crystal wavelength by external laser light and miss a purely interparticle-interaction-driven formation of density long-range order.

Scientific attention increasingly directed towards dipolar quantum gases, as their complex interparticle interactions spontaneously support a supersolid phase [141, 152]. Recently, four experiments, one in the group of Tilman Pfau in Stuttgart [153], one in the group of Giovanni Modugno in Florence [154] and two experiments in the group of Francesca Ferlaino in Innsbruck [155], achieved erbium and dysprosium supersolids

in absence of any optical cavity or optical lattice. The following paragraphs review the developments that led to this first observation of supersolidity in three-dimensional magnetically dipolar quantum gases.

In a pure mean-field description, the behavior of a trapped dipolar quantum gas follows the time-dependent GPE [110]

$$\mathrm{i}\hbar\frac{\partial}{\partial t}\psi_{\mathrm{BEC}}\left(\mathbf{r},t\right)=\left[-\frac{\hbar^2\nabla^2}{2m}+V_{\mathrm{trap}}\left(\mathbf{r},t\right)+\overline{V}_{\mathrm{int}}\left(\mathbf{r},t\right)\right]\psi_{\mathrm{BEC}}\left(\mathbf{r},t\right), \tag{5.1}$$

as Chapter 2 discussed in equation (2.17), predicting a non-modulated dBEC as the only stable phase. In general, an important characteristic of a BEC is its Bogoliubov-de Gennes excitation spectrum $\mathcal{E}$ [110], which depends on the momentum $\mathbf{q}$. A purely contact-interacting BEC shows a phononic (linear in q) and a free-particle (quadratic in q) dispersion for small and large momentum values q, respectively, where [6, 110]

$$\mathcal{E}\left(q\right)=\sqrt{\frac{\hbar^4}{4m^2}q^4+\frac{4\pi\hbar^4a_{\mathrm{s}}n_{\mathrm{BEC}}}{m^2}q^2}, \tag{5.2}$$

with the mass m, the s-wave scattering length a_{s} and the BEC number density n_{BEC} (see equation (2.19)). In comparison, an uniform dBEC exhibits a more complex excitation spectrum [110]

$$\mathcal{E}\left(q\right)=\sqrt{\frac{\hbar^4}{4m^2}q^4+\frac{4\pi\hbar^4a_{\mathrm{s}}n_{\mathrm{BEC}}}{m^2}q^2\left(1+\epsilon_{\mathrm{dd}}\left(3\cos^2\alpha-1\right)\right)}. \tag{5.3}$$

The additional term in equation (5.3) arises from the magnetic dipole-dipole interaction V_{dd} (see equation (2.23), $\mu_1=\mu_2=\mu$), and involves ϵ_{dd} (see equation (2.33)) as well as the Fourier transform of V_{dd} [66, 110]

$$\left(\mathcal{F}V_{\mathrm{dd}}\right)\left(\mathbf{q}\right)=\int\frac{\mu^2\mu_0}{4\pi}\frac{1-3\cos^2\theta}{\left|\mathbf{r}-\mathbf{r}'\right|^3}\mathrm{e}^{-\mathrm{i}\mathbf{q}\cdot\left(\mathbf{r}-\mathbf{r}'\right)}\mathrm{d}\left(\mathbf{r}-\mathbf{r}'\right)=\frac{\mu^2\mu_0}{3}\left(3\cos^2\alpha-1\right). \tag{5.4}$$

Here, α denotes the angle between $\mathbf{q}$ and the orientation of the dipoles, and thus introduces an anisotropy in equation (5.3). As a result, equation (5.3) combines, similarly to a purely contact-interacting BEC, a phononic and a free-particle dispersion, but additionally reveals via its α-dependence an anisotropic dispersion behavior for an uniform dBEC with anisotropic phonons differing in their sound velocities for $q\to0$ [110].

A non-uniform dBEC, however, for instance due to a pancake- or a cigar-shaped external harmonic trap V_{trap}, requires a more thorough analysis [116, 156, 157]. It shows, similarly to superfluid helium, a roton-maxon excitation spectrum [116, 157], which manifests itself in a characteristic maximum-minimum energy spectrum at intermediate q. Figure 5.1 (a) compares the corresponding basic dependence on q to the one of equation (5.2). The roton-maxon behavior arises from the $\mathbf{q}$-dependence of the non-local V_{dd} (or the electric dipole-dipole interaction for instance in a dBEC of polar molecules) [116], as evident from equation (5.4) via its α-dependence, and the interplay between V_{dd}, the contact interaction and the kinetic energy [157]. The rotonized $\mathcal{E}$ appears, depending on the geometry of V_{trap}, only along distinct spatial directions of the system [116, 157]. Moreover, it is adjustable for instance via V_{trap} (see below) or a_{s}, and thus ϵ_{dd} (see equation (2.33)) [116], as [158] demonstrated by Bragg spectroscopy in an erbium dBEC.

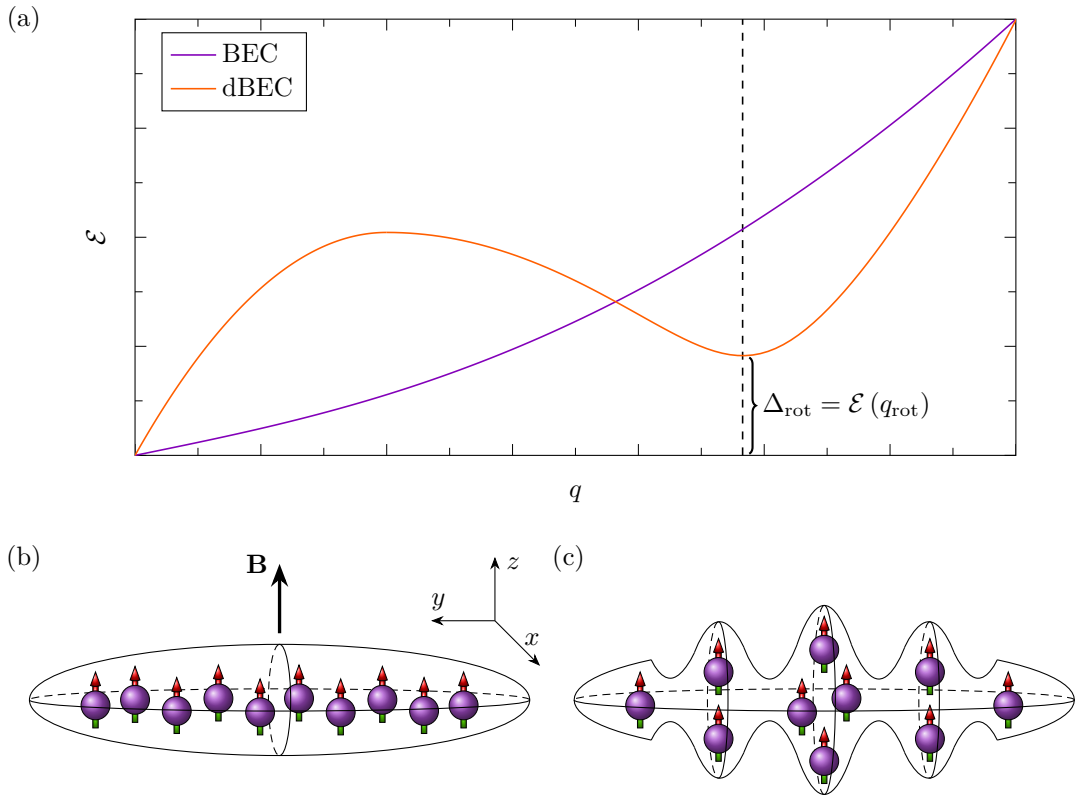

Figure 5.1: Bogoliubov-de Gennes excitation spectrum $\mathcal{E}$ and roton instability of a non-uniform dBEC. (a) Basic functional behavior of $\mathcal{E}$ with momentum value q for a purely contact-interacting BEC (violet) according to equation (5.2) and a non-uniform dBEC (orange) [116]. The comparison illustrates the phononic and the free-particle dispersion in a purely contact-interacting BEC, and the roton-maxon exciation spectrum in a non-uniform dBEC. Here, the roton gap Δ_{rot} characterizes the local minimum at the roton momentum q_{rot}. (b) Illustration of a non-modulated dBEC at $q = 0$ in a cigar-shaped harmonic trap V_{trap}. The symmetry axis of V_{trap} is along the y-axis and an external magnetic field $\mathbf{B}$, and thus the dipoles point along the z-axis. The rotonized $\mathcal{E}$ occurs along the y-axis. (c) Illustration of a macroscopic density modulation in a dBEC at q_{rot} along the symmetry axis of the cigar-shaped V_{trap}, arising due to the roton excitation. In the density maxima, the mean-field magnetic dipole-dipole interaction $\overline{V}_{\mathrm{dd}}$ is attractive. This forms the basis for the roton instability.

At particular interest is the local minimum in the excitation energy, the so-called roton minimum[60] at the roton momentum q_{rot} and the roton gap $\Delta_{\mathrm{rot}} = \mathcal{E}(q_{\mathrm{rot}})$ (see Figure 5.1 (a)). The following discussion considers the situation of a dBEC in a cigar-shaped V_{trap} with the trap symmetry axis along the y-axis (see Figure 5.1 (b)). An external magnetic field $\mathbf{B}$ aligns the dipoles along the z-axis orthogonal to the trap symmetry axis. Here, the rotonized $\mathcal{E}$ occurs along the y-axis with its minimum at $q_y = q_{\mathrm{rot}} \sim \sqrt{m\omega_z/\hbar}$ [157], with the $\mathbf{q}$-component q_y and the trapping frequency ω_z along

[60] The name 'roton' originates from superfluid helium, where in a vivid picture this excitation is a particle moving as the closely packed neighbors rotate out of its path [159].

the y- and z-axis, respectively. Remarkably, thermal and quantum fluctuations can provide an initial seed population to the roton excitation with far-reaching consequences. As Δ_{rot} decreases with increasing ϵ_{dd} softening the rotonized $\mathcal{E}$, the population of the roton excitation experiences an exponential growth upon Δ_{rot} turning imaginary [157]. In this regime, the dBEC in its initially non-modulated state at $q = 0$ (see Figure 5.1 (b)) spontaneously develops a macroscopic density modulation at q_{rot} along the y-axis (see Figure 5.1 (c)). As a result, the mean-field magnetic dipole-dipole interaction $\overline{V}_{\mathrm{dd}}$ (see equation (2.24)) turns in the density maxima from repulsive to locally attractive, surpassing the stabilizing characters of the mean-field contact interaction $\overline{V}_{\mathrm{con}}$ (see equation (2.22)) as well as of the kinetic energy. This leads, in an analogous discussion also for a dBEC in a pancake-shaped V_{trap}, to the roton instability [66, 116, 157], a collapse of a non-uniform dBEC in the applied mean-field description.

This was the physical picture prior to 2016. Independent theoretical and experimental work identified a stabilization mechanism beyond the mean-field description, which supports in a non-uniform dipolar quantum gas besides the dBEC phase two additional phases, an isolated droplet and a supersolid phase. Initially, [160] reported the fragmentation of a dysprosium dBEC in a pancake-shaped V_{trap} into individual droplets upon entering the roton instability. For a possible explanation, the results of [161] moved into focus, which considered quantum fluctuations in form of a Lee-Huang-Yang correction to the mean-field description as stabilization mechanism for an otherwise unstable Bose-Bose mixture. While a conservative three-body interaction was under debate as well [162, 163], further theoretical investigations on the Lee-Huang-Yang correction [164, 165, 166] as well as experimental work on droplets in a waveguide [167], the self-bound character of an individual droplet [168] or the transition from a dBEC to a macrodroplet [169] eventually confirmed quantum fluctuations as stabilization mechanism.

Hence, the theoretical description of a three-dimensional dipolar quantum gas, neglecting three-body processes, involves not only the mean-field terms $\overline{V}_{\mathrm{dd}}$ and $\overline{V}_{\mathrm{con}}$ but also a beyond-mean-field Lee-Huang-Yang term extending equation (5.1) to [164, 169]

$$\begin{aligned} \mathrm{i}\hbar\frac{\partial}{\partial t}\psi_{\mathrm{gs}}(\mathbf{r},t) = \Bigg[& -\frac{\hbar^2\nabla^2}{2m} + V_{\mathrm{trap}}(\mathbf{r},t) + \frac{4\pi\hbar^2 a_{\mathrm{s}}}{m} n_{\mathrm{gs}}(\mathbf{r},t) \\ & + \int \frac{\mu^2\mu_0}{4\pi}\frac{1-3\cos^2\theta}{|\mathbf{r}-\mathbf{r}'|^3} n_{\mathrm{gs}}(\mathbf{r}',t)\,\mathrm{d}\mathbf{r}' \\ & + \underbrace{\frac{128\sqrt{\pi}\hbar^2}{3m} n_{\mathrm{gs}}(\mathbf{r},t)^{3/2} a_{\mathrm{s}}^{5/2} F(\epsilon_{\mathrm{dd}})}_{\text{Lee-Huang-Yang term}} \Bigg] \psi_{\mathrm{gs}}(\mathbf{r},t)\,, \end{aligned} \tag{5.5}$$

with the ground state wave function ψ_{gs} and the number density n_{gs} (see equation (2.19)), respectively, and [164, 169]

$$F(\epsilon_{\mathrm{dd}}) = \frac{1}{2}\int \sin\alpha \left[1 + \epsilon_{\mathrm{dd}}\left(3\cos^2\alpha - 1\right)\right]^{5/2} \mathrm{d}\alpha. \tag{5.6}$$

Because of its scaling as $n_{\mathrm{gs}}^{3/2}$ in comparison to the linear scaling with n_{gs} of $\overline{V}_{\mathrm{con}}$ and $\overline{V}_{\mathrm{dd}}$, the additional beyond-mean-field Lee-Huang-Yang term plays a crucial role owing to its repulsive, and thus stabilizing character. It facilitates a radically different phase diagram to the one arising from equation (5.1) and supports a supersolid phase [153,

154, 155]. The broken continuous translational and gauge symmetry in this state of matter, corresponding to the initially described density long-range order and off-diagonal long-range order, respectively, give rise to a complex $\mathcal{E}$ with a crystal and a superfluid excitation branch, as recent work reported for erbium [170] or for dysprosium [171, 172], also including the confirmation of phase rigidity via the observation of the system's low-energy Goldstone mode [173]. For completeness, [174] and [175] provided first studies in dysprosium on the non-classical rotational inertia of the the supersolid phase, and further, [176] theoretically and experimentally investigated the response behavior of a erbium supersolid utilizing Bragg spectroscopy.

The extended GPE (eGPE, see equation (5.5)) offers a fully coherent description of a three-dimensional dipolar quantum gas, and thus does not capture any change in the phase coherence properties across the phase diagram. A stochastic eGPE approach would be an appropriate choice for a more thorough theoretical analysis, since the dBEC and the supersolid phase have a fundamentally different phase coherence behavior than the isolated droplet phase, but is so far not available.

The experimental realization of a long-lived dysprosium supersolid via direct evaporative cooling and well-established analysis tools capable to distinguish the isolated droplet and the supersolid phase [155], enabled a series of matter-wave-type experiments to study the rigidity of global phase coherence and the rephasing dynamics of an out-of-equilibrium dysprosium supersolid [177]. The remainder of this chapter presents in Sections 5.1 and 5.2 these results as this PhD thesis' third and fourth publication *Long-Lived and Transient Supersolid Behaviors in Dipolar Quantum Gases* [155] and *Phase coherence in out-of-equilibrium supersolid states of ultracold dipolar atoms* [177].

5.1 Publication III:

Long-Lived and Transient Supersolid Behaviors in Dipolar Quantum Gases

L. Chomaz[1], D. Petter[1], P. Ilzhöfer[2,†], G. Natale[1], A. Trautmann[2], C. Politi[2], G. Durastante[1,2], R. M. W. van Bijnen[2], A. Patscheider[1], M. Sohmen[1,2], M. J. Mark[1,2] and F. Ferlaino[1,2]

[1] *Institut für Experimentalphysik und Zentrum für Quantenoptik, Universität Innsbruck, Technikerstrasse 25, 6020 Innsbruck, Austria*

[2] *Institut für Quantenoptik und Quanteninformation, Österreichische Akademie der Wissenschaften, 6020 Innsbruck, Austria*

Physical Review X, **9**, 021012 (2019), DOI: 10.1103/PhysRevX.9.021012,
received 11 March 2019, published 19 April 2019, corrected 25 April 2019

Featured in Physics 12, 38, Viewpoint: Dipolar Quantum Gases go Supersolid

[†] The author of this PhD thesis participated in the recording of the dysprosium data as well as in the writing process of this publication.

Featured in Physics

Long-Lived and Transient Supersolid Behaviors in Dipolar Quantum Gases

L. Chomaz,[1] D. Petter,[1] P. Ilzhöfer,[2] G. Natale,[1] A. Trautmann,[2] C. Politi,[2] G. Durastante,[1,2] R. M. W. van Bijnen,[2] A. Patscheider,[1] M. Sohmen,[1,2] M. J. Mark,[1,2] and F. Ferlaino[1,2,*]

[1]*Institut für Experimentalphysik, Universität Innsbruck, Technikerstraße 25, 6020 Innsbruck, Austria*
[2]*Institut für Quantenoptik und Quanteninformation, Österreichische Akademie der Wissenschaften, Technikerstraße 21a, 6020 Innsbruck, Austria*

(Received 11 March 2019; published 19 April 2019; corrected 25 April 2019)

By combining theory and experiments, we demonstrate that dipolar quantum gases of both ^{166}Er and ^{164}Dy support a state with supersolid properties, where a spontaneous density modulation and a global phase coherence coexist. This paradoxical state occurs in a well-defined parameter range, separating the phases of a regular Bose-Einstein condensate and of an insulating droplet array, and is rooted in the roton mode softening, on the one side, and in the stabilization driven by quantum fluctuations, on the other side. Here, we identify the parameter regime for each of the three phases. In the experiment, we rely on a detailed analysis of the interference patterns resulting from the free expansion of the gas, quantifying both its density modulation and its global phase coherence. Reaching the phases via a slow interaction tuning, starting from a stable condensate, we observe that ^{166}Er and ^{164}Dy exhibit a striking difference in the lifetime of the supersolid properties, due to the different atom loss rates in the two systems. Indeed, while in ^{166}Er the supersolid behavior survives only a few tens of milliseconds, we observe coherent density modulations for more than 150 ms in ^{164}Dy. Building on this long lifetime, we demonstrate an alternative path to reach the supersolid regime, relying solely on evaporative cooling starting from a thermal gas.

DOI: 10.1103/PhysRevX.9.021012

Subject Areas: Atomic and Molecular Physics, Condensed Matter Physics, Quantum Physics

I. INTRODUCTION

Supersolidity is a paradoxical quantum phase of matter where both crystalline and superfluid order coexist [1–3]. Such a counterintuitive phase, featuring rather antithetic properties, has been originally considered for quantum crystals with mobile bosonic vacancies, the latter being responsible for the superfluid order. Solid ^{4}He has long been considered a prime system to observe such a phenomenon [4,5]. However, after decades of theoretical and experimental efforts, an unambiguous proof of supersolidity in solid ^{4}He is still missing [6,7].

In search of more favorable and controllable systems, ultracold atoms emerged as a very promising candidate, thanks to their highly tunable interactions. Theoretical works point to the existence of a supersolid ground state in different cold-atom settings, including dipolar [8] and Rydberg particles [9,10], cold atoms with a soft-core potential [11], or lattice-confined systems [7]. Breakthrough experiments with Bose-Einstein condensates (BECs) coupled to light have recently demonstrated a state with supersolid properties [12,13]. While in these systems indeed two continuous symmetries are broken, the crystal periodicity is set by the laser wavelength, making the supersolid incompressible.

Another key notion concerns the close relation between a possible transition to a supersolid ground state and the existence of a local energy minimum at large momentum in the excitation spectrum of a nonmodulated superfluid, known as the roton mode [14]. Since excitations corresponding to a periodic density modulation at the roton wavelength are energetically favored, the existence of this mode indicates the system's tendency to crystallize [15] and it is predicted to favor a transition to a supersolid ground state [4,5,9].

Remarkably, BECs of highly magnetic atoms, in which the particles interact through the long-range and anisotropic dipole-dipole interaction (DDI), appear to gather several key ingredients for realizing a supersolid phase. First, as predicted more than 15 years ago [16,17] and recently demonstrated in experiments [18,19], the partial attraction in momentum space due to the DDI gives rise to a roton

*Corresponding author.
Francesca.Ferlaino@uibk.ac.at

minimum. The corresponding excitation energy, i.e., the roton gap, can be tuned in the experiments down to vanishing values. Here, the excitation spectrum softens at the roton momentum and the system becomes unstable. Second, there is a nontrivial interplay between the trap geometry and the phase diagram of a dipolar BEC. For instance, our recent observations have pointed out the advantage of axially elongated trap geometries (i.e., cigar shaped) compared to the typically considered cylindrically symmetric ones (i.e., pancake shaped) in enhancing the visibility of the roton excitation in experiments. Last but not least, while the concept of a fully softened mode is typically related to instabilities and disruption of a coherent quantum phase, groundbreaking works in the quantum-gas community have demonstrated that quantum fluctuations can play a crucial role in stabilizing a dipolar BEC [20–26]. Such a stabilization mechanism enables the existence, beyond the mean-field instability, of a variety of stable ground states, from a single macrodroplet [22,24,27] to striped phases [28], and droplet crystals [29]; see also related works [30–33]. For multidroplet ground states, efforts have been devoted to understanding if a phase coherence among ground-state droplets could be established [28,29]. However, previous experiments with ^{164}Dy have shown the absence of phase coherence across the droplets [28], probably due to the limited atom numbers.

Droplet ground states, quantum stabilization, and dipolar rotons have caused a huge amount of excitement with very recent advancements adding key pieces of information to the supersolid scenario. The quench experiments in an ^{166}Er BEC at the roton instability have revealed out-of-equilibrium modulated states with an early-time phase coherence over a timescale shorter than a quarter of the oscillation period along the weak-trap axis [18]. In the same work, it has been suggested that the roton softening combined with the quantum stabilization mechanism may open a promising route towards a supersolid ground state. A first confirmation came from a recent theoretical work [34], considering an Er BEC in an infinite elongated trap with periodic boundary conditions and tight transverse confinement. The supersolid phase appears to exist within a narrow region in interaction strength, separating a roton excitation with a vanishing energy and an incoherent assembly of insulating droplets. Almost simultaneously, experiments with ^{162}Dy BECs in a shallow elongated trap, performing a slow tuning of the contact interaction, reported on the production of stripe states with phase coherence persisting up to half of the weak trapping period [35]. More recently, such observations have been confirmed in another ^{162}Dy experiment [36]. Here, theoretical calculations showed the existence of a phase-coherent droplet ground state, linking the experimental findings to the realization of a state with supersolid properties. The results on ^{162}Dy show, however, transient supersolid properties whose lifetime is limited by fast inelastic losses caused by three-body collisions [35,36]. These realizations raise the crucial question of whether a long-lived or stationary supersolid state can be created despite the usually non-negligble atom losses and the crossing of a discontinuous phase transition, which inherently creates excitations in the system.

In this work, we study both experimentally and theoretically the phase diagram of degenerate gases of highly magnetic atoms beyond the roton softening. Our investigations are carried out using two different experimental setups producing BECs of ^{166}Er [22,37] and of ^{164}Dy [38] and rely on a fine-tuning of the contact-interaction strength in both systems. In the regime of interest, these two atomic species have different contact-interaction scattering lengths a_s, whose precise dependence on the magnetic field is known only for Er [18,22,39], and different three-body-loss rate coefficients. Moreover, Er and Dy possess different magnetic moments μ and masses m, yielding the dipolar lengths, $a_{\mathrm{dd}} = \mu_0\mu^2 m/12\pi\hbar^2$, of $65.5a_0$ and $131a_0$, respectively. Here, μ_0 is the vacuum permeability, $\hbar = h/2\pi$ the reduced Planck constant, and a_0 the Bohr radius. For both systems, we find states showing hallmarks of supersolidity, namely, the coexistence of density modulation and global phase coherence. For such states, we quantify the extent of the a_s parameter range for their existence and study their lifetime. For ^{166}Er, we find results very similar to the one recently reported for ^{162}Dy [35,36], both systems being limited by strong three-body losses, which destroy the supersolid properties in about half of a trap period. However, for ^{164}Dy, we have identified an advantageous magnetic-field region where losses are very low and large BECs can be created. In this condition, we observe that the supersolid properties persist over a remarkably long time, well exceeding the trap period. Based on such a high stability, we finally demonstrate a novel route to reach the supersolid state, based on evaporative cooling from a thermal gas.

II. THEORETICAL DESCRIPTION

As a first step in our study of the supersolid phase in dipolar BECs, we compute the ground-state phase diagram for both ^{166}Er and ^{164}Dy quantum gases. The gases are confined in a cigar-shaped harmonic trap, as illustrated in Fig. 1(a). Our theory is based on numerical calculations of the extended Gross-Pitaevskii equation [40], which includes our anisotropic trapping potential, the short-range contact and long-range dipolar interactions at a mean-field level, as well as the first-order beyond-mean-field correction in the form of a Lee-Huang-Yang (LHY) term [18,22–24,27]. We note that, while both the exact strength of the LHY term and its dependence on the gas characteristics are under debate [18,19,25,31,41], the importance of such a term, scaling with a higher power in density, is essential for stabilizing states beyond the mean-field instability [18,25,41]; see also Refs. [8,42–44].

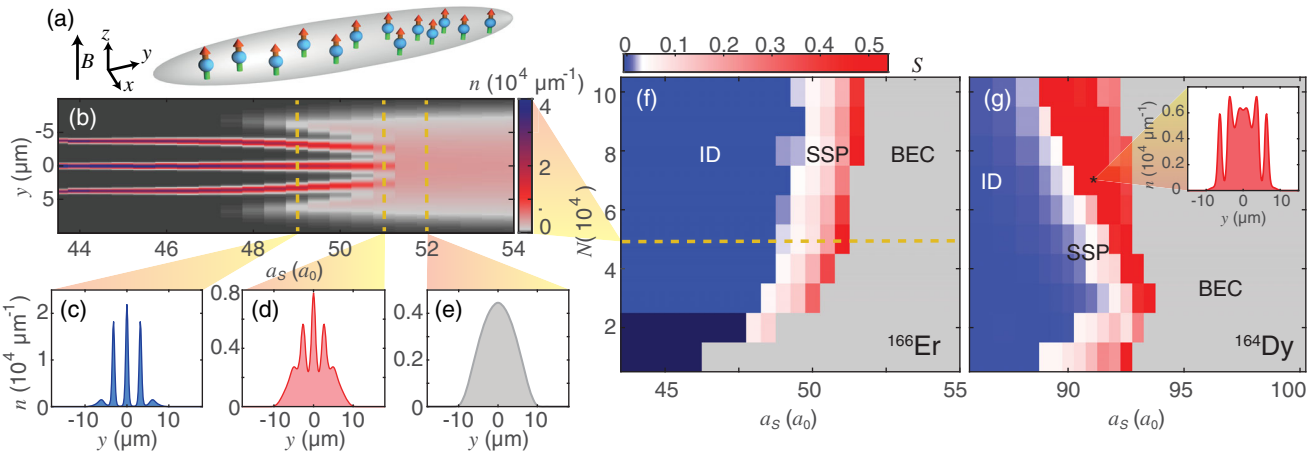

FIG. 1. Phase diagram of an ^{166}Er and a ^{164}Dy dipolar BEC in a cigar-shaped trap. (a) Illustration of the trap geometry with atomic dipoles oriented along z. (b) Integrated density profile as a function of a_s for an ^{166}Er ground state of $N = 5 \times 10^4$. In the color bar, the density scale is upper limited to 4×10^4 μm^{-1} in order to enhance the visibility in the supersolid regime. (c)–(e) Exemplary density profiles for an insulating droplet state (ID) at $a_s = 49a_0$, for a state with supersolid properties (SSP) at $51a_0$, and for a BEC at $52a_0$, respectively. (f),(g) Phase diagrams for ^{166}Er and ^{164}Dy for trap frequencies $\omega_{x,y,z} = 2\pi \times (227, 31.5, 151)$ and $2\pi \times (225, 37, 135)$ Hz, respectively. The gray color identifies ground states with a single peak in $n(y)$ of large Gaussian width, $\sigma_y > 2\ell_y$. The dark blue region in (f) shows the region where $n(y)$ exhibits a single sharp peak, $\sigma_y \leq 2\ell_y$, and no density modulation. The red-to-blue color map shows S in the case of a density-modulated $n(y)$. In (g) the color map is upper limited to use the same color code as in (f) and to enhance visibility in the low-N regime. The inset in (g) shows the calculated density profile for ^{164}Dy at $N = 7 \times 10^4$ and $a_s = 91a_0$.

Our theoretical results are summarized in Fig. 1. By varying the condensed-atom number N and a_s, the phase diagram shows three very distinct phases. To illustrate them, we first describe the evolution of the integrated *in situ* density profile $n(y)$ with fixed N for varying a_s, Fig. 1(b). The first phase, appearing at large a_s, resembles a regular dilute BEC. It corresponds to a nonmodulated density profile of low peak density and large axial size σ_y exceeding several times the corresponding harmonic oscillator length ($\ell_y = \sqrt{\hbar/m\omega_y}$); see Fig. 1(e) and the region denoted BEC in Figs. 1(f) and 1(g). The second phase appears when decreasing a_s down to a certain critical value, a_s^*. Here, the system undergoes an abrupt transition to a periodic density-modulated ground state, consisting of an array of overlapping narrow droplets, each of high peak density. Because the droplets are coupled to each other via a density overlap, later quantified in terms of the link strength S, particles can tunnel from one droplet to a neighboring one, establishing a global phase coherence across the cloud; see Fig. 1(d). Such a phase, in which periodic density modulation and phase coherence coexist, is identified as the supersolid (SSP) one [10,34]; see the SSP region in Figs. 1(f) and 1(g). When further decreasing a_s, we observe a fast reduction of the density overlap, which eventually vanishes; see Fig. 1(c). Here, the droplets become fully separated. Under realistic experimental conditions, it is expected that the phase relation between such droplets cannot be maintained; see later discussion. We identify this third phase as the one of an insulating droplet (ID) array [27,28,45]; see the ID region in Figs. 1(f) and 1(g). For low N, we find a single droplet of high peak density, as in Refs. [24,27]; see dark blue region in Fig. 1(f). Generally speaking, our calculations show that the number of droplets in the array decreases with lowering a_s or N. The existence of these three phases (BEC, SSP, ID) is consistent with recent calculations considering an infinitely elongated Er BEC [34] and a cigar-shaped ^{162}Dy BEC [36], illustrating the generality of this behavior in dipolar gases.

To study the supersolid character of the density-modulated phases, we compute the average of the wave function overlap between neighboring droplets S. As an ansatz to extract S, we use a Gaussian function to describe the wave function of each individual droplet. This is found to be an appropriate description from an analysis of the density profiles of Figs. 1(b)–1(d); see also Ref. [46]. For two droplets at a distance d and of identical Gaussian widths σ_y along the array direction, S is simply $S = \exp(-d^2/4\sigma_y^2)$. Here, we generalize the computation of the wave function overlap to account for the difference in widths and amplitudes among neighboring droplets. This analysis allows us to distinguish between the two types of modulated ground states, SSP and ID in Figs. 1(f) and 1(g). Within the Josephson-junction picture [47–49], the tunneling rate of atoms between neighboring droplets depends on the wave function overlap, and an estimate for the single-particle tunneling rate can be derived within the Gaussian approximation [46]; see also Ref. [40]. The ID phase corresponds to vanishingly small values of S, yielding

tunneling times extremely long compared to any other relevant timescale. In contrast, the supersolid phase is identified by a substantial value of S, with a correspondingly short tunneling time.

As shown in Figs. 1(f) and 1(g), a comparative analysis of the phase diagram for ^{166}Er and ^{164}Dy reveals similarities between the two species (see also Ref. [36]). A supersolid phase is found for sufficiently high N, in a narrow region of a_s, upper bounded by the critical value $a_s{}^*(N)$. For intermediate N, a_s^* increases with increasing N. We note that, for low N, the nonmodulated BEC evolves directly into a single droplet state for decreasing a_s [50]. In this case, no supersolid phase is found in between; see also Refs. [24,27]. Despite the general similarities, we see that the supersolid phase for ^{164}Dy appears for lower atom number than for Er and has a larger extension in a_s. This is mainly due to the different a_{dd} and strength of the LHY term. We note that, at large N and for decreasing a_s, Dy exhibits ground states with a density modulation appearing first in the wings, which then progresses inwards until a substantial modulation over the whole cloud is established [51]; see inset of Fig. 1(g). In this regime, we also observe that a_s^* decreases with increasing N. These types of states have not been previously reported and, although challenging to access in experiments because of the large N, they deserve further theoretical investigations.

III. EXPERIMENTAL SEQUENCE FOR ^{166}Er AND ^{164}Dy

To experimentally access the above-discussed physics, we produce dipolar BECs of either ^{166}Er or ^{164}Dy atoms. These two systems are created in different setups and below we summarize the main experimental steps; see also Ref. [40].

Erbium.—We prepare a stable ^{166}Er BEC following the scheme of Ref. [18]. At the end of the preparation, the Er BEC contains about $N = 8 \times 10^4$ atoms at $a_s = 64.5a_0$. The sample is confined in a cigar-shaped optical dipole trap with harmonic frequencies $\omega_{x,y,z} = 2\pi \times (227, 31.5, 151)$ Hz. A homogeneous magnetic field B polarizes the sample along z and controls the value of a_s via a magnetic Feshbach resonance (FR) [18,22,40]. Our measurements start by linearly ramping down a_s within 20 ms and waiting an additional 15 ms so that a_s reaches its target value [40]. We note that ramping times between 20 and 60 ms have been tested in the experiment and we do not record a significant difference in the system's behavior. After the 15-ms stabilization time, we then hold the sample for a variable time t_h before switching off the trap. Finally, we let the cloud expand for 30 ms and perform absorption imaging along the z (vertical) direction, from which we extract the density distribution of the cloud in momentum space, $n(k_x, k_y)$.

Dysprosium.—The experimental procedure to create a ^{164}Dy BEC follows the one described in Ref. [38]; see also Ref. [40]. Similarly to Er, the Dy BEC is also confined in a cigar-shaped optical dipole trap and a homogeneous magnetic field B sets the quantization axis along z and the value of a_s. For Dy, we will discuss our results in terms of magnetic field B, since the a_s-to-B conversion is not well known in the magnetic-field range considered [25,40,41,52]. In a first set of measurements, we first produce a stable BEC of about $N = 3.5 \times 10^4$ condensed atoms at a magnetic field of $B = 2.5$ G and then probe the phase diagram by tuning a_s. Here, before ramping the magnetic field to access the interesting a_s regions, we slowly increase the power of the trapping beams within 200 ms. The final trap frequencies are $\omega_{x,y,z} = 2\pi \times (300, 16, 222)$ Hz. After preparing a stable BEC, we ramp B to the desired value within 20 ms and hold the sample for t_h [40]. In a second set of measurements, we study a completely different approach to reach the supersolid state. As discussed later, here we first prepare a thermal sample at a B value where supersolid properties are observed and then further cool the sample until a transition to a coherent droplet-array state is reached. In both cases, at the end of the experimental sequence, we perform absorption imaging after typically 27 ms of time-of-flight (TOF) expansion. The imaging beam propagates horizontally under an angle α of $\approx 45°$ with respect to the weak axis of the trap (y). From the TOF images, we thus extract $n(k_Y, k_z)$ with $k_Y = \cos(\alpha)k_y + \sin(\alpha)k_x$.

A special property of ^{164}Dy is that its background scattering length is smaller than a_{dd}. This allows us to enter the supersolid regime without the need of setting B close to a FR, as is done for ^{166}Er and ^{162}Dy, which typically causes severe atom losses due to increased three-body-loss coefficients. In contrast, in the case of ^{164}Dy, the supersolid regime is reached by ramping B away from the FR pole used to produce the stable BEC via evaporative cooling, as the a_s range of Fig. 1(g) lies close to the background a_s reported in Ref. [52]; see also Ref. [40]. At the background level, three-body-loss coefficients below 1.3×10^{-41} m^6 s^{-1} have been reported for ^{164}Dy [25].

IV. DENSITY MODULATION AND PHASE COHERENCE

The coexistence of density modulation and phase coherence is the key feature that characterizes the supersolid phase and allows us to discriminate it from the BEC and ID cases. To experimentally probe this aspect in our dipolar quantum gases, we record their density distribution after a TOF expansion for various values of a_s across the phase diagram. As for a BEC in a weak optical lattice [53] or for an array of BECs [54–56], the appearance of interference patterns in the TOF images is associated with a density modulation of the *in situ* atomic distribution. Moreover, the shot-to-shot reproducibility of the patterns (in amplitude and position) and the persistence of fringes in averaged

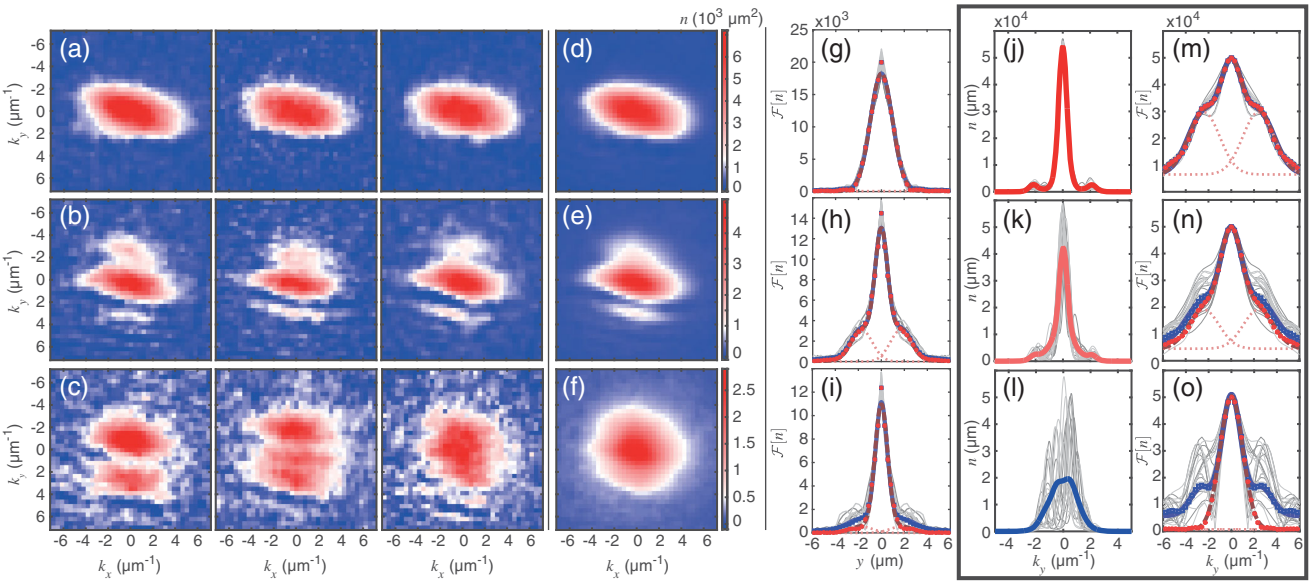

FIG. 2. Coherence in the interference patterns: measurement and toy model. (a)–(c) Examples of single TOF absorption images at $t_h = 5$ ms for ^{166}Er at $a_s = \{54.7(2), 53.8(2), 53.3(2)\}a_0$, respectively. Corresponding average pictures for 100 images obtained under the same experimental conditions (d)–(f) and their Fourier transform (FT) profiles (g)–(i). The gray lines show the FT norm $|\mathcal{F}[n](y)|$ of the individual profiles. The averages, $n_{\mathcal{M}}$ (blue squares) and n_Φ (red dots), are fitted to three-Gaussian functions (blue solid line and brown dashed line, respectively). The dotted lines show the components of the total fitted function corresponding to the two side peaks in n_Φ. (j)–(l) Interference patterns from the toy-model realizations with 100 independent draws using $N_D = 4$, $d = 2.8$ μm, $\sigma_y = 0.56$ μm (see text) and for different ϕ_i distributions: (j) $\phi_i = 0$, (k) ϕ_i normally distributed around 0 with 0.2π standard deviation, (l) ϕ_i uniformly distributed between 0 and 2π. (m)–(o) Corresponding FT profiles for the toy model, same color code as (g)–(i).

pictures, obtained from many repeated images taken under the same experimental conditions, reveals the presence of phase coherence across the sample [56].

Figure 2 exemplifies snapshots of the TOF distributions for Er, measured at three different a_s values; see Figs. 2(a)–2(c). Even if very close in scattering length, the recorded $n(k_x, k_y)$ shows a dramatic change in behavior. For $a_s = 54.7(2)a_0$, we observe a nonmodulated distribution with a density profile characteristic of a dilute BEC. When lowering a_s to $53.8(2)a_0$, we observe the appearance of an interference pattern in the density distribution, consisting of a high central peak and two almost symmetric low-density side peaks [57]. Remarkably, the observed pattern is very reproducible with a high shot-to-shot stability, as shown in the repeated single snapshots and in the average image [Figs. 2(b) and 2(e)]. This behavior indicates a coexistence of density modulation and global phase coherence in the *in situ* state, as expected in the supersolid phase. This observation is consistent with our previous quench experiments [18] and with the recent ^{162}Dy experiments [35,36]. When further lowering a_s to $53.3(2)a_0$, complicated patterns develop with fringes varying from shot to shot in number, position, and amplitude, signaling the persistence of *in situ* density modulation. However, the interference pattern is completely washed out in the averaged density profiles [Fig. 2(f)], pointing to the absence of a global phase coherence. We identify this behavior as the one of ID states.

Toy model—To get an intuitive understanding of the interplay between density modulation and phase coherence and to estimate the role of the different sources of fluctuations in our experiment, we here develop a simple toy model, which is inspired by Ref. [56]; see also Ref. [40]. In our model, the initial state is an array of N_D droplets containing in total N atoms. Each droplet is described by a one-dimensional Gaussian wave function $\psi_i(y)$ of amplitude α_i, phase ϕ_i, width σ_i, and center y_i. To account for fluctuations in the experiments, we allow α_i, $d_i = y_i - y_{i-1}$, and σ_i to vary by 10% around their expectation values. The spread of the phases ϕ_i among the droplets is treated specially as it controls the global phase coherence of the array. By fixing $\phi_i = 0$ for each droplet or by setting a random distribution of ϕ_i, we range from full phase coherence to the incoherent cases. Therefore, the degree of phase incoherence can be varied by changing the standard deviation of the distribution of ϕ_i.

To mimic our experiment, we compute the free evolution of each individual ψ_i over 30 ms, and then compute the axial distribution $n(y,t) = |\sum_i \psi_i(y,t)|^2$, from which we extract the momentum distribution $n(k_y)$, also accounting for the finite imaging resolution [40]. For each computation run, we randomly draw N_D values for ϕ_i, as well as of σ_i, d_i, and α_i, and extract $n(k_y)$. We then collect a set of $n(k_y)$

by drawing these values multiple times using the same statistical parameters and compute the expectation value, $\langle n(k_y)\rangle$; see Figs. 2(j)–2(l). The angled brackets denote the ensemble average.

The results of our toy model show large similarity with the observed behavior in the experiment. In particular, while for each single realization one can clearly distinguish multipeak structures regardless of the degree of phase coherence between the droplets, the visibility of the interference pattern in the averaged $n(k_y)$ survives only if the standard deviation of the phase fluctuations between droplets is small (roughly, below 0.3π). In the incoherent case, we note that the shape of the patterns strongly varies from shot to shot. Interestingly, the toy model also shows that the visibility of the coherent peaks in the average images is robust against the typical shot-to-shot fluctuations in droplet size, amplitude, and distance that occur in the experiments; see Figs. 2(j) and 2(k).

Probing density modulation and phase coherence.—To separate and quantify the information on the *in situ* density modulation and its phase coherence, we analyze the measured interference patterns in Fourier space [36,58–60]. Here, we extract two distinct averaged density profiles, $n_{\mathcal{M}}$ and n_{Φ}. Their structures at finite y spatial frequency (i.e., in Fourier space) quantify the two abovementioned properties.

More precisely, we perform a Fourier transform (FT) of the integrated momentum distributions $n(k_y)$ denoted $\mathcal{F}[n](y)$. Generally speaking, modulations in $n(k_y)$ induce peaks at finite spatial frequency, $y = y^*$, in the FT norm, $|\mathcal{F}[n](y)|$; see Figs. 2(g)–2(i) and 2(m)–2(o). Following the above discussion (see also Refs. [56,61]), such peaks in an individual realization hence reveal a density modulation of the corresponding *in situ* state, with a wavelength roughly equal to y^*. Consequently, we consider the average of the FT norm of the individual images, $n_{\mathcal{M}}(y) = \langle|\mathcal{F}[n](y)|\rangle$, as the first profile of interest. The peaks of $n_{\mathcal{M}}$ at finite y then indicate the mere existence of an *in situ* density modulation of roughly constant spacing within the different realizations. As the second profile of interest, we use the FT norm of the average profile $\langle n(k_y)\rangle$, $n_{\Phi}(y) = |\mathcal{F}[\langle n\rangle](y)|$. Connecting to our previous discussion, the peaks of n_{Φ} at finite y point to the persistence of a modulation in the average $\langle n(k_y)\rangle$, which we identified as a hallmark for a global phase coherence within the density-modulated state. In particular, we point out that a perfect phase coherence, implying identical interference patterns in all the individual realizations, yields $n_{\mathcal{M}} = n_{\Phi}$ and, thus, identical peaks at finite y in both profiles. We note that, by linearity, n_{Φ} also matches the norm of the average of the full FT of the individual images, i.e., $n_{\Phi}(y) = |\langle\mathcal{F}[n](y)\rangle|$; see also Ref. [40].

Figures 2(g)–2(i) and 2(m)–2(o) demonstrate the significance of our FT analysis scheme by applying it to the momentum distributions from the experiment [Figs. 2(d)–2(f)] and the momentum distributions from the toy model [Figs. 2(j)–2(l)], respectively. As expected, for the BEC case, both $n_{\mathcal{M}}$ and n_{Φ} show a single peak at zero spatial frequency, $y = 0$, characterizing the absence of density modulation, Fig. 2(g). In the case of phase-coherent droplets, Fig. 2(e), we observe that $n_{\mathcal{M}}$ and n_{Φ} are superimposed and both show two symmetric side peaks at finite y, in addition to a dominant peak at $y = 0$; see Fig. 2(h). In the incoherent droplet case, we find that, while $n_{\mathcal{M}}$ still shows side peaks at finite y, the ones in n_{Φ} wash out from the averaging, Figs. 2(f), 2(i), 2(l), and 2(o). For both coherent and incoherent droplet arrays, the toy-model results show behaviors matching the above description, providing a further justification of our FT analysis scheme; see Figs. 2(j)–2(o). Our toy model additionally proves two interesting features. First, it shows that the equality $n_{\mathcal{M}} = n_{\Phi}$, revealing the global phase coherence of a density-modulated state, is remarkably robust to noise in the structure of the droplet arrays; see Figs. 2(j) and 2(m). Second, our toy model, however, shows that phase fluctuations across the droplet array on the order of 0.2π standard deviation are already sufficient to make n_{Φ} and $n_{\mathcal{M}}$ deviate from each other; see Figs. 2(k) and 2(n). The incoherent behavior is also associated with strong variations in the side peak amplitude of the individual realizations of $|\mathcal{F}[n]|$, connecting, e.g., to the observations of Ref. [36].

Finally, to quantify the density modulation and the phase coherence, we fit a three-Gaussian function to both $n_{\mathcal{M}}(y)$ and $n_{\Phi}(y)$ and extract the amplitudes of the finite-spatial-frequency peaks, $A_{\mathcal{M}}$ and A_{Φ}, for both distributions, respectively. Note that for a BEC, which is a phase-coherent state, A_{Φ} will be zero since it probes only finite-spatial-frequency peaks; see Figs. 2(g)–2(i) and 2(m)–2(o).

V. CHARACTERIZATION OF THE SUPERSOLID STATE

We are now in the position to study two key aspects, namely, (i) the evolution of the density modulation and phase coherence across the BEC-supersolid-ID phases and (ii) the lifetime of the coherent density-modulated state in the supersolid regime.

Evolution of the supersolid properties across the phase diagram.—The first type of investigation is conducted with ^{166}Er since, contrary to ^{164}Dy, its scattering length and dependence on the magnetic field has been precisely characterized [18,22]. After preparing the sample, we ramp a_s to the desired value and study the density patterns as well as their phase coherence by probing the amplitudes $A_{\mathcal{M}}$ and A_{Φ} as a function of a_s after $t_h = 5$ ms. As shown in Fig. 3(a), in the BEC region (i.e., for large a_s), we observe that both $A_{\mathcal{M}}$ and A_{Φ} are almost zero, evidencing the expected absence of a density modulation in the system. As soon as a_s reaches a critical value a_s^*, the system's behavior dramatically changes with a sharp and simultaneous

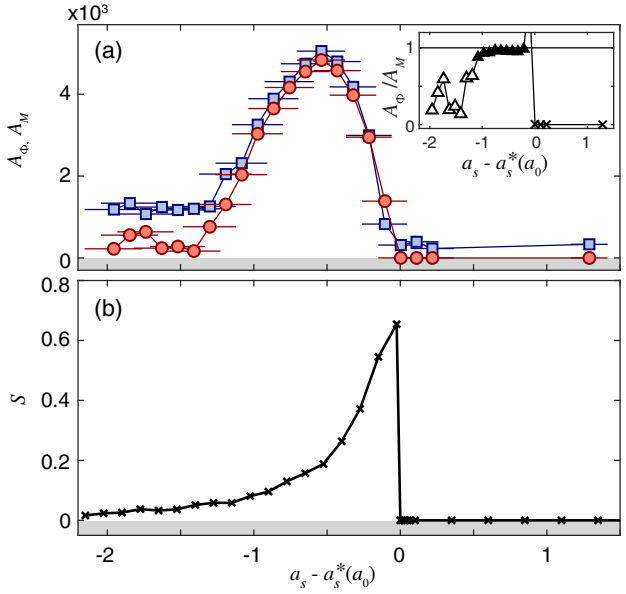

FIG. 3. Supersolid behavior across the phase diagram. Measured side peak amplitudes, A_Φ (circles) and $A_\mathcal{M}$ (squares), with their ratio in inset (a), and calculated link strength S (b) as a function of $a_s - a_s^*$ for ^{166}Er. For nonmodulated states, we set $S = 0$ in theory and $A_\Phi/A_\mathcal{M} = 0$ in experiment (crosses in inset). In the inset, open and closed symbols correspond to $A_\Phi/A_\mathcal{M} > 0.8$ and ≤ 0.8, respectively. In the experiments, we probe the system at a fixed $t_h = 5$ ms. Horizontal error bars are derived from our experimental uncertainty in B, vertical error bars corresponding to the statistical uncertainty from the fit are smaller than the data points. The measured and calculated critical scattering lengths are $a_s^* = 54.9(2)a_0$ and $51.15a_0$, respectively [62]. The numerical results are obtained for the experimental trap frequencies and for a constant $N = 5 \times 10^4$ [63].

increase of both $A_\mathcal{M}$ and A_Φ. While the strength of $A_\mathcal{M}$ and A_Φ varies with decreasing a_s—first increasing then decreasing—we observe that their ratio $A_\Phi/A_\mathcal{M}$ remains constant and close to unity over a narrow a_s range below a_s^* of $\gtrsim 1a_0$ width; see the inset of Fig. 3(a). This behavior pinpoints the coexistence in the system of phase coherence and density modulation, as predicted to occur in the supersolid regime. For $(a_s - a_s^*) < -1a_0$, we observe that the two amplitudes depart from each other. Here, while the density modulation still survives with $A_\mathcal{M}$ saturating to a lower finite value, the global phase coherence is lost with $A_\Phi/A_\mathcal{M} < 1$, as expected in the insulating droplet phase. Note that we also study the evolution of A_Φ and $A_\mathcal{M}$ in ^{164}Dy, but as a function of B, and find a qualitatively similar behavior.

To get a deeper insight on how our observations compare to the phase-diagram predictions (see Fig. 1), we study the link strength S as a function of a_s; see Fig. 3(b). Since S quantifies the density overlap between neighboring droplets and is related to the tunneling rate of atoms across the droplet array, it thus provides information on the ability of the system to establish or maintain a global phase coherence. In this plot, we set $S = 0$ in the case where no modulation is found in the ground state. At the BEC-to-supersolid transition, i.e., at $a_s = a_s^*$, a density modulation abruptly appears in the system's ground state with S taking a finite value. Here, S is maximal, corresponding to a density modulation of minimal amplitude. Below the transition, we observe a progressive decrease of S with lowering a_s, pointing to the gradual reduction of the tunneling rate in the droplet arrays. Close to the transition, we estimate a large tunneling compared to all other relevant timescales. However, we expect this rate to become vanishingly small, on the sub-Hertz level [40], when decreasing a_s 1–$2a_0$ below a_s^*. Our observation also hints at the smooth character of the transition from a supersolid to an ID phase.

The general trend of S, including the extension in a_s where it takes nonvanishing values, is similar to the a_s behavior of $A_\mathcal{M}$ and A_Φ observed in the experiments [62]. We observe in the experiments that the a_s dependence at the BEC-to-supersolid transition appears sharper than at the supersolid-to-ID interface, potentially suggesting a different nature of the two transitions. However, more investigations are needed since atom losses, finite temperature, and finite-size effects can affect, and in particular smoothen, the observed behavior [64–66]. Moreover, dynamical effects, induced by, e.g., excitations created at the crossing of the phase transitions or atom losses during the time evolution, can also play a substantial role in the experimental observations, complicating a direct comparison with the ground-state calculations. The time dynamics as well as a different scheme to achieve a state with supersolid properties is the focus of the remainder of the paper.

Lifetime of the supersolid properties.—Having identified the a_s range in which our dipolar quantum gas exhibits supersolid properties, the next central question concerns the stability and lifetime of such a fascinating state. Recent experiments on ^{162}Dy have shown the transient character of the supersolid properties, whose lifetime is limited by three-body losses [35,36]. In these experiments, the phase coherence is found to survive up to 20 ms after the density modulation has formed. This time corresponds to about half of the weak-trap period. Stability is a key issue in the supersolid regime, especially since the tuning of a_s, used to enter this regime, has a twofold consequence on the inelastic loss rate. First, it gives rise to an increase in the peak density [see Figs. 1(b)–1(d)] and, second, it may lead to an enhancement of the three-body-loss coefficient.

We address this question by conducting comparative studies on ^{166}Er and ^{164}Dy gases. These two species allow us to tackle two substantially different scattering scenarios. Indeed, the background value of a_s for ^{166}Er (as well as for ^{162}Dy) is larger than a_{dd}. Thus, reaching the supersolid regime, which occurs at $a_{dd}/a_s \approx 1.2$–1.4 in our geometry, requires us to tune B close to the pole of a FR. This tuning

also causes an increase of the three-body-loss rate. In contrast, ^{164}Dy realizes the opposite case with the background scattering length smaller than a_{dd}. This feature brings the important advantage of requiring tuning B away from the FR pole to reach the supersolid regime. As we describe below, this important difference in scattering properties leads to a strikingly longer lifetime of the ^{164}Dy supersolid properties with respect to ^{166}Er and to the recently observed behavior in ^{162}Dy [35,36].

The measurements proceed as follows. For both ^{166}Er and ^{164}Dy, we first prepare the quantum gas in the stable BEC regime and then ramp a_s to a fixed value in the supersolid regime for which the system exhibits a state of coherent droplets (i.e., $A_\Phi/A_\mathcal{M} \approx 1$); see previous discussion. Finally, we record the TOF images after a variable t_h and we extract the time evolution of both A_Φ and $A_\mathcal{M}$. The study of these two amplitudes will allow us to answer the question of whether the droplet structure—i.e., the density modulation in space—persists in time whereas the coherence among droplets is lost ($A_\mathcal{M} > A_\Phi \to 0$) or if the density structures themselves vanish in time ($A_\mathcal{M} \approx A_\Phi \to 0$).

As shown in Fig. 4, for both species, we observe that A_Φ and $A_\mathcal{M}$ decay almost synchronously with a remarkably longer lifetime for ^{164}Dy [Fig. 4(b)] than ^{166}Er [Fig. 4(a)].

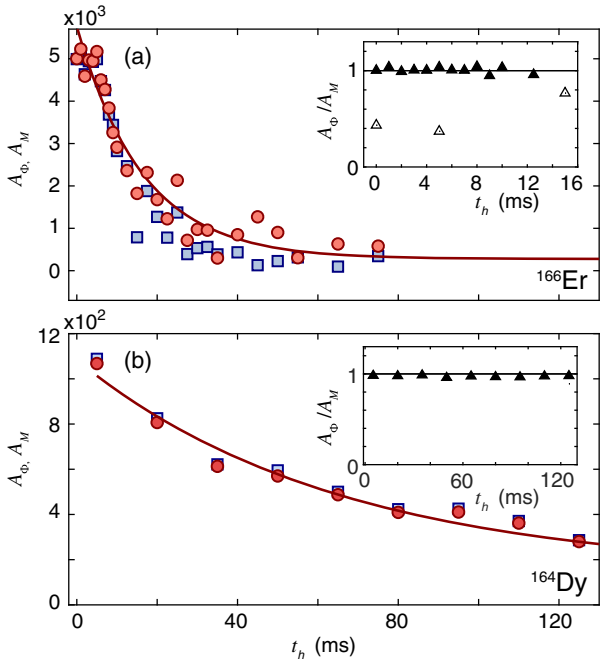

FIG. 4. Time evolution of the supersolid properties. Amplitudes A_Φ (circles) and $A_\mathcal{M}$ (squares) in the supersolid regime as a function of the holding time in trap for (a) ^{166}Er at $54.2(2)a_0$ and for (b) ^{164}Dy at 2.04 G. The solid lines are exponential fits to the data. The insets show the time evolution of $A_\Phi/A_\mathcal{M}$ for the above cases (filled triangles), and, for comparison, in the ID regime (empty triangles) for Er at $a_s = 53.1(2)a_0$ (a).

Interestingly, A_Φ and $A_\mathcal{M}$ remain approximately equal during the whole time dynamics; see insets of Figs. 4(a) and 4(b). This behavior indicates that it is the strength of the density modulation itself and not the phase coherence among droplets that decays over time. Similar results have been found theoretically in Ref. [67]. We connect this decay mainly to three-body losses, especially detrimental for ^{166}Er, and possible excitations created while crossing the BEC-to-supersolid phase transition [40]. For comparison, the inset of Fig. 4(a) shows also the behavior in the ID regime for ^{166}Er, where $A_\Phi/A_\mathcal{M} < 1$ already at short t_h and remains so during the time evolution [40].

To get a quantitative estimate of the survival time of the phase-coherent and density-modulated state, we fit a simple exponential function to A_Φ and extract t_Φ, defined as the 1/10 lifetime; see Fig. 4. For ^{166}Er, we extract $t_\Phi = 38(6)$ ms. For $t_h > t_\Phi$, the interference patterns become undetectable in our experiment and we recover a signal similar to the one of a nonmodulated BEC state [as in Figs. 2(a) and 2(d)]. These results are consistent with recent observations of transient supersolid properties in ^{162}Dy [35]. For ^{164}Dy, we observe that the coherent density-modulated state is remarkably long-lived. Here, we find $t_\Phi = 152(13)$ ms.

The striking difference in the lifetime and robustness of the supersolid properties between ^{166}Er and ^{164}Dy becomes even more visible when studying t_Φ as a function of a_s (B for Dy). As shown in Fig. 5, t_Φ for Er remains comparatively low in the investigated supersolid regime and slightly varies between 20 and 40 ms. Similarly to the recent studies with ^{162}Dy, this finding reveals the transient character of the state and opens the question of whether a stationary supersolid state can be reached with these species. On the contrary, for ^{164}Dy we observe that t_Φ first increases with B in the range from 1.8 G to about 1.98 G. Then, for $B > 1.98$ G, t_Φ acquires a remarkably large and almost constant value of about 150 ms over a wide B range. This shows the long-lived character of the supersolid properties in our ^{164}Dy quantum gas. We note that over the investigated range, a_s is expected to monotonously increase with B [40]. Such a large value of t_Φ exceeds not only the estimated tunneling time across neighboring droplets but also the weak-axis trap period, which together set the typical timescale to achieve global equilibrium and to study collective excitations.

VI. CREATION OF STATES WITH SUPERSOLID PROPERTIES BY EVAPORATIVE COOLING

The long-lived supersolid properties in ^{164}Dy motivate us to explore an alternative route to cross the supersolid phase transition, namely, by evaporative cooling instead of interaction tuning. For this set of experiments, we have modified the waists of our trapping beams in order to achieve quantum degeneracy in tighter traps with respect to

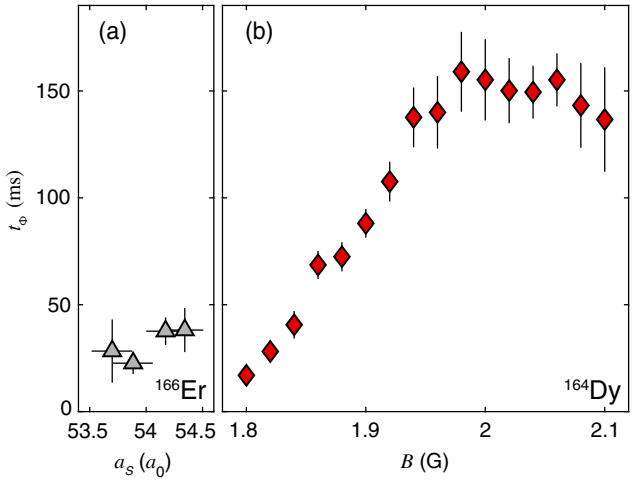

FIG. 5. Survival time of the coherent density-modulated state. t_Φ in ^{166}Er as a function of a_s (a) and ^{164}Dy as a function of B (b). The error bars refer to the statistical uncertainty from the fit. The range of investigation corresponds to the supersolid regime for which phase-coherent density-modulated states are observed. This range is particularly narrow for ^{166}Er.

the one used for condensation in the previous set of measurements. In this way, the interference peaks in the supersolid region are already visible without the need to apply a further compression of the trap since the side-to-central-peak distance in the momentum distribution scales roughly as $1/\ell_z$ [18]. Forced evaporative cooling is performed by reducing the power of the trapping beams piecewise linearly in subsequent evaporation steps until a final trap with frequencies $2\pi \times (225, 37, 134)$ Hz is achieved. During the whole evaporation process, which has an overall duration of about 3 s, the magnetic field is kept either at $B = 2.43$ G, where we observe long-lived interference patterns, or at $B = 2.55$ G, where we produce a stable nonmodulated BEC. We note that these two B values are very close without any FR lying in between [40].

Figure 6 shows the phase transition from a thermal cloud to a final state with supersolid properties by evaporative cooling. In particular, we study the phase transition by varying the duration of the last evaporation ramp, while maintaining the initial and final trap-beam power fixed. This procedure effectively changes the atom number and temperature in the final trap while keeping the trap parameters unchanged, which is important to not alter the final ground-state phase diagram of the system. At the end of the evaporation, we let the system equilibrate and thermalize for $t_h = 100$ ms, after which we switch off the trap, let the atoms expand for 26.5 ms, and finally perform absorption imaging. We record the TOF images for different ramp durations, i.e., for different thermalization times. For a short ramp, too many atoms are lost such that the critical atom number for condensation is not reached, and the atomic distribution remains thermal; see Fig. 6(a).

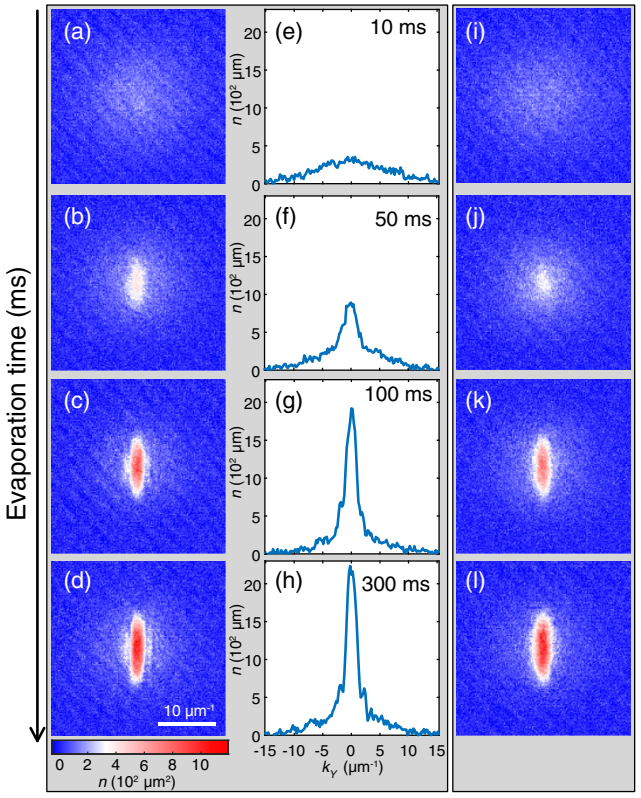

FIG. 6. Evaporative cooling to a state with supersolid properties. ^{164}Dy absorption images showing the transition to a state with supersolid properties at 2.43 G (a)–(d) and to a BEC state at 2.55 G (i)–(l), via different durations of the last evaporation step. These durations are 10 ms (a),(i), 50 ms (b),(j), 100 ms (c),(k), and 300 ms (d),(l). The density profiles (e)–(h) are integrated over the central regions of the corresponding absorption images (a)–(d). The color map indicates the atomic density in momentum space.

By increasing the ramp time, the evaporative cooling becomes more efficient and we observe the appearance of a bimodal density profile with a narrow and dense peak at the center, which we identify as a regular BEC; see Fig. 6(b). By further cooling, the BEC fraction increases and the characteristic pattern of the supersolid state emerges; see Figs. 6(c) and 6(d). The observed evaporation process shows a strikingly different behavior in comparison with the corresponding situation at $B = 2.55$ G, where the usual thermal-to-BEC phase transition is observed; see Figs. 6(i)–6(l).

We finally probe the lifetime of the supersolid properties by extracting the time evolution of both the amplitudes A_Φ and $A_\mathcal{M}$, as previously discussed. We use the same experimental sequence as the one in Fig. 6(d)—i.e., 300-ms duration of the last evaporation ramp and 100 ms of equilibration time—and subsequently hold the sample in the trap for a variable t_h. As shown in Fig. 7(a), we observe a very long lifetime with both amplitudes staying large and almost constant over more than 200 ms. At longer holding

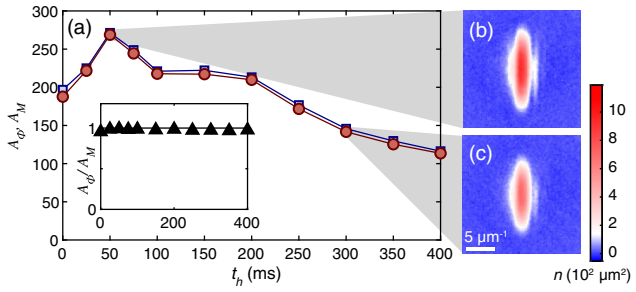

FIG. 7. Lifetime of the supersolid properties achieved via evaporative cooling. Time evolution of the amplitudes A_Φ (red circle) and $A_\mathcal{M}$ (square) after an evaporation time of 300 ms at 2.43 G and an equilibration time of 100 ms. The inset shows the time evolution of $A_\Phi/A_\mathcal{M}$. At $t_h = 0$ ms, the atom number in the phase-coherent density-modulated component is $N = 2.2(2) \times 10^4$. (b),(c) Averaged absorption images of 25 realizations after 50 and 300 ms of holding time, respectively. Note that the thermal background has been subtracted from the images. The color map indicates the atomic density in momentum space.

time, we observe a slow decay of A_Φ and $A_\mathcal{M}$, following the decay of the atom number. Moreover, during the dynamics, the ratio $A_\Phi/A_\mathcal{M}$ stays constant. The long lifetime of the phase-coherent density modulation is also directly visible in the persistence of the interference patterns in the averaged momentum density profiles [similar to Fig. 2(e)], both at intermediate and long times; see Figs. 7(b) and 7(c), respectively. For even longer t_h, we cannot resolve anymore interference patterns in the TOF images. Here, we recover a signal consistent with a regular BEC of low N.

Achieving the coherent droplet phase via evaporative cooling is a very powerful alternative path to supersolidity. We speculate that, for instance, excitations, which might be important when crossing the phase transitions by interaction tuning, may be small or removed by evaporation when reaching this state kinematically. Other interesting questions, open to future investigations, are the nature of the phase transition, the critical atom number, and the role of noncondensed atoms.

VII. CONCLUSIONS

For both ^{166}Er and ^{164}Dy dipolar quantum gases, we have identified and studied states showing hallmarks of supersolidity, namely, global phase coherence and spontaneous density modulations. These states exist in a narrow scattering-length region, lying between a regular BEC phase and a phase of an insulating droplet array. While for ^{166}Er, similarly to the recently reported ^{162}Dy case [35,36], the observed supersolid properties fade out over a comparatively short time because of atom losses, we find that ^{164}Dy exhibits remarkably long-lived supersolid properties. Moreover, we are able to directly create stationary states with supersolid properties by evaporative cooling, demonstrating a powerful alternative approach to interaction tuning on a BEC. This novel technique provides prospects of creating states with supersolid properties while avoiding additional excitations and dynamics. The ability to produce long-lived supersolid states paves the way for future investigations on quantum fluctuations and many-body correlations, as well as of collective excitations in such an intriguing many-body quantum state. A central goal of these future investigations lies in proving the superfluid character of this phase, beyond its global phase coherence [7,34,68–70].

ACKNOWLEDGMENTS

We thank R. Bisset, B. Blakie, M. Boninsegni, G. Modugno, T. Pfau, and, in particular, L. Santos for many stimulating discussions. Part of the computational results presented have been achieved using the HPC infrastructure LEO of the University of Innsbruck. We acknowledge support by the Austrian Science Fund FWF through the DFG/FWF Forschergruppe (FOR 2247/PI2790), by the ERC Consolidator Grant (RARE, No. 681432), and by a NFRI Grant (MIRARE, No. ÖAW0600) from the Austrian Academy of Science. G. D. and M. S. acknowledge support by the Austrian Science Fund FWF within the DK-ALM (No. W1259-N27).

Note added.—Recently, we became aware of related works reporting theoretical studies of the ground-state phase diagram [71,72].

[1] A. F. Andreev and I. M. Lifshitz, *Many-Body Problem in Quantum Mechanics and Quantum Statistical Mechanics*, Sov. Phys. JETP **29**, 1107 (1969).
[2] G. V. Chester, *Speculations on Bose-Einstein Condensation and Quantum Crystals*, Phys. Rev. A **2**, 256 (1970).
[3] A. J. Leggett, *Can a Solid Be "Superfluid"?*, Phys. Rev. Lett. **25**, 1543 (1970).
[4] D. A. Kirzhnits and Y. A. Nepomnyashchii, *Coherent Crystallization of Quantum Liquid*, Sov. Phys. JETP **32**, 1191 (1971).
[5] T. Schneider and C. P. Enz, *Theory of the Superfluid-Solid Transition of* ^{4}He, Phys. Rev. Lett. **27**, 1186 (1971).
[6] S. Balibar, *The Enigma of Supersolidity*, Nature (London) **464**, 176 (2010).
[7] M. Boninsegni and N. V. Prokof'ev, *Colloquium: Supersolids: What and Where Are They?*, Rev. Mod. Phys. **84**, 759 (2012).
[8] Z.-K. Lu, Y. Li, D. S. Petrov, and G. V. Shlyapnikov, *Stable Dilute Supersolid of Two-Dimensional Dipolar Bosons*, Phys. Rev. Lett. **115**, 075303 (2015).
[9] N. Henkel, R. Nath, and T. Pohl, *Three-Dimensional Roton Excitations and Supersolid Formation in Rydberg-Excited Bose-Einstein Condensates*, Phys. Rev. Lett. **104**, 195302 (2010).

[10] F. Cinti, P. Jain, M. Boninsegni, A. Micheli, P. Zoller, and G. Pupillo, *Supersolid Droplet Crystal in a Dipole-Blockaded Gas*, Phys. Rev. Lett. **105**, 135301 (2010).

[11] M. Boninsegni, *Supersolid Phases of Cold Atom Assemblies*, J. Low Temp. Phys. **168**, 137 (2012).

[12] J. Léonard, A. Morales, P. Zupancic, T. Esslinger, and T. Donner, *Supersolid Formation in a Quantum Gas Breaking a Continuous Translational Symmetry*, Nature (London) **543**, 87 (2017).

[13] J.-R. Li, J. Lee, W. Huang, S. Burchesky, B. Shteynas, F. Ç. Top, A. O. Jamison, and W. Ketterle, *A Stripe Phase with Supersolid Properties in Spin–Orbit-Coupled Bose–Einstein Condensates*, Nature (London) **543**, 91 (2017).

[14] L. D. Landau, *The Theory of Superfluidity of Helium II*, J. Phys. (Moscow) **5**, 71 (1941).

[15] P. Nozières, *Is the Roton in Superfluid* ^{4}He *the Ghost of a Bragg Spot?*, J. Low Temp. Phys. **137**, 45 (2004).

[16] D. H. J. O'Dell, S. Giovanazzi, and G. Kurizki, *Rotons in Gaseous Bose-Einstein Condensates Irradiated by a Laser*, Phys. Rev. Lett. **90**, 110402 (2003).

[17] L. Santos, G. V. Shlyapnikov, and M. Lewenstein, *Roton-Maxon Spectrum and Stability of Trapped Dipolar Bose-Einstein Condensates*, Phys. Rev. Lett. **90**, 250403 (2003).

[18] L. Chomaz, R. M. W. van Bijnen, D. Petter, G. Faraoni, S. Baier, J. H. Becher, M. J. Mark, F. Wächtler, L. Santos, and F. Ferlaino, *Observation of Roton Mode Population in a Dipolar Quantum Gas*, Nat. Phys. **14**, 442 (2018).

[19] D. Petter, G. Natale, R. M. W. van Bijnen, A. Patscheider, M. J. Mark, L. Chomaz, and F. Ferlaino, *Probing the Roton Excitation Spectrum of a Stable Dipolar Bose Gas*, arXiv:1811.12115.

[20] H. Kadau, M. Schmitt, M. Wenzel, C. Wink, T. Maier, I. Ferrier-Barbut, and T. Pfau, *Observing the Rosensweig Instability of a Quantum Ferrofluid*, Nature (London) **530**, 194 (2016).

[21] I. Ferrier-Barbut, H. Kadau, M. Schmitt, M. Wenzel, and T. Pfau, *Observation of Quantum Droplets in a Strongly Dipolar Bose Gas*, Phys. Rev. Lett. **116**, 215301 (2016).

[22] L. Chomaz, S. Baier, D. Petter, M. J. Mark, F. Wächtler, L. Santos, and F. Ferlaino, *Quantum-Fluctuation-Driven Crossover from a Dilute Bose-Einstein Condensate to a Macrodroplet in a Dipolar Quantum Fluid*, Phys. Rev. X **6**, 041039 (2016).

[23] F. Wächtler and L. Santos, *Quantum Filaments in Dipolar Bose-Einstein Condensates*, Phys. Rev. A **93**, 061603(R) (2016).

[24] F. Wächtler and L. Santos, *Ground-State Properties and Elementary Excitations of Quantum Droplets in Dipolar Bose-Einstein Condensates*, Phys. Rev. A **94**, 043618 (2016).

[25] M. Schmitt, M. Wenzel, F. Böttcher, I. Ferrier-Barbut, and T. Pfau, *Self-Bound Droplets of a Dilute Magnetic Quantum Liquid*, Nature (London) **539**, 259 (2016).

[26] I. Ferrier-Barbut, M. Wenzel, M. Schmitt, F. Böttcher, and T. Pfau, *Onset of a Modulational Instability in Trapped Dipolar Bose-Einstein Condensates*, Phys. Rev. A **97**, 011604(R) (2018).

[27] R. N. Bisset, R. M. Wilson, D. Baillie, and P. B. Blakie, *Ground-State Phase Diagram of a Dipolar Condensate with Quantum Fluctuations*, Phys. Rev. A **94**, 033619 (2016).

[28] M. Wenzel, F. Böttcher, T. Langen, I. Ferrier-Barbut, and T. Pfau, *Striped States in a Many-Body System of Tilted Dipoles*, Phys. Rev. A **96**, 053630 (2017).

[29] D. Baillie and P. B. Blakie, *Droplet Crystal Ground States of a Dipolar Bose Gas*, Phys. Rev. Lett. **121**, 195301 (2018).

[30] D. S. Petrov, *Quantum Mechanical Stabilization of a Collapsing Bose-Bose Mixture*, Phys. Rev. Lett. **115**, 155302 (2015).

[31] C. R. Cabrera, L. Tanzi, J. Sanz, B. Naylor, P. Thomas, P. Cheiney, and L. Tarruell, *Quantum Liquid Droplets in a Mixture of Bose-Einstein Condensates*, Science **359**, 301 (2018).

[32] G. Semeghini, G. Ferioli, L. Masi, C. Mazzinghi, L. Wolswijk, F. Minardi, M. Modugno, G. Modugno, M. Inguscio, and M. Fattori, *Self-Bound Quantum Droplets of Atomic Mixtures in Free Space*, Phys. Rev. Lett. **120**, 235301 (2018).

[33] P. Cheiney, C. R. Cabrera, J. Sanz, B. Naylor, L. Tanzi, and L. Tarruell, *Bright Soliton to Quantum Droplet Transition in a Mixture of Bose-Einstein Condensates*, Phys. Rev. Lett. **120**, 135301 (2018).

[34] S. M. Roccuzzo and F. Ancilotto, *Supersolid Behaviour of a Dipolar Bose-Einstein Condensate Confined in a Tube*, Phys. Rev. A **99**, 041601(R) (2019).

[35] L. Tanzi, E. Lucioni, F. Fama, J. Catani, A. Fioretti, C. Gabbanini, R. N. Bisset, L. Santos, and G. Modugno, *Observation of a Dipolar Quantum Gas with Metastable Supersolid Properties*, Phys. Rev. Lett. **122**, 130405 (2019).

[36] F. Böttcher, J.-N. Schmidt, M. Wenzel, J. Hertkorn, M. Guo, T. Langen, and T. Pfau, *Transient Supersolid Properties in an Array of Dipolar Quantum Droplets*, Phys. Rev. X **9**, 011051 (2019).

[37] K. Aikawa, A. Frisch, M. Mark, S. Baier, A. Rietzler, R. Grimm, and F. Ferlaino, *Bose-Einstein Condensation of Erbium*, Phys. Rev. Lett. **108**, 210401 (2012).

[38] A. Trautmann, P. Ilzhöfer, G. Durastante, C. Politi, M. Sohmen, M. J. Mark, and F. Ferlaino, *Dipolar Quantum Mixtures of Erbium and Dysprosium Atoms*, Phys. Rev. Lett. **121**, 213601 (2018).

[39] S. Baier, M. J. Mark, D. Petter, K. Aikawa, L. Chomaz, Z. Cai, M. Baranov, P. Zoller, and F. Ferlaino, *Extended Bose-Hubbard Models with Ultracold Magnetic Atoms*, Science **352**, 201 (2016).

[40] See Supplemental Material at http://link.aps.org/supplemental/10.1103/PhysRevX.9.021012 for details on the experimental setup, measurement schemes, analysis, and theory calculations.

[41] I. Ferrier-Barbut, M. Wenzel, F. Böttcher, T. Langen, M. Isoard, S. Stringari, and T. Pfau, *Scissors Mode of Dipolar Quantum Droplets of Dysprosium Atoms*, Phys. Rev. Lett. **120**, 160402 (2018).

[42] A. Gammal, T. Frederico, L. Tomio, and P. Chomaz, *Atomic Bose-Einstein Condensation with Three-Body Interactions and Collective Excitations*, J. Phys. B **33**, 4053 (2000).

[43] A. Bulgac, *Dilute Quantum Droplets*, Phys. Rev. Lett. **89**, 050402 (2002).

[44] D. S. Petrov, *Quantum Mechanical Stabilization of a Collapsing Bose-Bose Mixture*, Phys. Rev. Lett. **115**, 155302 (2015).

[45] F. Wächtler and L. Santos, *Ground-State Properties and Elementary Excitations of Quantum Droplets in Dipolar Bose-Einstein Condensates*, Phys. Rev. A **94**, 043618 (2016).
[46] M. Wenzel, F. Böttcher, J.-N. Schmidt, M. Eisenmann, T. Langen, T. Pfau, and I. Ferrier-Barbut, *Anisotropic Superfluid Behavior of a Dipolar Bose-Einstein Condensate*, Phys. Rev. Lett. **121**, 030401 (2018).
[47] B. D. Josephson, *Possible New Effects in Superconductive Tunnelling*, Phys. Lett. **1**, 251 (1962).
[48] J. Javanainen, *Oscillatory Exchange of Atoms between Traps Containing Bose Condensates*, Phys. Rev. Lett. **57**, 3164 (1986).
[49] S. Raghavan, A. Smerzi, S. Fantoni, and S. R. Shenoy, *Coherent Oscillations between Two Weakly Coupled Bose-Einstein Condensates: Josephson Effects, π Oscillations, and Macroscopic Quantum Self-Trapping*, Phys. Rev. A **59**, 620 (1999).
[50] A similar behavior is also seen for ^{164}Dy for $N < 4000$ [out of the scale of Fig. 1(g)].
[51] We note that a similar behavior is also found in our ^{166}Er phase diagram but for larger N than the one reported here.
[52] Y. Tang, A. Sykes, N. Q. Burdick, J. L. Bohn, and B. L. Lev, *s-Wave Scattering Lengths of the Strongly Dipolar Bosons ^{162}Dy and ^{164}Dy*, Phys. Rev. A **92**, 022703 (2015).
[53] M. Greiner, O. Mandel, T. Esslinger, T. W. Hänsch, and I. Bloch, *Quantum Phase Transition from a Superfluid to a Mott Insulator in a Gas of Ultracold Atoms*, Nature (London) **415**, 39 (2002).
[54] M. Greiner, I. Bloch, O. Mandel, T. W. Hänsch, and T. Esslinger, *Exploring Phase Coherence in a 2D Lattice of Bose-Einstein Condensates*, Phys. Rev. Lett. **87**, 160405 (2001).
[55] B. Paredes, A. Widera, V. Murg, O. Mandel, S. Fölling, I. Cirac, G. V. Shlyapnikov, T. W. Hänsch, and I. Bloch, *Tonks–Girardeau Gas of Ultracold Atoms in an Optical Lattice*, Nature (London) **429**, 277 (2004).
[56] Z. Hadzibabic, S. Stock, B. Battelier, V. Bretin, and J. Dalibard, *Interference of an Array of Independent Bose-Einstein Condensates*, Phys. Rev. Lett. **93**, 180403 (2004).
[57] In our absorption imaging a residual asymmetry can be observed between $\pm k_y$. This asymmetry, providing a sharper peak at $k_y > 0$, stems from optical aberrations in our imperfect optical setup. These imperfections make the quantitative analysis of our data more challenging, yet they do not affect the quantitative interpretation. In particular, we have checked that the peak structures are also observable along a distinct imaging axis, nonorthogonal to y, using an independent imaging setup.
[58] M. Takeda, H. Ina, and S. Kobayashi, *Fourier-Transform Method of Fringe-Pattern Analysis for Computer-Based Topography and Interferometry*, J. Opt. Soc. Am. **72**, 156 (1982).
[59] C. Kohstall, S. Riedl, E. R. S. Guajardo, L. A. Sidorenkov, J. H. Denschlag, and R. Grimm, *Observation of Interference between Two Molecular Bose–Einstein Condensates*, New J. Phys. **13**, 065027 (2011).
[60] L. Chomaz, L. Corman, T. Bienaimé, R. Desbuquois, C. Weitenberg, S. Nascimbène, J. Beugnon, and J. Dalibard, *Emergence of Coherence via Transverse Condensation in a Uniform Quasi-Two-Dimensional Bose Gas*, Nat. Commun. **6**, 6162 (2015).
[61] S. Hofferberth, I. Lesanovsky, B. Fischer, T. Schumm, and J. Schmiedmayer, *Non-Equilibrium Coherence Dynamics in One-Dimensional Bose Gases*, Nature (London) **449**, 324 (2007).
[62] The values of a_s^* extracted from experiments and from theory disagree by $3.8a_0$. Such a mismatch is similar to the one observed in our previous work on the roton instability [18,19]. This behavior might be related to the possibility that beyond-mean-field effects are not properly accounted for by the conventional LHY correction term; see main text. In addition, other effects, such as the dynamics and the atom losses [40], can affect the experimental observations.
[63] This atom number corresponds to the condensed atom number measured within the stabilization time of a_s [40].
[64] M. E. Fisher and A. E. Ferdinand, *Interfacial, Boundary, and Size Effects at Critical Points*, Phys. Rev. Lett. **19**, 169 (1967).
[65] Y. Imry and D. Bergman, *Critical Points and Scaling Laws for Finite Systems*, Phys. Rev. A **3**, 1416 (1971).
[66] Y. Imry, *Finite-Size Rounding of a First-Order Phase Transition*, Phys. Rev. B **21**, 2042 (1980).
[67] See the theoretical analysis in the revised version of Ref. [35].
[68] V. W. Scarola, E. Demler, and S. D. Sarma, *Searching for a Supersolid in Cold-Atom Optical Lattices*, Phys. Rev. A **73**, 051601(R) (2006).
[69] Z.-K. Lu, Y. Li, D. S. Petrov, and G. V. Shlyapnikov, *Stable Dilute Supersolid of Two-Dimensional Dipolar Bosons*, Phys. Rev. Lett. **115**, 075303 (2015).
[70] F. Cinti and M. Boninsegni, *Classical and Quantum Filaments in the Ground State of Trapped Dipolar Bose Gases*, Phys. Rev. A **96**, 013627 (2017).
[71] Y. Kora and M. Boninsegni, *Patterned Supersolids in Dipolar Bose Systems*, arXiv:1902.08256.
[72] Y.-C. Zhang, F. Maucher, and T. Pohl, *Supersolidity around a Critical Point in Dipolar Bose Einstein Condensates*, arXiv:1903.06161.

Correction: The inadvertent omission of a marker indicating "Featured in Physics" has been fixed.

Supplemental Material: Long-lived and transient supersolid behaviors in dipolar quantum gases

L. Chomaz,[1] D. Petter,[1] P. Ilzhöfer,[2] G. Natale,[1] A. Trautmann,[2] C. Politi,[2] G. Durastante,[1,2]
R. M. W. van Bijnen,[2] A. Patscheider,[1] M. Sohmen,[1,2] M. J. Mark,[1,2] and F. Ferlaino[1,2,*]
[1] *Institut für Experimentalphysik, Universität Innsbruck, Technikerstraße 25, 6020 Innsbruck, Austria*
[2] *Institut für Quantenoptik und Quanteninformation, Österreichische Akademie der Wissenschaften, Technikerstraße 21a, 6020 Innsbruck, Austria*

(Dated: March 27, 2019)

GROUND STATE CALCULATIONS

We perform numerical calculations of the ground state following the procedure detailed in the supplementary information of Ref. [1]. The calculations are based on the conjugate-gradients technique to minimize the energy functional of an eGPE [2]. In particular, the eGPE accounts for the effect of quantum fluctuations, by including the LHY term $\Delta\mu[n] = 32g(na_s)^{3/2}(1+3\epsilon_{dd}^2/2)/3\sqrt{\pi}$ in the system's Hamiltonian (here $g = 4\pi\hbar^2 a_s/m$ and $n = |\psi|^2$ is the spatial density of the macroscopic state ψ). $\Delta\mu[n]$ has been obtained under a local density approximation in Refs. [3, 4]. The relevance of the LHY correction has been demonstrated in various studies of dipolar Bose gases close to the mean-field instability [1, 5–9] as it brings an additional repulsive potential, stabilizing the gas against mean-field collapse at large density. We note that the exact functional form of the potential, originating from beyond mean-field effects, has been questioned by several experimental results in finite-size trapped systems [1, 9–11], calling for further theory developments [12].

Our numerical calculations provide us with the three-dimensional ground-state wavefunctions $\psi(\boldsymbol{r})$. From this, we compute the axial in-situ density profile along the trap's weak axis, $n(y) = \int |\psi(\boldsymbol{r})|^2 dxdz$ and find density profiles, corresponding to the BEC, the supersolid or the ID phase, that we plot in Fig. 1. From the density profiles that exhibit a density modulation, we evaluate S by performing Gaussian fits to each droplet, i. e. to $n(y)$ with y ranging between two neighboring local density minima. From these Gaussian fits, we evaluate the sets of centers $\{y_i^{(0)}\}_i$ and widths $\{\sigma_i\}_i$ corresponding to the macroscopic Gaussian wavefunctions $\{\psi_i\}_i$ associated to the individual droplets in the array. We then approximate the droplet wavefunction via $\psi_i(y) \approx \sqrt{n(y \approx y_i^{(0)})} = \alpha_i \exp\left(-(y-y_i^{(0)})^2/2\sigma_i^2\right)$ with α_i a normalization coefficient such that $\int |\psi_i(y)|^2 dy = 1$. We then evaluate the wavefunction overlap S_i between the neighboring droplets $i-1$ and i via:

$$S_i \equiv \int \psi_{i-1}^*(y)\psi_i(y)dy \tag{1}$$

$$= \sqrt{\frac{2\sigma_i\sigma_{i-1}}{\sigma_i^2+\sigma_{i-1}^2}} \exp\left(-\frac{(y_i^{(0)}-y_{i-1}^{(0)})^2}{2(\sigma_i^2+\sigma_{i-1}^2)}\right). \tag{2}$$

The latter equation is obtained via an analytical evaluation of the Gaussian integral. The characteristic link strength defined in the paper is then computed by averaging S_i over all droplet links in the array: $S = \langle S_i \rangle_i$. In our calculation, we only consider as droplets all density peaks of at least 5 % of the global density maximum.

LINK STRENGTH AND ESTIMATE OF TUNNELING RATE

Generally speaking, the wavefunction overlap between neighboring droplets relates to a tunneling term, which sets a particle exchange term between two neighboring droplets [13–16]. Following the work of Ref. [17], we perform a first estimate of the tunneling coefficient by simply considering the single-particle part of the Hamiltonian and evaluate it between two neighboring droplets. We note that, in our particular setting where the density modulation is not externally imposed but arises from the mere interparticle interactions, the inter-droplet interaction may also play a crucial role. To perform a more precise estimation of the tunneling between droplets, one would certainly need to properly account for this effect. Here, we stress that our approach simply gives a rough idea of the magnitude of tunneling while it does not aim to be a quantitative description of it. This consideration calls for further studies making a systematic analysis of the full Hamiltonian and of the full phase diagram within the Josephson junction formalism and beyond.

Generalizing the description of Ref. [17] to neighboring droplets of different sizes and amplitudes, which are described by a three-dimensional wavefunction $\psi_i(\boldsymbol{r})$ approximated to a three-dimensional Gaussian of widths

$(\sigma_{i,x}, \sigma_{i,y}, \sigma_{i,z})$ with $\sigma_{i,y} = \sigma_i$, our estimate writes:

$$J_i = \frac{\hbar^2 S_i}{2m}\left[\sum_{k=x,y,z}\frac{1+\left(\frac{\sigma_{i,k}\sigma_{i-1,k}}{\ell_k^2}\right)^2}{\sigma_{i,k}^2+\sigma_{i-1,k}^2} + \frac{(y_i^{(0)}-y_{i-1}^{(0)})^2}{2\sigma_i\sigma_{i-1}}\frac{(\sigma_i\sigma_{i-1}/\ell_y)^4-1}{\sigma_i^2+\sigma_{i-1}^2}\right], \quad (3)$$

where $\ell_{x,y,z} = \sqrt{\hbar/m\omega_{x,y,z}}$ are the harmonic oscillator lengths.

In general, the tunnelling coefficients set two typical rates relevant for equilibration processes. The first one is the bare single-particle tunneling rate, which is equal to J_i/h, while the second accounts for the bosonic enhancement from the occupation of the droplet modes and writes $\tilde{t}_i = \sqrt{N_i N_{i-1}}|J_i|/h$ where N_i is the number of atoms in droplet i. In our analysis, we then define the average rates over the droplet arrays as characteristic rates $J/h = \langle J_i\rangle_i/h$, and $\tilde{t} = \langle \tilde{t}_i\rangle_i$; see e.g. [18]. While the ground state evolves from a BEC to a supersolid to an ID, the relevant timescale for achieving (global) equilibrium crosses from being set by the trap frequencies to the above-mentioned tunneling rates.

Using our approximate model, we here give a first estimate of the rates J/h and $\tilde{t}$ as a function of a_s, for the parameters of Fig. 1(b-d) of the main text (i.e. Er quantum gas with $N = 5\times10^4$ atoms). Here we find that, for $a_s = a_s^*$, $J/h \sim 400\,\text{Hz}$ and $\tilde{t} \sim 10\,\text{MHz}$ while for $a_s = a_s^* - 2.5\,a_0$, $J/h \sim 10^{-7}\,\text{Hz}$ and $\tilde{t} \sim 10^{-3}\,\text{Hz}$.

TOY MODEL FOR THE INTERFERENCE PATTERN

As described in the main text we use a simple toy model, adapted from Ref. [18], to identify the main features of the TOF interference patterns obtained from an insitu density-modulated state. As a quick reminder, our model considers a one-dimensional array of N_D Gaussian droplets, described by a single classical field, ψ_i, thus neglecting quantum and thermal fluctuations. We compute the TOF density distribution from the free-expansion of the individual ψ_i during a time t via $n(y,t) = |\sum_i \psi_i(y,t)|^2$. In our calculations, we also account for the finite imaging resolution by convolving the resulting $n(y,t)$ with a gaussian function of width σ_{im}. Here we allow the characteristics of the individual ψ_i to fluctuate. In this aim, we introduce noise on the corresponding parameter with a normal distribution around its expectation value and with a variable standard deviation (only ϕ_i can also have a uniform distribution). We then perform a Monte-Carlo study and perform ensemble averages, similar to our experimental analysis procedure. We note that, in this simple implementation, the noise on the different parameters – droplet amplitudes, widths and distances – are uncorrelated.

In the main text, we present results for a single set of parameters, namely $N_D = 4$, $d \equiv \langle d_i\rangle_i = 2.8\,\mu\text{m}$ (mean droplet distance), $\sigma_y \equiv \langle\sigma_i\rangle_i = 0.56\,\mu\text{m}$ (mean droplet size), $t = 30\,\text{ms}$, and $\sigma_{\text{im}} = 3\,\mu\text{m}$, typical for our experimental Er setting and the corresponding theory expectations in the supersolid regime. $\langle\cdot\rangle_i$ denotes the average over the droplets. In this section, we have a deeper look at the impact of the different parameters on both the TOF signal and our FT analysis. We study both the fully phase coherent and fully incoherent case, and the unchanged parameters are set as in Fig. 2(j,m) and (l,o).

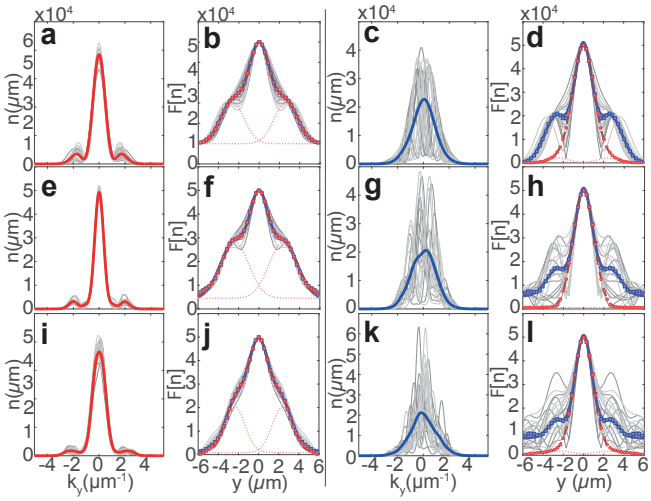

FIG. S1. **Toy model realizations with varying number of droplets** N_D. We use 100 independent draws, and expectation values $d = 2.85\,\mu\text{m}$, $\sigma_y = 0.56\,\mu\text{m}$ (with 10% noise) and either $\phi_i = 0$ (a,b,e,f,i,j), or ϕ_i uniformly distributed between 0 and 2π (c,d,g,h,k,l). (a–d) $N_D = 2$, (e–h) $N_D = 3$ and (i–l) $N_D = 8$. (a,c,e,g,i,k) TOF density profiles and (b,d,f,h,j,l) corresponding FT analysis of the interference patterns, same color code as Fig .2.

In Fig. S1, we first exemplify the TOF and FT profiles for a varying number of droplets, between 2 and 8, which cover the range of relevant N_D over the phase diagram of Fig. 1. The results remain remarkably similar to the realization of Fig. 2 with only slight quantitative changes. The main difference lies in the individual interference patterns obtained in the phase incoherent case. With increasing N_D, those profiles become more complex and made of a larger number of peaks (see (c,g,k)). Yet, in this incoherent case, a similar (non-modulated) profile is recovered in the averaged $n(k_y)$ for all N_D. Additionally, we note that for the coherent case with $N_D = 8$, the side peaks in the FT analysis (see (j)) become less visible. By performing additional tests, we attribute this behavior to the limited TOF duration, t, used in our experiment yielding a typical length scale, $\sqrt{\hbar t/m}$ ($= 3.4\mu\text{m}$), which becomes small compared to the system size ($\approx (N_D-1)d + \sigma_y$) for large N_D. This intermediate regime in the TOF expansion leads to more

complex features, including smaller-sized motifs, in the interference patterns. Finally, when accounting for our imaging resolution, it yields a broadening of the structure observed in the TOF images and less visible peaks in the FT (see (i)). We note that our experiments, because of limited N and additional losses, should rather lie in the regime $2 \leq N_D \leq 5$; see Fig. 1(b).

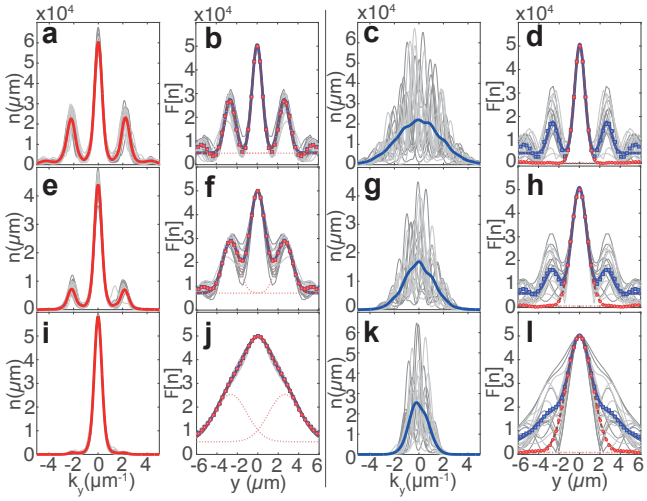

FIG. S2. **Toy model realizations with varying σ_y/d.** We use 100 independent draws, with $N_D = 4$, $d = 2.85\,\mu$m (with 10% noise) and either $\phi_i = 0$ (a,b,e,f,i,j), or ϕ_i uniformly distributed between 0 and 2π (c,d,g,h,k,l). For each realization we also compute the associated mean S. (a–d) $\sigma_y/d = 0.1$, yielding $S = 1.8\times10^{-7}$ (e–h)$\sigma_y/d = 0.15$, matching $S = 1.7\times10^{-4}$ and (i–l) $\sigma_y/d = 0.25$, matching $S = 0.028$. (a,c,e,g,i,k) TOF density profiles and (b,d,f,h,j,l) Corresponding FT analysis of the interference patterns, same color code as Fig. 2.

We then investigate the evolution of the interference patterns and their FT analysis for a varying mean droplet size, σ_y, while keeping their mean distance, d, fixed. This study is particularly relevant recalling that, within the Josephson junction formalism (see main text and corresponding section of this Supplemental Material), the key parameter controlling the tunneling rate between the droplets is set by the ratio σ_y/d, and the link strength parameter that we use to characterize the supersolid regime scales roughly as $\exp(-(d/2\sigma_y)^2)$. Thus, in our experiment, σ_y/d is intrinsically expected to decrease with the scattering length (see Fig. 3). Performing a direct estimate of the average droplet link from the initial state of our toy model, we find $S = 0.004$ for the calculations of Fig. 2(j-o), lying in an expected supersolid regime yet rather close to the supersolid-to-ID transition. Figure S2 investigates the effect of smaller and larger values of σ_y/d (and consequently of S) on the TOF and FT profiles while independently assuming phase coherence or incoherence. Qualitatively, the features remain similar as in Fig. 2(j-o). In the coherent case, side peaks are visible in the individual as well as in the mean $n(k_y)$ (see (a,e,i)) and yield side peaks in the FT profiles, with $n_{\mathcal{M}} \approx n$ (see (b,f,j)). Increasing (decreasing) σ/d mainly results in a stronger (weaker) signal both in the interference pattern and their FT analysis. Within our toy model, we find that, already for $\sigma/d = 0.25$, the signal nearly vanishes; see (i,j). Even if, given the approximations used in our toy model, this exact value may not fully hold for our experimental conditions, we expect a similar trend. It is interesting to keep in mind that this effect may limit our capacity of detecting an underlying supersolid state via matter-wave interference in experiments. In the incoherent case, the effect of decreasing σ_y/d mainly results in a broader shape of the mean density profile, while it remains non-modulated; see (c,g,k). In the FT analysis n_Φ remains structure-less independently of σ_y/d while the structures in $n_{\mathcal{M}}$ becomes sharper with decreasing σ_y/d, as in the coherent case; see (d,h,l).

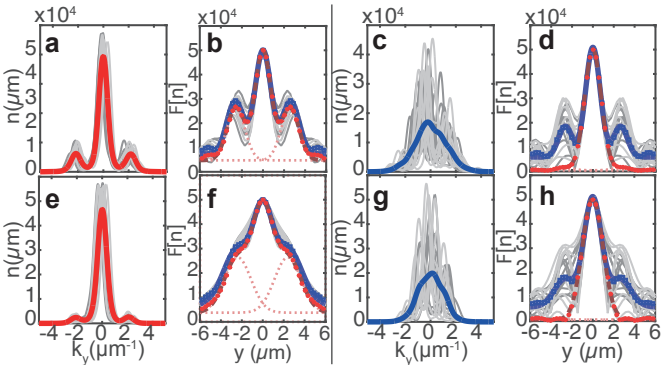

FIG. S3. **Toy model realizations allowing noise in the center position.** We use 100 independent draws, with $N_D = 4$, $d = 2.85\,\mu$m (with 10% noise), $\sigma_y/d = 0.15$ (a–d) or $\sigma_y/d = 0.2$ (e–h), and either $\phi_i = 0$ (a,b,e,f,i,j), or ϕ_i uniformly distributed between 0 and 2π (c,d,g,h,k,l). Center fluctuation are introduced as normal noise around 0 with standard deviation of $2\,\mu\text{m}^{-1}$ in situ (a,c,e,g,i,k) TOF density profiles and (b,d,f,h,j,l) corresponding FT analysis of the interference patterns, same color code as Fig. 2.

Finally, we investigate how a possible shot-to-shot noise on the position of the central interference peak could affect our observables of the density modulation and phase coherence. In the experiments, such fluctuations may occur, for instance, because of beam-pointing fluctuations or excitations of the gas. Although we compensate for such effects by recentering the individual images (see Imaging Analysis section), residual effects may remain, in particular due to center misestimation in the mere presence of the interference patterns of interest. To investigate this aspect, we repeat our toy model calculations now including noise in the global droplet array position and using a standard deviation of $2\,\mu$m for two values of σ_y/d; see Fig.S3. Again, qualitatively the observed features remains similar to our prediction in the main text. The main effect lies in the appearance of a

small discrepancy in the coherent case between n_Φ and $n_\mathcal{M}$, while the structure in the incoherent case remains similar. As the center misestimation should be the most severe in the latter case (due to the variability of the interference patterns observed here), our test shows the robustness of our analysis procedure against this issue.

IMAGING ANALYSIS: ^{164}Dy AND ^{166}Er

The density distributions in momentum space are extracted from the TOF images using the free-expansion expectation. In the Dy case, the thermal component is subtracted from the individual distribution by cutting out the central region of the cloud and performing an isotropic Gaussian fit on the outer region. This subtraction is beneficial because of the large thermal fraction. In the ^{166}Er case, such a subtraction is on the contrary complicated because of the weak thermal component and this pre-treatment may lead to improper estimation of $A_\mathcal{M}$ and A_Φ in the later analysis. The obtained momentum density distributions are then recentered and integrated numerically along $k_z(k_x)$ between $[-2.0, +2.0]\,\mu\mathrm{m}^{-1}$ ($[-1.28, +1.28]\,\mu\mathrm{m}^{-1}$) to obtain $n(k_Y)$ ($n(k_y)$) for ^{164}Dy (^{166}Er). The recentering procedure uses the result a single Gauss fit to the TOF images. The fit is performed after convoluting each image with a Gaussian function of width $0.5\,\mu$m whose purpose is to reduce the impact of the interference pattern on the center estimation [19].

In order to characterise the system's state, we use the Fourier transform, $\mathcal{F}[n](y)$ of the single density profile, $n(k_y)$. We then compute two average profiles, $n_\mathcal{M}$ and n_Φ, relying on ensemble average over all measurements under the same experimental conditions; see below for a detailed discussion on $n_\mathcal{M}$ and n_Φ. In all the measurements reported in this work we use averages over typically 15 to 100 realizations.

To quantify both the existence of a density modulation and global phase coherence on top of this modulation, we fit both $n_\mathcal{M}(y)$ and $n_\Phi(y)$ with a triple-Gaussian function, where one Gaussian accounts for the central peak and the other Gaussians are accounting for the symmetric side peaks. The amplitudes of the latter give $A_\mathcal{M}$ and A_Φ, respectively. The distance between the side peaks and the central one is allowed to vary between $[2.5, 2.7]\,\mu$m ($[2.3, 2.5]\,\mu$m) in the case of ^{164}Dy (^{166}Er).

DETAILS ON THE FOURIER ANALYSIS

In our analysis we rely on two averaged profiles, named $n_\mathcal{M}$ or n_Φ, to quantify both the density modulation and its phase coherence. Here we detail the meaning of the average performed.

The Fourier transform (FT) of the integrated momentum distributions, $n(k_y)$, which reads $\mathcal{F}[n](y) = |\mathcal{F}[n](y)|\exp(i\arg(\mathcal{F}[n](y)))$ sets the ground for our analysis. As stated in the main text, an in-situ density modulation of wavelength y^* yields patterns in $n(k_y)$ and consequently induce peaks at $y \approx y^*$, in the FT norm, $|\mathcal{F}[n](y)|$, see Fig. 2(g-i) and (m-o). Spatial variations of the phase relation within the above-mentioned density modulation translate into phase shifts of the interference patterns, which are stored in the FT argument at $y \approx y^*$, $\arg(\mathcal{F}[n](y^*))$; see also Ref. [18, 20].

The first average that we use is $n_\mathcal{M}(y) = \langle|\mathcal{F}[n](y)|\rangle$, i. e. the average of the FT norm of the individual images. As the phase information contained in $\arg(\mathcal{F}[n](y))$ is discarded from $n_\mathcal{M}$ when taking the norm, the peaks in $n_\mathcal{M}$ probe the mere existence of an insitu density modulation of roughly constant spacing within the different realizations. The second average of interest is $n_\Phi(y) = |\langle\mathcal{F}[n](y)\rangle|$, i. e. the average of the full FT of the individual images. In contrast to $n_\mathcal{M}$, n_Φ keeps the phase information of the individual realizations contained in $\arg(\mathcal{F}[n](y^*))$. Consequently, peaks in n_Φ indicate that the phase relation is maintained over the density modulation, in a similar way for all realizations. Their presence thus provides information on the global phase coherence of a density-modulated state.

EXPERIMENTAL SEQUENCE: ^{164}Dy AND ^{166}Er

^{166}Erbium - The BEC of ^{166}Er is prepared similarly to Refs. [1, 8, 21, 22]. We start from a magneto-optical trap with 2.4×10^7 ^{166}Er atoms at a temperature of 10μK, spin-polarized in the lowest Zeeman sub-level. In a next step we load about 3×10^6 atoms into a crossed optical dipole trap (ODT) operated at 1064 nm. We evaporatively cool the atomic cloud by reducing the power and then increasing the ellipticity of one of the ODT beams. During the whole evaporation a constant magnetic field of $B = 1.9\,\mathrm{G}$ ($a_\mathrm{s} = 80\,a_0$) along z is applied. We typically achieve BEC with 1.4×10^5 atoms and a condensed fraction of 70%. In a next step the ODT is reshaped in 300 ms into the final trapping frequencies $\omega_{x,y,z} = 2\pi \times (227, 31.5, 151)\,\mathrm{Hz}$. Consecutively, we ramp B linearly to $0.62\,\mathrm{G}$ ($64.5\,a_0$) in 50 ms and obtain a BEC with 8.5×10^4 atoms, which are surrounded by 3.5×10^4 thermal atoms. This point marks the start of the ramp to the final a_s.

^{164}Dysprosium - For the production of a ^{164}Dy BEC we closely follow the scheme presented in [23]. Starting from a 3 s loading phase of our 5-beam MOT in open-top configuration [24], we overlap a 1064 nm single-beam dipole trap with a $1/e^2$-waist of about $22\,\mu$m, for 120 ms. Eventually, we transfer typically 8×10^6 atoms utilizing a time averaging potential technique to increase the spatial overlap with the MOT. After an initial 1.1 s evaporative

cooling phase by lowering the power of the beam, we add a vertically propagating beam, derived from the same laser, with a $1/e^2$-waist of about 130 μm to form a crossed optical dipole trap for additional confinement. Subsequently, we proceed forced evaporative cooling to reach quantum degeneracy by nearly exponentially decreasing the laser powers in the two dipole-trap beams over 3.6 s. We achieve BECs of ^{164}Dy with typically 10^5 atoms and condensate fractions of about 40%. During the entire evaporation sequence the magnetic field is kept constant at 2.5 G pointing along the vertical (z-) axis.

To be able to condense directly into the supersolid, we modify the dipole trap to condense at a stronger confinement of $\omega_{x,y,z} = 2\pi \times (225, 37, 134)$ Hz. After a total evaporative cooling duration of 3.1 s, we achieve Bose-Einstein condensation at 2.55 G and reach a state with supersolid properties at 2.43 G, keeping the magnetic field constant throughout the entire evaporation sequence for both cases.

Time of flight and imaging for ^{166}Er *and* ^{164}Dy - In order to probe the momentum distribution of the Dy (Er) gases, we switch off the confining laser beams and let the atoms expand freely for 18 ms (15 ms), while keeping the magnetic field constant. Consecutively the amplitude of B is increased to a fixed amplitude of 5.4 G (0.6 G). In the case of ^{164}Dy, the magnetic field orientation is rotated in order to point along the imaging axis. This ensures constant imaging conditions for different a_s. After an additional 9 ms (15 ms) we perform a standard absorption imaging.

TUNING THE SCATTERING LENGTH IN ^{166}Er AND ^{164}Dy

^{166}*Erbium* - All measurements start with a BEC at 64.5 a_0. In order to probe the BEC-supersolid-ID region, we linearly ramp a_s to its target value in $t_r = 20$ ms by performing a corresponding ramp in B. Due to a finite time delay of the magnetic field in our experimental setup and the highly precise values of a_s needed for the experiment, we let the magnetic field stabilize for another 15 ms before $t_h = 0$ starts. By this, we ensure that the residual lowering of a_s during the entire hold time is $\lesssim 0.3\, a_0$. In the main text, we always give the a_s at $t_h = 0$. Furthermore, we estimate our magnetic field uncertainty to be ± 2.5 mG, leading to a $\pm 0.2\, a_0$ uncertainty of a_s in our experiments.

To choose the best ramping scheme, we have performed experiments varying t_r from 0.5 ms to 60 ms, ramping to a fixed a_s lying in the supersolid regime, and holding for $t_h = 5$ ms after a fixed 15 ms waiting time. We record the evolution of A_Φ as a function of t_r; see Fig. S4. When increasing t_r, we first observe that A_Φ increases, up to $t_r = 20$ ms, and then A_Φ gradually decreases. The initial increase can be due to diabatic effects and larger excitation when fast-crossing the phase transition. On the other hand, the slow decrease at longer t_r can be explained by larger atom loss during the ramp. We then choose $t_r = 20$ ms as an optimum value where a supersolid behavior develops and maintains itself over a significant time while the losses are minimal.

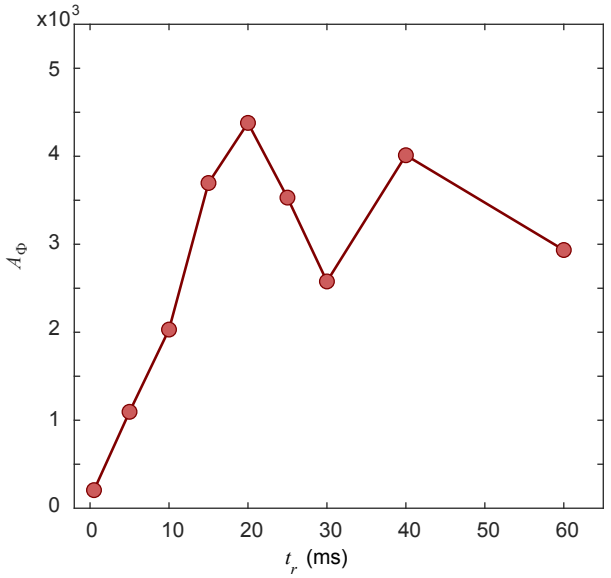

FIG. S4. **Ramp time effect on the supersolid behavior** Measured A_Φ for various durations of the scattering-length ramp with ^{166}Er and a final $a_s = 54.1(2)\, a_0$. All measurements include a 15 ms stabilization time after t_r and are performed with an additional hold of $t_h = 5$ ms.

^{164}*Dysprosium* - As the value of the background scattering, a_{bg} length for ^{164}Dy is still under debate [9, 10, 25], we discuss the experimental settings in terms of magnetic field. Yet, to gain a better understanding of the tunability of a_s in our experiment, we first perform a Feshbach spectroscopy scan on a BEC at $T = 60$ nK. After evaporative cooling at $B = 2.5$ G, we jump to B varying from 1 G to 7.5 G and we hold the sample for 100 ms. Finally, we switch off the trap, let the cloud expand for 26 ms and record the total atom number as a function of B. We then fit the observed loss features with a gaussian fit to obtain the position $B_{0,i}$ and width ΔB_i of the FRs, numbered i. We finally use the standard Feshbach resonance formula to estimate the a_s-to-B dependence via $a_s(B) = a_{bg} \prod_i (1 - \Delta B_i/(B - B_{0,i}))$. Here we account for 8 FRs located between 1.2 G and 7.2 G. Depending on the background scattering length a_{bg}, the overall magnitude of $a_s(B)$ changes. We can get an estimate of a_{bg} from literature. In Fig. S5, we use the value of a_s from Ref. [25] obtained at 1.58 G close to the B-region investigated in our experiment, $a_s = 92(8)\, a_0$. By reverting

the $a_s(B)$ formula, we set $a_{bg} = 87(8)\,a_0$. For the measurements of Figs. 4-5, we ramp B linearly from 2.5 G in 20 ms to a final value ranging from 1.8 to 2.1 G, for which we estimate a_s ranging from $97(9)\,a_0$ to $105(10)\,a_0$. We calibrate our magnetic field using RF spectroscopy, with a stability of about 2 mG. In the Dy case, we do not apply an additional stabilization time. This is justified because of the more mellow a_s-to-B dependence in the B-range of interest as well as of the wider a_s-range of the supersolid regime (see Fig. 1) compared to the Er case. For the measurements of Figs. 6–7, we use two B-values, namely 2.43 G and 2.55 G, at which we perform the evaporative cooling scheme. Here we estimate $a_s = 109(10)\,a_0$ and $a_s = 134(12)\,a_0$, respectively.

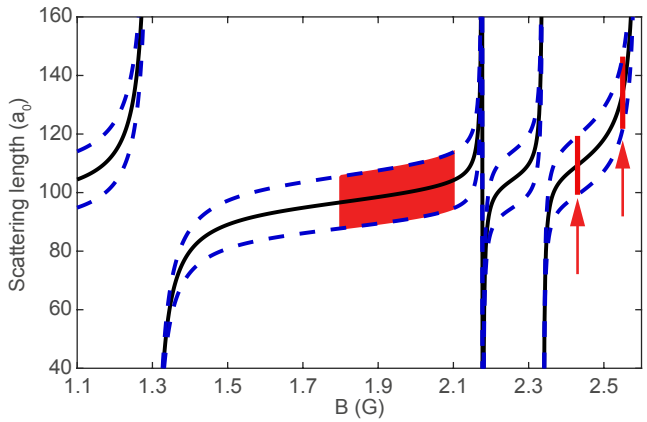

FIG. S5. **Estimated scattering length tuning in** ^{164}Dy Estimated dependence of a_s on B for ^{164}Dy. The FR positions and widths have been extracted from trap-loss spectroscopy measurements, the background scattering length is estimated to $a_{bg} = 87(8)\,a_0$, see text. The blue dashed line gives an error-estimate considering only the errorbar on a_{bg} from the mere a_s measurement of Ref. [25] and not accounting for uncertainty of the Feshhach scan. For Figs. 4-5, we use B between 1.8 G and 2.1 G (red area); for Figs. 6–7, we keep at two constant B-values, namely 2.43 G and 2.55 G (red arrows).

ATOM LOSSES IN ^{166}Er AND ^{164}Dy

As pointed out in the main text, in the time evolution of the quantum gases in both the supersolid and the ID regime, inelastic atom losses play a crucial role. The atom losses are increased in the above mentioned regime as (i) higher densities are required so that a stabilization under quantum fluctuation effects becomes relevant and (ii) the magnetic field may need to be tune close to a FR pole to access the relevant regime of interaction parameters. (i) is at play for all magnetic species but more significant for ^{166}Er due to the smaller value of a_{dd}. (ii) is relevant for both ^{166}Er and ^{162}Dy but conveniently avoided for ^{164}Dy thanks to the special short-range properties of this isotope.

To quantify the role of these losses, we report here the evolution of the number of condensed atoms, N, as a function of the hold time in parallel to the phase coherent character of the density modulation observed. We count N by fitting the thermal fraction of each individual image with a two-dimensional Gaussian function. To ensure that only the thermal atoms are fitted, we mask out the central region of the cloud associated with the quantum gas. Afterwards we subtract this fit from the image and perform a numerical integration of the resulting image (so called pixel count) to obtain N.

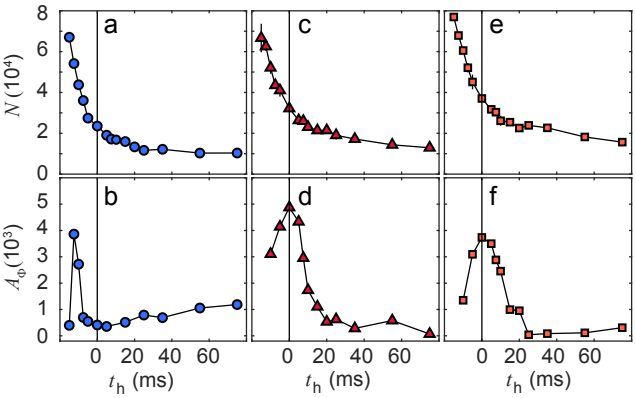

FIG. S6. **atom number and coherence decays in** ^{166}Er Time evolution of N and A_Φ for ^{166}Er at different a_s, including points before $t_h = 0$ ms in the experiment. The corresponding scattering lengths are $53.3(2)\,a_0$ (a,b), $54.0(2)\,a_0$ (c,d), $54.2(2)\,a_0$ (e,f).

^{166}*Erbium* - In the Er case, a 15 ms stabilization time is added to ensure that a_s is reached up to $0.3\,a_0$. During this time, i. e. for $t_h < 0$, we suspect that the time-evolution of the cloud properties is mainly dictated by the mere evolution of the scattering length. Therefore, in the main text, we report on the time evolution for $t_h \geq 0$. We note that because of the narrow a_s-range for the supersolid regime, the long stabilization time for a_s is crucial. However, because of the significant role of the atom losses in our system, in particular for ^{166}Er, the early evolution of N and the cloud's properties are intimately connected. Therefore, the early time evolution at $t_h < 0$ is certainly of high importance for our observations at $t_h \geq 0$.

To fully report on this behavior, we show the evolution of N and A_Φ during both the stabilization and the holding time in Fig. S6 for three different a_s values – either in the ID (a, b) or supersolid regime (c-f). The time evolution shows significant atom loss, prominent already during the stabilization time, and levels off towards a remaining atom number at longer holding times in which we recover small BECs. Simultaneously, in each case reported here, we observe that during the stabilization time A_Φ increases and a coherent density modulated state grows.

TABLE I. Extracted 1/10-lifetime of ^{166}Er atom number decay for $t_h \geq 0$ and remaining atom number at long holding time for data in Fig. S6.

$a_s(a_0)$	t_N (ms)	$N_r(10^4)$	t_Φ (ms)
53.3(2)	32(5)	1.03(5)	-
54.0(2)	51(9)	1.29(11)	25(6)
54.2(2)	46(12)	1.7(2)	32(9)

This density modulation starts to appear at a typical atom number of $N \gtrsim 6 \times 10^4$ and consecutively decays. For the lower $a_s = 53.3(2)\,a_0$ case, we observe that the coherent state does not survive the a_s stabilization time, and decays faster than the atoms loss; see Fig. S6 (a, b). This behavior corresponds to the ID case discussed in the main text. The central point of the present work is to identify a parameter range where the coherence of the density modulated state survives for $t_h > 0$ and its decay time scale is similar to the one of the atom loss. In order to quantify a timescale for the atom number decay, we fit an exponential decay to $t_h \geq 0$ ms. Here we allow an offset N_r of the fit, accounting for the BEC recovered at long holding times. In Table I, we report on the typical 1/10-decay times of the atom number, which are up to 50 ms. These values are of the order as the extracted t_Φ, see Table I and Fig. 5 of the main text. This reveals that in ^{166}Er the extracted lifetime of the coherent density modulated states are mainly limited by atom loss.

Furthermore we note that the extracted N_r values for the recovered BECs are smaller than 2×10^4, which is consistent with the BEC region found in the phase diagram of Fig. 1(f).

^{164}Dysprosium - Differently from the ^{166}Er case, for ^{164}Dy, we operate in a magnetic-field range in which the three-body collision coefficients are small and only moderate atom losses occur. This enables the observation of an unprecendented long-lived supersolid behavior. To understand the effects limiting the supersolid lifetime, we study the lifetime of the condensed-atom number for different B. We perform this detailed study for the data of Fig. 5 of the main text, which are obtained after preparing a stable BEC and then ramping B to the target value. Fig. S7 shows the parallel evolution of N and A_Φ for three different magnetic field values 1.8 G, 2.04 G and 2.1 G. Here we observe that, for all B values, A_Φ seems to decay faster than the atom number. This suggests that the lifetime of the density-modulated state in our ^{164}Dy experiment is not limited by atom losses. To confirm this observation, we extract the 1/10 lifetimes of both N and A_Φ; see Table II. The values confirm our observation and shows an atom number lifetime larger than t_Φ at least by a factor of ≈ 5. In addition, we find that the ratio t_N/t_Φ varies, indicating that atom losses are not the only mechanism limiting the lifetime of the supersolid properties in Dy.

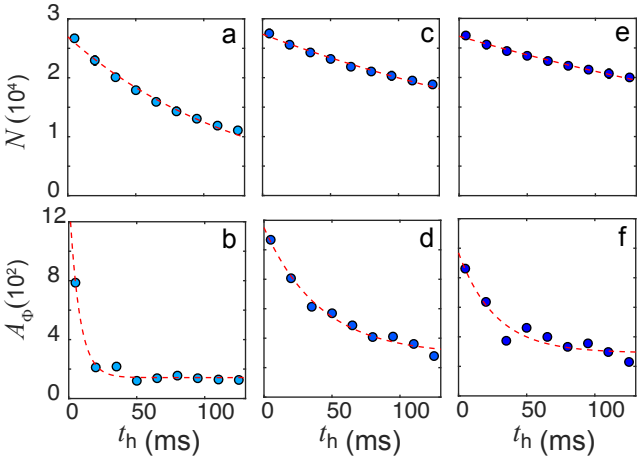

FIG. S7. **atom number and coherence decays in ^{164}Dy** Time evolution of N and A_Φ for ^{164}Dy at different B for the data of Fig. 5. The corresponding magnetic fields are 1.8 G (a,b), 2.04 G (c,d), 2.1 G (e,f).

TABLE II. Extracted 1/10-lifetime of ^{164}Dy atom number decay and A_Φ decay for data in Fig. S7.

B (G)	t_N (ms)	t_Φ (ms)
1.8	300(12)	12(5)
2.04	728(34)	152(13)
2.1	926(36)	133(25)

[1] L. Chomaz, R. M. W. van Bijnen, D. Petter, G. Faraoni, S. Baier, J. H. Becher, M. J. Mark, F. Wächtler, L. Santos, and F. Ferlaino, "Observation of roton mode population in a dipolar quantum gas," Nat. Phys. **14**, 442 (2018).

[2] S. Ronen, D. C. E. Bortolotti, and J. L. Bohn, "Bogoliubov modes of a dipolar condensate in a cylindrical trap," Phys. Rev. A **74**, 013623 (2006).

[3] A. R. P. Lima and A. Pelster, "Quantum fluctuations in dipolar Bose gases," Phys. Rev. A **84**, 041604 (2011).

[4] A. R. P. Lima and A. Pelster, "Beyond mean-field low-lying excitations of dipolar Bose gases," Phys. Rev. A **86**, 063609 (2012).

[5] F. Wächtler and L. Santos, "Quantum filaments in dipolar Bose-Einstein condensates," Phys. Rev. A **93**, 061603(R) (2016).

[6] F. Wächtler and L. Santos, "Ground-state properties and elementary excitations of quantum droplets in dipolar Bose-Einstein condensates," Phys. Rev. A **94**, 043618 (2016).

[7] R. N. Bisset, R. M. Wilson, D. Baillie, and P. B. Blakie, "Ground-state phase diagram of a dipolar condensate

with quantum fluctuations," Phys. Rev. A **94**, 033619 (2016).
[8] L. Chomaz, S. Baier, D. Petter, M. J. Mark, F. Wächtler, L. Santos, and F. Ferlaino, "Quantum-fluctuation-driven crossover from a dilute Bose-Einstein condensate to a macrodroplet in a dipolar quantum fluid," Phys. Rev. X **6**, 041039 (2016).
[9] M. Schmitt, M. Wenzel, F. Böttcher, I. Ferrier-Barbut, and T. Pfau, "Self-bound droplets of a dilute magnetic quantum liquid," Nature (London) **539**, 259–262 (2016).
[10] I. Ferrier-Barbut, M. Wenzel, F. Böttcher, T. Langen, M. Isoard, S. Stringari, and T. Pfau, "Scissors Mode of Dipolar Quantum Droplets of Dysprosium Atoms," Phys. Rev. Lett. **120**, 160402 (2018).
[11] C. R. Cabrera, L. Tanzi, J. Sanz, B. Naylor, P. Thomas, P. Cheiney, and L. Tarruell, "Quantum liquid droplets in a mixture of Bose-Einstein condensates," Science **359**, 301–304 (2018).
[12] V. Cikojevi, L. Vranje Marki, G. E. Astrakharchik, and J. Boronat, "Universality in ultradilute liquid Bose-Bose mixtures," arXiv:1811.04436 (2018).
[13] B. D. Josephson, "Possible new effects in superconductive tunnelling," Phys. Lett. **1**, 251 – 253 (1962).
[14] A. Barone and G. Patern, *Physics and applications of the Josephson effect* (Wiley, New York, NY, 1982).
[15] J. Javanainen, "Oscillatory exchange of atoms between traps containing Bose condensates," Phys. Rev. Lett. **57**, 3164–3166 (1986).
[16] S. Raghavan, A. Smerzi, S. Fantoni, and S. R. Shenoy, "Coherent oscillations between two weakly coupled bose-einstein condensates: Josephson effects, π oscillations, and macroscopic quantum self-trapping," Phys. Rev. A **59**, 620–633 (1999).
[17] M. Wenzel, F. Böttcher, J.-N. Schmidt, M. Eisenmann, T. Langen, T. Pfau, and I. Ferrier-Barbut, "Anisotropic Superfluid Behavior of a Dipolar Bose-Einstein Condensate," Phys. Rev. Lett. **121**, 030401 (2018).
[18] Z. Hadzibabic, S. Stock, B. Battelier, V. Bretin, and J. Dalibard, "Interference of an Array of Independent Bose-Einstein Condensates," Phys. Rev. Lett. **93**, 180403 (2004).
[19] We note that we have also checked our analysis without performing the recentering step and the same features remain. For instance, for our test data of Fig. 2, the effect being mainly that the side peaks in (e) are more washed out and a slight difference occurs between $n_{\mathcal{M}}$ and n_{Φ}, both showing still side peaks.
[20] S. Hofferberth, I. Lesanovsky, B. Fischer, T. Schumm, and J. Schmiedmayer, "Non-equilibrium coherence dynamics in one-dimensional Bose gases," Nature (London) **449**, 324 (2007).
[21] K. Aikawa, A. Frisch, M. Mark, S. Baier, A. Rietzler, R. Grimm, and F. Ferlaino, "Bose-Einstein condensation of Erbium," Phys. Rev. Lett. **108**, 210401 (2012).
[22] D. Petter, G. Natale, R. M. W. van Bijnen, A. Patscheider, M. J. Mark, L. Chomaz, and F. Ferlaino, "Probing the roton excitation spectrum of a stable dipolar Bose gas," arXiv:1811.12115 (2018).
[23] A. Trautmann, P. Ilzhöfer, G. Durastante, C. Politi, M. Sohmen, M. J. Mark, and F. Ferlaino, "Dipolar Quantum Mixtures of Erbium and Dysprosium Atoms," Phys. Rev. Lett. **121**, 213601 (2018).
[24] P. Ilzhöfer, G. Durastante, A. Patscheider, A. Trautmann, M. J. Mark, and F. Ferlaino, "Two-species five-beam magneto-optical trap for erbium and dysprosium," Phys. Rev. A **97**, 023633 (2018).
[25] Y. Tang, A. Sykes, N. Q. Burdick, J. L. Bohn, and B. L. Lev, "s-wave scattering lengths of the strongly dipolar bosons ^{162}Dy and ^{164}Dy," Phys. Rev. A **92**, 022703 (2015).

5.2 Publication IV:

Phase coherence in out-of-equilibrium supersolid states of ultracold dipolar atoms

P. Ilzhöfer[1,†], M. Sohmen[1,2], G. Durastante[1,2], C. Politi[1], A. Trautmann[1], G. Morpurgo[3], T. Giamarchi[3], L. Chomaz[2], M. J. Mark[1,2] and F. Ferlaino[1,2]

[1] *Institut für Quantenoptik und Quanteninformation, Österreichische Akademie der Wissenschaften, 6020 Innsbruck, Austria*

[2] *Institut für Experimentalphysik und Zentrum für Quantenoptik, Universität Innsbruck, Technikerstrasse 25, 6020 Innsbruck, Austria*

[3] *DQMP, University of Geneva, 24 Quai Ernest-Ansermet, CH-1211 Geneva, Switzerland*

arXiv-preprint, arXiv:1912.10892,
submitted 23 December 2019

[†] The author of this PhD thesis participated in the data recording as well as in the writing process of this publication.

Phase coherence in out-of-equilibrium supersolid states of ultracold dipolar atoms

P. Ilzhöfer,[1] M. Sohmen,[1,2] G. Durastante,[1,2] C. Politi,[1] A. Trautmann,[1]
G. Morpurgo,[3] T. Giamarchi,[3] L. Chomaz,[2] M. J. Mark,[1,2] and F. Ferlaino[1,2,*]

[1]*Institut für Quantenoptik und Quanteninformation, Österreichische Akademie der Wissenschaften, 6020 Innsbruck, Austria*
[2]*Institut für Experimentalphysik und Zentrum für Quantenoptik, Universität Innsbruck, Technikerstraße 25, 6020 Innsbruck, Austria*
[3]*DQMP, University of Geneva, 24 Quai Ernest-Ansermet, CH-1211 Geneva, Switzerland*

(Dated: December 24, 2019)

A supersolid is a fascinating phase of matter, combining the global phase coherence of a superfluid with hallmarks of solids, e. g. a spontaneous breaking of the translational symmetry. Recently, states with such counter-intuitive properties have been realized in experiments using ultracold quantum gases with strong dipolar interactions. Here, we investigate the response of a supersolid state to phase excitations which shatter the global phase coherence. After the creation of those excitations, we observe a rapid re-establishment of a global phase coherence, suggesting the presence of a superfluid flow across the whole sample and an efficient dissipation mechanism. We are able to identify a well-defined region where rephasing occurs, indicating the phase boundary between the solid-like and the supersolid phase. Our observations call for the development of theoretical descriptions able to capture the non-equilibrium dynamics in the recently discovered supersolid states of quantum matter.

The notion of phase coherence lies at the foundation of quantum physics. It is considered a master property in understanding many-body quantum phenomena [1, 2], ranging from superfluidity and the Josephson effect to the more applied examples of matter-wave interference, atom lasing processes, and quantum transport in mesoscopic and macroscopic systems. A coherent state can be described in terms of single amplitude and phase fields. However, the phase itself is not a physical observable and the study of coherence relies on measurements of phase differences between a set of coherent matter waves. In the context of atomic Bose–Einstein condensates (BECs), sets of spatially separated clouds have been created, for instance, by splitting a BEC into two or more parts or by loading an ultracold gas into an optical lattice or into a double-well potential [3].

The reverse process, i. e. in-trap merging of BECs, and the related study of the phase evolution, is a much less explored and more subtle problem, invoking, for instance, the growth of thermal correlations in isolated systems [4], the complex interaction-mediated collapse and revival of many-body coherence [5], dissipative dynamics [6], or even the exponential growth of unstable modes and topological defects in connection with the Kibble-Zurek mechanism [7–9]. Despite important theoretical and experimental progress, no generic framework exists yet to understand the quantum-phase evolution and relaxation dynamics in quantum many-body systems out of equilibrium [10].

The physical understanding of the dynamical re-establishment of coherence remains even more elusive for many-body quantum states that feature a spontaneous breaking of the translational symmetry. Prime examples are the supersolid states. For a long time mainly considered a theoretical notion [11–14], such states have been recently observed in quantum gases [15–19]. These supersolids can be seen as coherent matter waves with short-wavelength modulations – shorter than the system size. Remarkably, in dipolar quantum gases the density modulation is not imprinted by external fields but truly emerges from the many-body interactions between atoms. Here, the symmetry breaking is driven by the interplay between short- (contact) and long-range (dipolar) interactions [20–25] and is connected to the softening of the roton mode in the excitation spectrum [26, 27].

The density modulation is predicted to robustly survive both in the limit of infinite system size [21] and trapped quantum gases [17, 19]. In the latter case, for a given trap geometry, the modulation contrast can be controlled by tuning the scattering length a_s – parametrizing the contact interaction – or changing the atom number, N, in the system. The different quantum phases of a cigar-shaped dipolar quantum gas with vertical dipole orientation are shown in Fig. 1a. The phase diagram is constructed by numerically solving the extended Gross-Pitaevskii equation (eGPE; Methods) [19], describing our trapped system and including the recently discovered quantum-fluctuation-driven stabilization mechanism [28–31]. The color map encodes the strength of the density modulation via the number $\widetilde{C} = 1 - C$, with $C = (n_{\max} - n_{\min})/(n_{\max} + n_{\min})$ the dimensionless modulation contrast. Here, $n_{\max}$ ($n_{\min}$) is the density maximum (minimum) in the central region of the calculated in-situ density distribution. $\widetilde{C}$ equals unity for a non-modulated and zero for a fully modulated state.

The phase diagram shows three distinct regions; see Fig. 1a. For large enough a_s, the system is a non-modulated dipolar BEC with $\widetilde{C} = 1$ (grey region). By lowering a_s, the influence of the dipolar interaction increases. When reaching a critical value of a_s, the system undergoes a phase transition to a supersolid phase (SSP). Here, a density modulation with $\widetilde{C} < 1$ appears in the ground-state density profile (red region). By further lowering a_s, the system evolves into an array of independent droplets (ID) with an exponentially vanishing density link between individual droplets and $\widetilde{C}$ approaching zero (blue region).

Recent experiments have shown a connection between the strength of the density modulation and the coherence proper-

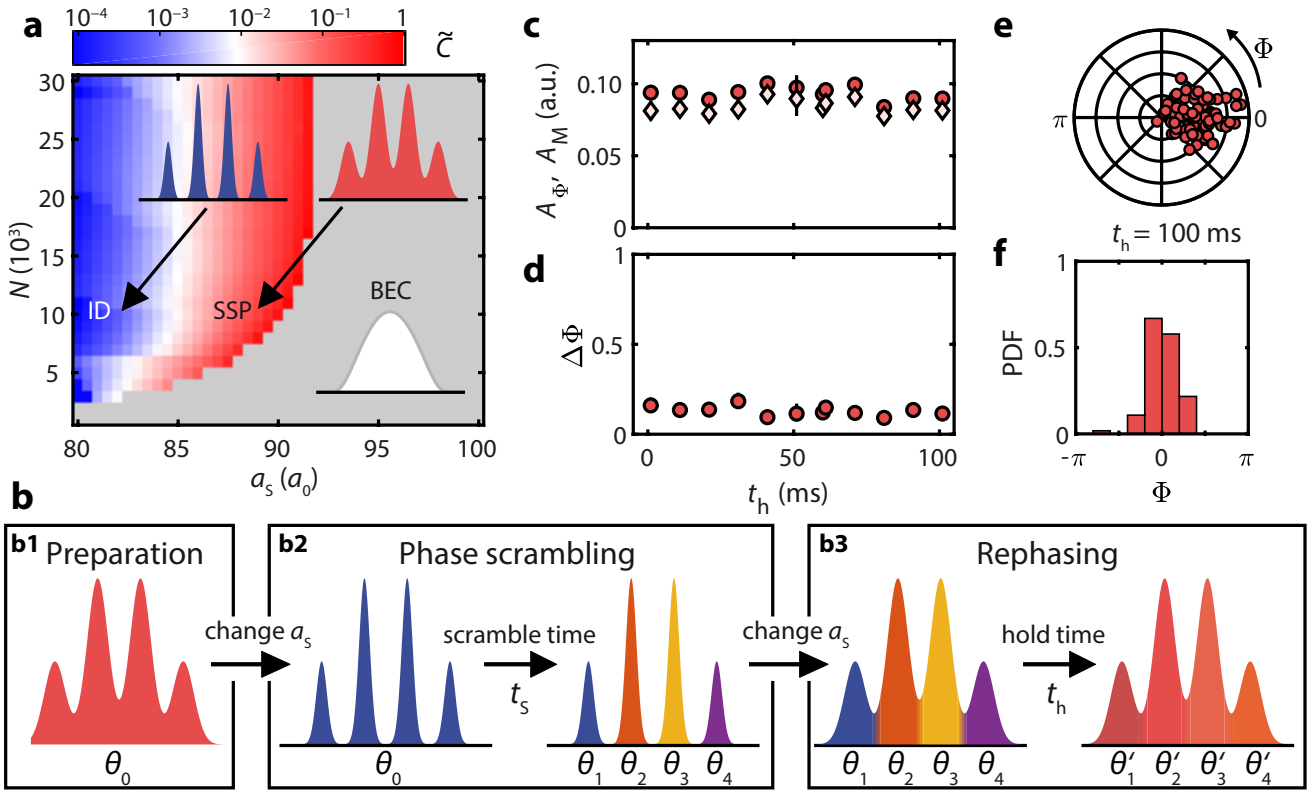

Fig. 1 | Phase diagram, experimental sequence, and starting conditions. a, Ground-state phase diagram for our cigar-shaped trapped ^{164}Dy gas. The color map shows the values of $\widetilde{C}$. The grey color indicates a non-modulated BEC, while the red and blue regions correspond to a SSP and ID phase, respectively. The insets show illustrations of the density profiles along the weak axis for the different phases. **b,** Illustration of the phase scrambling sequence: Starting from a SSP (b1), we reduce a_s to enter the ID regime (b2). During t_S, the phases of the droplets can evolve differently, leading to a phase scrambling between the individual droplets. Eventually, we jump a_s back to its initial value, re-entering the supersolid regime (b3), where we study the time evolution of the global phase coherence. **c,** Amplitudes A_M and A_Φ, and **d,** $\Delta\Phi$ for our evaporatively cooled SSP plotted over t_h. Each data point is derived from $q = 80$–90 individual experimental realizations. The error bars (almost covered by plot symbols) are the one-σ confidence intervals calculated using a bias-corrected accelerated bootstrapping analysis (Methods) [32]. **e,** Polar scatter plot for P_i and **f,** histogram of the probability density function (PDF) for Φ_i at $t_h = 100$ ms.

ties of the system, revealing a clear difference between the SSP and ID phase [17–19]. In the SSP, a global phase is present along the whole system, whereas, in the ID case, phase coherence is absent. The latter behavior can be understood by considering that any fluctuation or excitation within a single isolated droplet will drive an independent evolution of the phases, which cannot lock to each other since particle flow is absent [3]. This type of dephasing has been studied in split BECs and atomic Josephson-junction arrays [3].

While the phase evolution when moving from a SSP to an ID can be understood intuitively, highly fundamental and non-trivial questions arise when considering the opposite route, i. e. when phase-incoherent isolated droplets are linked back together. First, will the out-of-equilibrium system spontaneously re-establish phase coherence? And, if yes, will it relax into its supersolid ground state or reach a quasi-stationary state? Second, which mechanism sets the rephasing timescale? Finally, whereto will the excitation energy be dissipated? Many-body quantum descriptions, as e. g. a standard eGPE approach, are often inherently phase coherent and thus cannot capture such types of non-equilibrium dynamics.

Here, we take first steps to experimentally answer those questions by studying the out-of-equilibrium phase dynamics of a supersolid state after a *phase-scrambling* excitation. Our excitation scheme relies on an interaction quench and exploits the different coherence characters of the SSP and ID phase, as illustrated in Fig. 1b. In particular, after preparing a dipolar quantum gas in the SSP via direct evaporative cooling (b1), we drive the system into the ID regime by lowering a_s (b2). Here, we observe that the phase coherence gets quickly lost while the system remains density modulated. When going back to the parameter regime where the SSP is again the ground state (b3), we observe efficient rephasing dynamics, re-establishing the global phase coherence of the supersolid. Our measurements indicate the presence of superfluid flow with particles delocalizing across the density mod-

ulated gas as well as a dynamical mechanism dissipating the created phase excitations.

As starting point for the experiments, we produce the initial supersolid state by direct evaporative cooling from a thermal sample. As demonstrated in Ref. [19], this is a powerful approach to create a long-lived supersolid state with a high degree of phase coherence. For the present work, our supersolid state contains about $N = 1.4 \times 10^4$ ^{164}Dy atoms and is confined in an axially elongated optical-dipole trap of harmonic frequencies $\omega_{x,y,z} = 2\pi \times (225, 37, 165)\,\mathrm{s}^{-1}$. During the whole evaporation sequence, we apply a vertical magnetic field of $B = 2.430(4)\,\mathrm{G}$ to set the dipole orientation and the desired a_s-value in the SSP region.

Our investigation relies on the ability to probe the system's phase coherence and density modulation, whose co-existence is a hallmark of supersolidity. To this aim, we developed an analysis based on matter-wave-interference [17, 19, 33–36], which is capable of capturing the degree of phase coherence and the density-modulation strength (Methods). In brief, for each individual experimental realization i, we take an absorption image after a time-of-flight (TOF) expansion, which exhibits an interference pattern in case of an in-situ density modulation. Via Fourier transform, we extract the phasor $P_i = \rho_i \cdot \mathrm{e}^{-\mathrm{i}\cdot\Phi_i}$, revealing the amplitude ρ_i and phase Φ_i at the spatial frequency of the interference pattern. Whereas a single P_i characterises the degree of density modulation, the statistical average over an ensemble q of many realizations reveals information about the global phase coherence. We calculate the phase amplitude, $A_\Phi = |\langle P_i \rangle|$, and the density-modulation amplitude, $A_\mathrm{M} = \langle |P_i| \rangle$, as well as the circular phase variance $\Delta\Phi = 1 - \frac{1}{q}\sqrt{\left(\sum_{i=1}^{q}\cos(\Phi_i)\right)^2 + \left(\sum_{i=1}^{q}\sin(\Phi_i)\right)^2}$ [37]. We note that for a perfect supersolid (resp. ID) state and in the limit $q \to \infty$, $A_\Phi = A_\mathrm{M} > 0$ (resp. $A_\Phi = 0, A_\mathrm{M} > 0$) and $\Delta\Phi = 0$ (resp. 1).

To demonstrate the power of this analysis, we apply it to our initial state, whose supersolid properties have been previously investigated [19]. As shown in Fig. 1c–d, A_Φ, A_M and $\Delta\Phi$ are roughly constant during holding times t_h up to 100 ms. We observe almost equal values for A_Φ and A_M and a mean value $\langle\Delta\Phi\rangle = 0.142(8)$, confirming a high degree of global phase coherence for our density-modulated initial state. For $t_\mathrm{h} = 100\,\mathrm{ms}$, we also show a polar plot of P_i (Fig. 1e) as well as the corresponding histogram for Φ_i (Fig. 1f), both displaying a narrow distribution.

After preparing the initial supersolid state, we apply our phase-scrambling protocol; see Fig. 1b2. We ramp the B-field within 20 ms from 2.43 G (SSP) to 1.65 G (ID phase) and let the system evolve for a variable time t_S. Exploiting the magnetic-field tunability of a_s via Feshbach resonances, the B-field ramp corresponds to a change from about $a_{\mathrm{s,SSP}} = 88\,a_0$ to $a_{\mathrm{s,ID}} = 77\,a_0$ (Methods). As shown in Fig. 2a, we observe a rapid initial increase of $\Delta\Phi$ on a time scale of $t_\mathrm{S} \simeq 20\,\mathrm{ms}$ [38], after which $\Delta\Phi$ saturates close at a mean value of $\langle\Delta\Phi\rangle_{t_\mathrm{S}\geq 30\,\mathrm{ms}} = 0.92(2)$. We note that the saturation value is not expected to reach unity because of our finite sample size ($q \simeq 95$). Indeed, it is comparable to the one calculated from a toy model, which considers a sample with the same q and fully random (i. e. uniformly distributed) phases (Methods).

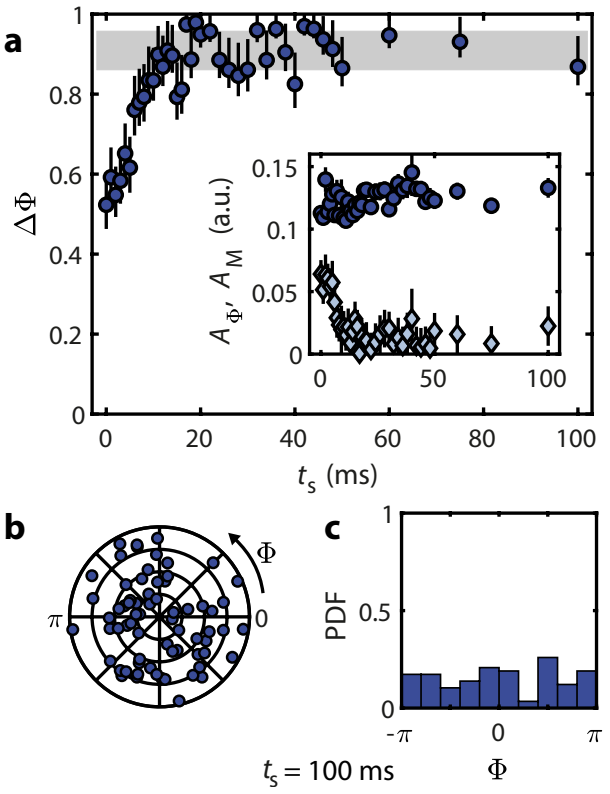

Fig. 2 | Phase scrambling. **a,** $\Delta\Phi$ as a function of t_S for the ID phase at 1.65 G ($a_{\mathrm{s,ID}} = 77\,a_0$). Each point is derived from $q = 90$–100 independent experimental realizations. The error bars are the one-σ confidence intervals calculated using a bias-corrected accelerated bootstrapping analysis (Methods) [32]. The grey shaded area indicates the theoretical one-σ confidence interval for $\Delta\Phi$ using the same sample size and a uniformly random phase. The inset shows the according A_Φ (cyan) as well as A_M (blue). **b,** Polar scatter plot for P_i and **c,** histogram of the PDF for Φ_i at $t_\mathrm{S} = 100\,\mathrm{ms}$.

Simultaneous to the increase of $\Delta\Phi$, we observe that A_Φ decreases quickly towards zero, while A_M slightly increases. This behavior shows that the density modulation is maintained while losing global phase coherence; see inset. As expected, in the ID phase, quantum and thermal fluctuations as well as atom losses can give rise to a different time evolution for the phases of the individual droplets. Apparently the vanishing small density overlap between droplets ($\widetilde{C} \simeq 0$) prevents an efficient phase locking, resulting in the observed loss of global phase coherence.

We now move to the core of our experiment and investigate the phase-relocking after the phase scrambling. We set a_s back to its initial value, i. e. where the system's ground state is a supersolid, by a B-field jump, and study the system's evolution; see Fig. 1b3. As shown in Fig. 3a, we observe first a rapid reduction of $\Delta\Phi$, occurring in the first 20 ms, and then a much slower dynamics with $\Delta\Phi$ saturating

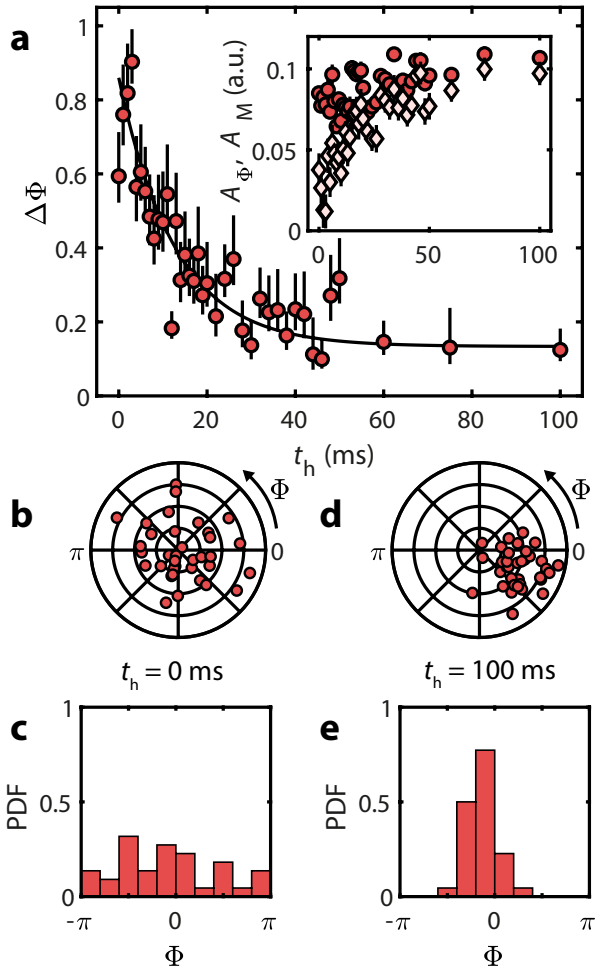

Fig. 3 | Rephasing dynamics. a, $\Delta\Phi$ as a function of t_h after a jump from the ID phase back to the SSP regime at 2.43 G ($a_{\mathrm{s,SSP}} = 88\,a_0$). For each point $q = 66$–74. The error bars are the one-σ confidence intervals calculated using a bias-corrected accelerated bootstrapping analysis (Methods) [32]. The solid black line is an exponential fit to guide the eye. The inset shows the according A_Φ (light red) as well as A_M (red). **b,** Polar scatter plot for P_i and **c,** histogram of the PDF for Φ_i at $t_\mathrm{h} = 0$ ms and at $t_\mathrm{h} = 100$ ms (**d**–**e**).

to $\langle\Delta\Phi\rangle_{t_\mathrm{h}\geq 30\,\mathrm{ms}} = 0.20(2)$. Accordingly, A_Φ approaches A_M on the same time scale, whereas A_M remains nearly constant. This re-establishment of global phase coherence is further illustrated with individual polar scatter plots and histograms in Fig. 3, confirming a reduction of the phase distribution's width with increasing t_h.

Our system of multiple superfluid parts with different phases interconnected via weak links is reminiscent of a Josephson-Junction array (JJA) [39], opening the question whether a JJA framework can capture the main ingredients of our system's dynamics. Although our array of droplets is soft, meaning that the droplets' shape and their distance change with a_s, we construct a simple model in terms of a one-dimensional array of coupled grains (Methods). This is justified as the strongest effect of the change of the system's state with a_s is the change of the wavefunction overlap between the droplets, i. e. the tunneling rate. Using this model, we simulate quenches of the tunneling rate and look at the time evolution of the correlation function of the phases in the array, which corresponds to the experimental observable A_Φ/A_M.

The model gives dephasing and rephasing dynamics, similar to the observations of Fig. 2-3. A more quantitative description goes beyond the scope of this paper. It would require (i) to find proper relations between the parameters of the JJA model and the real system, (ii) to achieve a macroscopic modelling of the dissipation mechanisms by including coupling with a thermal bath and/or with the excited droplet modes [40], or even (iii) to go beyond the hard-grain model. Even in experiments with non-dipolar coupled quasi-condensates, realizing a case closer to an ideal JJA, the observed phase dynamics and full phase-locking have no theoretical explanation up to now [41]. Another important ingredient in the phase relaxation dynamics is the phase defects formed at the boundaries between the distinct grains when they merge [6, 8, 9, 42]. These defects, forming e. g. solitons, are expected to propagate and interact with each other and with excitations from the thermal bath, and thus eventually decay.

To further investigate the role of the density links among droplets – i. e. the Josephson coupling –, we study the rephasing dynamics as a function of the theoretically calculated $\widetilde{C}$; see Fig. 1a. Although our system is out of equilibrium, we use the ground-state quantity $\widetilde{C}$ as an estimate for the strength of the density link [17–19]. For each value of a_s, we assign $\widetilde{C}$ and record the time trace of $\Delta\Phi$ for different t_h. As shown in Fig. 4a, we see different rephasing dynamics depending on $\widetilde{C}$. In the case of small $\widetilde{C}$, associated with the ID regime, no rephasing occurs with $\Delta\Phi$ remaining large (> 0.5) for all t_h (blue region). As $\widetilde{C}$ and thus the link strength increases, the system starts to rephase with $\Delta\Phi$ approaching a small saturation value (≈ 0.15) at long evolution times (red region).

The time traces clearly show the existence of two regimes for $\Delta\Phi$, one in which phase re-locking occurs and one in which the system remains incoherent. To further investigate these regimes and their interface, we study the long-time dynamics of A_Φ and A_M and record their asymptotic values. As shown in Fig. 4b, A_M remains large and shows only slight variations over the full investigated range of $\widetilde{C}$. This indicates the persistence of density modulation in the system. In contrast, a striking change is found in the evolution of the ratio between A_Φ and A_M. At large $\widetilde{C} > 0.01$, A_Φ and A_M are nearly equal. This shows the re-establishement of a global phase coherence, and the relaxation towards a SSP. Differently, at small $\widetilde{C} < 0.001$, A_Φ nearly vanishes while A_M remains large and almost constant, evidencing a final phase-incoherent state (ID regime). At intermediate $\widetilde{C}$, A_Φ and A_M show an in-between behavior with A_Φ smaller than A_M but non-vanishing, showing a partial recoherence of the state. These three distinct behaviors are also reflected in the asymptotic values of $\Delta\Phi$ (Fig. 4c), showing full recoherence ($\Delta\Phi \approx 0.15$) in the supersolid regime, persistence of a full incoherence ($\Delta\Phi \approx 0.9$) in

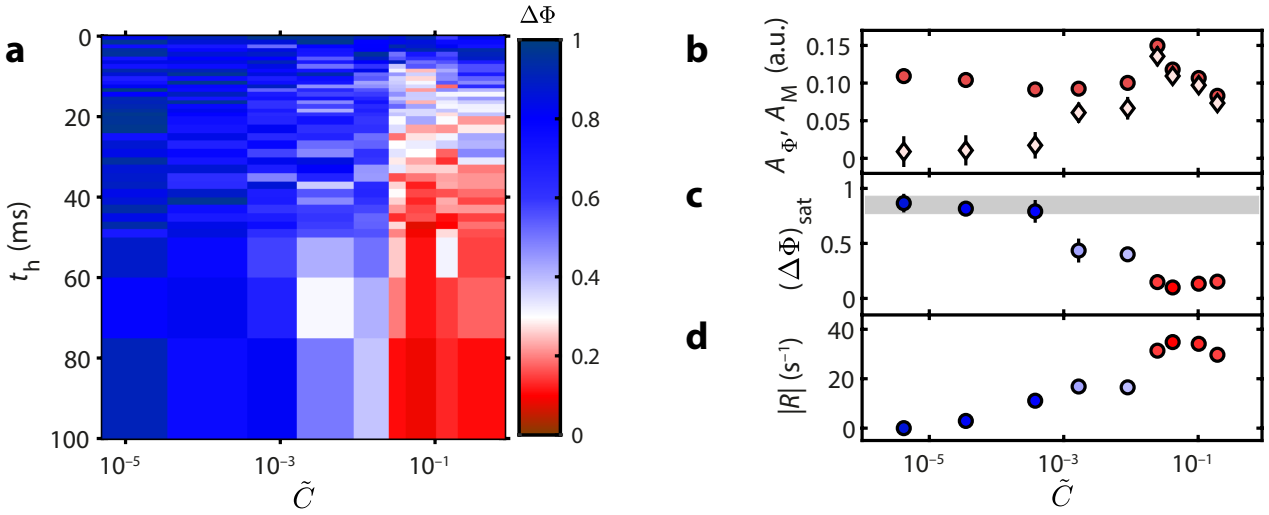

Fig. 4 | Time traces of the phase dynamics and their characterization. a, Temporal evolution of $\Delta\Phi$ (color map) after the complete phase scrambling sequence plotted as a function of t_h and $\widetilde{C}$. For each t_h we record $q \geq 35$ individual experimental realizations. In the red region ($\Delta\Phi \simeq 0$) the system has recovered its global phase coherence, while for the blue one ($\Delta\Phi \simeq 1$) no global phase coherence is present. **b,** A_Φ (light red) and A_M (red), **c,** saturation value $(\Delta\Phi)_{sat}$ and **d,** rephasing rate $|R|$ as a function of $\widetilde{C}$. A_Φ, A_M, and $(\Delta\Phi)_{sat}$ are the mean values at long t_h. The grey shaded area indicates the theoretical one-σ confidence interval for $\Delta\Phi$ using the same sample size as the experiment and a uniformly random phase.

the ID regime, and partial recoherence ($\Delta\Phi \approx 0.5$) in the intermediate regime.

A further question is whether the value of $\widetilde{C}$, i. e. the different regimes, also dictates the speed of the rephasing dynamics. To explore this aspect, we study the early time dynamics of $\Delta\Phi$ by performing a linear fit to the data for $t_h \leq 20$ ms. The extracted slope characterizes the initial rephasing rate $|R|$. As shown in Fig. 4d, in the supersolid regime, we always record a large rephasing rate, which remarkably is roughly independent of $\widetilde{C}$, with $|R| \approx 30 s^{-1}$. This value is comparable to the weak-axis trap frequency, $\omega_y/2\pi$, and compatible with the time needed for a sound wave or soliton to propagate along the system [8, 43]. In contrast, when crossing from the supersolid to the intermediate regime, we observe a sudden decrease of $|R|$ by almost a factor of two. Evolving from this intermediate regime to the ID, $|R|$ continuously decreases with decreasing $\widetilde{C}$ until it vanishes. While such a decrease of $|R|$ is consistent with a JJA picture in which the tunneling between the droplets dictates the rephasing dynamics, the underlying reason for a constant rephasing rate in the supersolid regime remains an open question. It might indicate the action of other mechanisms, related for instance to the soft nature of our JJA, or the formation and slow decay of phase defects in the array.

In conclusion, we have reported the first study of the out-of-equilibrium dynamics of a dipolar supersolid after an interaction-driven phase excitation that fully randomizes the phases. In the SSP regime, we have demonstrated that the system re-establishes a high-degree of phase coherence on the timescale of one trap period by almost perfect rephasing. When tunneling is suppressed by a too weak density link across our spontaneously-modulated quantum state, the rephasing substantially slows down at a rate depending on the tunneling and eventually ceases in the deep ID regime. Our observations might shed new light on the properties of the particle flow in a SSP and its superfluid properties, whose general understanding is still elusive. Future experimental works, combined with advanced out-of-equilibrium theoretical models, will be crucial to understand the relaxation dynamics and dissipation mechanisms in isolated and open supersolid states of quantum matter.

[1] Cohen-Tannoudji , C. & Gury-Odelin, D. *Advances in Atomic Physics: An Overview* (World Scientific, 2011). URL https://doi.org/10.1142/6631.

[2] Svistunov, B. V., Babaev, E. S. & Prokof'ev, N. V. *Superfluid States of Matter* (CRC Press, 2015). URL https://doi.org/10.1201/b18346.

[3] Bloch, I., Dalibard, J. & Zwerger, W. Many-body physics with ultracold gases. *Rev. Mod. Phys.* **80**, 885–964 (2008). URL https://doi.org/10.1103/RevModPhys.80.885.

[4] Langen, T., Geiger, R., Kuhnert, M., Rauer, B. & Schmiedmayer, J. Local emergence of thermal correlations in an isolated quantum many-body system. *Nature Physics* **9**, 640–643 (2013). URL https://doi.org/10.1038/nphys2739.

[5] Wright, E. M., Walls, D. F. & Garrison, J. C. Collapses and Revivals of Bose-Einstein Condensates Formed in Small Atomic Samples. *Phys. Rev. Lett.* **77**, 2158–2161 (1996). URL

https://doi.org/10.1103/PhysRevLett.77.2158.

[6] Jo, G.-B. *et al.* Phase-Sensitive Recombination of Two Bose-Einstein Condensates on an Atom Chip. *Phys. Rev. Lett.* **98**, 180401 (2007). URL https://doi.org/10.1103/PhysRevLett.98.180401.

[7] Scherer, D. R., Weiler, C. N., Neely, T. W. & Anderson, B. P. Vortex Formation by Merging of Multiple Trapped Bose-Einstein Condensates. *Phys. Rev. Lett.* **98**, 110402 (2007). URL https://doi.org/10.1103/PhysRevLett.98.110402.

[8] Aidelsburger, M. *et al.* Relaxation Dynamics in the Merging of *N* Independent Condensates. *Phys. Rev. Lett.* **119**, 190403 (2017). URL https://doi.org/10.1103/PhysRevLett.119.190403.

[9] del Campo , A. & Zurek, W. H. Universality of phase transition dynamics: Topological defects from symmetry breaking. *Int. J. Mod. Phys. A* **29**, 1430018 (2014). URL https://doi.org/10.1142/S0217751X1430018X.

[10] Langen, T., Geiger, R. & Schmiedmayer, J. Ultracold Atoms Out of Equilibrium. *Annu. Rev. Condens. Matter Phys* **6**, 201–217 (2015). URL https://doi.org/10.1146/annurev-conmatphys-031214-014548.

[11] Andreev , A. F. & Lifshitz, I. M. Quantum Theory of Defects in Crystals. *Sov. Phys. JETP* **29**, 1107 (1969).

[12] Chester, G. V. Speculations on Bose-Einstein Condensation and Quantum Crystals. *Phys. Rev. A* **2**, 256–258 (1970). URL https://doi.org/10.1103/PhysRevA.2.256.

[13] Leggett, A. J. Can a Solid Be "Superfluid"? *Phys. Rev. Lett.* **25**, 1543–1546 (1970). URL https://doi.org/10.1103/PhysRevLett.25.1543.

[14] Boninsegni , M. & Prokof'ev, N. V. Colloquium: Supersolids: What and where are they? *Rev. Mod. Phys.* **84**, 759–776 (2012). URL https://doi.org/10.1103/RevModPhys.84.759.

[15] Li, J.-R. *et al.* A stripe phase with supersolid properties in spinorbit-coupled BoseEinstein condensates. *Nature* **543**, 91–94 (2017). URL https://doi.org/10.1038/nature21431.

[16] Léonard, J., Morales, A., Zupancic, P., Esslinger, T. & Donner, T. Supersolid formation in a quantum gas breaking a continuous translational symmetry. *Nature* **543**, 87–90 (2017). URL https://doi.org/10.1038/nature21067.

[17] Böttcher, F. *et al.* Transient Supersolid Properties in an Array of Dipolar Quantum Droplets. *Phys. Rev. X* **9**, 011051 (2019). URL https://doi.org/10.1103/PhysRevX.9.011051.

[18] Tanzi, L. *et al.* Observation of a Dipolar Quantum Gas with Metastable Supersolid Properties. *Phys. Rev. Lett.* **122**, 130405 (2019). URL https://doi.org/10.1103/PhysRevLett.122.130405.

[19] Chomaz, L. *et al.* Long-Lived and Transient Supersolid Behaviors in Dipolar Quantum Gases. *Phys. Rev. X* **9**, 021012 (2019). URL https://doi.org/10.1103/PhysRevX.9.021012.

[20] Lu, Z.-K., Li, Y., Petrov, D. S. & Shlyapnikov, G. V. Stable Dilute Supersolid of Two-Dimensional Dipolar Bosons. *Phys. Rev. Lett.* **115**, 075303 (2015). URL https://doi.org/10.1103/PhysRevLett.115.075303.

[21] Roccuzzo , S. M. & Ancilotto, F. Supersolid behavior of a dipolar Bose-Einstein condensate confined in a tube. *Phys. Rev. A* **99**, 041601 (2019). URL https://doi.org/10.1103/PhysRevA.99.041601.

[22] Kora , Y. & Boninsegni, M. Patterned Supersolids in Dipolar Bose Systems. *J. Low Temp. Phys.* **197**, 337–347 (2019). URL https://doi.org/10.1007/s10909-019-02229-z.

[23] Wenzel, M., Böttcher, F., Langen, T., Ferrier-Barbut, I. & Pfau, T. Striped states in a many-body system of tilted dipoles. *Phys. Rev. A* **96**, 053630 (2017). URL https://doi.org/10.1103/PhysRevA.96.053630.

[24] Baillie , D. & Blakie, P. B. Droplet Crystal Ground States of a Dipolar Bose Gas. *Phys. Rev. Lett.* **121**, 195301 (2018). URL https://doi.org/10.1103/PhysRevLett.121.195301.

[25] Cinti , F. & Boninsegni, M. Classical and quantum filaments in the ground state of trapped dipolar Bose gases. *Phys. Rev. A* **96**, 013627 (2017). URL https://doi.org/10.1103/PhysRevA.96.013627.

[26] Santos, L., Shlyapnikov, G. V. & Lewenstein, M. Roton-Maxon Spectrum and Stability of Trapped Dipolar Bose-Einstein Condensates. *Phys. Rev. Lett.* **90**, 250403 (2003). URL https://doi.org/10.1103/PhysRevLett.90.250403.

[27] Chomaz, L. *et al.* Observation of roton mode population in a dipolar quantum gas. *Nat. Phys.* **14**, 442 (2018). URL https://doi.org/10.1038/s41567-018-0054-7.

[28] Ferrier-Barbut, I., Kadau, H., Schmitt, M., Wenzel, M. & Pfau, T. Observation of Quantum Droplets in a Strongly Dipolar Bose Gas. *Phys. Rev. Lett.* **116**, 215301 (2016). URL https://doi.org/10.1103/PhysRevLett.116.215301.

[29] Chomaz, L. *et al.* Quantum-Fluctuation-Driven Crossover from a Dilute Bose-Einstein Condensate to a Macrodroplet in a Dipolar Quantum Fluid. *Phys. Rev. X* **6**, 041039 (2016). URL https://doi.org/10.1103/PhysRevX.6.041039.

[30] Wächtler , F. & Santos, L. Quantum filaments in dipolar Bose-Einstein condensates. *Phys. Rev. A* **93**, 061603 (2016). URL https://doi.org/10.1103/PhysRevA.93.061603.

[31] Bisset, R. N., Wilson, R. M., Baillie, D. & Blakie, P. B. Ground-state phase diagram of a dipolar condensate with quantum fluctuations. *Phys. Rev. A* **94**, 033619 (2016). URL https://doi.org/10.1103/PhysRevA.94.033619.

[32] Efron, B. Better Bootstrap Confidence Intervals. *Journal of the American statistical Association* **82**, 171–185 (1987). URL https://doi.org/10.2307/2289144.

[33] Hadzibabic, Z., Stock, S., Battelier, B., Bretin, V. & Dalibard, J. Interference of an Array of Independent Bose-Einstein Condensates. *Phys. Rev. Lett.* **93**, 180403 (2004). URL https://doi.org/10.1103/PhysRevLett.93.180403.

[34] Takeda, M., Ina, H. & Kobayashi, S. Fourier-transform method of fringe-pattern analysis for computer-based topography and interferometry. *J. Opt. Soc. Am.* **72**, 156–160 (1982). URL https://doi.org/10.1364/JOSA.72.000156.

[35] Kohstall, C. *et al.* Observation of interference between two molecular Bose–Einstein condensates. *New J. Phys.* **13**, 065027 (2011). URL https://doi.org/10.1088/1367-2630/13/6/065027.

[36] Chomaz, L. *et al.* Emergence of coherence via transverse condensation in a uniform quasi-two-dimensional Bose gas. *Nat. Commun.* **6**, 6162 (2015). URL https://doi.org/10.1038/ncomms7162.

[37] Fisher, N. I. *Statistical Analysis Of Circular Data* (Cambridge University Press, Cambridge, 1993). URL https://doi.org/10.1017/CBO9780511564345.

[38] Note that $\Delta\Phi\,(t_S = 0) \simeq 0.5$. We attribute this large value to dephasing dynamics taking place already within the *B*-field ramp duration and the initial time of the TOF.

[39] Fazio , R. & van der Zant, H. Quantum phase transitions and vortex dynamics in superconducting networks. *Physics Reports* **355**, 235 (2001). URL https://doi.org/10.1016/S0370-1573(01)00022-9.

[40] Dalla Torre, E. G., Demler, E. & Polkovnikov, A. Universal Rephasing Dynamics after a Quantum Quench via Sudden Coupling of Two Initially Independent Condensates. *Phys. Rev. Lett.* **110**, 090404 (2013). URL https://doi.org/10.1103/PhysRevLett.110.090404.

[41] Pigneur, M. *et al.* Relaxation to a Phase-Locked Equilibrium

State in a One-Dimensional Bosonic Josephson Junction. *Phys. Rev. Lett.* **120**, 173601 (2018). URL https://doi.org/10.1103/PhysRevLett.120.173601.

[42] Frantzeskakis, D. Dark solitons in atomic Bose–Einstein condensates: from theory to experiments. *J. Phys. A: Math. Theor.* **43**, 213001 (2010). URL https://doi.org/10.1088/1751-8113/43/21/213001.

[43] Natale, G. *et al.* Excitation Spectrum of a Trapped Dipolar Supersolid and Its Experimental Evidence. *Phys. Rev. Lett.* **123**, 050402 (2019). URL https://doi.org/10.1103/PhysRevLett.123.050402.

- We are grateful to S. Erne, J. Schmiedmayer and the ERBIUM team for insightful discussions. We acknowledge R. M. W. van Bijnen for developing the code for our eGPE ground-state simulations. This work is financially supported through an ERC Consolidator Grant (RARE, No. 681432), a NFRI Grant (MIRARE, No. ÖAW0600) from the Austrian Academy of Science and a DFG/FWF (FOR 2247/PI2790), and by the Swiss National Science Fundation under Division II. M. S. and G. D. acknowledge support by the Austrian Science Fund FWF within the DK-ALM (No. W1259-N27). A. T. acknowledges support by the Austrian Science Fund FWF within the Lise-Meitner-Programm (No. M2683-N36). We also acknowledge the Innsbruck Laser Core Facility, financed by the Austrian Federal Ministry of Science, Research and Economy. Part of the computational results presented have been achieved using the HPC infrastructure LEO of the University of Innsbruck.

- Competing Interests: The authors declare no competing interests.

- Author information: Correspondence to F. F. (e-mail: Francesca.Ferlaino@uibk.ac.at).

- Author contributions: P. I. , G. D. and A T. conducted the experiment and collected the experimental data. M. S. and C. P. analyzed the data. M. J. M. performed the eGPE ground-state simulations. G. M. and T. G. contributed to the theoretical analysis. All authors contributed to the writing of the paper. F. F. supervised the project.

I. METHODS

A. Phase diagram and contrast.

Our numerical calculations of the ground-state phase diagram of a cigar-shaped ^{164}Dy dipolar quantum gas follow the procedure described in our earlier works [19, 27]. In brief, the calculations are based on minimizing the energy functional of the extended Gross-Pitaevskii equation (eGPE) using the conjugate-gradients technique [44]. The eGPE includes our anisotropic trapping potential, the short-range contact and long-range dipolar interactions at a mean-field level, as well as the first-order beyond-mean-field correction in the form of a Lee-Huang-Yang (LHY) term [29, 30] and [45]. From the derived three-dimensional wavefunction $\psi(\mathbf{r})$ we calculate the one-dimensional in-situ density profile $n(y) = \int |\psi(\mathbf{r})|^2 \mathrm{d}x\mathrm{d}z$. We evaluate the in-situ density contrast $C = (n_{\max} - n_{\min})/(n_{\max} + n_{\min})$ for profiles which feature density modulations by searching central extrema of $n(y)$ and determining the overall maximum ($n_{\max}$) and minimum ($n_{\min}$) value. For profiles without density modulation (ordinary BEC), we set $C = 0$. We use the quantity $\widetilde{C} = 1 - C$ to estimate the density link between the droplets, which is connected to the tunneling strength [19].

B. Experimental sequence.

We apply our phase scrambling protocol to the evaporatively cooled SSP of ^{164}Dy atoms [19]. For this, we initially load our 5-beam open-top magneto-optical trap (MOT) for 3 s and apply a MOT compression phase, which lasts 400 ms [46]. We then load about 8×10^6 atoms into a single-beam horizontal optical dipole trap (hODT), propagating along our y-axis. The hODT is derived from a 1064 nm focused laser beam. After loading, we apply forced evaporative cooling by exponentially reducing the optical power in the hODT for 0.9 s. Subsequently, we switch on a second ODT beam along the vertical z-axis to form a crossed ODT and continue with the last stage of evaporative cooling for 2 s [47], until the SSP is reached. During the entire evaporation sequence, a magnetic field of $B = 2.43$ G, pointing opposite to gravity along our z-direction, is maintained. The final trap geometry is cigar-shaped with harmonic frequencies $\omega_{x,y,z} = 2\pi \times (225, 37, 165)\,\mathrm{s}^{-1}$. After the initial-state preparation (SSP), we apply our phase-scrambling protocol. For that, without any additional waiting time after the evaporative cooling, we change the B-field to 1.65 G deep in the ID regime. Here, we allow the system's global phase to freely evolve for $t_S = 20$ ms. We have explored two types of protocols: jumping, which results in an effective ≈ 1 ms change of the B-field due to the finite time response of the system, and ramping within 20 ms. We observe a similar scrambling behavior in $\Delta\Phi$ for both the jump and the ramp protocol. We complete our phase-scrambling sequence by jumping the B-field back to its initial value and by letting the system evolve for a variable hold time t_h. Finally, we perform a matter-wave interference-type experiment during time-of-flight (TOF) expansion and record the resulting interference pattern by absorption imaging. A TOF duration of 26.5 ms ensures a mapping onto momentum space. The imaging beam propagates along $\tilde{x}$ in the horizontal x–y-plane at an angle of $\sim 45^\circ$ with respect to the weak trap axis along y.

C. Tuning the scattering length.

To connect the experimental B-field values with the contact scattering length a_s, we use the well established formula for overlapping Feshbach resonances $a_s(B) = a_{bg} \prod_i (1 - \Delta B_i/(B - B_{0,i}))$ [48], with $B_{0,i}$ the poles, ΔB_i the corresponding distance from the pole to the zero-crossing and a_{bg} the (local) background scattering length. We determine the poles and zero-crossings in our B-field region of interest by performing loss spectroscopy and thermalization measurements. Starting from a thermal cloud prepared at 2.55 G we first ramp the magnetic field to the final value within 5 ms, then lower the trap depth to its final value within 50 ms, and wait an additional hold time of about 400 ms. In absence of Feshbach resonances, we typically end up with a thermal gas of 5×10^5 atoms with a temperature of about 500 nK. When scanning the magnetic field in our region of interest, we observe several atom loss features together with peaks in the atom cloud temperature, which we fit with gaussian functions to extract the positions of the poles $B_{0,i}$ and the widths ΔB_i.

The value of the background scattering length of ^{164}Dy is a more subtle topic, as several measurements give varying values in the range between 60–100 a_0 [49]. These measurements were using different methods (e. g. cross-thermalization, theory-experiment comparisons of oscillation frequencies), different initial states (thermal gases and quantum droplets) and were performed at different magnetic fields. Especially the existence of very broad resonances at higher magnetic fields [50] will affect the measured local background scattering lengths. Therefore, we set the value of a_{bg} in such a way that the B-to-a_s conversion reproduces the calculated critical scattering length $a_s = 91\,a_0$ at the experimentally estimated phase transition point between BEC and SSP around 2.5 G. This gives a value of $a_{bg} = 73\,a_0$ which lies within the error bars of the latest published value of $a_{bg} = 69(4)\,a_0$ [49]. Extended Data Figure 1 shows the resulting calculated B-to-a_s conversion from which we estimate $a_{s,SSP} = 88\,a_0$ at 2.43 G in the SSP and $a_{s,ID} = 77\,a_0$ at 1.65 G in the ID as used in the experiment.

D. Interference pattern analysis.

Our analysis is similar to the one described in Ref. [19]. We record $q = 30$–100 experimental repetitions for each parameter set $\mathscr{P}$. Each recorded picture i ($i = 1 \ldots q$) is processed by first subtracting the thermal background via a symmetric 2D-Gaussian fit to the wings of the density distribution. Next, we recenter the image of the degenerate cloud and integrate its central region, where the matter-wave interference signal is concentrated, along the z-direction within $\pm 2\,\mu\mathrm{m}^{-1}$. We

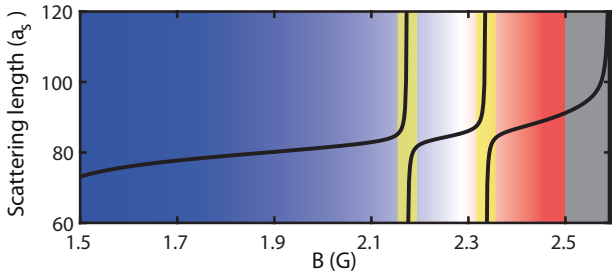

Extended Data Figure 1 | Estimated scattering length. Calculated B-to-a_s conversion for ^{164}Dy. Red and blue shaded areas indicate the SSP and the ID region, respectively. The grey area indicates the BEC region, while the yellow areas indicate regions around the two narrow Feshbach resonances located at 2.174 G and 2.336 G where we observe increased atom loss. We estimate $a_{s,SSP} = 88\,a_0$ in the SSP at 2.43 G and $a_{s,ID} = 77\,a_0$ in the ID at 1.65 G.

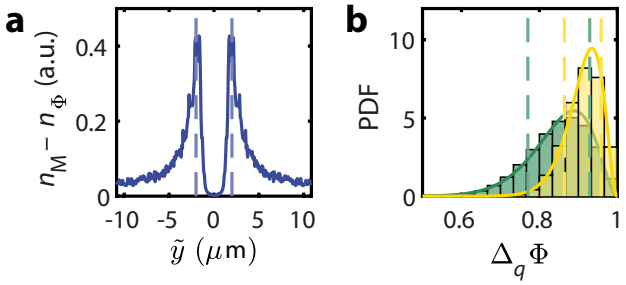

Extended Data Figure 2 | Wavelength of the modulation and finite-sampling effect. a, Difference between incoherent and coherent mean of the density profiles in the ID regime (1.65 G), peaking at the modulation wavelength $d \simeq \pm 2\,\mu$m (dashed lines). **b,** Histograms of 10^6 realisations (each) for calculations of $\Delta_q\Phi$ from uniformly random phases Φ_i, for $q = 35$ (green) and $q = 100$ (yellow) draws, respectively. The dashed vertical lines reflect the confidence interval enclosing 68.3 % ('one σ') of the calculated values. The solid lines reflect a Beta distribution with same mean and variance as the drawn distributions of $\Delta_q\Phi$ (no free fit parameters).

obtain a momentum density profile which we normalize by its sum. From such a momentum profile, a fast Fourier transformation (FFT) yields the 1D density profile $n_i(\tilde{y})$. An in-situ density modulation in an atomic cloud will lead to side peaks in $n_i(\tilde{y})$, symmetrically centred around the zero-momentum peak. To isolate the centre of this specific modulation, we calculate the incoherent and coherent means of $n_i(\tilde{y})$, which we denote $n_M(\tilde{y}) = \langle |n_i(\tilde{y})| \rangle_{\mathscr{P}}$ and $n_\Phi(\tilde{y}) = |\langle n_i(\tilde{y}) \rangle_{\mathscr{P}}|$, respectively. The incoherent mean n_M reflects the mean modulation amplitude of the cloud at the respective wavelength $\tilde{y}$. The coherent mean $n_\Phi \lesssim n_M$ if the phases of the interference pattern among the q repetitions at the respective $\tilde{y}$ are roughly constant, and $n_\Phi \to 0$ (and hence $n_\Phi \ll n_M$) if the phases are random. Therefore, the most pronounced difference $n_M - n_\Phi$ is observed for the ID regime (see Extended Data Fig. 2a). From the maximum of this difference we read off the modulation wavelength (or 'droplet distance') $\tilde{y} \equiv d$. The FFT phasors at d we call $P_i = n_i(d) = \rho_i \cdot e^{-i\cdot\Phi_i}$, yielding sets $\{P_1, \ldots, P_q\}_{\mathscr{P}}$. To characterise the distribution of phases Φ_i within our sets, we calculate the circular variance $\Delta\Phi = 1 - \frac{1}{q}\sqrt{\left(\sum_{i=1}^q \cos(\Phi_i)\right)^2 + \left(\sum_{i=1}^q \sin(\Phi_i)\right)^2}$ [37]. For a phase-coherent sample, and hence interference fringes stable within the envelope, $\Delta\Phi$ is small, whereas for an incoherent sample it approaches unity. To estimate the confidence intervals of our circular variance data we apply a bias-corrected accelerated bootstrapping scheme [32] for each $\mathscr{P}$, resampling 10^6 times from the respective q experimental values.

E. Effect of finite sample size

Even the circular variance $\Delta\Phi$ of a sample of q angles $\Phi_1, \ldots, \Phi_q$ drawn from a completely random distribution will approach unity only in the limit $q \to \infty$. To estimate the fully-incoherent limit of $\Delta\Phi$ for our finite q, we calculate 10^6 values for $\Delta_q\Phi$, each for q independent draws from a theoretical, uniform distribution in $[0, 2\pi)$. The histograms of $\Delta_q\Phi$ are shown in Extended Data Fig. 2b. The indicated one-σ confidence intervals are $[0.77, 0.93]$ for $q = 35$ and $[0.86, 0.96]$ for $q = 100$ draws. We note that the histograms of $\Delta_q\Phi$ follow a Beta distribution [51], even if one generalizes the underlying distribution of phases Φ_i to a von Mises distribution, of which the uniform distribution is just a degenerate case.

F. Interference pattern analysis and simple model of a droplet array

For simplicity let us consider here that the state is made of N_D identical droplets. In that case the total wavefunction of the system would be

$$\psi(x,y,z) = \sum_{j=1}^{N_D} f(x, y - R_j, z)\, e^{i\theta_j} \tag{1}$$

where R_j is the spatial coordinate of the jth droplet, θ_j is its phase, taken to be uniform over the droplet, and f is the wavefunction of a single droplet localized around $y = 0$. With such a wavefunction, the phasor extracted from one realization would be

$$P_i = \int dk_y \sum_{j_1, j_2 = 1}^{N_D} e^{ik_y(R_{j_1} - R_{j_2} - d)} e^{i(\theta_{j_1} - \theta_{j_2})} |\tilde{f}(k_y)|^2 \tag{2}$$

where $\tilde{f}$ is the Fourier transform of the function f and d is the distance between neighboring droplets $d = \langle R_{j+1} - R_j \rangle$. It simplifies in

$$P_i = \sum_{j_1, j_2 = 1}^{N_D} g(R_{j_1} - R_{j_2} - d)\, e^{i(\theta_{j_1} - \theta_{j_2})} \tag{3}$$

$$\approx g(0) \sum_j e^{i(\theta_{j+1} - \theta_j)} \tag{4}$$

with $g(y)$ the Fourier transform of $|\tilde{f}(k_y)|^2$, which is thus a peak function with a width of the order of the droplet size.

Formula (4) yields

$$A_{\mathrm{M}} = \langle |P_i| \rangle_{\mathscr{P}} \approx (N_{\mathrm{D}} - 1)\, g(0)\,, \tag{5}$$

which is essentially independent on the phase relation between the droplets and shows only a weak dependence on the droplets' shape. Here $\langle . \rangle_{\mathscr{P}}$ denote the average over an ensemble of realizations $\mathscr{P}$.

On the contrary the function $A_\Phi = |\langle P_i \rangle_{\mathscr{P}}|$ contains the average of the phases with

$$\frac{A_\Phi}{A_{\mathrm{M}}} = \frac{|\langle P_i \rangle_{\mathscr{P}}|}{\langle |P_i| \rangle_{\mathscr{P}}} \simeq |\langle \langle \mathrm{e}^{\mathrm{i}(\theta_{j+1} - \theta_j)} \rangle_j \rangle_{\mathscr{P}}|. \tag{6}$$

$\langle . \rangle_j$ denotes the average over the droplet array. The ratio A_Φ / A_{M} thus measures essentially the mean difference of phases between two neighboring droplets in the array. We also read from Eq. (4) that the phase of the phasor is $\Phi \approx \langle \theta_{j+1} - \theta_j \rangle_j$.

The circular variance $\Delta\Phi$ for q realizations can be expressed as

$$\Delta\Phi = 1 - \frac{1}{q} \sqrt{\sum_{i_1=1}^{q} \mathrm{e}^{\mathrm{i}\Phi_{i_1}} \sum_{i_2=1}^{q} \mathrm{e}^{-\mathrm{i}\Phi_{i_2}}} \tag{7}$$

For a totally phase coherent state, $\Phi = 0$ for all realizations leading to $\Delta\Phi = 0$ while for a totally phase incoherent sample only the diagonal terms in (7) survive, leading to $\Delta\Phi = 1 - \frac{1}{\sqrt{q}}$ for q independent measurements.

G. Modelization by a Josephson junction array

Let us modelize the system by a set of independent droplets, each one having a number of particles N_j (whose average will be denoted $\overline{N_j}$) and a phase θ_j. The Hamiltonian of such a system is

$$H = \sum_j \left[\frac{\left(N_j - \overline{N_j}\right)^2}{2C_j} - J_j \cos\left(\theta_{j+1} - \theta_j\right) \right] \tag{8}$$

The first term is the "charging" energy of the droplet (corresponding to its mean interaction energy) with the "capacitance" C_j while the second term describes the Josephson tunnelling of particles between droplets with the Josephson amplitude J_j. This is the well known JJA description [39]. Such a description is well adapted if the droplets are reasonably well separated in space, and thus should work adequately when the SSP is established. For simplicity we assume in the subsequent calculations that all parameters C_j and J_j are independent of the droplet and their values are later denoted C and J respectively. In addition, C is taken as constant.

H. Time evolution for the JJA model

To follow the experimental protocol, we used the equilibrium state of our Hamiltonian as initial state and looked at its evolution when we applied quenches to the Hamiltonian. We took a set of 4 droplets with, for simplicity, periodic boundary conditions. First, we quenched our initial state with a Hamiltonian having a J_{S} much smaller than the original J for a given time t_{S}. This corresponds to a decrease of the tunneling between droplets and therefore lets them evolve independently from each other. Then, we quenched our state again by letting it evolve a time t_{h} with the original Hamiltonian (J). This means that we reinstate the original tunneling between the droplets which is what happens in the experimental protocol.

We then looked at the correlation function $|\langle \psi(t)| \langle \mathrm{e}^{\mathrm{i}\theta_{j+1}} \mathrm{e}^{-\mathrm{i}\theta_j} \rangle_j |\psi(t)\rangle|$ which corresponds to A_Φ / A_{M}.

Given the perfect coherence that exists in the JJA model described above, this correlation function would show undamped oscillations corresponding to the time periodic nature of a system with a finite number of frequencies. In order to make the plateaus apparent in the correlation function we have damped these oscillations by an artificial damping term $\mathrm{e}^{-\omega_k t}$ for the mode with a frequency ω_k. The choice of such damping rather than the usual constant exponential one, is to get rid efficiently of the high frequency oscillations without having to recourse to the coupling to a bath for example. It is clear that a more precise and microscopically correct way of including the damping should be considered, but as discussed in the main text, what mechanism leads to damping is a whole question in itself in this system.

From time 0 to t_{s}, this correlation function shows the decrease in A_Φ / A_{M} and corresponds qualitatively to the phase scrambling as can be seen in Extended Data Figure 3a. The first minimum in the figure and the corresponding time scale would correspond to the dephasing discussed in the main text. In total absence of residual coupling between the droplets one would have lost completely the phase coherence on this timescale. Because we have put a small but finite coupling J_{S} remaining between the droplets one can also see at later times a partial recovery of the phase coherence whose value is of course controlled by the value of J_{S}.

Furthermore, if looked up to time t_{h}, this correlation function shows the increase in A_Φ / A_{M} and therefore corresponds to the rephasing of the system as shown in Extended Data Figure 3b. In the calculation, the correlation does not go back to a value of 1, which means that the rephasing is not perfect, in contrast with the experiment. This happens since this simplified model has no energy dissipation mechanism. The initial state not being an eigenstate of the final Hamiltonian thus leads to a final state which is a thermal-like state (with possibly more complicated distributions than a simple thermal one), where the extra energy has been converted to a distribution over the eigenstates. An energy dissipation mechanism, for example via the normal part of the fluid, will thus be necessary to converge back to the initial state. Such extra effects can be potentially incorporated in subsequent studies.

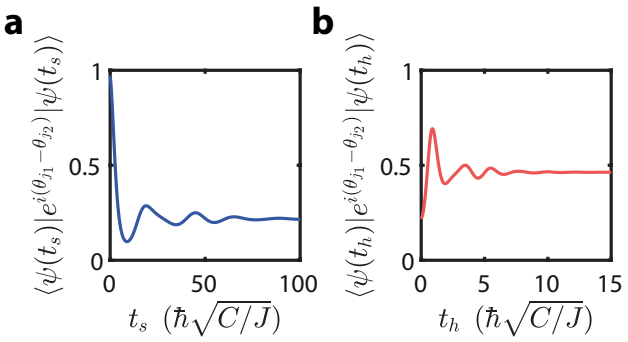

Extended Data Figure 3 | Theoretical predictions for the JJA model with parameters $J = 100$, $J_S = 1$, $C = 1$, $\hbar = 1$ and j_1, j_2 are neighbours. **a,** Evolution of the correlation when the droplets evolve independently from each other as a function of scrambling time t_S. **b,** Evolution of the correlation when the droplets are re-coupled to each other as a function of t_h with $t_S = 1000$ $[\hbar\sqrt{C/J}]$.

[44] Ronen, S., Bortolotti, D. C. E. & Bohn, J. L. Bogoliubov modes of a dipolar condensate in a cylindrical trap. *Phys. Rev. A* **74**, 013623 (2006). URL https://doi.org/10.1103/PhysRevA.74.013623.

[45] Wächtler , F. & Santos, L. Ground-state properties and elementary excitations of quantum droplets in dipolar Bose-Einstein condensates. *Phys. Rev. A* **94**, 043618 (2016). URL https://doi.org/10.1103/PhysRevA.94.043618.

[46] Ilzhöfer, P. *et al.* Two-species five-beam magneto-optical trap for erbium and dysprosium. *Phys. Rev. A* **97**, 023633 (2018). URL https://doi.org/10.1103/PhysRevA.97.023633.

[47] Trautmann, A. *et al.* Dipolar Quantum Mixtures of Erbium and Dysprosium Atoms. *Phys. Rev. Lett.* **121**, 213601 (2018). URL https://doi.org/10.1103/PhysRevLett.121.213601.

[48] Chin, C., Grimm, R., Julienne, P. S. & Tiesinga, E. Feshbach resonances in ultracold gases. *Rev. Mod. Phys.* **82**, 1225–1286 (2010). URL https://doi.org/10.1103/RevModPhys.82.1225.

[49] Ferrier-Barbut, I. *et al.* Scissors Mode of Dipolar Quantum Droplets of Dysprosium Atoms. *Phys. Rev. Lett.* **120**, 160402 (2018). URL https://doi.org/10.1103/PhysRevLett.120.160402.

[50] Maier, T. *et al.* Broad universal Feshbach resonances in the chaotic spectrum of dysprosium atoms. *Phys. Rev. A* **92**, 060702 (2015). URL https://doi.org/10.1103/PhysRevA.92.060702.

[51] Evans, M., Hastings, N. & Peacock, B. Beta distribution. In *Statistical Distributions*, chap. 5, 34–42 (Wiley, New York, 2000), 3 edn. URL https://doi.org/10.1002/9780470627242.

Chapter 6

Conclusion and Outlook

This PhD thesis covered the evolution of the first experimental apparatus for heteronuclear quantum-degenerate dipolar mixtures of erbium and dysprosium over the first five years from its initial development process and construction phase to first experiments on dipolar quantum many-body physics.

Exploiting the great similarities between both elements not only in physical but also in atomic and in laser cooling properties, as well as the pioneering work from respective single-species experiments [74, 75] allowed for a straightforward and overall robust layout of the experimental apparatus. The initial experiment stages involve a dual-species atomic beam source, a single spin-flip Zeeman slower and a dual-species intercombination-line MOT. After a development process and a construction phase of approximately two and a half years, the dual-species MOT began to operate reliably in a novel open-top configuration, possible due to its narrow-line laser cooling character. This first milestone led to the publication *Two-species five-beam magneto-optical trap for erbium and dysprosium* [88], which presented a thorough characterization of the system.

This achievement paved the way to further extend the experimental apparatus by an ODT for evaporative cooling to quantum degeneracy. While initial progress led to single-species dBECs soon after, the actual production of heteronuclear dBECs required deep insight into both elements' specific differences and their influence on the evaporation dynamics. Eventually, after another year, the experimental apparatus achieved single-species dBECs for five bosonic isotopes, including for the first time also ^{170}Er, as well as the first quantum-degenerate dipolar mixtures of erbium and dysprosium with five different heteronuclear dBECs and one quantum-degnerate Bose-Fermi mixture. The second publication *Dipolar Quantum Mixtures of Erbium and Dysprosium Atoms* presented this second milestone and additionally reported first evidence for in-trap interspecies interactions between the dBECs of the isotope mixtures. [117].

At this point, the experimental apparatus started to prove its capabilities as it joined the search for a supersolid phase in dipolar quantum gases. In single-species operation, it achieved with ^{164}Dy a supersolid phase with long lifetimes and the direct evaporative cooling into it, and thus made an important contribution to the third publication *Long-Lived and Transient Supersolid Behaviors in Dipolar Quantum Gases* [155]. Utilizing this unique setting, it then focused, as this PhD work's last project, on the rigidity of global phase coherence and the rephasing dynamics of an out-of-equilibrium dysprosium supersolid by exploiting the isolated droplet phase. This led to the fourth publication *Phase coherence in out-of-equilibrium supersolid states of ultracold dipolar atoms* [177].

The experimental apparatus adds with quantum-degenerate dipolar mixtures of erbium and dysprosium a new type to the existing selection of heteronuclear mixtures, namely almost mass-balanced ones with not only contact but also magnetic dipole-dipole intra- and interspecies interactions. Many properties of such dipolar mixtures are still unknown and demand careful determination, before more advanced experiments are feasible.

Furthermore, the experimental apparatus allows for two additional science modules. By optically transporting single- or dual-species samples in either of the two, more advanced experiments in an optimized environment and with specific experimental techniques will be possible. During this PhD work two ideas took shape, the realization of a quantum-gas microscope and the exploration of multivalent Rydberg atoms, for which this PhD work developed a complete Rydberg science module.

The following Section 6.1 presents the next steps in the direction of dipolar quantum few-/many-body physics and Section 6.2 summarizes basic conceptual ideas on multivalent Rydberg atoms as well as the main aspects of the Rydberg science module.

6.1 Dipolar quantum few-/many-body physics

An important first upgrade to the experimental apparatus, and thus to its capabilities will be a high-resolution imaging system along the vertical z-axis above the upper inverted viewport of the main chamber. It comprises a commercial infinity-corrected objective[61] with a working distance of 55 mm, an effective focal length of 65 mm and a numerical aperture of 0.45. The objective is achromatic for $\lambda_{\mathrm{Er}} = 401\,\mathrm{nm}$ and $\lambda_{\mathrm{Dy}} = 421\,\mathrm{nm}$, and provides a diffraction-limited resolution of 0.54 µm and 0.57 µm, respectively. Moreover, with an adjustment of the focusing plane and a reduction of the numerical aperture to 0.38, it operates non-achromatically at $\lambda_{\mathrm{Er}} = 583\,\mathrm{nm}$ and $\lambda_{\mathrm{Dy}} = 626\,\mathrm{nm}$ with a diffraction-limited resolution of 0.94 µm or 1 µm. The entire imaging setup is easily switchable from absorption imaging to non-destructive insitu phase-contrast imaging and vice versa. The superior overall performance compared to the horizontal absorption imaging will be of major importance for all future experiments.

Near future studies will characterize the quantum-degenerate dipolar mixtures, in particular in view of their interactions, their miscibility or immiscibility as well as their stability diagrams. Currently, there is ongoing work on high-resolution Feshbach spectroscopy with the aim of identifying broad heteronuclear Feshbach resonances applicable for interaction control [49]. As a first result, [178] investigated various isotope mixtures and confirmed for instance a multitude of heteronuclear resonances exceeding the homonuclear ones [76, 77, 78]. However, as the homonuclear Feshbach spectra are already too complex to extract a global single-species background scattering length for the respective isotope, also for the isotope mixtures a careful determination of the intra- and interspecies scattering lengths $a_{\mathrm{s,Er\text{-}Er}}$, $a_{\mathrm{s,Dy\text{-}Dy}}$ and $a_{\mathrm{s,Er\text{-}Dy}}$ for a given magnetic field range of interest is necessary. Here, either a well established technique such as a cross-species thermalization measurement [178, 179, 180], or the recorded TOF center-of-mass oscillations [117], which arise from an interspecies-interaction-induced in-trap shift, are viable possibilities. These results will directly connect to the miscibility behavior [181, 182, 183, 184], which is the basis for all future experiments. Here, the vertical high-resolution imaging will be crucial, as it will provide direct insight to the in-trap behavior of the isotope mixtures.

[61] Special Optics, A Navitar Company

Once the experimental apparatus establishes full control over the produced quantum-degenerate dipolar mixtures, an interesting question concerns quantized vortices, which served as probe to demonstrate superfluidity in purely contact-interacting BECs [13, 14, 15] or in strongly interacting DFGs within the BEC-BCS crossover [185]. Despite that their experimental realization in dipolar quantum gases is still missing, extensive theoretical work studied their properties in dBECs [66]. More recently, [186] and [187] investigated the formation of vortex lattices and patterns specifically in heteronuclear dBECs of erbium and dysprosium, and [188] the creation of a vortex line in a dBEC of dysprosium. The high-resolution imaging system in combination with a digital mirror device will offer the possibility to study quantized vortices in single-species or in dual-species operation. Following the recent observation of a supersolid phase in dipolar quantum gases [153, 154, 155], this probe will also be applicable to confirm the superfluid character of such a state of matter, and thus its phase coherence as well as to answer whether and how supersolidity is inducible in one species via the presence of the other.

6.2 Multivalent Rydberg atoms

Rydberg atoms are a diverse research field, with the conceptual idea to explore and exploit the exaggerated characteristics of atoms with valence electrons in highly excited states [189]. There is a great interest in their large polarizability, and thus their high sensitivity to an external electric field **E** [189] or their strong and long-range interactions [190] and associated effects such as the Rydberg blockade [191, 192, 193].

So far, atomic physics platforms focused mainly on the alkali metals rubidium and cesium due to their favorable laser excitation schemes. Hot vapor Rydberg systems demonstrated for instance the measurement of microwave **E**-fields [194], terahertz imaging [195] or a single-photon source [196]. Ultracold Rydberg systems for instance proved the formation of ultralong-range Rydberg molecules [197, 198], determined the van der Waals interaction utilizing optical tweezers [199], or reported a CNOT quantum gate [200], single-photon sources [201, 202] and single-photon transistors [203, 204].

More recently, strontium and ytterbium with their two 5s and 6s valence electrons, respectively, moved into the focus, as their core remains optically active upon a single Rydberg excitation, and thus facilitate additional possibilities for Rydberg manipulation. Corresponding experiments investigated with strontium the autoionization process and the arising electron-Rydberg atom collisions [205] or the direct imaging of Rydberg atoms and the impact of an ultracold seed plasma [206], and demonstrated with ytterbium the trapping of Rydberg atoms in optical tweezers [207].

At this point, lanthanoids with their more complicated valence electron configurations of 4f and 6s valence electrons (see Chapter 2) allow not only for the same concepts but possibly also for an extended range of experimental techniques. Their electronic ground states' large total electronic angular momentum **J** leads with a non-zero nuclear spin **I** to a large set of hyperfine sublevels in the ground state manifold. For instance, the 128 hyperfine sublevels of holmium could serve for collective register encoding in a Rydberg gate quantum computer [208].

Furthermore, the lanthanoids' highly complex energy level diagrams open new paths for very different Rydberg excitation schemes. Figure 6.1 shows exemplarily the energy level diagrams of neutral erbium (Er I) and of singly ionized erbium (Er II) up to

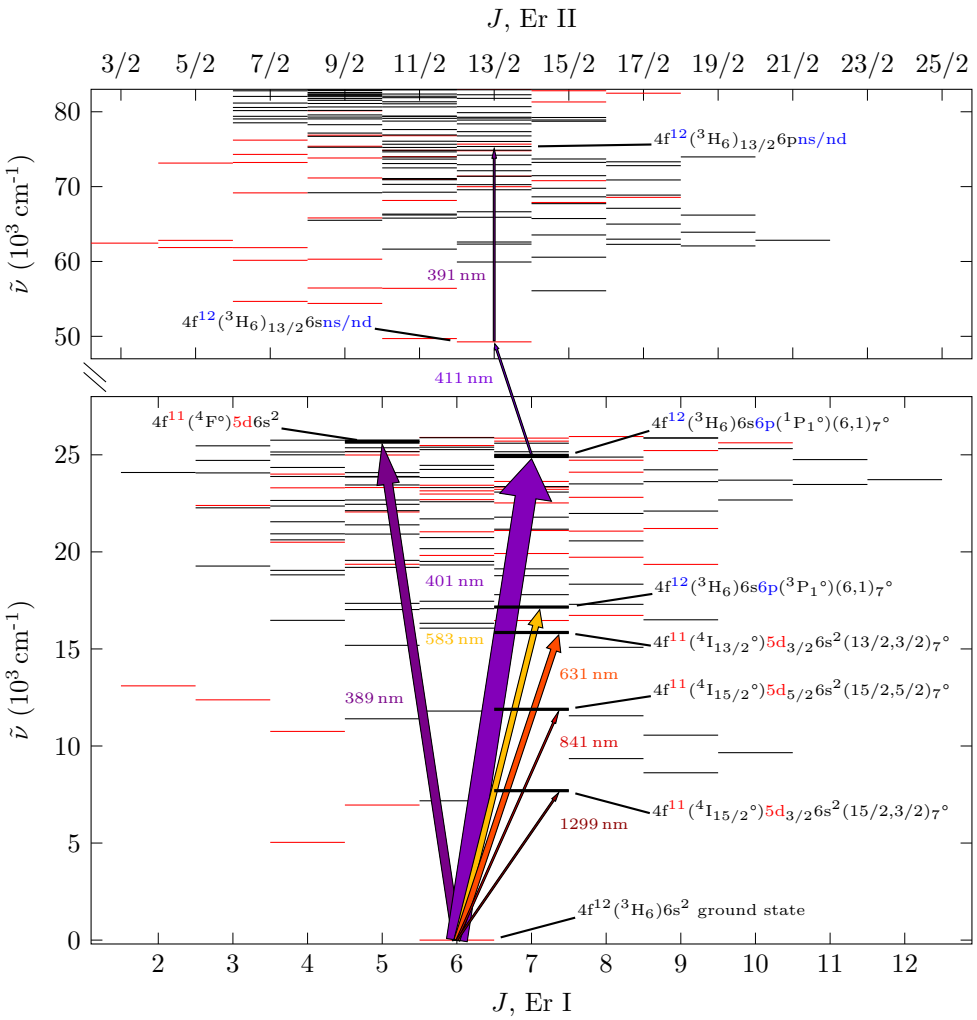

Figure 6.1: Extended energy level diagram of erbium up to wavenumbers $\tilde{\nu}$ of 26 000 cm^{-1} for neutral erbium (Er I, bottom) and of 83 000 cm^{-1} for singly ionized erbium (Er II, top) over the total angular momentum quantum number J. The violet and the yellow arrow indicate, identically to Figure 2.4, the broad and the intercombinatione-line transition to the $\left(^1\mathrm{P}_1\right)(6,1)_7$ and the $\left(^3\mathrm{P}_1\right)(6,1)_7$ state at $\lambda_{\mathrm{Er}} = 401\,\mathrm{nm}$ and $\lambda_{\mathrm{Er}} = 583\,\mathrm{nm}$, respectively. The remaining four arrows from the electronic ground state in Er I indicate transitions of a 4f valence electron to a $5d_{3/2}$ or a $5d_{5/2}$ state in a wavelength range $\lambda_{\mathrm{Er}} = 389\,\mathrm{nm} - 1299\,\mathrm{nm}$. Starting from the $\left(^1\mathrm{P}_1\right)(6,1)_7$ state, the ns or the nd Rydberg series connected to the lowest ionization threshold are addressable with 411 nm laser light. Accordingly, singly ionized erbium Er II in its electronic ground state offers for instance a transition of the remaining 6s valence electron to a 6p state at 391 nm. The figure originates from [209] with data from [87].

wavenumbers $\tilde{\nu}$ of 26 000 cm^{-1} and of 83 000 cm^{-1} with respect to the electronic ground state in Er I over the total angular momentum quantum number J [87]. Besides the broad and the intercombination-line transition to the $\left(^1\mathrm{P}_1\right)(6,1)_7$ or the $\left(^3\mathrm{P}_1\right)(6,1)_7$ state (see Chapter 2), it highlights from the electronic ground state in Er I four transitions

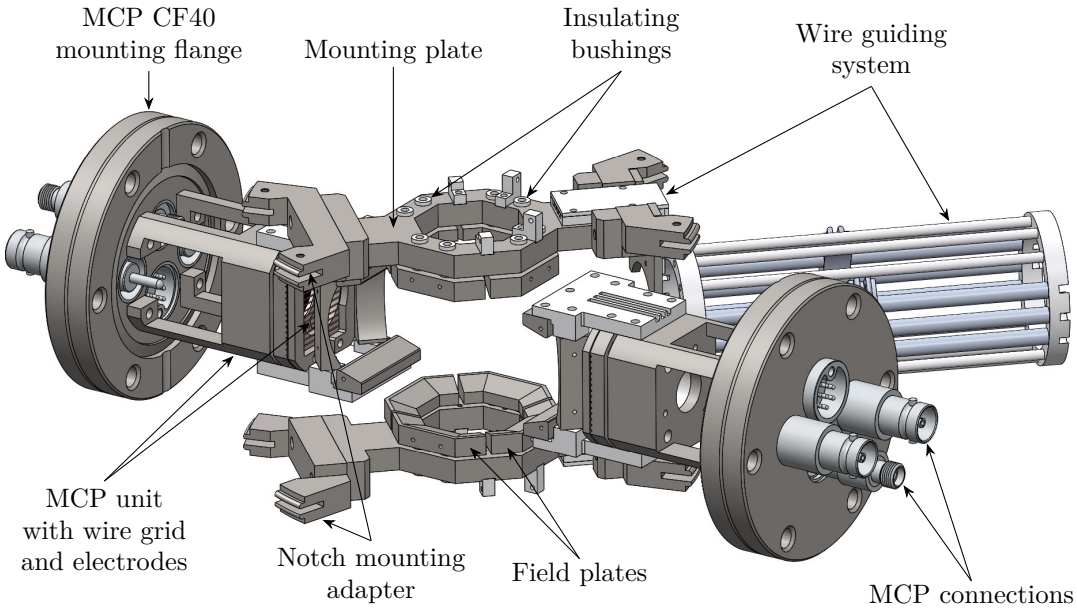

Figure 6.2: In-vacuum **E**-field control system. In total eight field plates in a cloverleaf-octupole arrangement provide a complete three-dimensional **E**-field control to either compensate external stray **E**-fields, to apply precise **E**-fields during the experiment or for field ionization of the excited Rydberg atoms. Two microchannel plate detector (MCP) units, each consisting of an MCP, a housing, a wire grid as well as four electrodes, can detect ions or electrons after field ionization. All these parts are from 1.4429 stainless steel. A wire-guiding system and insulating bushings, all from macor (white), lead the connection wires (not shown) from the field plates and MCP units to their respective electrical feedthroughs (not shown for the field plates). The entire **E**-field control system connects via four notch mounting adapters to a notch system within the surrounding 1.4429 stainless steel octagon chamber (not shown).

of a 4f valence electron to a $5d_{3/2}$ or a $5d_{5/2}$ state differing in natural linewidths $\Delta\nu$ and transition wavelengths λ within the range $\lambda_{\mathrm{Er}} = 389\,\mathrm{nm} - 1299\,\mathrm{nm}$. Hence, corresponding two-photon excitation schemes can couple to Rydberg series of relatively high angular momentum quantum numbers l in comparison to the two 6s valence electrons. This might suppress undesirable autoionization processes. Moreover, the corresponding Rydberg states might offer real parts of their polarizabilities $\Re\left\{\alpha_{\mathrm{Ryd}}\right\}$ sufficiently large for trapping, as the 6s valence electrons remain unchanged and provide a significant contribution to $\Re\{\alpha\}$. As a direct consequence, this might enable the trapping and cooling of Rydberg atoms. Additionally, Figure 6.1 illustrates the 401 nm-411 nm two-photon Rydberg excitation scheme of a 6s valence electron via the broad transition to the ns or the nd Rydberg series connected to the lowest ionization threshold, with the principal quantum number n. Here, the ionic core excitation of the second 6s valence electron to the 6p state at 391 nm could serve for instance for Rydberg imaging or further Rydberg manipulation.

This PhD work developed a complete layout for a Rydberg science module. It comprises a custom-made stainless steel octagon chamber from 1.4429 stainless steel with four pairs of CF40 ports in-plane and two opposing CF100 ports orthogonal to the plane, and provides optical access along three orthogonal axes via six anti-reflection coated

viewports[62]. Further, it features a high-resolution imaging objective identical to the one at the main chamber (see above). Its core feature, however, is an in-vacuum **E**-field control system from 1.4429 stainless steel, as Figure 6.2 illustrates. Here, two opposing sets of four field plates in a cloverleaf arrangement, at a distance of 36 mm and with 25.5 mm inner diameter, form an octupole. Each field plate is individually addressable with up to 5 kV via a separate electrical feedthrough. High-voltage solid-state switches[63] for four out of the eight field plates allow for a dynamic switching between low but highly precise, and high voltage[64] sources. During the experimental sequence, this enables not only the compensation of stray **E**-fields in all three dimensions but also the creation of high **E**-fields of up to $E = 830\,\mathrm{V/cm}$. Thus, the combined operation with two microchannel plate detector (MCP) units allows for Rydberg detection via field-ionization [189]. Each MCP unit encloses the MCP[65] to prevent any additional stray **E**-fields. A wire grid serves as shielding on the entrance of the MCP unit and is together with four additional electrodes individually addressable to redirect the ions or the electrons emerging from field ionization onto the MCP.

However, due to the overall complexity of this project, the results from Rydberg tweezer experiments in one [210] and two [211] dimensions as well as the recent developments with strontium [212, 213] and ytterbium [207], this Rydberg project split off. An entirely new experimental apparatus aiming to study erbium Rydberg atoms in optical tweezer arrays will mostly replicate the presented UHV apparatus (see Chapter 3) and will integrate the developed science module as its core element in a slightly modified form.

[62] Four CF40 viewports, MgF_2 anti-reflection coating, and two CF100 viewports, 68 mm diameter viewport, anti-reflection coating for 401 nm, 421 nm, 1064 nm and 1570 nm

[63] Behlke Power Electronics GmbH, HTS 31-02-HB-LC-C

[64] iseg Spezialelektronik GmbH, ECH 124-INH rack with four slide-in modules, DPr 30 405 24 5, voltages up to 3 kV

[65] Hamamatsu Photonics K.K., F4655-10S184

Chapter 7

Bibliography

[1] S. N. Bose. "Plancks Gesetz und Lichtquantenhypothese". *Zeitschrift für Physik* **26** (1924), 178–181. DOI: 10.1007/BF01327326.

[2] A. Einstein. "Quantentheorie des einatomigen idealen Gases." *Sitzungsber. Preuss. Akad. Wiss.* **12** (1924).

[3] A. Einstein. "Quantentheorie des einatomigen idealen Gases. Zweite Abhandlung." *Sitzungsber. Preuss. Akad. Wiss., Phys. Math. Kl.* **1** (1925).

[4] E. Fermi. "Zur Quantelung des idealen einatomigen Gases". *Zeitschrift für Physik* **36** (1926), 902–912. DOI: 10.1007/BF01400221.

[5] P. A. M. Dirac. "On the theory of quantum mechanics". *Proc. R. Soc. Lond. A* **112** (1926), 661–677. DOI: 10.1098/rspa.1926.0133.

[6] C. J. Pethick and H. Smith. *Bose–Einstein Condensation in Dilute Gases*. 2nd ed. Cambridge University Press, 2008. ISBN: 9780521846516.

[7] W. Ketterle, D. S. Durfee, and D. M. Stamper-Kurn. "Making, probing and understanding Bose-Einstein condensates" (1999). arXiv: cond-mat/9904034.

[8] W. Ketterle and M. W. Zwierlein. "Making, probing and understanding ultracold Fermi gases" (2008). arXiv: 0801.2500.

[9] The Nobel Prize in Physics 1997. NobelPrize.org. Nobel Media AB 2020. Wed. 20 May 2020. https://www.nobelprize.org/prizes/physics/1997/summary/.

[10] M. H. Anderson et al. "Observation of Bose-Einstein Condensation in a Dilute Atomic Vapor". *Science* **269** (1995), 198–201. DOI: 10.1126/science.269.5221.198.

[11] K. B. Davis et al. "Bose-Einstein Condensation in a Gas of Sodium Atoms". *Phys. Rev. Lett.* **75** (1995), 3969–3973. DOI: 10.1103/PhysRevLett.75.3969.

[12] M. R. Andrews et al. "Observation of Interference Between Two Bose Condensates". *Science* **275** (1997), 637–641. DOI: 10.1126/science.275.5300.637.

[13] M. R. Matthews et al. "Vortices in a Bose-Einstein Condensate". *Phys. Rev. Lett.* **83** (1999), 2498–2501. DOI: 10.1103/PhysRevLett.83.2498.

[14] K. W. Madison et al. "Vortex Formation in a Stirred Bose-Einstein Condensate". *Phys. Rev. Lett.* **84** (2000), 806–809. DOI: 10.1103/PhysRevLett.84.806.

[15] J. R. Abo-Shaeer et al. “Observation of Vortex Lattices in Bose-Einstein Condensates”. *Science* **292** (2001), 476–479. DOI: 10.1126/science.1060182.

[16] The Nobel Prize in Physics 2001. NobelPrize.org. Nobel Media AB 2020. Thu. 21 May 2020. https://www.nobelprize.org/prizes/physics/2001/summary/.

[17] B. DeMarco and D. S. Jin. “Onset of Fermi Degeneracy in a Trapped Atomic Gas”. *Science* **285** (1999), 1703–1706. DOI: 10.1126/science.285.5434.1703.

[18] K. M. O’Hara et al. “Observation of a Strongly Interacting Degenerate Fermi Gas of Atoms”. *Science* **298** (2002), 2179–2182. DOI: 10.1126/science.1079107.

[19] M. Greiner, C. A. Regal, and D. S. Jin. “Emergence of a molecular Bose–Einstein condensate from a Fermi gas”. *Nature* **426** (2003), 537–540. DOI: 10.1038/nature02199.

[20] S. Jochim et al. “Bose-Einstein Condensation of Molecules”. *Science* **302** (2003), 2101–2103. DOI: 10.1126/science.1093280.

[21] M. W. Zwierlein et al. “Observation of Bose-Einstein Condensation of Molecules”. *Phys. Rev. Lett.* **91** (2003), 250401. DOI: 10.1103/PhysRevLett.91.250401.

[22] D. G. Fried et al. “Bose-Einstein Condensation of Atomic Hydrogen”. *Phys. Rev. Lett.* **81** (1998), 3811–3814. DOI: 10.1103/PhysRevLett.81.3811.

[23] C. C. Bradley et al. “Evidence of Bose-Einstein Condensation in an Atomic Gas with Attractive Interactions”. *Phys. Rev. Lett.* **75** (1995), 1687–1690. DOI: 10.1103/PhysRevLett.75.1687.

[24] G. Modugno et al. “Bose-Einstein Condensation of Potassium Atoms by Sympathetic Cooling”. *Science* **294** (2001), 1320–1322. DOI: 10.1126/science.1066687.

[25] T. Weber et al. “Bose-Einstein Condensation of Cesium”. *Science* **299** (2003), 232–235. DOI: 10.1126/science.1079699.

[26] S. Kraft et al. “Bose-Einstein Condensation of Alkaline Earth Atoms: ^{40}Ca”. *Phys. Rev. Lett.* **103** (2009), 130401. DOI: 10.1103/PhysRevLett.103.130401.

[27] S. Stellmer et al. “Bose-Einstein Condensation of Strontium”. *Phys. Rev. Lett.* **103** (2009), 200401. DOI: 10.1103/PhysRevLett.103.200401.

[28] A. Griesmaier et al. “Bose-Einstein Condensation of Chromium”. *Phys. Rev. Lett.* **94** (2005), 160401. DOI: 10.1103/PhysRevLett.94.160401.

[29] M. Lu et al. “Strongly Dipolar Bose-Einstein Condensate of Dysprosium”. *Phys. Rev. Lett.* **107** (2011), 190401. DOI: 10.1103/PhysRevLett.107.190401.

[30] K. Aikawa et al. “Bose-Einstein Condensation of Erbium”. *Phys. Rev. Lett.* **108** (2012), 210401. DOI: 10.1103/PhysRevLett.108.210401.

[31] E. T. Davletov et al. “Machine learning for achieving Bose-Einstein condensation of thulium atoms”. *Phys. Rev. A* **102** (2020), 011302. DOI: 10.1103/PhysRevA.102.011302.

[32] Y. Takasu et al. “Spin-Singlet Bose-Einstein Condensation of Two-Electron Atoms”. *Phys. Rev. Lett.* **91** (2003), 040404. DOI: 10.1103/PhysRevLett.91.040404.

[33] A. Robert et al. “A Bose-Einstein Condensate of Metastable Atoms”. *Science* **292** (2001), 461–464. DOI: 10.1126/science.1060622.

[34] A. G. Truscott et al. “Observation of Fermi Pressure in a Gas of Trapped Atoms”. *Science* **291** (2001), 2570–2572. DOI: 10.1126/science.1059318.

[35] B. J. DeSalvo et al. “Degenerate Fermi Gas of ^{87}Sr”. *Phys. Rev. Lett.* **105** (2010), 030402. DOI: 10.1103/PhysRevLett.105.030402.

[36] B. Naylor et al. “Chromium dipolar Fermi sea”. *Phys. Rev. A* **91** (2015), 011603. DOI: 10.1103/PhysRevA.91.011603.

[37] M. Lu, N. Q. Burdick, and B. L. Lev. “Quantum Degenerate Dipolar Fermi Gas”. *Phys. Rev. Lett.* **108** (2012), 215301. DOI: 10.1103/PhysRevLett.108.215301.

[38] K. Aikawa et al. “Reaching Fermi Degeneracy via Universal Dipolar Scattering”. *Phys. Rev. Lett.* **112** (2014), 010404. DOI: 10.1103/PhysRevLett.112.010404.

[39] T. Fukuhara et al. “Degenerate Fermi Gases of Ytterbium”. *Phys. Rev. Lett.* **98** (2007), 030401. DOI: 10.1103/PhysRevLett.98.030401.

[40] W. Vassen et al. “Production of a degenerate Fermi gas of metastable helium-3 atoms” (2006). arXiv: cond-mat/0610414.

[41] I. Bloch, J. Dalibard, and S. Nascimbène. “Quantum simulations with ultracold quantum gases”. *Nature Physics* **8** (2012), 267–276. DOI: 10.1038/nphys2259.

[42] L. Pezzè et al. “Quantum metrology with nonclassical states of atomic ensembles”. *Rev. Mod. Phys.* **90** (2018), 035005. DOI: 10.1103/RevModPhys.90.035005.

[43] S. L. Campbell et al. “A Fermi-degenerate three-dimensional optical lattice clock”. *Science* **358** (2017), 90–94. DOI: 10.1126/science.aam5538.

[44] R. Grimm, M. Weidemüller, and Y. B. Ovchinnikov. “Optical Dipole Traps for Neutral Atoms”. *Advances In Atomic, Molecular, and Optical Physics* **42** (2000), 95–170. DOI: 10.1016/S1049-250X(08)60186-X.

[45] M. Greiner et al. “Quantum phase transition from a superfluid to a Mott insulator in a gas of ultracold atoms”. *Nature* **415** (2002), 39–44. DOI: 10.1038/415039a.

[46] W. S. Bakr et al. “Probing the Superfluid–to–Mott Insulator Transition at the Single-Atom Level”. *Science* **329** (2010), 547–550. DOI: 10.1126/science.1192368.

[47] J. F. Sherson et al. “Single-atom-resolved fluorescence imaging of an atomic Mott insulator”. *Nature* **467** (2010), 68–72. DOI: 10.1038/nature09378.

[48] A. Mazurenko et al. “A cold-atom Fermi–Hubbard antiferromagnet”. *Nature* **545** (2017), 462–466. DOI: 10.1038/nature22362.

[49] C. Chin et al. “Feshbach resonances in ultracold gases”. *Rev. Mod. Phys.* **82** (2010), 1225–1286. DOI: 10.1103/RevModPhys.82.1225.

[50] G. Modugno et al. “Two Atomic Species Superfluid”. *Phys. Rev. Lett.* **89** (2002), 190404. DOI: 10.1103/PhysRevLett.89.190404.

[51] Z. Hadzibabic et al. “Two-Species Mixture of Quantum Degenerate Bose and Fermi Gases”. *Phys. Rev. Lett.* **88** (2002), 160401. DOI: 10.1103/PhysRevLett.88.160401.

[52] M. Taglieber et al. “Quantum Degenerate Two-Species Fermi-Fermi Mixture Coexisting with a Bose-Einstein Condensate”. *Phys. Rev. Lett.* **100** (2008), 010401. DOI: 10.1103/PhysRevLett.100.010401.

[53] K.-K. Ni et al. "A High Phase-Space-Density Gas of Polar Molecules". *Science* **322** (2008), 231–235. DOI: 10.1126/science.1163861.

[54] T. Takekoshi et al. "Ultracold Dense Samples of Dipolar RbCs Molecules in the Rovibrational and Hyperfine Ground State". *Phys. Rev. Lett.* **113** (2014), 205301. DOI: 10.1103/PhysRevLett.113.205301.

[55] P. K. Molony et al. "Creation of Ultracold $^{87}Rb^{133}Cs$ Molecules in the Rovibrational Ground State". *Phys. Rev. Lett.* **113** (2014), 255301. DOI: 10.1103/PhysRevLett.113.255301.

[56] J. W. Park, S. A. Will, and M. W. Zwierlein. "Ultracold Dipolar Gas of Fermionic $^{23}Na^{40}K$ Molecules in Their Absolute Ground State". *Phys. Rev. Lett.* **114** (2015), 205302. DOI: 10.1103/PhysRevLett.114.205302.

[57] L. De Marco et al. "A degenerate Fermi gas of polar molecules". *Science* **363** (2019), 853–856. DOI: 10.1126/science.aau7230.

[58] L. D. Carr et al. "Cold and ultracold molecules: science, technology and applications". *New Journal of Physics* **11** (2009), 055049. DOI: 10.1088/1367-2630/11/5/055049.

[59] E. S. Shuman, J. F. Barry, and D. DeMille. "Laser cooling of a diatomic molecule". *Nature* **467** (2010), 820–823. DOI: 10.1038/nature09443.

[60] J. F. Barry et al. "Magneto-optical trapping of a diatomic molecule". *Nature* **512** (2014), 286–289. DOI: 10.1038/nature13634.

[61] D. J. McCarron et al. "Magnetic Trapping of an Ultracold Gas of Polar Molecules". *Phys. Rev. Lett.* **121** (2018), 013202. DOI: 10.1103/PhysRevLett.121.013202.

[62] M. T. Hummon et al. "2D Magneto-Optical Trapping of Diatomic Molecules". *Phys. Rev. Lett.* **110** (2013), 143001. DOI: 10.1103/PhysRevLett.110.143001.

[63] V. Zhelyazkova et al. "Laser cooling and slowing of CaF molecules". *Phys. Rev. A* **89** (2014), 053416. DOI: 10.1103/PhysRevA.89.053416.

[64] S. Truppe et al. "Molecules cooled below the Doppler limit". *Nature Physics* **13** (2017), 1173–1176. DOI: 10.1038/nphys4241.

[65] L. Baum et al. "1D Magneto-Optical Trap of Polyatomic Molecules". *Phys. Rev. Lett.* **124** (2020), 133201. DOI: 10.1103/PhysRevLett.124.133201.

[66] T. Lahaye et al. "The physics of dipolar bosonic quantum gases". *Rep. Prog. Phys.* **72** (2009), 126401. DOI: 10.1088/0034-4885/72/12/126401.

[67] M. Fattori et al. "Demagnetization cooling of a gas". *Nature Physics* **2** (2006), 765–768. DOI: 10.1038/nphys443.

[68] T. Lahaye et al. "Strong dipolar effects in a quantum ferrofluid". *Nature* **448** (2007), 672–675. DOI: 10.1038/nature06036.

[69] T. Koch et al. "Stabilization of a purely dipolar quantum gas against collapse". *Nature Physics* **4** (2008), 218–222. DOI: 10.1038/nphys887.

[70] T. Lahaye et al. "*d*-Wave Collapse and Explosion of a Dipolar Bose-Einstein Condensate". *Phys. Rev. Lett.* **101** (2008), 080401. DOI: 10.1103/PhysRevLett.101.080401.

[71] J. J. McClelland and J. L. Hanssen. "Laser Cooling without Repumping: A Magneto-Optical Trap for Erbium Atoms". *Phys. Rev. Lett.* **96** (2006), 143005. DOI: 10.1103/PhysRevLett.96.143005.

[72] A. J. Berglund, J. L. Hanssen, and J. J. McClelland. "Narrow-Line Magneto-Optical Cooling and Trapping of Strongly Magnetic Atoms". *Phys. Rev. Lett.* **100** (2008), 113002. DOI: 10.1103/PhysRevLett.100.113002.

[73] M. Lu, S. H. Youn, and B. L. Lev. "Trapping Ultracold Dysprosium: A Highly Magnetic Gas for Dipolar Physics". *Phys. Rev. Lett.* **104** (2010), 063001. DOI: 10.1103/PhysRevLett.104.063001.

[74] A. Frisch et al. "Narrow-line magneto-optical trap for erbium". *Phys. Rev. A* **85** (2012), 051401. DOI: 10.1103/PhysRevA.85.051401.

[75] T. Maier et al. "Narrow-line magneto-optical trap for dysprosium atoms". *Opt. Lett.* **39** (2014), 3138–3141. DOI: 10.1364/OL.39.003138.

[76] K. Baumann et al. "Observation of low-field Fano-Feshbach resonances in ultracold gases of dysprosium". *Phys. Rev. A* **89** (2014), 020701. DOI: 10.1103/PhysRevA.89.020701.

[77] A. Frisch et al. "Quantum chaos in ultracold collisions of gas-phase erbium atoms". *Nature* **507** (2014), 475–479. DOI: 10.1038/nature13137.

[78] T. Maier et al. "Emergence of Chaotic Scattering in Ultracold Er and Dy". *Phys. Rev. X* **5** (2015), 041029. DOI: 10.1103/PhysRevX.5.041029.

[79] J. R. Rumble, ed. *CRC handbook of chemistry and physics: a ready-reference book of chemical and physical data*. 100th ed. CRC Press, Taylor & Francis Group, 2019. ISBN: 9781138367296.

[80] W. C. Martin, R. Zalubas, and L. Hagan. *Atomic Energy Levels – The Rare-Earth Elements*. in Nat. Stand. Ref. Data Ser. , NSRDS-NBS 60, 422 pp. (Nat. Bur. Stand. , U. S. , 1978). DOI: 10.6028/NBS.NSRDS.60.

[81] V. A. Finkel' and V. V. Vorob'ev. "Crystal Structure of Dysprosium at 77-300°K". *Zh. Eksp. Teor. Fiz.* **51** (1966), 786–790. (Sov. Phys. - JETP, 1967, v. 24, n. 3, p. 524–526).

[82] V. A. Finkel' and M. I. Palatnik. "Crystal Structure of Holmium and Erbium between 77° and 300°K". *Zh. Eksp. Teor. Fiz.* **59** (1970), 1518–1523. (Sov. Phys. - JETP, 1971, v. 32, n. 5, p. 828–831).

[83] C. J. Foot. *Atomic Physics*. Oxford Master Series in Atomic, Optical and Laser Physics. Oxford University Press, 2014. ISBN: 9780198506966.

[84] S. H. Youn et al. "Dysprosium magneto-optical traps". *Phys. Rev. A* **82** (2010), 043425. DOI: 10.1103/PhysRevA.82.043425.

[85] B. R. Judd and I. Lindgren. "Theory of Zeeman Effect in the Ground Multiplets of Rare-Earth Atoms". *Phys. Rev.* **122** (1961), 1802–1812. DOI: 10.1103/PhysRev.122.1802.

[86] J. G. Conway and B. G. Wybourne. "Low-Lying Energy Levels of Lanthanide Atoms and Intermediate Coupling". *Phys. Rev.* **130** (1963), 2325–2332. DOI: 10.1103/PhysRev.130.2325.

[87] A. Kramida et al. NIST Atomic Spectra Database (ver. 5.7.1), [Online]. Available: https://physics.nist.gov/asd [2020, February 27]. National Institute of Standards and Technology, Gaithersburg, MD. 2019. DOI: https://doi.org/10.18434/T4W30F.

[88] P. Ilzhöfer et al. "Two-species five-beam magneto-optical trap for erbium and dysprosium". *Phys. Rev. A* **97** (2018), 023633. DOI: 10.1103/PhysRevA.97.023633.

[89] A. Frisch. "Dipolar Quantum Gases of Erbium". PhD Thesis. University of Innsbruck, 2014.

[90] M. Lu, S. H. Youn, and B. L. Lev. "Spectroscopy of a narrow-line laser-cooling transition in atomic dysprosium". *Phys. Rev. A* **83** (2011), 012510. DOI: 10.1103/PhysRevA.83.012510.

[91] J. E. Lawler, J.-F. Wyart, and E. A. Den Hartog. "Atomic transition probabilities of Er i". *J. Phys. B: At. Mol. Opt. Phys.* **43** (2010), 235001. DOI: 10.1088/0953-4075/43/23/235001.

[92] D. Dreon et al. "Optical cooling and trapping of highly magnetic atoms: the benefits of a spontaneous spin polarization". *J. Phys. B: At. Mol. Opt. Phys.* **50** (2017), 065005. DOI: 10.1088/1361-6455/aa5db5.

[93] R. Inoue, Y. Miyazawa, and M. Kozuma. "Magneto-optical trapping of optically pumped metastable europium". *Phys. Rev. A* **97** (2018), 061607. DOI: 10.1103/PhysRevA.97.061607.

[94] C. S. Adams and I. G. Hughes. *Optics f2f From Fourier to Fresnel*. 1st ed. Oxford University Press, 2019. ISBN: 9780198786795.

[95] H. Haken and H. C. Wolf. *Molecular Physics and Elements of Quantum Chemistry: Introduction to Experiments and Theory*. 2nd ed. Springer-Verlag, 2004. ISBN: 9783642074004.

[96] R. W. Boyd. *Nonlinear Optics*. 3rd ed. Academic Press, 2008. ISBN: 9780123694706.

[97] J. H. Becher et al. "Anisotropic polarizability of erbium atoms". *Phys. Rev. A* **97** (2018), 012509. DOI: 10.1103/PhysRevA.97.012509.

[98] M. Lepers, J.-F. Wyart, and O. Dulieu. "Anisotropic optical trapping of ultracold erbium atoms". *Phys. Rev. A* **89** (2014), 022505. DOI: 10.1103/PhysRevA.89.022505.

[99] H. Li et al. "Optical trapping of ultracold dysprosium atoms: transition probabilities, dynamic dipole polarizabilities and van der Waals C_6 coefficients". *J. Phys. B: At. Mol. Opt. Phys.* **50** (2017), 014005. DOI: 10.1088/1361-6455/50/1/014005.

[100] R. Dumke et al. "Micro-optical Realization of Arrays of Selectively Addressable Dipole Traps: A Scalable Configuration for Quantum Computation with Atomic Qubits". *Phys. Rev. Lett.* **89** (2002), 097903. DOI: 10.1103/PhysRevLett.89.097903.

[101] J. Kruse et al. "Reconfigurable site-selective manipulation of atomic quantum systems in two-dimensional arrays of dipole traps". *Phys. Rev. A* **81** (2010), 060308. DOI: 10.1103/PhysRevA.81.060308.

[102] I. Bloch. "Ultracold quantum gases in optical lattices". *Nature Physics* **1** (2005), 23–30. DOI: 10.1038/nphys138.

[103] H. Katori et al. "Ultrastable Optical Clock with Neutral Atoms in an Engineered Light Shift Trap". *Phys. Rev. Lett.* **91** (2003), 173005. DOI: 10.1103/PhysRevLett.91.173005.

[104] M. Takamoto et al. "An optical lattice clock". *Nature* **435** (2005), 321–324. DOI: 10.1038/nature03541.

[105] J. Sebby-Strabley et al. "Lattice of double wells for manipulating pairs of cold atoms". *Phys. Rev. A* **73** (2006), 033605. DOI: 10.1103/PhysRevA.73.033605.

[106] L. J. LeBlanc and J. H. Thywissen. "Species-specific optical lattices". *Phys. Rev. A* **75** (2007), 053612. DOI: 10.1103/PhysRevA.75.053612.

[107] M. Lepers. Private Communication.

[108] C. Ravensbergen et al. "Accurate Determination of the Dynamical Polarizability of Dysprosium". *Phys. Rev. Lett.* **120** (2018), 223001. DOI: 10.1103/PhysRevLett.120.223001.

[109] Y. Castin. *Bose-Einstein Condensates in Atomic Gases: Simple Theoretical Results.* Coherent atomic matter waves (Kaiser R., Westbrook C., David F. (eds)). Springer Berlin Heidelberg. ISBN: 9783540410478. DOI: 10.1007/3-540-45338-5_1.

[110] L. Pitaevskii and S. Stringari. *Bose-Einstein Condensation and Superfluidity.* 1st ed. International Series of Monographs on Physics. Oxford University Press, 2016. ISBN: 9780198758884.

[111] S. Hensler et al. "Dipolar relaxation in an ultra-cold gas of magnetically trapped chromium atoms". *Appl. Phys. B* **77** (2003), 765–772. DOI: 10.1007/s00340-003-1334-0.

[112] A. Petrov, E. Tiesinga, and S. Kotochigova. "Anisotropy-Induced Feshbach Resonances in a Quantum Dipolar Gas of Highly Magnetic Atoms". *Phys. Rev. Lett.* **109** (2012), 103002. DOI: 10.1103/PhysRevLett.109.103002.

[113] S. Kotochigova. "Controlling interactions between highly magnetic atoms with Feshbach resonances". *Rep. Prog. Phys.* **77** (2014), 093901. DOI: 10.1088/0034-4885/77/9/093901.

[114] V. A. Khlebnikov et al. "Random to Chaotic Statistic Transformation in Low-Field Fano-Feshbach Resonances of Cold Thulium Atoms". *Phys. Rev. Lett.* **123** (2019), 213402. DOI: 10.1103/PhysRevLett.123.213402.

[115] Y. Tang et al. "Tuning the Dipole-Dipole Interaction in a Quantum Gas with a Rotating Magnetic Field". *Phys. Rev. Lett.* **120** (2018), 230401. DOI: 10.1103/PhysRevLett.120.230401.

[116] L. Santos, G. V. Shlyapnikov, and M. Lewenstein. "Roton-Maxon Spectrum and Stability of Trapped Dipolar Bose-Einstein Condensates". *Phys. Rev. Lett.* **90** (2003), 250403. DOI: 10.1103/PhysRevLett.90.250403.

[117] A. Trautmann et al. "Dipolar Quantum Mixtures of Erbium and Dysprosium Atoms". *Phys. Rev. Lett.* **121** (2018), 213601. DOI: 10.1103/PhysRevLett.121.213601.

[118] G. F. Vander Voort. *Metallography and Microstructures*. Vol. 9. ASM International, 2004. ISBN: 978-1-62708-177-1.

[119] J. Schindler. "Characterization of an Erbium Atomic Beam". Master's Thesis. University of Innsbruck, 2011.

[120] H. J. Metcalf and P. van der Straten. *Laser Cooling and Trapping*. Springer-Verlag, 1999. ISBN: 9780387987286.

[121] W. D. Phillips and H. Metcalf. "Laser Deceleration of an Atomic Beam". *Phys. Rev. Lett.* **48** (1982), 596–599. DOI: 10.1103/PhysRevLett.48.596.

[122] J. H. Shirley. "Modulation transfer processes in optical heterodyne saturation spectroscopy". *Opt. Lett.* **7** (1982), 537–539. DOI: 10.1364/OL.7.000537.

[123] A. Frisch et al. "Hyperfine structure of laser-cooling transitions in fermionic erbium-167". *Phys. Rev. A* **88** (2013), 032508. DOI: 10.1103/PhysRevA.88.032508.

[124] T. Maier. "Interactions in a Quantum Gas of Dysprosium Atoms". PhD Thesis. University of Stuttgart, 2015.

[125] G. D. Boyd and D. A. Kleinman. "Parametric Interaction of Focused Gaussian Light Beams". *J. Appl. Phys.* **39** (1968), 3597–3639. DOI: 10.1063/1.1656831.

[126] R. W. P. Drever et al. "Laser phase and frequency stabilization using an optical resonator". *Appl. Phys. B* **31** (1983), 97–105. DOI: 10.1007/BF00702605.

[127] E. D. Black. "An introduction to Pound–Drever–Hall laser frequency stabilization". *Am. J. Phys.* **69** (2001), 79–87. DOI: 10.1119/1.1286663.

[128] A. Patscheider. "Stable Reference Cavity for Er and Dy MOT Light". Master's Thesis. University of Innsbruck, 2017.

[129] E. L. Raab et al. "Trapping of Neutral Sodium Atoms with Radiation Pressure". *Phys. Rev. Lett.* **59** (1987), 2631–2634. DOI: 10.1103/PhysRevLett.59.2631.

[130] T. H. Loftus et al. "Narrow line cooling and momentum-space crystals". *Phys. Rev. A* **70** (2004), 063413. DOI: 10.1103/PhysRevA.70.063413.

[131] W. Ketterle and N. J. Van Druten. "Evaporative Cooling of Trapped Atoms". *Advances In Atomic, Molecular, and Optical Physics* **37** (1996), 181–236. DOI: 10.1016/S1049-250X(08)60101-9.

[132] C. S. Adams et al. "Evaporative Cooling in a Crossed Dipole Trap". *Phys. Rev. Lett.* **74** (1995), 3577–3580. DOI: 10.1103/PhysRevLett.74.3577.

[133] N. Masuhara et al. "Evaporative Cooling of Spin-Polarized Atomic Hydrogen". *Phys. Rev. Lett.* **61** (1988), 935–938. DOI: 10.1103/PhysRevLett.61.935.

[134] S. Stellmer et al. "Laser Cooling to Quantum Degeneracy". *Phys. Rev. Lett.* **110** (2013), 263003. DOI: 10.1103/PhysRevLett.110.263003.

[135] J. Hu et al. "Creation of a Bose-condensed gas of ^{87}Rb by laser cooling". *Science* **358** (2017), 1078–1080. DOI: 10.1126/science.aan5614.

[136] A. Urvoy et al. "Direct Laser Cooling to Bose-Einstein Condensation in a Dipole Trap". *Phys. Rev. Lett.* **122** (2019), 203202. DOI: 10.1103/PhysRevLett.122.203202.

[137] S. Baier. "An optical dipole trap for Erbium with tunable geometry". Master's Thesis. University of Innsbruck, 2012.

[138] A. F. Andreev and I. M. Lifshitz. "Quantum Theory of Defects in Crystals". *Zh. Eksp. Teor. Fiz.* **56** (1969), 2057–2068. (Sov. Phys. - JETP, 1969, v. 29, n. 6, p. 1107–1113).

[139] G. V. Chester. "Speculations on Bose-Einstein Condensation and Quantum Crystals". *Phys. Rev. A* **2** (1970), 256–258. DOI: 10.1103/PhysRevA.2.256.

[140] A. J. Leggett. "Can a Solid Be "Superfluid"?" *Phys. Rev. Lett.* **25** (1970), 1543–1546. DOI: 10.1103/PhysRevLett.25.1543.

[141] M. Boninsegni and N. V. Prokof'ev. "Colloquium: Supersolids: What and where are they?" *Rev. Mod. Phys.* **84** (2012), 759–776. DOI: 10.1103/RevModPhys.84.759.

[142] E. Kim and M. H. W. Chan. "Probable observation of a supersolid helium phase". *Nature* **427** (2004), 225–227. DOI: 10.1038/nature02220.

[143] E. Kim and M. H. W. Chan. "Observation of Superflow in Solid Helium". *Science* **305** (2004), 1941–1944. DOI: 10.1126/science.1101501.

[144] D. Y. Kim and M. H. W. Chan. "Absence of Supersolidity in Solid Helium in Porous Vycor Glass". *Phys. Rev. Lett.* **109** (2012), 155301. DOI: 10.1103/PhysRevLett.109.155301.

[145] M. H. W. Chan, R. B. Hallock, and L. Reatto. "Overview on Solid ^{4}He and the Issue of Supersolidity". *J. Low Temp. Phys.* **172** (2013), 317–363. DOI: 10.1007/s10909-013-0882-x.

[146] Y. Aoki, H. Kojima, and X. Lin. "Search for fourth sound propagation in supersolid ^{4}He". *Low Temp. Phys.* **34** (2008), 329–339. DOI: 10.1063/1.2911651.

[147] A. Eyal et al. "Search for supersolidity in solid ^{4}He using multiple-mode torsional oscillators". *Proc. Natl. Acad. Sci. U.S.A* **113** (2016), E3203–E3212. DOI: 10.1073/pnas.1605738113.

[148] R. Mottl et al. "Roton-Type Mode Softening in a Quantum Gas with Cavity-Mediated Long-Range Interactions". *Science* **336** (2012), 1570–1573. DOI: 10.1126/science.1220314.

[149] J. Léonard et al. "Supersolid formation in a quantum gas breaking a continuous translational symmetry". *Nature* **543** (2017), 87–90. DOI: 10.1038/nature21067.

[150] J. Léonard et al. "Monitoring and manipulating Higgs and Goldstone modes in a supersolid quantum gas". *Science* **358** (2017), 1415–1418. DOI: 10.1126/science.aan2608.

[151] J.-R. Li et al. "A stripe phase with supersolid properties in spin–orbit-coupled Bose–Einstein condensates". *Nature* **543** (2017), 91–94. DOI: 10.1038/nature21431.

[152] Z.-K. Lu et al. "Stable Dilute Supersolid of Two-Dimensional Dipolar Bosons". *Phys. Rev. Lett.* **115** (2015), 075303. DOI: 10.1103/PhysRevLett.115.075303.

[153] F. Böttcher et al. "Transient Supersolid Properties in an Array of Dipolar Quantum Droplets". *Phys. Rev. X* **9** (2019), 011051. DOI: 10.1103/PhysRevX.9.011051.

[154] L. Tanzi et al. "Observation of a Dipolar Quantum Gas with Metastable Supersolid Properties". *Phys. Rev. Lett.* **122** (2019), 130405. DOI: 10.1103/PhysRevLett.122.130405.

[155] L. Chomaz et al. "Long-Lived and Transient Supersolid Behaviors in Dipolar Quantum Gases". *Phys. Rev. X* **9** (2019), 021012. DOI: 10.1103/PhysRevX.9.021012.

[156] P. B. Blakie, D. Baillie, and R. N. Bisset. "Roton spectroscopy in a harmonically trapped dipolar Bose-Einstein condensate". *Phys. Rev. A* **86** (2012), 021604. DOI: 10.1103/PhysRevA.86.021604.

[157] L. Chomaz et al. "Observation of roton mode population in a dipolar quantum gas". *Nature Physics* **14** (2018), 442–446. DOI: 10.1038/s41567-018-0054-7.

[158] D. Petter et al. "Probing the Roton Excitation Spectrum of a Stable Dipolar Bose Gas". *Phys. Rev. Lett.* **122** (2019), 183401. DOI: 10.1103/PhysRevLett.122.183401.

[159] J. F. Annett. *Superconductivity, Superfluids and Condensates*. Oxford Master Series in Condensed Matter Physics. Oxford University Press, 2012. ISBN: 9780198507567.

[160] H. Kadau et al. "Observing the Rosensweig instability of a quantum ferrofluid". *Nature* **530** (2016), 194–197. DOI: 10.1038/nature16485.

[161] D. S. Petrov. "Quantum Mechanical Stabilization of a Collapsing Bose-Bose Mixture". *Phys. Rev. Lett.* **115** (2015), 155302. DOI: 10.1103/PhysRevLett.115.155302.

[162] R. N. Bisset and P. B. Blakie. "Crystallization of a dilute atomic dipolar condensate". *Phys. Rev. A* **92** (2015), 061603. DOI: 10.1103/PhysRevA.92.061603.

[163] P. B. Blakie. "Properties of a dipolar condensate with three-body interactions". *Phys. Rev. A* **93** (2016), 033644. DOI: 10.1103/PhysRevA.93.033644.

[164] F. Wächtler and L. Santos. "Quantum filaments in dipolar Bose-Einstein condensates". *Phys. Rev. A* **93** (2016), 061603. DOI: 10.1103/PhysRevA.93.061603.

[165] D. Baillie et al. "Self-bound dipolar droplet: A localized matter wave in free space". *Phys. Rev. A* **94** (2016), 021602. DOI: 10.1103/PhysRevA.94.021602.

[166] R. N. Bisset et al. "Ground-state phase diagram of a dipolar condensate with quantum fluctuations". *Phys. Rev. A* **94** (2016), 033619. DOI: 10.1103/PhysRevA.94.033619.

[167] I. Ferrier-Barbut et al. "Observation of Quantum Droplets in a Strongly Dipolar Bose Gas". *Phys. Rev. Lett.* **116** (2016), 215301. DOI: 10.1103/PhysRevLett.116.215301.

[168] M. Schmitt et al. "Self-bound droplets of a dilute magnetic quantum liquid". *Nature* **539** (2016), 259–262. DOI: 10.1038/nature20126.

[169] L. Chomaz et al. "Quantum-Fluctuation-Driven Crossover from a Dilute Bose-Einstein Condensate to a Macrodroplet in a Dipolar Quantum Fluid". *Phys. Rev. X* **6** (2016), 041039. DOI: 10.1103/PhysRevX.6.041039.

[170] G. Natale et al. "Excitation Spectrum of a Trapped Dipolar Supersolid and Its Experimental Evidence". *Phys. Rev. Lett.* **123** (2019), 050402. DOI: 10.1103/PhysRevLett.123.050402.

[171] L. Tanzi et al. "Supersolid symmetry breaking from compressional oscillations in a dipolar quantum gas". *Nature* **574** (2019), 382–385. DOI: 10.1038/s41586-019-1568-6.

[172] J. Hertkorn et al. "Fate of the Amplitude Mode in a Trapped Dipolar Supersolid". *Phys. Rev. Lett.* **123** (2019), 193002. DOI: 10.1103/PhysRevLett.123.193002.

[173] M. Guo et al. "The low-energy Goldstone mode in a trapped dipolar supersolid". *Nature* **574** (2019), 386–389. DOI: 10.1038/s41586-019-1569-5.

[174] S. M. Roccuzzo et al. "Rotating a Supersolid Dipolar Gas". *Phys. Rev. Lett.* **124** (2020), 045702. DOI: 10.1103/PhysRevLett.124.045702.

[175] L. Tanzi et al. "Evidence of superfluidity in a dipolar supersolid from non-classical rotational inertia" (2019). arXiv: 1912.01910.

[176] D. Petter et al. "High-energy Bragg scattering measurements of a dipolar supersolid" (2020). arXiv: 2005.02213.

[177] P. Ilzhöfer et al. "Phase coherence in out-of-equilibrium supersolid states of ultracold dipolar atoms" (2019). arXiv: 1912.10892.

[178] G. Durastante et al. "Feshbach Resonances in an Erbium-Dysprosium Dipolar Mixture" (2020). arXiv: 2006.06456.

[179] A. Mosk et al. "Mixture of ultracold lithium and cesium atoms in an optical dipole trap". *Appl. Phys. B* **73** (2001), 791–799. DOI: 10.1007/s003400100743.

[180] C. Ravensbergen et al. "Production of a degenerate Fermi-Fermi mixture of dysprosium and potassium atoms". *Phys. Rev. A* **98** (2018), 063624. DOI: 10.1103/PhysRevA.98.063624.

[181] G. Gligorić et al. "Transition to miscibility in linearly coupled binary dipolar Bose-Einstein condensates". *Phys. Rev. A* **82** (2010), 033624. DOI: 10.1103/PhysRevA.82.033624.

[182] R. K. Kumar et al. "Miscibility in coupled dipolar and non-dipolar Bose–Einstein condensates". *J. Phys. Commun.* **1** (2017), 035012. DOI: 10.1088/2399-6528/aa8db5.

[183] R. K. Kumar, L. Tomio, and A. Gammal. "Spatial separation of rotating binary Bose-Einstein condensates by tuning the dipolar interactions". *Phys. Rev. A* **99** (2019), 043606. DOI: 10.1103/PhysRevA.99.043606.

[184] L. Tomio, R. K. Kumar, and A. Gammal. "Dipolar condensed atomic mixtures and miscibility under rotation" (2019). arXiv: 1911.02734.

[185] M. W. Zwierlein et al. "Vortices and superfluidity in a strongly interacting Fermi gas". *Nature* **435** (2005), 1047–1051. DOI: 10.1038/nature03858.

[186] R. K. Kumar et al. "Vortex lattices in binary Bose-Einstein condensates with dipole-dipole interactions". *Phys. Rev. A* **96** (2017), 063624. DOI: 10.1103/PhysRevA.96.063624.

[187] R. K. Kumar, L. Tomio, and A. Gammal. "Vortex patterns in rotating dipolar Bose–Einstein condensate mixtures with squared optical lattices". *J. Phys. B: At. Mol. Opt. Phys.* **52** (2018), 025302. DOI: 10.1088/1361-6455/aaf332.

[188] A.-C. Lee et al. "Excitations of a vortex line in an elongated dipolar condensate". *Phys. Rev. A* **98** (2018), 063620. DOI: 10.1103/PhysRevA.98.063620.

[189] T. F. Gallagher. *Rydberg Atoms*. Cambridge Monographs on Atomic, Molecular and Chemical Physics. Cambridge University Press, 2005. ISBN: 9780521021661.

[190] N. Šibalić and C. S Adams. *Rydberg Physics*. 2399-2891. IOP Publishing, 2018. ISBN: 978-0-7503-1635-4. DOI: 10.1088/978-0-7503-1635-4.

[191] M. D. Lukin et al. "Dipole Blockade and Quantum Information Processing in Mesoscopic Atomic Ensembles". *Phys. Rev. Lett.* **87** (2001), 037901. DOI: 10.1103/PhysRevLett.87.037901.

[192] E. Urban et al. "Observation of Rydberg blockade between two atoms". *Nature Physics* **5** (2009), 110–114. DOI: 10.1038/nphys1178.

[193] A. Gaëtan et al. "Observation of collective excitation of two individual atoms in the Rydberg blockade regime". *Nature Physics* **5** (2009), 115–118. DOI: 10.1038/nphys1183.

[194] J. A. Sedlacek et al. "Microwave electrometry with Rydberg atoms in a vapour cell using bright atomic resonances". *Nature Physics* **8** (2012), 819–824. DOI: 10.1038/nphys2423.

[195] C. G. Wade et al. "Real-time near-field terahertz imaging with atomic optical fluorescence". *Nature Photonics* **11** (2017), 40–43. DOI: 10.1038/nphoton.2016.214.

[196] F. Ripka et al. "A room-temperature single-photon source based on strongly interacting Rydberg atoms". *Science* **362** (2018), 446–449. DOI: 10.1126/science.aau1949.

[197] C. H. Greene, A. S. Dickinson, and H. R. Sadeghpour. "Creation of Polar and Nonpolar Ultra-Long-Range Rydberg Molecules". *Phys. Rev. Lett.* **85** (2000), 2458–2461. DOI: 10.1103/PhysRevLett.85.2458.

[198] V. Bendkowsky et al. "Observation of ultralong-range Rydberg molecules". *Nature* **458** (2009), 1005–1008. DOI: 10.1038/nature07945.

[199] L. Béguin et al. "Direct Measurement of the van der Waals Interaction between Two Rydberg Atoms". *Phys. Rev. Lett.* **110** (2013), 263201. DOI: 10.1103/PhysRevLett.110.263201.

[200] L. Isenhower et al. "Demonstration of a Neutral Atom Controlled-NOT Quantum Gate". *Phys. Rev. Lett.* **104** (2010), 010503. DOI: 10.1103/PhysRevLett.104.010503.

[201] Y. O. Dudin and A. Kuzmich. "Strongly Interacting Rydberg Excitations of a Cold Atomic Gas". *Science* **336** (2012), 887–889. DOI: 10.1126/science.1217901.

[202] T. Peyronel et al. "Quantum nonlinear optics with single photons enabled by strongly interacting atoms". *Nature* **488** (2012), 57–60. DOI: 10.1038/nature11361.

[203] H. Gorniaczyk et al. "Single-Photon Transistor Mediated by Interstate Rydberg Interactions". *Phys. Rev. Lett.* **113** (2014), 053601. DOI: 10.1103/PhysRevLett.113.053601.

[204] D. Tiarks et al. "Single-Photon Transistor Using a Förster Resonance". *Phys. Rev. Lett.* **113** (2014), 053602. DOI: 10.1103/PhysRevLett.113.053602.

[205] J. Millen, G. Lochead, and M. P. A. Jones. "Two-Electron Excitation of an Interacting Cold Rydberg Gas". *Phys. Rev. Lett.* **105** (2010), 213004. DOI: 10.1103/PhysRevLett.105.213004.

[206] P. McQuillen et al. “Imaging the evolution of an ultracold strontium Rydberg gas”. *Phys. Rev. A* **87** (2013), 013407. DOI: 10.1103/PhysRevA.87.013407.

[207] J. Wilson et al. “Trapped arrays of alkaline earth Rydberg atoms in optical tweezers” (2019). arXiv: 1912.08754.

[208] M. Saffman and K. Mølmer. “Scaling the neutral-atom Rydberg gate quantum computer by collective encoding in holmium atoms”. *Phys. Rev. A* **78** (2008), 012336. DOI: 10.1103/PhysRevA.78.012336.

[209] A. Trautmann. Private Communication.

[210] H. Bernien et al. “Probing many-body dynamics on a 51-atom quantum simulator”. *Nature* **551** (2017), 579–584. DOI: 10.1038/nature24622.

[211] H. Labuhn et al. “Tunable two-dimensional arrays of single Rydberg atoms for realizing quantum Ising models”. *Nature* **534** (2016), 667–670. DOI: 10.1038/nature18274.

[212] M. A. Norcia, A. W. Young, and A. M. Kaufman. “Microscopic Control and Detection of Ultracold Strontium in Optical-Tweezer Arrays”. *Phys. Rev. X* **8** (2018), 041054. DOI: 10.1103/PhysRevX.8.041054.

[213] A. Cooper et al. “Alkaline-Earth Atoms in Optical Tweezers”. *Phys. Rev. X* **8** (2018), 041055. DOI: 10.1103/PhysRevX.8.041055.

Acknowledgments

Finally, I would like to take the opportunity and acknowledge and thank all the people without whose support and contributions over the past five years this PhD thesis would not have been possible.

First of all, I would like to thank my supervisor Francesca Ferlaino for the opportunity to pursue a PhD in her research group. Thank you for your trust in me to lay and shape the foundation of this ambitious project as the very first PhD student. I truly hope that this new experimental apparatus will push the frontiers to unexplored areas and will provide the right answers for many more years to come.

It is hardly possible to build and operate such a complex experimental apparatus alone, therefore a big thank you to the RARE team, our senior scientist Manfred J. Mark, our first Postdoc Arno Trautmann, and to my fellow PhD students Gianmaria Durastante, Maximilian Sohmen and Claudia Politi. Looking at the work over the past five years, all this was only possible thanks to the hard work and commitment of all of us. I wish you all, including the new team members Matthew Norcia and Lauritz Klaus, an absolutely successful time and many exciting scientific questions to explore.

I would especially like to thank Arno. You absolutely made sure that I will remember your strong opinions on random topics and the many new insights into LaTeX. Our countless long nights and weekends in the lab were an absolute pleasure, I just want to recall our successful run when we were able to condense various mixtures during a single night simply in the spirit of *condensing heavy metals with heavy metal*.

I also would like to thank Max. Your tireless dedication to guide us to Innsbruck's famous karaoke bar resulted in many memorable nights out. Many thanks also for proofreading this PhD thesis.

A big thank you also goes to the Erbium team, the postdoc Lauriane Chomaz and the PhD students Daniel Petter, Alexander Patscheider and Gabriele Natale, for many interesting discussions and the big fun during our joint group activities.

I would especially like to thank Alex. It was a great help having you as the first Master student during the construction phase of this experimental apparatus. Without you, it would not have been possible to assemble the entire UHV apparatus in a few days time.

I also would like to express my gratitude to Bernhard Öttl, Andreas Strasser, Stefan Haslwanter and Gerhard Hendl from the mechanical and electronics workshop of the IQOQI Innsbruck. Only your phenomenal work made it possible that many ideas for the experimental apparatus not only remained ideas, but actually became reality.

A special thank you goes to Christian Veit, Matthias Wenzel and Tobias Bäuerle. Looking back to autumn 2009, when the four of us began our studies in Stuttgart, and now in 2020, when eventually all of us will finish this journey with a PhD, makes me realize how far we have come and how many shared memories we have collected over the years.

The very last words of this PhD thesis I would like to devote to my parents and my brother. Without your unconditional support over the years, I would not have been able to pursue my studies in all the freedom I had. From all of my heart - thank you!